UNIVERSITY OF OKLAHOMA

GRADUATE COLLEGE

QUANTIFY THE SPATIO-TEMPORAL VARIABILITY AND CHANGES OF TERRESTRIAL GROSS PRIMARY PRODUCTION ACROSS THE GLOBE DURING 2000-2024

A DISSERTATION

SUBMITTED TO THE GRADUATE FACULTY

in partial fulfillment of the requirements for the

Degree of

DOCTOR OF PHILOSOPHY

By LI PAN
Norman, Oklahoma
2025

QUANTIFY THE SPATIO-TEMPORAL VARIABILITY AND CHANGES OF TERRESTRIAL GROSS PRIMARY PRODUCTION ACROSS THE GLOBE DURING 2000-2024

A DISSERTATION APPROVED FOR THE
SCHOOL OF BIOLOGICAL SCIENCES

BY THE COMMITTEE CONSISTING OF

Dr. Xiangming Xiao, Chair

Dr. Nishan Bhattarai

Dr. Heather McCarthy

Dr. James Hung

Dr. Chongle Pan

Acknowledgements

Time flies. Before I realized it, I had already spent three years in the United States, and now my Ph.D. journey is nearing its end.

OU has always been a dream school for me. When I received an offer from Dr. Xiao, it truly felt like a dream come true. I was thrilled to embark on what I hoped would be an exciting and fulfilling scientific journey. Prior to joining Dr. Xiao's lab, I had only one and a half years of academic experience in the fields of remote sensing and ecology. Yet Dr. Xiao never viewed my background as a limitation. Instead, he patiently guided me through the foundational knowledge of remote sensing. What I remember most clearly is the beginning of my Ph.D. program. Dr. Xiao held morning meetings with us almost every day, even in his extremely busy schedule. That intense and focused period of learning laid the groundwork for all of my future research. It's no exaggeration to say that without Dr. Xiao's patient mentorship and dedication to sharing knowledge, I would not have made it this far. Over the next three years, I came to admire not only Dr. Xiao's academic brilliance, his rigor, vision, creativity, and inclusiveness, but also his encouragement, kindness, and warmth in daily life. His care for both our personality and academic development deeply touched me. Wherever I go in the future, I will always remember Dr. Xiao. His wisdom and character will continue to guide me for years to come.

OU is a vibrant and welcoming place. From the very first day, I was embraced by a community that values freedom, inclusiveness, and equality. Here, I had the

opportunity to learn cutting-edge knowledge from exceptional faculty. I would especially like to thank my committee members, many of whom were also my instructors. Dr. Nishan Bhattarai introduced me to foundational concepts in remote sensing and taught me many valuable skills using Google Earth Engine. Dr. Heather McCarthy deepened my understanding of plant physiology, which was critical for my research. Dr. James Hung and Dr. Chongle Pan also played important roles in shaping my Ph.D. journey through their feedback and guidance.

I also want to thank my colleagues at CEOM: Baihong Pan, Yuan Yao, Cheng Meng, Chenglong Yin, Chengcheng Zhang, Shenglai Yin, and Jorge A. Rodriguez. Their support in both work and life made my time at OU enjoyable and meaningful. Their companionship was one of the key reasons I was able to thrive in OU.

Finally, and most importantly, I owe everything to my family. Without them, I would not be where I am today. Their selfless love, unwavering encouragement, and quiet sacrifices are the pillars that supported me throughout this journey. I am especially grateful to my partner, Jiaqi Li, my girlfriend. Since the day I left for the United States, we have not seen each other in person. Despite the long separation, she has been my unwavering source of strength. She has stood by me longer than anyone else during this journey, and words fail to capture the depth of her impact on my life.

The Ph.D. journey has been long, challenging, and often lonely, but it has also been transformative and deeply rewarding. I will carry the lessons, memories, and gratitude from this chapter with me for the rest of my life.

Table of Contents

List of Tables

List of Figures

ABSTRACT

Gross Primary Production (GPP) is the largest carbon flux in terrestrial ecosystems and plays a critical role in the global carbon cycle, climate regulation, ecosystem integrity, biodiversity maintenance, and food security. The ability to continuously and accurately observe and simulate GPP is fundamental for improving our understanding of biogeochemical feedback, assessing ecosystem responses to environmental change, and informing land management and sustainability strategies. Currently, GPP is primarily derived from eddy covariance flux tower observations and remote sensing-driven model products. However, existing global GPP datasets show considerable disagreement in both magnitude and seasonal dynamics, underscoring the need to improve GPP modeling frameworks for more robust global estimates. Additionally, the impact of natural disturbances (e.g., wildfire) on GPP and its post-disturbance recovery patterns remains poorly understood due to a lack of systematic assessments. This dissertation presents the development, improvement, and application of the Vegetation Photosynthesis Model (VPM), a light use efficiency (LUE) model, as a tool for global GPP estimation. This dissertation addresses two central research questions: (1) Can the newly developed improved versions of the VPM model (v3.0 and v4.0) accurately simulate both the magnitude and seasonal variation of GPP across site and global scales (Chapters 2–5)? (2) How do wildfire disturbances alter ecosystem carbon uptake (GPP), and what are the environmental drivers of post-fire GPP recovery trajectories (Chapters 6–7)? Key findings show that VPM v3.0 can effectively capture observed GPP seasonality at four long-term deciduous broadleaf forest flux tower sites (2000–2020)

and across 205 globally distributed sites (spanning 1658 site-years and 11 biomes), with high agreement to flux data (slope = 0.97, R^2 = 0.78, RMSE = 1.46 g C m^{-2} day^{-1}). The model-derived global GPP was estimated at 143 ± 4 Pg C yr^{-1}, and its 8-day time-series product showed strong agreement with other benchmark GPP datasets (e.g., VPM v2.0, BEPS, MOD17, GOSIF, BESS, and FLUXCOM), with correlation coefficients ranging from 0.88 to 0.95. Further extending the model, I incorporated atmospheric CO_2 effects into VPM to develop VPM v4.0, which produced a higher global GPP estimate of 155 ± 6 Pg C yr^{-1}, aligning with recent global estimations (150-175 Pg C yr^{-1}). The model also captured interannual GPP variability (1.18 Pg C yr^{-1}) and long-term increasing trends (0.78 Pg C yr^{-2}). Using the GPP dataset estimated by VPM v3.0, I investigated the impacts of fire in two contrasting fire-prone regions: Australia and high-latitude forests. In Australia, I found that ecosystems show strong and rapid post-fire GPP recovery, primarily driven by post-fire precipitation. As a result, interannual variations in continental-scale GPP were more influenced by climate and land-use change than by fire, due to effective compensatory recovery. In high-latitude forests, the first-year post-fire GPP recovery rate has declined since the early 2000s, mainly due to intensifying fire severity, increasing temperature, and vapor pressure deficit (VPD), and decreasing soil moisture. Overall, this dissertation highlights the importance of estimating long-term, high-accuracy GPP products and improves our understanding of ecosystem responses to disturbance through a refined modeling framework. The insights gained offer valuable contributions to carbon cycle research and provide actionable tools for evaluating biosphere–atmosphere feedback under ongoing global change.

Chapter 1 : Introduction

1.1 Background

The global carbon cycle is a comprehensive network governing the movement, transformation, and storage of carbon among the atmosphere, oceans, terrestrial biosphere, and lithosphere (Change, 2007; Falkowski et al., 2000). Since the Industrial Revolution, human activities have profoundly altered this cycle. Atmospheric CO_2 concentrations have increased from 278 ppm in the pre-industrial era to over 420 ppm today (Friedlingstein et al., 2024), contributing to a rise in the global average temperature of 0.95°C to 1.2°C (Masson-Delmotte et al., 2021). This rise is largely driven by growing energy demand, abundant fossil fuel reserves, the lack of a globally coordinated strategy for alternative energy production, and continued population growth (Falkowski et al., 2000).

The terrestrial carbon cycle refers to the dynamic processes through which carbon is exchanged and stored between the atmosphere and land ecosystems via photosynthesis, respiration, fire disturbances, and litter decomposition (Friedlingstein et al., 2024). Terrestrial ecosystems absorb atmospheric carbon through photosynthesis and release a comparable amount of CO_2 through plant and soil respiration, making them one of the largest active carbon reservoirs on Earth. Their carbon sink function plays a crucial role in slowing the rise of atmospheric CO_2 concentrations (Beer et al., 2010; Friedlingstein et al., 2024; Pan et al., 2011). Understanding the interannual variability and long-term trends of terrestrial carbon sinks is therefore essential for

achieving national greenhouse gas reduction targets, promoting sustainable development, mitigating climate change, optimizing land use, and implementing ecological restoration strategies (Masson-Delmotte et al., 2021). Currently, terrestrial carbon sinks exhibit large interannual variability across both temporal and spatial scales, representing one of the most significant sources of uncertainty in global carbon cycle projections (Anav et al., 2015; Ryu et al., 2019).

Terrestrial gross primary production (GPP) represents the largest carbon flux within the global land carbon cycle (Beer et al., 2010). As the total flux of carbon fixed by terrestrial vegetation through photosynthesis, GPP is the primary pathway through which atmospheric CO_2 enters land ecosystems (Anav et al., 2015; Frankenberg et al., 2011). It not only defines the upper limit of terrestrial carbon sink potential but also underpins ecosystem respiration, litter decomposition, and the structure of food webs by providing essential carbon and energy inputs (Davidson et al., 2006; Xia et al., 2015). Recent advances estimate global GPP at 150–175 Pg C $year^{-1}$. Its interannual variability strongly influences the terrestrial carbon sink and, in turn, drives year-to-year fluctuations in atmospheric CO_2 concentrations. These CO_2 fluctuations feed back into climate processes, which then further affect GPP, forming a complex system of interactions and feedback (Jian et al., 2022; Lai et al., 2024; Lisa R. Welp et al., 2011a). As such, GPP serves as a critical link between the climate system and terrestrial ecosystems. Continuous and accurate observation and modeling of GPP are essential for advancing understanding of carbon cycling and climate regulation, ecosystem health and biodiversity, global food security and sustainable development, and land

management and restoration strategies (Lieth, 1973).

To date, GPP data have primarily been derived from two primary sources: ground-based observations and model simulations. Among ground-based observations, the eddy covariance (EC) technique is the most widely used for measuring carbon, water, and energy fluxes at the ecosystem and site scales (Chu et al., 2021). EC technique, typically installed on flux towers, records net ecosystem exchange (NEE) (Baldocchi, 2003). Under nighttime conditions, when photosynthesis ceases, NEE approximates ecosystem respiration (R_{eco}). By modeling the relationship between nighttime NEE and temperature, a respiration model can be established and then extrapolated to daytime conditions to estimate daytime respiration. GPP is subsequently calculated as the difference between estimated R_{eco} and measured NEE ($GPP = R_{eco} - NEE$) (Baldocchi, 2020). This method enables continuous, non-destructive monitoring of GPP at the ecosystem scale with high temporal resolution (half-hourly to hourly), offering essential insights into carbon cycle dynamics and the stability of natural carbon sinks (Pastorello et al., 2014). The EC technique has been implemented across numerous sites representing a wide range of biomes, climates, and years, many of which are organized into regional and global flux networks such as FLUXNET and AmeriFlux (Baldocchi, 2014; Baldocchi et al., 2001). However, despite the steady expansion of flux tower installations, the number of operational sites remains limited due to the high costs associated with instrumentation, personnel, and long-term maintenance (Baldocchi, 2014). Only a small subset of flux towers has measurement records exceeding a decade (Pan, Xiao, Pan, et al., 2024). Moreover, each tower provides flux data over a relatively

limited footprint scale, typically ranging from several hundred to a few thousand meters (Papale et al., 2006).

Over the recent decades, numerous prognostic and diagnostic terrestrial biosphere models (TBMs) have been developed and applied to estimate global GPP (Anav et al., 2015; Ryu et al., 2019). Beyond differences in input datasets, these models vary in structure, including the processes, variables, algorithms, and parameterizations employed. They encompass a broad range of approaches, such as independent inversion models using carbonyl sulfide, oxygen isotopes, or soil respiration data (Jian et al., 2022; Lai et al., 2024; Lisa R. Welp et al., 2011a), complex process-based Earth system models with detailed physiology, such as dynamic global vegetation models (DGVMs) (Sitch et al., 2003), and remote sensing-driven process models like PR, BESS, and BEPS (Keenan et al., 2016; Leng et al., 2023; B. Li et al., 2023). Light use efficiency (LUE) models, such as GLASS, VPM, EC-LUE, and MOD17, use remote sensing data to estimate GPP based on absorbed radiation and light use efficiency (Liang et al., 2021; Running et al., 2000; Xiao, Zhang, et al., 2004; Zheng et al., 2020a). In addition, statistical methods (e.g., GOSIF, NIRv) (Badgley et al., 2019; Li et al., 2019) and machine learning (e.g., FLUXCOM) (Jung et al., 2019) have also emerged as powerful tools for large-scale GPP estimation. Together, these models overcome the spatial and temporal limitations of the eddy covariance technique, enabling continuous monitoring of GPP dynamics and long-term trends across diverse geographic regions and ecosystems. As a result, a wide array of global GPP datasets has been generated, playing a critical role in advancing our understanding of the global carbon cycle and evaluating

feedback between terrestrial ecosystems and climate change.

Among these models, one class explicitly calculates light absorption and approximates the complex process of carbon fixation using light use efficiency (LUE) (Monteith, 1972). The fundamental assumption of LUE models is that photosynthesis is a relationship with the amount of absorbed photosynthetically active radiation (APAR) and the light use efficiency (ϵ_g), expressed as:

$$GPP = APAR \times \epsilon_g \quad (1.1)$$

ϵ_g is a parameter related to the maximum light use efficiency (ϵ_{max}), which represents the theoretical upper limit of light use efficiency under non-stressed or optimal growing conditions (Monteith, 1972, 1977). In reality, photosynthetic capacity is influenced not only by light availability but also by environmental constraints such as temperature and water. Therefore, ϵ_g is commonly adjusted by incorporating environmental factors:

$$\epsilon_g = \epsilon_{max} \times f(\text{Environmental factors}) \quad (1.2)$$

Compared to fully process-based models, which require the explicit simulation of physiological mechanisms, involve numerous parameters, and demand high computational resources, the LUE model offers a more streamlined and efficient framework (Pei et al., 2022). Its key advantages include: (1) Scalability: Driven by remote sensing inputs, LUE models can be applied from site-level to global-scale analyses (Running et al., 2004). (2) Simplicity and transparency: With fewer parameters and a clear structure, LUE models are easier to calibrate, transfer across regions, and integrate with multi-source datasets, reducing the propagation of uncertainty (Zheng et al., 2018). (3) Mechanistic yet practical: By adjusting light use efficiency with dynamic

stress functions, the model can incorporate environmental factors in structure, balancing mechanistic interpretability with operational simplicity and low cost (Xiao, Zhang, et al., 2004). As results, LUE models have been widely adopted in current research and represent an efficient approach for long-term, large-scale GPP estimation.

Over the past few decades, numerous LUE models have been developed to estimate GPP. Representative models include the MODIS GPP model (MOD17) (Running et al., 2000), the Photosynthetic Capacity Model (PCM) (Gao et al., 2014), the Vegetation Photosynthesis Model (VPM) (Xiao, Zhang, et al., 2004), the Carnegie–Ames–Stanford Approach (CASA) (Potter et al., 1993), EC-LUE (Yuan et al., 2007), and the Terrestrial Ecosystem Carbon (TEC) flux model (Yan et al., 2015). However, these models differ in several key aspects, including the satellite-based inversion of APAR and the parameterization of light use efficiency. These differences contribute to substantial inconsistencies in both the magnitude and interannual variability of global GPP estimates. Notable issues include: (1) Systematic underestimation of APAR, particularly in high-latitude broadleaf forests (B. Pan et al., 2025). (2) Biome-specific fixed values or empirical regressions for the light use efficiency parameter, which fail to account for physiological differences and climatic adaptations across geographic regions (Yao Zhang et al., 2017). (3) Overly simplified environmental stress functions, leading to underestimation of drought impacts on GPP in arid regions (Meng et al., 2025), and the omission of the effects of rising atmospheric CO_2 concentration on light use efficiency (Keenan et al., 2023). As a result, current LUE models produce widely varying global annual GPP estimates, ranging widely from 100 to 160 Pg C yr^{-1}, with

weak signals of interannual variability or long-term trends (Anav et al., 2015; Ryu et al., 2019). Additionally, when compared with process-based models, LUE models often significantly underestimate GPP in tropical regions (Lai et al., 2024).

The VPM model is an LUE model that calculates PAR absorbed by chlorophyll ($APAR_{chl}$) (Xiao, Hollinger, et al., 2004; Xiao, Zhang, et al., 2004), distinguishing it from other models that calculate PAR absorbed by the canopy ($APAR_{canopy}$) (Potter et al., 1993; Running et al., 2000). Vegetation canopies consist of chlorophyll and other components unrelated to photosynthesis, with photosynthetic activities occurring in chloroplasts. The VPM model excludes PAR absorbed by components unrelated to photosynthesis (e.g., leaf veins, senescent leaves, early branches, and stems), reducing their impacts on the simulation of photosynthesis in the canopy (Xiao, Hollinger, et al., 2004; Xiao, Zhang, et al., 2004). The VPM model (v1.0 and v2.0) used the maximum LUE for individual land cover types (or biome-specific LUE) and accounts for the environmental stressors such as air temperature (T_{scalar}) and water (W_{scalar}), in the maximum LUE parameter. Many publications evaluated the VPM model at eddy flux tower sites and reported that VPM v2.0 provided reasonably satisfactory performance in estimating GPP (Table 1.1). Simulations of VPM v2.0 were already carried out for North America (2010), China (2007 to 2014), and the globe (2000 to 2016) (Ma et al., 2018; Yao Zhang et al., 2016; Yao Zhang et al., 2017).

Table 1.1: A list of publications involving the VPM model and its simulations at site, region, and global scales. ENF: Evergreen needleleaf forest; DBF: Deciduous broadleaf forest; GRA: Grassland; WET: Wetland; SHL: Shrubland; CRO:

Cropland; MF: Mix forest; SAV: Savana; EBF: Evergreen broadleaf forest; WSA: woody savanna.

Model and version	Scale	Biome and Publications
VPM v1.0	Site	ENF (Xiao, Hollinger, et al., 2004; Xiao et al., 2005), DBF (John et al., 2013; Xiao, Zhang, et al., 2004), GRA (He et al., 2014; Li et al., 2007; Wang et al., 2010), WET (Kang et al., 2014), SHL (John et al., 2013; Li et al., 2007), CRO (John et al., 2013; Kalfas et al., 2011; Wang et al., 2010; Yan et al., 2009), MF (Wu et al., 2009), SAV (Jin et al., 2013)
	Region	Tibetan Plateau (He et al., 2014)
	Globe	/
VPM v2.0	Site	ENF (Yao Zhang et al., 2016), DBF (Yao Zhang et al., 2016), CSH (Yao Zhang et al., 2016), GRA (Celis et al., 2024; Doughty et al., 2018; Wagle et al., 2015; Wagle et al., 2014; Yao Zhang et al., 2016), CRO (Celis et al., 2024; Doughty et al., 2018; Huang et al., 2021; Wagle et al., 2015; Wu et al., 2018; Xin, Xiao, Dong, et al., 2020; Xin et al., 2017; Yao Zhang et al., 2016), MF (Yao Zhang et al., 2016), OSH (Yao Zhang et al., 2016), WET (Yao Zhang et al., 2016), WSA (Yao Zhang et al., 2016), Sugarcane (Celis et al., 2023; Xin, Xiao, Cabral, et al., 2020)
	Region	North America (Yao Zhang et al., 2016), China (Ma et al., 2018)
	Globe	Global (Yao Zhang et al., 2017)

Although VPM has been widely applied and has demonstrated robust performance, its current framework still presents several notable limitations. First, both VPM v1.0

and v2.0 rely on biome-specific fixed parameters, which fail to adequately capture the physiological differences and climate adaptations of vegetation across geographic gradients (Chang et al., 2021a; Chang et al., 2020). Second, site-level simulations suggest that VPM underestimates APAR in northern needleleaf forests (B. Pan et al., 2025) and exhibits overly conservative responses to water stress, resulting in an overestimation in arid/semi-arid ecosystems (Meng et al., 2025). In addition, current versions do not explicitly incorporate the CO_2 fertilization effect—the enhancement of photosynthesis due to rising atmospheric CO_2 concentrations—potentially underestimating the magnitude of GPP and its interannual variability, which becomes more pronounced when scaled to the global level (Anav et al., 2015). Due to these combined limitations, VPM v2.0 produces global GPP estimates in the range of 120–130 Pg C yr^{-1} (Yao Zhang et al., 2017), significantly lower than recent estimates based on independent inversion methods, which estimate global GPP between 150 and 175 Pg C yr^{-1} (Lisa R. Welp et al., 2011b). These gaps highlight the urgent need to improve model parameterization, update high-quality meteorological and remote sensing inputs, and refine environmental stress functions to produce a more reliable and robust long-term global GPP dataset.

Long-term, continuous, and highly robust global GPP datasets provide unprecedented capabilities for quantifying the responses of terrestrial ecosystems to climate change, disturbances, and land-use transitions at both regional and global scales (Running et al., 2004). In recent decades, the combined effects of global warming and intensifying droughts have led to a widespread increase in fire risk. Wildfires are

occurring with greater frequency, intensity, and severity (Richardson et al., 2022). By consuming canopy biomass and surface litter, fires directly reduce leaf area index (LAI) and APAR, resulting in significant negative GPP anomalies in the year of the fire (Zong et al., 2024). Recent studies indicate that over the past two decades, substantial CO2 emissions from fires have weakened terrestrial carbon storage, reinforcing the warming–drought–fire–carbon emission feedback loop and further elevating future fire risk (Jones et al., 2022).

Australia, due to its unique climatic and ecological conditions, has long been a global hotspot for wildfires. The 2019–2020 “Black Summer” fires highlight the region's significance as a case study for evaluating fire-induced GPP losses and post-fire recovery dynamics (Qin et al., 2022). Similarly, northern high-latitude forests are experiencing rising fire frequency and intensity. Model projections suggest that some of these regions could shift from net carbon sinks to persistent carbon sources by mid-century (Virkkala et al., 2025).

Therefore, systematically quantifying wildfire impacts on terrestrial GPP and mapping post-fire recovery trajectories using global GPP datasets has become one of the most urgent tasks in carbon cycle research and carbon budget assessments. Such efforts will provide critical scientific support for fire risk early warning systems, ecosystem restoration planning, and greenhouse gas mitigation policies.

1.2 Overall research objectives

This dissertation has two main objectives: (1) Improvement and development of new versions of the Vegetation Photosynthesis Model (VPM v3.0 and VPM v4.0) and to

construct a long-term global GPP dataset with high spatial and temporal resolution (Chapter 2 – Chapter 5). (2) The application of the global GPP dataset focuses on investigating the responses of terrestrial ecosystems to wildfire disturbances and identifying their underlying drivers (Chapter 6 – Chapter 7).

Building upon the existing VPM v2.0 framework, this study first developed VPM v3.0 by introducing key parameterization improvements related to vegetation and environmental drivers. Specifically, leaf trait differences between broadleaf and needleleaf vegetation types were incorporated on the light absorption side, while distinctions between C_3 and C_4 photosynthetic pathways were used to refine the regulation of maximum light use efficiency. In addition, a global site-specific apparent optimum temperature dataset ($T_{opt\text{-}site}$) was constructed using long-term flux tower records, surface reflectance datasets, and climate reanalysis data. The water stress function was updated to enhance model sensitivity to drought. VPM v3.0 performance was first evaluated at four long-term observed deciduous broadleaf forest sites (CA-Cbo, US-Ha1, US-MMS, and US-WCr) by comparing GPP estimates against in situ eddy covariance GPP observations. Subsequently, the site-specific T_{opt} was estimated globally to drive VPM v3.0 for global GPP estimation. It is important to note that VPM v3.0 does not explicitly account for atmospheric CO_2 concentration. To incorporate CO_2 in the model, VPM v4.0 is developed by incorporating the direct CO_2 effect into the model based on the biochemical photosynthetic CO_2 assimilation theory (FvCB model). Using VPM v4.0, global GPP was re-estimated, and analyses were conducted on the interannual variability and long-term trends of global annual GPP.

Using the global GPP dataset estimated with VPM v3.0, this dissertation focuses on the impacts of wildfire disturbances on terrestrial ecosystems and their post-fire recovery processes. The analysis centers on two key regions: Australia and high-latitude forests. In Australia, the post-fire recovery trajectories of vegetation productivity were explored for the period 2011–2019 following fire events. In high-latitude forests, the study investigated the spatial and temporal patterns of first-year post-fire recovery from 2002 to 2022.

By integrating eddy covariance observations with multi-source satellite data, this dissertation aims to construct a more robust global GPP dataset. The goal is to provide a robust benchmark for quantifying both the impacts of wildfires on the carbon cycle and the resilience of ecosystem recovery, while also offering new scientific insights to improve national greenhouse gas inventories, fire risk management, and ecological restoration strategies.

1.3 Organization of the dissertation

This dissertation proposal consists of six main chapters, each focusing on the following key content:

Chapter 2：Modeling gross primary production at four deciduous broadleaf forest eddy flux tower site using Vegetation Photosynthesis Model (VPM v3.0). This chapter presents the development and evaluation of VPM v3.0 based on the existing VPM framework. Key modifications include the integration of MODIS MOD19A1 surface reflectance data and ERA5-Land reanalysis climate data as model inputs, along with the incorporation of site-specific apparent optimum temperature

(Topt-site) in the parameterization scheme. VPM v3.0 was applied to four long-term observed eddy covariance flux tower sites located in temperate deciduous broadleaf forests across North America (CA-Cbo, US-Ha1, US-MMS, and US-WCr) to estimate 8-day GPP from 2000 to 2020. Model outputs were compared against observed GPP from flux towers to assess the robustness and applicability of VPM v3.0 at the site scale. Additionally, this chapter explores the interannual variability of atmospheric CO_2 concentration, climate variables, vegetation indices, phenological metrics, and carbon fluxes at these four sites, and discusses the potential drivers underlying year-to-year variations in GPP.

Chapter 3：Site-specific apparent optimum air temperature for vegetation photosynthesis across the globe. Building on the findings of Chapter 2, which demonstrated the high robustness of VPM v3.0 in site-level GPP estimation when incorporating site-specific apparent optimum temperature ($T_{opt\text{-}site}$), this chapter focuses on generating a global $T_{opt\text{-}site}$ dataset to enable global GPP estimation using VPM v3.0. Specifically, MODIS MOD19A1 surface reflectance data and ERA5-Land daytime air temperature data are used to construct site-specific EVI-temperature response curves. These curves are used to estimate the $T_{opt\text{-}site}$, producing a global dataset of $T_{opt\text{-}site}$ at 500-meter spatial resolution. This dataset serves as a key model input for VPM v3.0 in global GPP estimation. In addition, the chapter examines the spatial distribution of $T_{opt\text{-}site}$ globally and analyzes its variation across different biomes, providing insights into how vegetation physiological responses to temperature differ by climate zone and ecosystem type.

Chapter 4：Modeling gross primary production across the globe using Vegetation Photosynthesis Model (VPM v3.0). This chapter applies VPM v3.0 to estimate global GPP at an 8-day temporal resolution and 500-meter spatial resolution. The model is driven by MODIS MOD19A1 surface reflectance data, ERA5-Land climate reanalysis data, and the global $T_{opt\text{-}site}$ dataset generated by Chapter 3. To evaluate the VPM v3.0's performance, a comprehensive set of in situ GPP observations was collected from 205 eddy covariance flux tower sites, covering 11 biomes and totaling 1,658 site-years. Additionally, satellite-derived solar-induced chlorophyll fluorescence (SIF) data from the TROPOMI (2018–2021) are used to validate the seasonal dynamics of GPP estimates independently. This chapter also compares GPP from VPM v3.0 with widely used global GPP products, analyzing both the magnitude and seasonality to assess consistency and divergence. The findings provide a methodological and empirical foundation for generating a long-term, highly robust global GPP dataset using VPM v3.0.

Chapter 5：Incorporating CO_2 into VPM to improve global gross primary production estimates. This chapter builds upon the VPM v3.0 framework by integrating the biochemical photosynthetic CO_2 assimilation theory (FvCB model) to develop VPM v4.0, which explicitly accounts for the effects of rising atmospheric CO_2 concentration on photosynthesis. VPM v4.0 considers distinctions in chlorophyll absorption characteristics between broadleaf and needleleaf vegetation types, as well as between C_3 and C_4 photosynthetic pathways. It also refines the parameterization of light use efficiency by jointly considering site-specific temperature, water availability,

and atmospheric CO_2 concentration. Global GPP was estimated from 2000 to 2023 using VPM v4.0. Model outputs were evaluated against in-situ GPP observations from eddy covariance flux tower sites and compared with other widely used global GPP products. The assessment focused on GPP estimation magnitude, interannual variability, and sensitivity to rising CO_2 concentration.

Chapter 6：Application of GPP dataset: a case study of post-fire recovery of vegetation productivity in Australia. Building on the global GPP dataset generated in Chapter 4, this chapter investigates the impact of wildfire disturbances on ecosystem productivity in Australia. By integrating the 1-km resolution satellite-based active fire product with the 500-meter GPP dataset, this study investigates post-fire vegetation productivity recovery trajectories of fire-affected pixels in Australia from 2011 to 2019. Key recovery metrics include recovery ratio, recovery magnitude, recovery slope, and recovery years. ERA5-Land precipitation data and fire behavior indicators (e.g., fire frequency and fire severity) are incorporated to identify the drivers of post-fire vegetation recovery. This chapter also quantifies the role that fire-induced interannual GPP differences contribute to the overall interannual differences of continental-scale GPP in Australia.

Chapter 7：Application of GPP dataset: a case study of first-year post-fire recovery of vegetation productivity in northern high latitude forests. This chapter investigates the impact of wildfire disturbances on high-latitude forests located north of 40°N, using the global GPP dataset developed in Chapter 4. By integrating a 500-meter satellite-derived burned area product with 500-meter GPP dataset, this chapter

investigates the spatial and temporal patterns, as well as the underlying drivers, of first-year post-fire vegetation productivity recovery across northern high-latitude forests from 2002 to 2022. The chapter begins by characterizing the spatial distribution of fire area, severity, and intensity in high-latitude forests. It then analyzes the spatial and temporal patterns of first-year post-fire GPP recovery, stratified by forest functional types (needleleaf and broadleaf forests) and by four major geographic regions (Siberia, Northern North America, Northern Asia, and Northern Europe). Interannual variability and decadal trends in first-year post-fire GPP recovery are assessed, followed by an evaluation of key drivers, including fire intensity, fire severity, and climate conditions.

1.4 List of publications from the dissertation

Chapter 2

Pan, L., Xiao, X., et al. (2024). Interannual variations and trends of gross primary production and transpiration of four mature deciduous broadleaf forest sites during 2000–2020. *Remote Sensing of Environment*, 304, 114042, (https://doi.org/10.1016/j.rse.2024.114042).

Chapter 3

Pan, L., Xiao, X., et al. (2024). Site-specific apparent optimum air temperature for vegetation photosynthesis across the globe. *Scientific Data*, 11(1), 758, (https://www.nature.com/articles/s41597-024-03603-7).

Chapter 4

Pan, L., Xiao, X., et al. (2025). Vegetation Photosynthesis Model v3.0: Improved Estimates of Terrestrial Gross Primary Production from Individual Eddy Flux Tower

Sites to the Globe. *Journal of Remote Sensing*. 2025;5: Article 0471, (https://doi.org/10.34133/remotesensing.0471).

Chapter 5

Pan, L., Xiao, X., et al. Global terrestrial photosynthesis was large and increased substantially in 2000-2023 (Under review).

Chapter 6

Pan, L., Xiao, X., Qin, Y., Canadell, J.G., Huete, A., Ciais, P., et al. Strong and rapid post-fire recovery of vegetation productivity in Australia (Global Change Biology, Accepted).

Chapter 7

Pan, L., Xiao, X., Qin, Y., Canadell, J.G., Ciais, P., Declining post-fire CO_2 uptake in northern high latitude forests since late 2000s (Under review).

Chapter 2 : Modeling gross primary production at four deciduous broadleaf forest eddy flux tower site using Vegetation Photosynthesis Model (VPM v3.0)

ABSTRACT

Accurate modeling of gross primary production (GPP) and its interannual variability in deciduous broadleaf forests is essential for understanding forest responses to environmental change. This chapter evaluates the performance of the improved VPM v3.0 model in estimating GPP at the site scale. Compared to its earlier versions (VPM v1.0 and VPM v2.0), VPM v3.0 integrates site-specific apparent optimum temperature ($T_{opt\text{-}site}$) parameters and utilizes ERA5-Land reanalysis dataset to improve estimation accuracy. Specifically, VPM v3.0 was applied to four long-term eddy covariance flux tower sites located in temperate deciduous broadleaf forests in Canada (CA-Cbo) and the United States (US-Ha1, US-MMS, US-WCr) and Canada, estimating 8-day GPP time series from 2000 to 2020. Results show that GPP estimated by VPM (GPP_{VPM}) closely matched flux tower observations (GPP_{EC}) in both magnitude (slopes ranging from 0.85 to 1.25) and seasonal dynamics (R^2 ranging from 0.77 to 0.89). The chapter further explores decadal trends in atmospheric CO_2 concentration, climate variables, vegetation indices, phenology, and carbon fluxes at these sites. From 2000 to 2020, trends in GPP varied by site, ranging from positive (CA-Cbo) to negligible (US-Ha1, US-MMS, and US-WCr), depending on local changes in CO_2 concentration and climate conditions. These findings demonstrate the robust performance of VPM v3.0 in

estimating GPP over two decades in deciduous broadleaf forests, supporting its potential for global-scale application and high-precision GPP dataset development.

2.1 Introduction

The exchange of carbon fluxes between land ecosystems and the atmosphere represents a fundamental physiological function and serves as a key metric for evaluating ecosystem services (Keenan et al., 2014; Piao et al., 2007; Piao et al., 2013). Among these fluxes, gross primary production (GPP), which represents the total amount of CO_2 assimilated by vegetation through photosynthesis, plays a central role in regulating the global carbon balance (Anav et al., 2015; Frankenberg et al., 2011). Accurate measurement and estimation of GPP is essential for assessing terrestrial carbon dynamics, whether across the site scale to the global scale.

The eddy covariance (EC) technique is widely recognized as the most precise micrometeorological approach for monitoring ecosystem-scale exchanges of carbon, water, and energy. It has been extensively applied across diverse ecosystems, climatic zones, and time periods, with many observation sites integrated into international flux monitoring networks such as FLUXNET and AmeriFlux (Baldocchi et al., 2001; Chu et al., 2021). The measurement from these flux towers serves as a critical reference for evaluating GPP estimation from various modeling frameworks (Li et al., 2021; Salazar-Martínez et al., 2022).

Despite the growing number of flux towers worldwide, their deployment remains constrained by substantial financial and logistical demands, including high costs for instruments, labor, and maintenance (Baldocchi, 2014). As a result, long-term

measurement records exceeding a decade are rare. Furthermore, the spatial footprint of an EC tower is inherently limited, capturing fluxes only within the order of hundreds of meters to a few kilometers (Papale et al., 2006). These constraints mean that many studies are confined to short temporal windows, making it difficult to draw robust conclusions about long-term vegetation-climate interactions.

In recent decades, although significant progress has been made in estimating the spatial and temporal dynamics of GPP across the site scale to global scale, large discrepancies still exist among terrestrial biosphere models (TBMs), particularly in terms of simulations of GPP magnitude and seasonality (Anav et al., 2015; Arora et al., 2013). Process-based model, statistical empirical model, and machine learning methods show considerable promise for advancing GPP estimation (Jung et al., 2020; Li et al., 2019; Wagle et al., 2016), yet substantial uncertainties persist due to differences in model structures, parameter complexity, and input requirements (Anav et al., 2015; Rogers, 2014; Rogers et al., 2017).

Among various models, light use efficiency (LUE) models provide a more streamlined and computationally efficient framework by linking GPP directly to absorbed photosynthetically active radiation (APAR) and light use efficiency (Monteith, 1972). LUE models can be broadly categorized into two groups. The first group estimates APAR based on the fraction of incident photosynthetically active radiation (PAR) absorbed by the canopy ($fPAR_{canopy}$), often characterized by using normalized difference vegetation index (NDVI) or leaf area index (LAI) as proxies (Potter et al., 1993; Zhao et al., 2005). However, this approach does not differentiate between

photosynthetically active and non-active materials (e.g., senescent leaves, woody tissue), which fluctuate seasonally and contribute to substantial overestimation of effective light absorption. The second group refines this approach by estimating the fraction of PAR explicitly absorbed by chlorophyll ($fPAR_{chl}$), which more directly represents the light used in photosynthesis. The Enhanced Vegetation Index (EVI) is often used as a proxy for $APAR_{chl}$ (Xiao, Hollinger, et al., 2004; Xiao, Zhang, et al., 2004). A leading model in this category is the Vegetation Photosynthesis Model (VPM), which explicitly incorporates $APAR_{chl}$ into its structure.

VPM has been widely applied to estimate GPP across a variety of ecosystems, including forests (Xiao, Hollinger, et al., 2004; Xiao et al., 2005), grasslands (Doughty et al., 2018; Wang et al., 2018), croplands (Wu et al., 2021; Xin et al., 2017) and wetlands (Kang et al., 2016; Kang et al., 2014). VPM has evolved into its second version (VPM v2.0), which estimated the global GPP at 120 - 130 Pg C yr^{-1} (Yao Zhang et al., 2017) —notably lower than more recent estimates that global GPP at 150 - 175 Pg C yr^{-1} (Lisa R Welp et al., 2011). Given these discrepancies and the known sensitivities of VPM outputs to both climatic inputs and model parameterization, there is a clear need to refine and advance VPM beyond its current version to improve global GPP estimation accuracy.

This chapter focuses on four long-term eddy flux tower sites, located in deciduous broadleaf forests (DBF), with continuous observations spanning from 2000 to 2020. Using the newly developed VPM v3.0 model, this chapter estimated 8-day GPP and evaluated the model's performance against flux tower measurements. Two key research

questions guided this analysis: (1) To what extent can VPM v3.0 estimate the magnitude and seasonal dynamics of GPP in these four DBF sites over the past two decades? (2) What are the patterns of interannual variability and long-term trends in atmospheric CO2 concentration, climatic variables, vegetation indices, phenology, and carbon uptake at these sites? By conducting a two-decade estimation and evaluation, this chapter aims to establish a benchmark for future regional and global estimations of VPM v3.0. It also offers valuable insights into how atmospheric CO2 concentration has risen and climate variability has influenced the functioning of long-term deciduous forest ecosystems.

2.2 Materials and Methods

2.2.1 Study area

To better understand multi-decadal variations of carbon and water fluxes of mature deciduous broadleaf forests and to assess the performance of the VPM and VTM models in estimating forest carbon and water fluxes over multiple decades, we screened all eddy flux sites within the AmeriFlux networks. Among all the deciduous broadleaf forest sites, four sites with observation spanning from 2000 to 2020 met the purpose of this study. These four sites are Borden Forest Research Station (CA-Cbo), Harvard Forest EMS Tower (US-Ha1), Morgan Monroe State (US-MMS), and Willow Creek (US-WCr). Note in US-WCr, the site underwent some unique events. In the late spring of 2001, a severe pest infestation led to a complete canopy drop in June. Additionally, commercial logging activities during the winters of 2013 and 2014 resulted in a 30%

reduction in the upper biomass. All four sites are located on flat terrain, and the distribution of these four sites is shown in Figure 2.1. Table 2.1 is brief summary and detailed descriptions can be obtained via AmeriFlux (https://ameriflux.lbl.gov/).

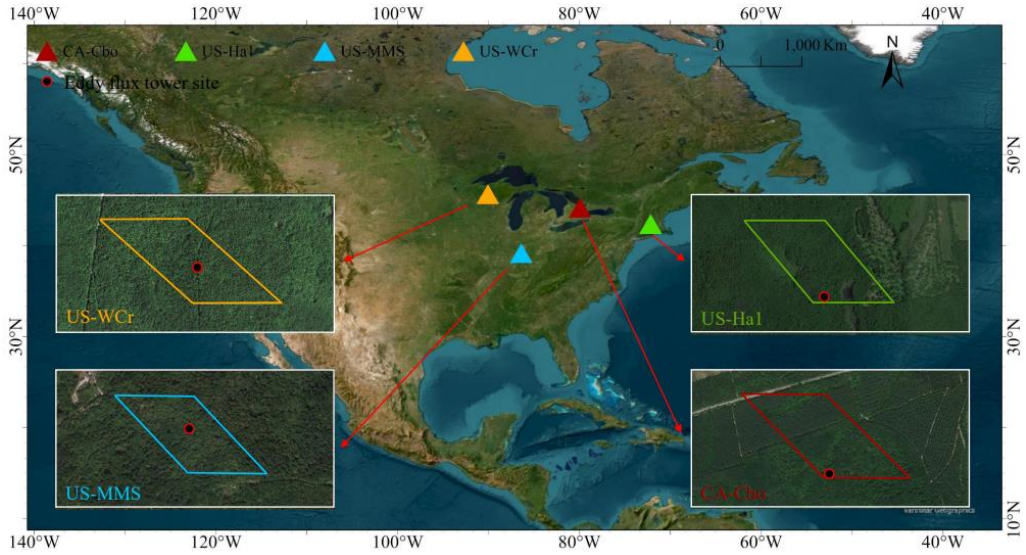

Figure 2.1: The location and surrounding landscapes of four deciduous broadleaf forest sites. The polygon is the MODIS pixel at 500-meter spatial resolution where the eddy flux tower is located.

Table 2.1: The characteristics of the four deciduous broadleaf forest tower sites (three in the U.S.A., one in Canada). MAP: mean annual precipitation (mm); MAT: mean annual temperature (°C); MH: mean height (m); MLAI: mean leaf area index (m^2 m^{-2}).

	CA-Cbo	US-Ha1	US-MMS	US-WCr
Country	Canada	U.S.A.	U.S.A.	U.S.A.
Lat	44.3167	42.5378	39.3232	45.8059
Lon	-79.9333	-72.1715	-86.4131	-90.0799
Elevation	120	340	275	520
MAP	932	1216	1108	697
MAT	6.66	6.62	10.85	4.02
Main species	1.red maple (*Acer rubrum*); 2. eastern white pine (*Pinus strobus*); 3.large-tooth aspen (*Populus grandidentata*); 4.white ash (*Fraxinus americana*)	1.oak-maple (*Quercus rubra-Acer rubrum*); 2. eastern hemlock (*Tsuga canadensis*); 3. red maple (*Acer.rubrum*)	1. sugar maple (*Acer saccharum*); 2. tulip poplar (*Liriodendr-on tulipifera*); 3. sassafras (*Sassafras albidum*); 4. Oaks (*Quercus*)	1.sugar maple (*Acer saccharum*); 2. basswood (*Tilia americana*); 3. green ash (*Fraxinus pennsylvanica*); 4. red oak (*Quercus rubra*)
MH (m)	21	20-24	27	25
MLAI	3.58	3.91	4.48	4.44
Forest age	110	88~123	90~100	74~96
Literature	(Lee et al., 1999)	(Motzkin et al., 1999)	(Dragoni et al., 2011)	(Cook et al., 2004)

2.2.2 In-situ data from the eddy flux tower sites

Eddy flux tower data for the four sites were downloaded from the AmeriFlux data portal

(http://ameriflux.ornl.gov/). The EC technology measures the net ecosystem exchange (NEE) of CO_2 between the land surface and the atmosphere, and the NEE data are partitioned to estimate GPP_{EC} and ecosystem respiration (ER) by the equation NEE = GPP - ER (Lasslop et al., 2010; Reichstein et al., 2005). The ET is converted from the latent heat flux (LE) using the Penman-Monteith equation (Cai et al., 2007), LE is estimated from direct measurements of the product of vertical velocity fluctuations and scalar concentration fluctuations by the EC technique. Considering that the energy balance of the eddy flux tower is usually not closed (Jung et al., 2011a), we also selected the LE corrected by the energy closure factor (LE_{corr}), which is only included in the CA-Cbo, US-MMS, and US-WCr sites. We generated two sets of ETs based on two LE sources (Eqs. (2.1) - (2.3)):

$$ET_{EC} = \frac{LE}{\lambda} \quad (2.1)$$

$$ET_{EC\text{-}corr} = \frac{LE_{corr}}{\lambda} \quad (2.2)$$

$$\lambda = 10^3 \times (2500 - 2.37T_{DT}) \quad (2.3)$$

where LE is the latent heat flux (W m^{-2}) measured by eddy flux tower, LE_{corr} is LE corrected by energy balance closure correction factor, λ is the latent heat of vaporization (J Kg^{-1}), and T_{DT} is the daytime air temperature (℃).

2.2.3 MODIS surface reflectance and vegetation indices

The Moderate Resolution Imaging Spectroradiometer (MODIS) is a key instrument on the Terra satellite, which was successfully launched in December 1999 (Justice, Townshend, et al., 2002). The MODIS sensor monitors the changes of the earth's surface in 36 spectral bands in the wavelength range from 0.405 μm to 14.385 μm with

a high temporal resolution of 1 day, and the seven bands in the wavelength range from 0.459 μm to 2.155 μm are mainly used to study vegetation and land surface: blue (0.459–0.479 μm), green (0.545–0.565 μm), red (0.620– 0.670 μm), near infrared (0.841–0.875 μm, 1.230–1.250 μm), and shortwave infrared (1.628–1,652 μm, 2.105–2.155 μm). The MOD09A1 product provides the highest quality observation of the seven bands of surface spectral reflectance in the Level 2G MOD09GHK data at 500m spatial resolution and 8-day temporal resolution, and the data are radiometrically and geometrically corrected (Anderson et al., 2005).

To generate continuous high-quality surface reflectance time series data, we use the quality detect method of QA bands to identify bad-quality observations. The QA band provides binary information for each pixel about clouds (1 << 10), cloud shadows (1 << 2), and snow (1 << 12). If these binary checks result in 0, it indicates that the pixel is a good-quality observation, not covered by clouds, shadows, or snow. For those pixels with bad-quality observations, the gaps are filled using a linear interpolation method based on the high-quality observations. Then, we used the processed 8-day surface spectral reflectance data to generate high-quality and continuous time series data of Normalized Difference Vegetation Index (NDVI) (Rouse et al., 1974), Enhanced Vegetation Index (EVI) (Huete et al., 2002), and Land Surface Water Index (LSWI) (Huete et al., 2002). These indices are useful for monitoring vegetation changes over time. The equations of three vegetation indices are as follows (Eq. (2.4) - (2.6)):

$$NDVI = \frac{\rho_{nir} - \rho_{red}}{\rho_{nir} + \rho_{red}} \tag{2.4}$$

$$EVI = 2.5 \times \frac{\rho_{nir} - \rho_{red}}{\rho_{nir} + (6 \times \rho_{red} - 7.5 \times \rho_{blue}) + 1} \tag{2.5}$$

$$LSWI = \frac{\rho_{nir} - \rho_{swir}}{\rho_{nir} + \rho_{swir}} \quad (2.6)$$

where ρ_{nir} , ρ_{red}, ρ_{blue}, and ρ_{swir} are the surface reflectance bands of near infrared, red, blue, and shortwave infrared, respectively. Since the flux towers might be located on the border of a MODIS pixel, we conducted tests using a 3x3 MODIS pixel window to ensure that the pixel containing the tower matches the flux tower's footprint (Figure 2.2). Taking the EVI as an example, at three sites surrounded by pure forests (US-Ha1, US-MMS, US-WCr), the EVI of the pixel where the flux tower is located closely matches the mean EVI of the 3x3 MODIS pixels. However, a significant disparity was observed at the heterogeneous site CA-Cbo site, and thus, we use only the pixel where the tower is located as the input for model simulation.

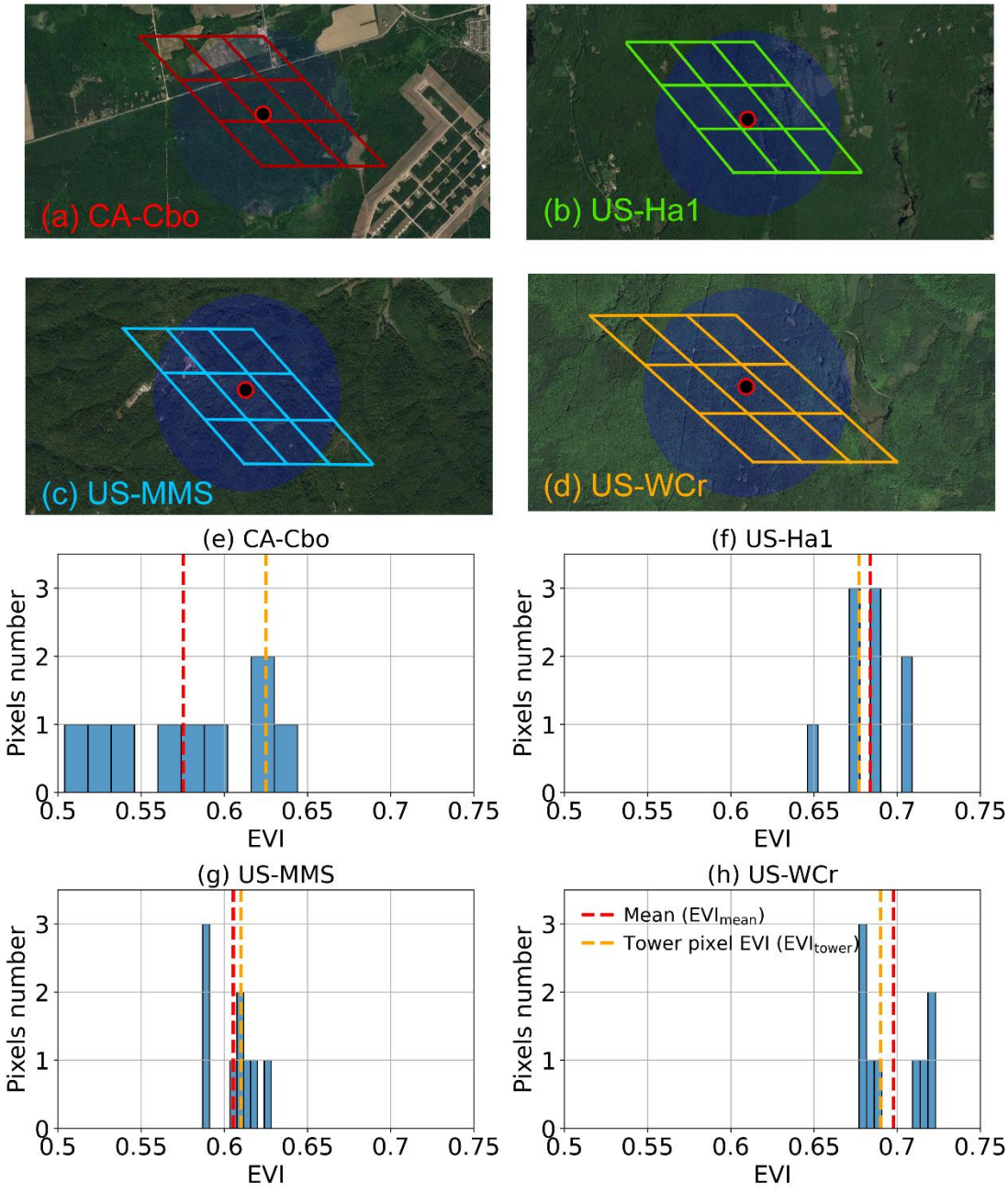

Figure 2.2: Distribution of EVI values in 3x3 MODIS pixels window of sites. (a) to (d) are the landscape of the four flux towers and their surrounding 3x3 MODIS pixels window; (e) to (h) are the histograms of EVI for the 3x3 MODIS pixels of the four flux towers, using data from July 27, 2020, as an example. The red dot line indicates the mean EVI of the nine pixels (EVI_{mean}), and the yellow dot line

denoting the EVI of the pixel where the tower is located (EVI_{tower}, which is utilized as an input in VPM v3.0).

2.2.4 ERA5-Land climate data

We used the ERA5-Land Hourly Climate Reanalysis dataset produced by the European Center for Medium-Range Weather Forecasts (ECMWF) (Zhu et al., 2021). The air temperature and shortwave radiation downward are selected and converted to daily daytime from hourly. In this study, we set the time resolution of the time series data to an 8-day interval to match the MODIS dataset. These daily interval data were then aggregated over 8-day periods by computing the average value within the period. The formulae of converting shortwave radiation downward to PAR_{DT_ERA5} is as follows (Ryu et al., 2018):

$$PAR_{DT\_ERA5} = SW_{rad} \times r_{PAR\_SW} \times \beta \quad (2.7)$$

where SW_{rad} (J m^{-2}) is downward shortwave radiation in the ERA5-Land dataset; $r_{PAR\_SW} = 0.45$ is the ratio of PAR to SW (Ma et al., 2014; Meek et al., 1984), $\beta = 4.56$ μmol J^{-1} is the energy-quanta conversion factor (Dye, 2004). We compared T_{DT} and PAR_{DT} from ERA5-Land and the eddy flux tower (Figure 2.3, Figure 2.4). The four sites have small differences in T_{DT} and PAR_{DT} between the ERA5 dataset and the eddy flux tower measurement, T_{DT} having R^2 of 0.99 and RMSE ranging from 1.09 ℃ to 1.55 ℃, and PAR_{DT} having R^2 of 0.95 and RMSE ranging from 2.98 mol m^{-2} day^{-1} to 4.33 mol m^{-2} day^{-1}.

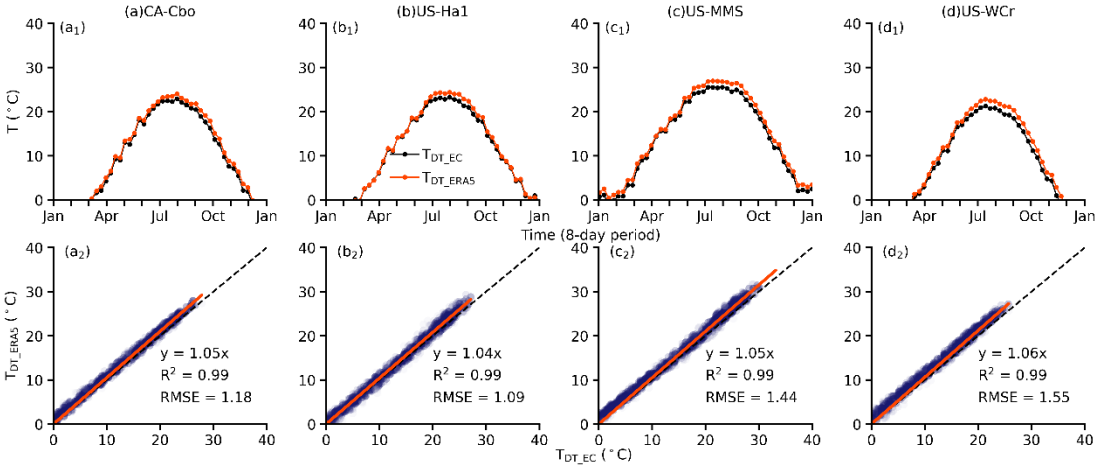

Figure 2.3: Comparison of daytime air temperature (T_{DT}) from tower-based measurements (T_{DT_EC}), and ERA5 dataset (T_{DT_ERA5}). The first row is the seasonal dynamics of the 21-year mean T_{DT}. The second row is the result of simple linear regression between T_{DT_EC} and T_{DT_ERA5} using all year's data at an 8-day scale, respectively.

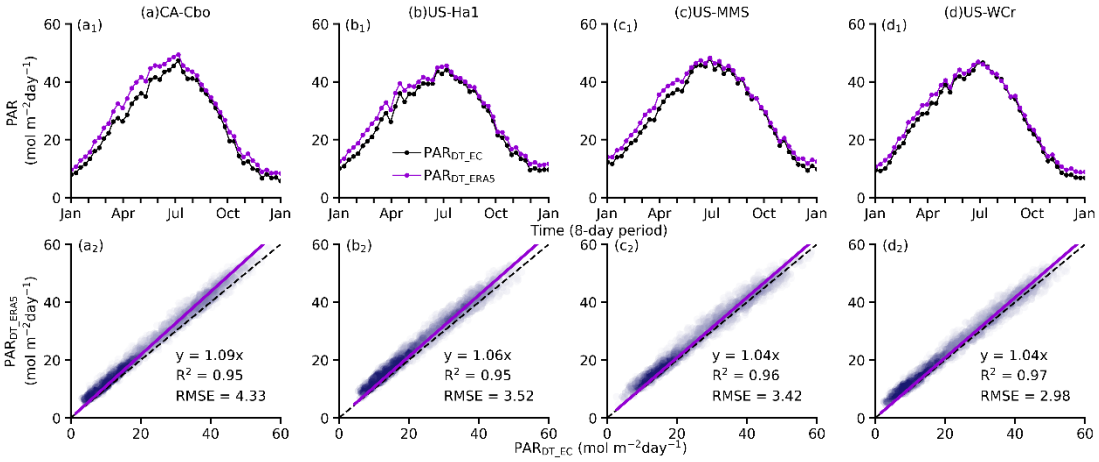

Figure 2.4: Comparison of photosynthetically active radiation in daytime (PAR_{DT}) from tower-based measurements (PAR_{DT_EC}), and ERA5 dataset (PAR_{DT_ERA5}). The first row is the seasonal dynamics of the 21-year mean PAR_{DT}. The second row is the result of simple linear regression between PAR_{DT_EC} and PAR_{DT_ERA5} using

all years' data at an 8-day scale, respectively.

2.2.5 GPP data from the old version of the Vegetation Photosynthesis Model (VPM v2.0) and MODIS production

In this study, VPM v2.0 and MOD17 GPP products are used to compare with VPM v3.0. The major differences between VPM v2.0 and VPM v3.0 lie in the source of climate data and temperature parameter. VPM v2.0 employs biome-specific apparent opyimum temperature with climate data from NCEP Reanalysis II (Yao Zhang et al., 2017). VPM v2.0 dataset can be downloaded in the portal: https://doi.pangaea.de/10.1594/PANGAEA.879560. MODIS Land Science Team's GPP data product (MOD17A2H) is derived from an $APAR_{canopy}$-based PSN model (Running et al., 2004; Running et al., 2000). This widely used product, available from 2000 onwards, can be accessed at https://lpdaac.usgs.gov/products/mod17a2hv006/.

2.2.6 Vegetation Photosynthesis Model (VPM v3.0)

The simulation of satellite-based VPM is calculated as the product of absorbed photosynthetically active radiation by chlorophyll ($APAR_{chl}$) and light use efficiency (LUE, ε_g) (Xiao, Hollinger, et al., 2004; Xiao, Zhang, et al., 2004). In this paper, the simulations of VPM v3.0 are labeled GPP_{VPM}:

$$GPP_{VPM} = APAR_{chl} \times \varepsilon_g \quad (2.8)$$

where $APAR_{chl}$ is calculated as a product of photosynthetically active radiation (PAR) and the fraction of PAR absorbed by chlorophyll ($fPAR_{chl}$):

$$APAR_{chl} = PAR \times fPAR_{chl} \quad (2.9)$$

The $fPAR_{chl}$ is calculated as a linear function of EVI and modified from (Yao Zhang et al., 2016):

$$fPAR_{chl} = EVI - 0.1 \tag{2.10}$$

Light use efficiency (ε_g) is highly related to air temperature (T_{scalar}) and water (W_{scalar}):

$$\varepsilon_g = \varepsilon_0 \times W_{scalar} \times T_{scalar} \tag{2.11}$$

where ε_0 = 0.53 (g C mol^{-1} APAR) is the apparent quantum yield or maximum light use efficiency (Xiao, 2006). The W_{scalar} is calculated as follows:

$$W_{scalar} = \frac{1 + LSWI}{1 + LSWI_{max}} \tag{2.12}$$

where $LSWI_{max}$ is the largest value of LSWI during the growing season within one year. T_{scalar} is calculated as follows:

$$T_{scalar} = \frac{(T - T_{max}) \times (T - T_{min})}{(T - T_{max}) \times (T - T_{min}) - (T - T_{opt})^2} \tag{2.13}$$

where the T_{max}, T_{min} and T_{opt} is the maximum, minimum and optimum temperature for photosynthesis activities. T_{max} and T_{min} can be obtained from a biome-based look-up table (Yao Zhang et al., 2017). Different from VPM v1.0 and VPM v2.0, VPM v3.0 adopts site-specific T_{opt} rather than the T_{opt_biome} as the input of the model. T_{opt} is obtained based on the response curves of vegetation indices and GPP to T_{DT} (Figure 2.5).

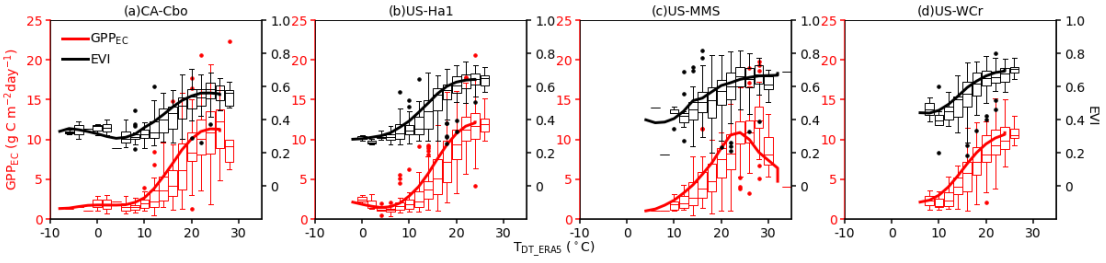

Figure 2.5: Relationship between GPP_{EC}, EVI, and T_{DT_ERA5} across four deciduous

forest sites. The solid black and red lines represent curves that have been fitted to EVI and GPP_{EC}, respectively, using cubic regression splines. This figure also shows boxplot with points every 2 ℃ bins.

Both GPP_{EC} and EVI continued to rise as daytime air temperature increased, and reached the peak, then began to decline at higher T_{DT_ERA5}. These GPP_{EC} - T_{DT_ERA5} and EVI - T_{DT_ERA5} response curves reveal the effect of air temperature (T_{DT_ERA5}) on GPP and EVI. $T_{opt\text{-}GPP}$ and $T_{opt\text{-}EVI}$ are defined as the average T_{DT} associated with the 95% percentile of maximum GPP and EVI values on the response curve (Chang et al., 2021a; Chang et al., 2020). Table 2.2 lists the site-specific T_{opt} estimates from the GPP_{EC} - T_{DT_ERA5} ($T_{opt\text{-}site\text{-}GPP}$) and from the EVI - T_{DT_ERA5} ($T_{opt\text{-}site\text{-}EVI}$). It is worth noting that the site-specific $T_{opt\text{-}site}$ values vary among the four sites and differ slightly from the biome-specific $T_{opt\text{-}biome}$. Considering the global availability of EVI and the limited availability of GPP_{EC} data (only at specific flux tower sites), this study selected $T_{opt\text{-}EVI}$ as the input for the VPM model to verify its potential for global simulations.

Table 2.2: Site-specific apparent optimum temperature parameter values used in VPM v3.0 across the four deciduous forest sites.

Sites	T_{min} (℃)	T_{max} (℃)	$T_{opt\text{-}biome}$ (℃)	$T_{opt\text{-}site\text{-}GPP}$ (℃)	$T_{opt\text{-}site\_EVI}$ (℃)
CA-Cbo	-1	40	20	22	23
US-Ha1	-1	40	20	23	23
US-MMS	-1	40	20	24	22
US-WCr	-1	40	20	21	20

2.2.7 Method for defining physiological-based phenology

In this study, we define the physiological-based phenology of four deciduous broadleaf forests. As reported by previous research, the growing season occurs when GPP exceeds 1 g C $m^{-2}day^{-1}$ (Xia et al., 2015; Xin et al., 2017). However, due to data noise or short-term anomalies that can cause fluctuations in GPP estimation, GPP may be greater than 1 g C $m^{-2}day^{-1}$ in winter. To avoid mis-identifying SOS or EOS with anomalous GPP, SOS and EOS are defined as the first date where the sum of three consecutive values is greater than 3 g C $m^{-2}day^{-1}$ and lower than 3 g C $m^{-2}day^{-1}$ in the reconstructed GPP_{VPM} time series data, respectively. This approach helps to smooth out short-term fluctuations and provides a more accurate delineation of the growing season. The interval spanning from SOS to EOS is defined as the growing season (GS), wherein the temporal span of the GS is defined as the GS length (GSL).

2.2.8 Method for calculating growing degree days (GDD)

Growing Degree Days (GDD) were used to define the degree of warmth of the winter and early spring seasons (WESS) and GS. GDD is computed by determining the difference between the daily air temperature (T_{DT_ERA5}) and the base temperature (T_{BASE}) for each day. If the T_{DT} for any given day is higher than the T_{BASE}, then the difference for that day is added to the cumulative GDD sum. Conversely, if the T_{DT_ERA5} is for a day below T_{BASE}, the T_{DT} is assigned a value of zero for that day:

$$GDD = \sum_{i=1}^{n} T_{DT\_ERA5(i)} - T_{BASE} \quad (2.14)$$

where $T_{DT\_ERA5(i)}$ is the daily air temperature on the day i; T_{BASE} is set to 0 ℃; n is the

number of days in GDD. In this paper, the cumulative GDD_{WESS} is calculated for the period extending from January 1 to March 31. We also calculated GDD_{GS}. The period of GDD_{GS} is to cover the whole GS.

2.2.9 Statistical analysis

To evaluate the performance of the VPM v3.0, we used a simple line regression between the model-estimate GPP_{VPM} and tower-estimated GPP_{EC} with three statistical criteria for the comparison: the coefficient of determination (R^2), slope (α), root mean square error (RMSE), and significance (p-value) (Janssen et al., 1995).

Mann-Kendall statistical test (M-K test) is a non-parametric statistical method widely used in hydrometeorological fields, which can effectively test the long-term trend of natural indicators and is not affected by extreme and missing values (Basistha et al., 2009; Yue et al., 2002). We used the M-K test to assess whether there is a decadent trend of CO_2, climate, VIs, phenology, carbon uptake during 2000-2020. In addition, we also calculated the Theil-Sen's slope (s) for estimating the trend value.

To explore the effects of atmospheric CO_2 concentration and climate on annual GPP, we use ridge regression to quantify the contribution of different driving factors to annual GPP_{EC} (Fang et al., 2020; Xie et al., 2020). In this study, we primarily investigated the influence of atmospheric CO_2 concentrations and climatic factors on the interannual variations of annual GPP_{EC}. The selected driving factors include atmospheric CO_2 concentrations, GDD_{WESS}, GDD_{GS}, the sum of PAR during the GS (PAR_{GS}), and the sum of precipitation during the GS (P_{GS}). The standard ridge regression coefficient (a_i), significance (P), and relative contribution (η_s) are used to

evaluate the impact of different driving factors on annual GPP_{EC}.

2.3 Results

2.3.1 Seasonal dynamics of climate, vegetation indices, and carbon uptake

Figure 2.6 shows the average seasonal dynamics (climatology) of PAR_{DT_ERA5}, T_{DT_ERA5}, precipitation, vegetation indices, and carbon and water fluxes at the four sites over 2000-2020. PAR at the four sites had similar and strong seasonal dynamics (Figure 2.6 a_1~d_1). Air temperature had strong seasonal dynamics with a multi-month winter season (<0 ℃). Precipitation had no strong seasonal dynamics, and there was a multi-month snow season at the CA-Cbo, US-Hal, and US-WCr sites.

Vegetation indices (NDVI, EVI, and LSWI) had strong seasonal dynamics (Figure 2.6 a_2~d_2). At the snow-covered sites (CA-Cbo, US-Ha1, and US-WCr stie), NDVI and EVI have noticeable differences in their seasonal dynamics. NDVI started to rise in March, peaked in June and then maintained a high value until October, and started to decline. EVI started to rise in April, reached its peak in June, and then started to decline gradually. The timing of NDVI rises in early spring agrees with the timing of snow-melting at these three sites, as shown by LSWI data, which shows the effect of snow-melting (wet soils) on NDVI data. In comparison, the US-MMS site is not covered by snow in the winter season, and both NDVI and EVI started to rise in April, and EVI started to decline after reaching its peak and NDVI remained at a stable high value at this time.

Carbon flux (GPP_{EC}) had strong seasonal dynamics (Figure 2.6 a_3~d_3). GPP_{EC} at

the CA-Cbo, US-Ha1 and US-MMS sites started to rise in April (≥1 gC m^{-2} day^{-1}) and declined below 1 gC m^{-2} day^{-1} in November. At the US-WCr site, GPP_{EC} started to rise in May (1 gC m^{-2} day^{-1}) and declined below 1 gC m^{-2} day^{-1} in October.

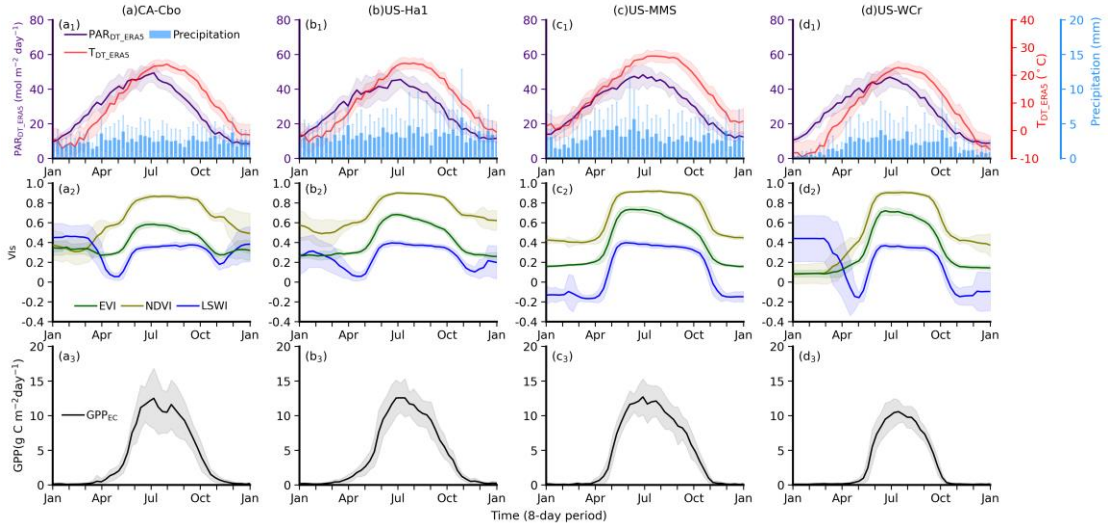

Figure 2.6: The seasonal dynamics of climate (air temperature, photosynthetically active radiation, and precipitation), vegetation indices (EVI, NDVI, and LSWI), and GPP_{EC}. Each column in (a)~(d) represents a specific site, the first row, second row, and third row are the seasonal dynamics of the climate, vegetation indices, and tower-measured carbon and water fluxes, respectively. The curves shown in this figure are mean values from 2000 to 2020, and the shadow and light blue bars for precipitation represent the 21-year range.

2.3.2 Comparison of GPP_{EC} and GPP_{VPM} at the temporal scales of 8-day period and the growing season

Figure 2.7 shows a comparison between GPP_{EC} and $GPP_{VPM\text{-}v3.0}$. In terms of seasonal dynamics (start of the season, end of the season, peak of the season, and growing season length), $GPP_{VPM\text{-}v3.0}$ agreed very well with GPP_{EC}. The 2-d scatterplots and the simple

linear regression models show high correlation between $GPP_{VPM\text{-}v3.0}$ and GPP_{EC} at the four sites, with R^2 range from 0.77 to 0.89 and RMSE range from 1.89 g C m^{-2} day^{-1} to 2.46 g C m^{-2} day^{-1}. The slope values of the regression models show varying differences, ranging from -15% to CA-Cbo, -3% to US-Ha1, +10% to US-MMS, and +25% to US-WCr.

For $GPP_{VPM\text{-}v2.0}$, the seasonal dynamics also agreed with GPP_{EC} very well, with R^2 values ranging from 0.74 to 0.83. In terms of magnitude, $GPP_{VPM\text{-}v2.0}$ shows significant overestimates at three sites (US-Ha1, US-MMS, and US-WCr). The slope values of the regression models show varying differences, ranging from -11% to CA-Cbo, +18% to US-Ha1, +20% to US-MMS, and +41% to US-WCr site.

We also compared the MODIS GPP product (GPP_{MOD17}) with GPP_{EC} across the four sites. GPP_{MOD17} does not track well the seasonal dynamics of GPP_{EC} at the US-Ha1 and US-MMS sites. R^2 values for all four sites ranged between 0.69 to 0.80. In terms of magnitude, GPP_{MOD17} significantly underestimates at CA-Cbo, US-Ha1, and US-MMS sites, while outperforms the VPM model at US-WCr site. The difference between GPP_{MOD17} and GPP_{EC} ranges from -28% to CA-Cbo and US-Ha1, -20% to US-MMS, and -6% to US-WCr site.

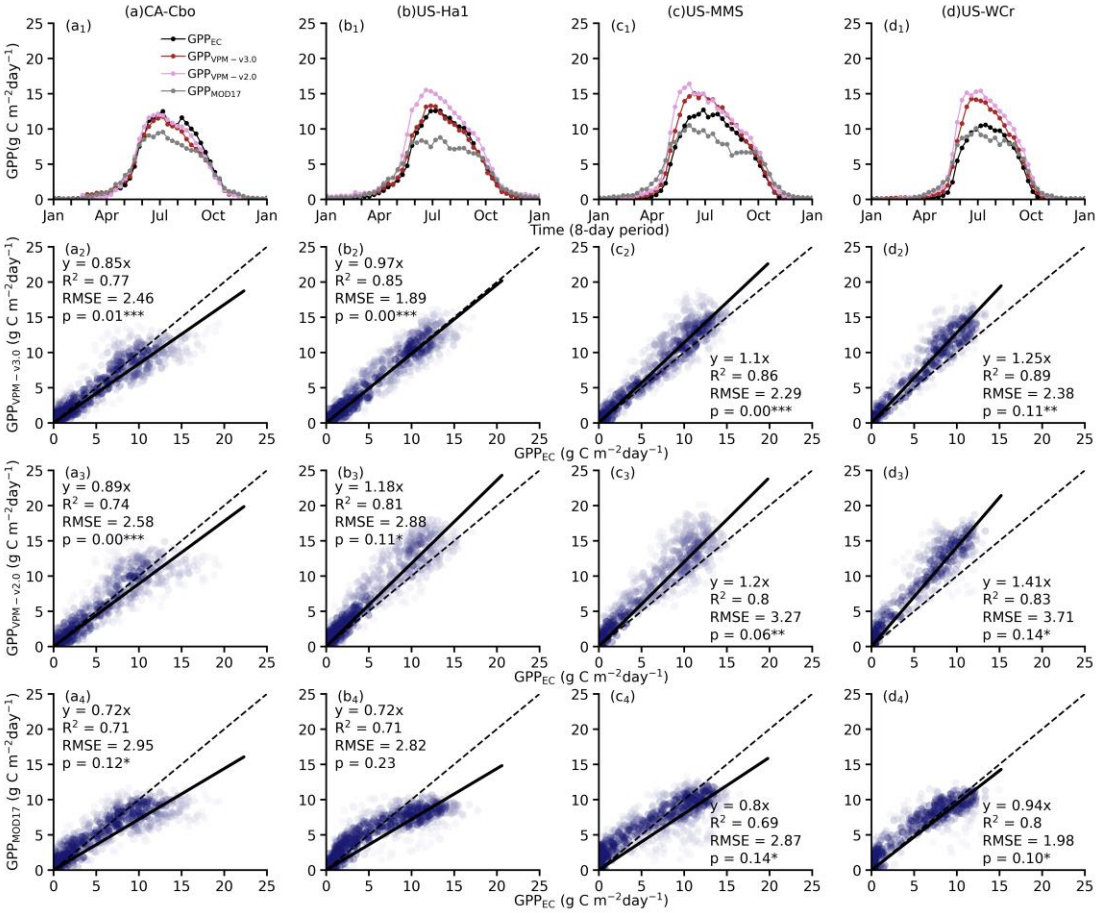

Figure 2.7: Comparison of GPP from VPM v3.0 ($GPP_{VPM\text{-}v3.0}$), VPM v2.0 ($GPP_{VPM\text{-}v2.0}$), MOD17 dataset (GPP_{MOD17}), and tower-based estimates (GPP_{EC}) at 8-day scale. $GPP_{VPM\text{-}v3.0}$ in this section is equal to GPP_{VPM}. The first row is the seasonal dynamics of the 21-year mean GPP. The second to fourth rows are the result of simple linear regression between different GPP models ($GPP_{VPM\text{-}v3.0}$, $GPP_{VPM\text{-}v2.0}$, GPP_{MOD17}) and GPP_{EC} using all years' data at an 8-day scale, respectively.

The interannual variations of different GPP products are shown in Figure 2.8. For $GPP_{VPM\text{-}v3.0}$, it shows consistent interannual variations and decadal trends with GPP_{EC} across most site years, and exceptions at certain site years, such as CA-Cbo in 2017, US-Ha1 in 2006 and 2009, US-MMS in 2007, and US-WCr in 2011 and 2012. Overall,

$GPP_{VPM\text{-}v3.0}$ closely tracks the interannual variability of GPP_{EC}. Simple linear regression results between $GPP_{VPM\text{-}v3.0}$ and GPP_{EC} indicate R^2 values of above 0.62 for four sites, with RMSE ranging from 186.29 g C $m^{-2}year^{-1}$ to 356.89 g C $m^{-2}year^{-1}$. In contrast, $GPP_{VPM\text{-}v2.0}$ shows a similar trend as $GPP_{VPM\text{-}v3.0}$, but with a lower R^2 value, ranging from 0.46 to 0.75, and a larger RMSE, ranging from 186.30 g C $m^{-2}year^{-1}$ to 562.81 g C $m^{-2}year^{-1}$. For GPP_{MOD17}, the R^2 values for all four sites are below 0.50, with RMSE values between 164.19 g C m^{-2} $year^{-1}$ and 325.49 gC m^{-2} $year^{-1}$. In conclusion, among the three products, $GPP_{VPM\text{-}v3.0}$ aligns closest with GPP_{EC}, effectively capturing the interannual variations and decadal trends of GPP_{EC}.

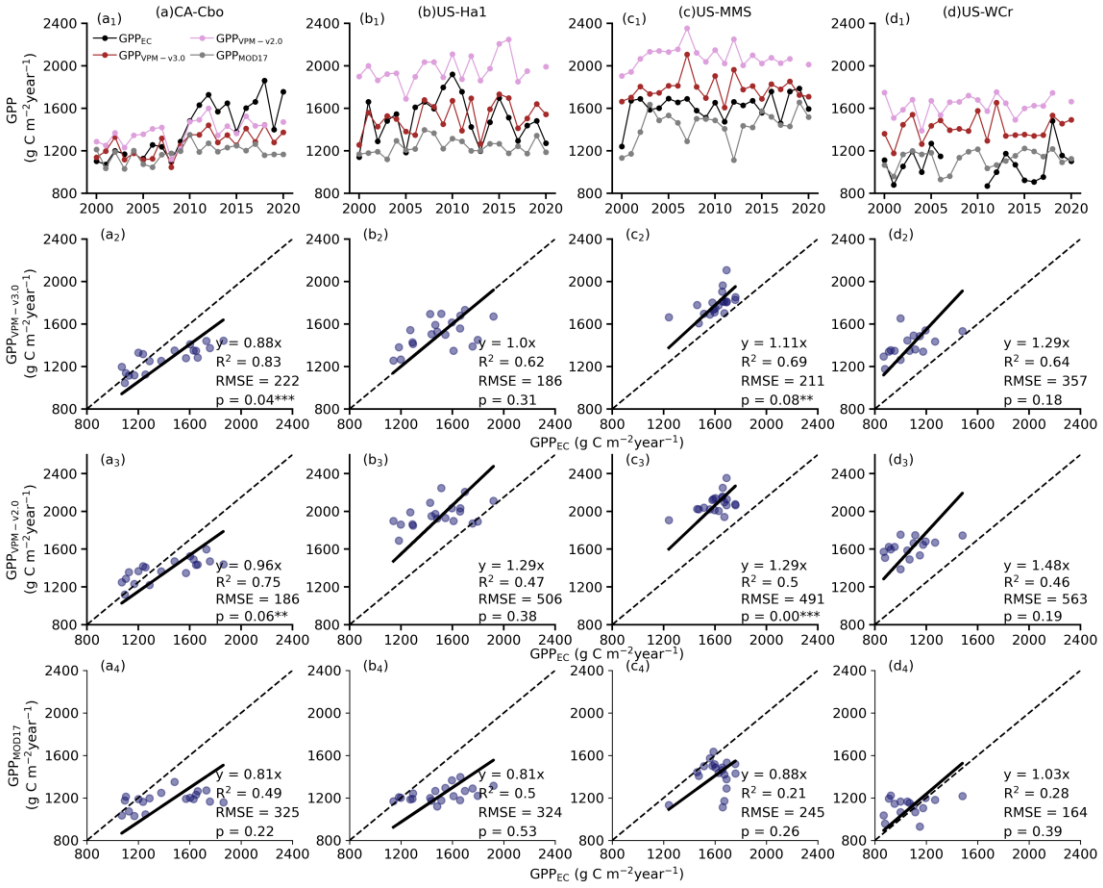

Figure 2.8: Comparison of GPP from VPM v3.0 ($GPP_{VPM\text{-}v3.0}$), VPM v2.0 ($GPP_{VPM\text{-}v2.0}$), MOD17 dataset (GPP_{MOD17}), and tower-based estimates (GPP_{EC}) at

annual scale. $GPP_{VPM\text{-}v3.0}$ in this section is equal to GPP_{VPM}. The first row is the interannual variations of four GPP productions. The second to fourth rows are the result of simple linear regression between different GPP productions ($GPP_{VPM\text{-}v3.0}$, $GPP_{VPM\text{-}v2.0}$, GPP_{MOD17}) and GPP_{EC} using all years' data during the growing season, respectively.

2.3.3 Interannual changes of CO_2 concentration, climate, vegetation indices, phenology, and carbon and water fluxes during 2000-2020

We explore interannual changes in atmospheric CO_2 concentrations and climate across the four sites (Figure 2.9). Atmospheric CO_2 concentrations increased significantly at all the sites (from +1.46 ppm yr^{-1} to +2.33 ppm yr^{-1}). For climate factors (GDD_{WESS}, GDD_{GS}, PAR_{GS}, and P_{GS}), no significant trends were observed, except for PAR_{GS} at CA-Cbo, which showed a significant increase (+41.64 mol m^{-2} yr^{-1}).

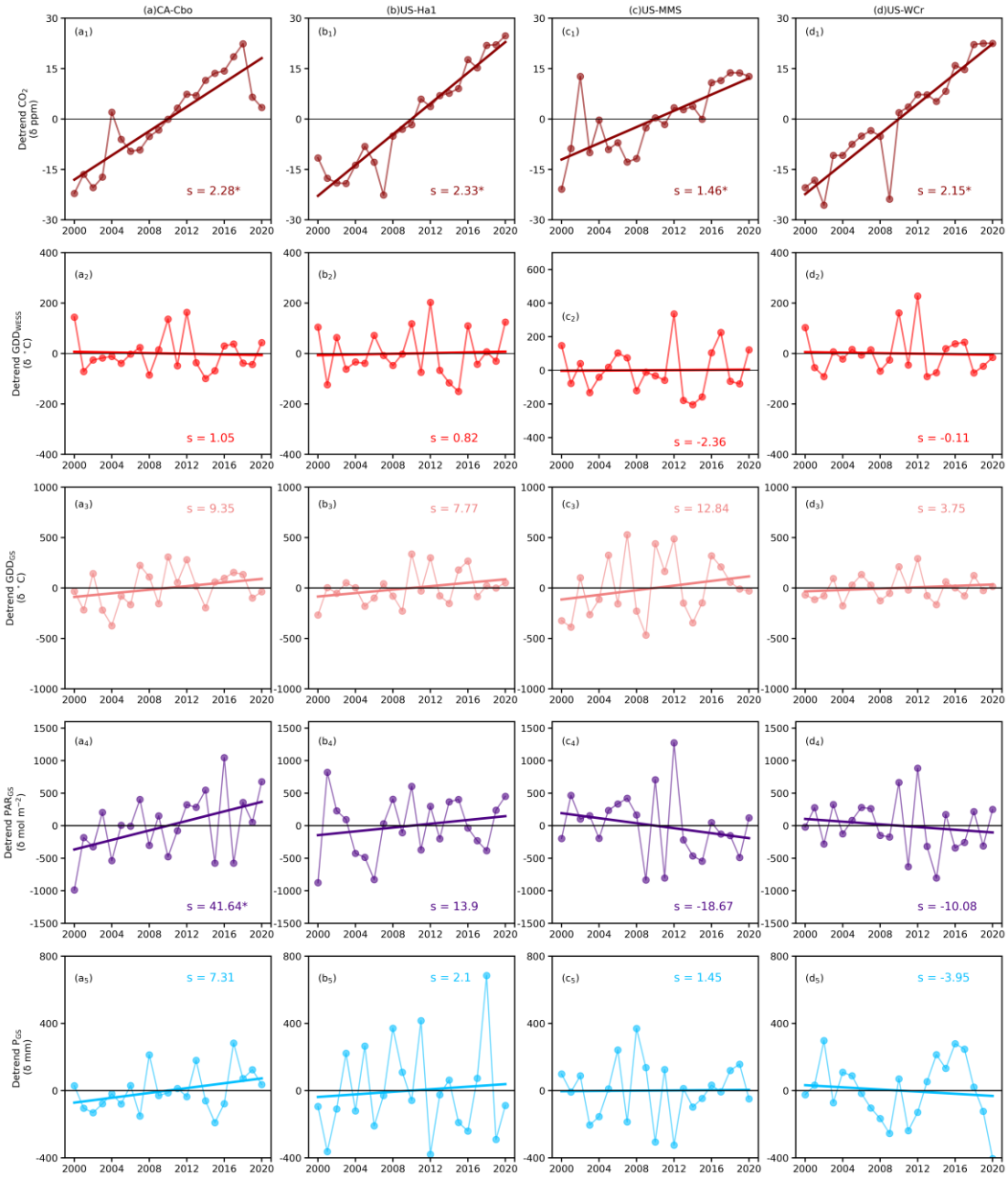

Figure 2.9: The interannual detrend of in-situ atmospheric CO_2 concentration, GDD_{WESS}, GDD_{GS}, PAR_{GS}, and P_{GS} from 2000 to 2020 across four deciduous forest sites. CO_2 concentration is average within the growing season. GDD_{WESS}, GDD_{GS}, PAR_{GS}, and P_{GS} are the sums within the growing season. *s* represents the Theil-Sen slope, and the * represents a significant trend through the M-K test. The Y-axis are the interannual variations after detrend processing.

For vegetation indices, only the CA-Cbo site showed a significant increase in EVI (+0.0037 yr^{-1}) and NDVI (+0.0034 yr^{-1}), and no significant trend was found in the other three sites (Figure 2.10).

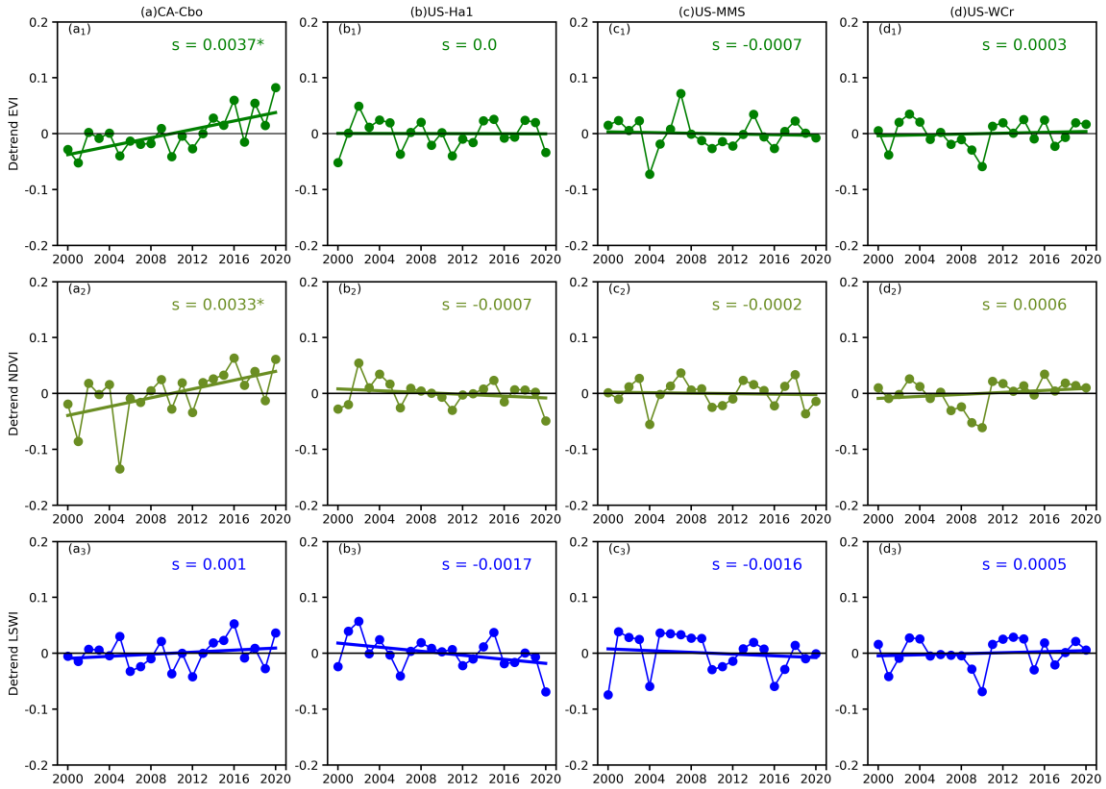

Figure 2.10: The interannual detrend of VIs from 2000 to 2020 across four deciduous forest sites. VIs are average values within the growing season. s represents the Theil-Sen slope, and the * represents a significant trend through the Mann-Kendall test. The Y-axis are the interannual variations after detrend processing.

There were no significant interannual trends in the physiological-based phenology metrics (SOS, EOS, GSL) across the four sites during the years 2000-2020, as depicted in Figure 2.11 and Figure 2.12. However, it is worth noting that in years characterized by a hot WESS (marked by red color in Figure 2.11 and Figure 2.12), the SOS tended

to occur earlier. Conversely, EOS has remained relatively stable and did not exhibit significant changes during the hot WESS years. By considering the combined effects of changes in SOS and EOS, the GSL was longer in years with a hot WESS.

For carbon fluxes, the decadal trends of GPP_{EC} and GPP_{VPM} are consistent, but they differ in magnitude. Only the CA-Cbo site shows a significantly increased trend in both GPP_{VPM} (+11.37 g C m^{-2} yr^{-1}) and GPP_{EC} (+31.03 g C m^{-2} yr^{-1}) over the last two decades (Figure 2.11, Figure 2.12). GPP_{VPM} at the US-Ha1 increased, but not significantly, while GPP_{EC} was stable. Both GPP_{VPM} and GPP_{EC} at US-MMS and US-WCr were relatively stable.

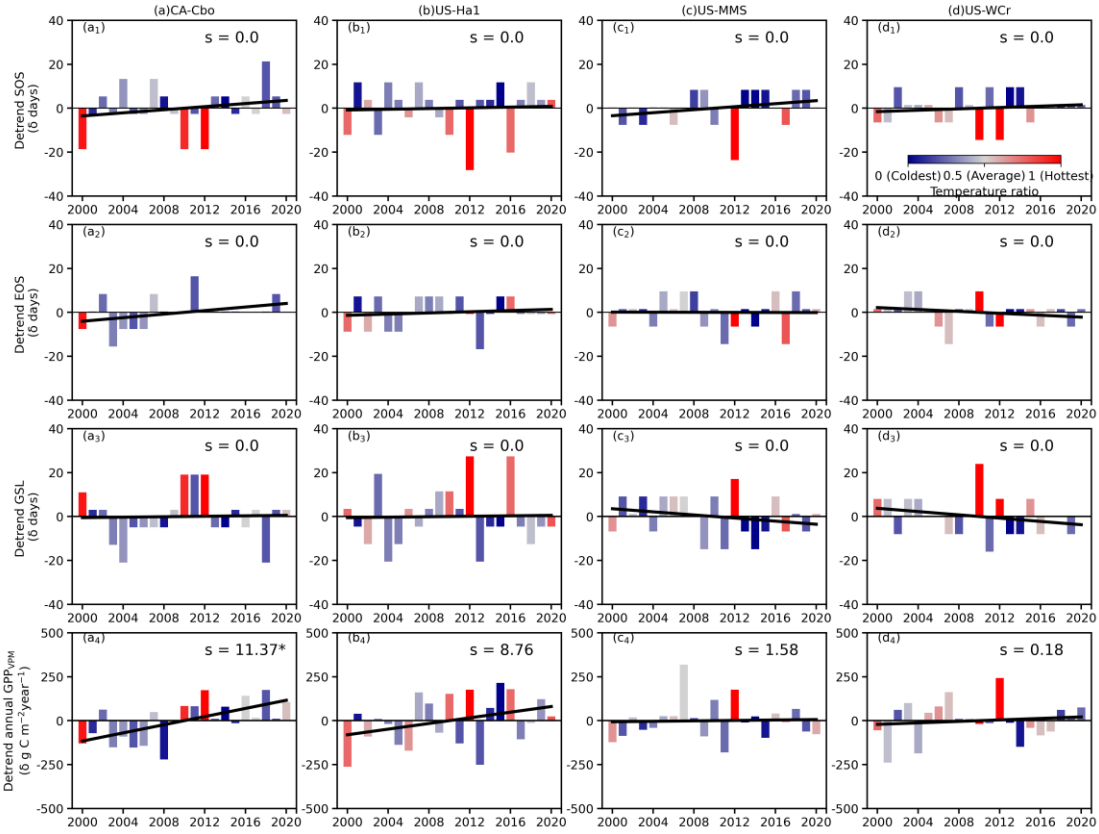

Figure 2.11: The interannual variations of physiological-based phenology (derived from GPP_{VPM}) and GPP_{VPM} from 2000 to 2020. GPP_{VPM} is the sums within the

growing season. *s* represents the Theil-Sen slope, and the * indicates passing the M-K significance test. The color bar is given the color according to the gradient of the normalized WESS temperature. The Y-axis is the interannual variation after detrend processing.

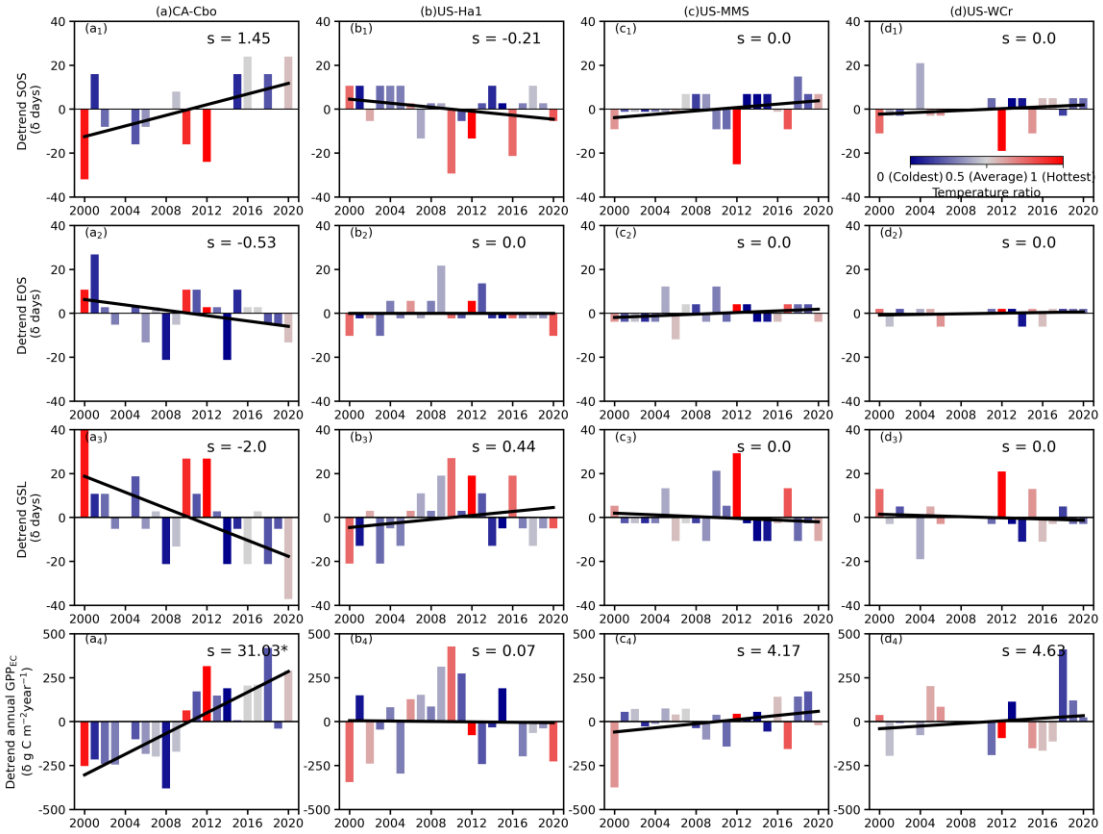

Figure 2.12: The interannual variations of physiological-based phenology (derived from GPP_{EC}) and GPP_{EC} from 2000 to 2020. GPP_{EC} is the sums within the growing season. *s* represents the Theil-Sen slope, and the * indicates passing the M-K significance test. The color bar is given the color according to the gradient of the normalized WESS temperature. The Y-axis is the interannual variation after detrend processing.

2.3.4 Attribution of interannual variations of annual GPP to atmosphere CO_2 concentration and climate

The results of the annual GPP_{EC} attribution analysis based on ridge regression are shown in Figure 2.13. Atmosphere CO_2 concentration only exhibited a slightly significant impact on annual GPP_{EC} (*, $p<0.15$) at CA-Cbo, whereas its influence was not significant in the other three sites. GDD_{GS} consistently demonstrated a significant impact on annual GPP_{EC} across all sites, especially at the US-Ha1, US-MMS, and US-WCr sites (***, $p<0.05$), followed by CA-Cbo (*, $p<0.15$). In contrast, GDD_{WESS} did not show any significant impact on annual GPP_{EC} across all sites ($p>0.15$). The impacts of PAR_{GS} on annual GPP_{EC} varied among sites, where it had a significant positive impact at CA-Cbo (*, $p<0.15$), US-Ha1 (**, $p<0.1$), and US-MMS (*, $p<0.15$), but was not significant at the US-WCr site ($p>0.15$). Throughout all sites, P_{GS} did not significantly affect annual GPP_{EC} ($p>0.15$). Notably, a negative correlation between P_{GS} and annual GPP_{EC} was observed at the CA-Cbo, US-Ha1, and US-WCr sites. In a comprehensive view, GDD_{GS} emerges as the primary driver for the annual GPP_{EC}, contributing between 23% and 63% to the annual GPP_{EC} across the four sites. The impacts of atmosphere CO_2 concentration and PAR on annual GPP_{EC} vary by site. Specifically, the contribution of atmospheric CO_2 on annual GPP_{EC} at the CA-Cbo site can reach up to 25%, but it is 8% or lower at other sites. PAR_{GS} contributes to annual GPP_{EC} in the range of 26% to 38% at the CA-Cbo, US-Ha1, and US-MMS sites respectively, while it only accounts for 13% at the US-WCr site. Both GDD_{WESS} and P_{GS} show minimal contributions across all sites.

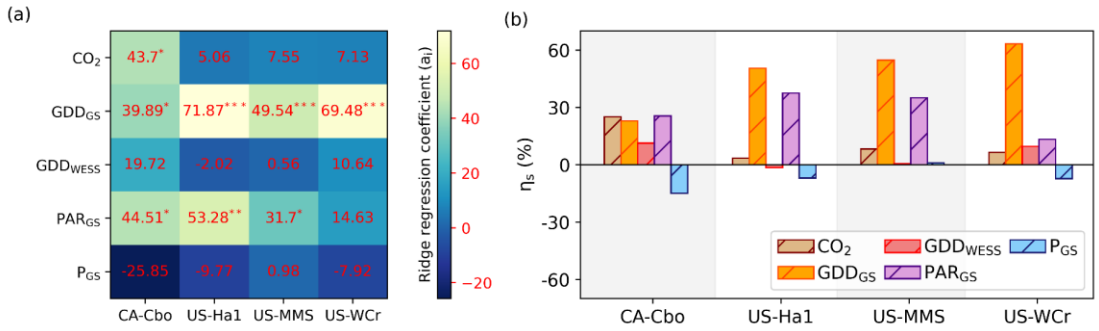

Figure 2.13: Ridge regression results of atmosphere CO_2 concentration and climate on annual GPP_{EC}. GPP_{EC} is the dependent variable, and CO_2, GDD_{GS}, GDD_{WESS}, PAR_{GS}, and P_{GS} are the independent variables. (a) The ridge regression coefficients of the five independent variables. The values indicate the changes in annual GPP when the normalized independent variable increases by one unit. *, **, and * represent the significance at 0.15, 0.1, and 0.05 levels. (b) The relative contribution (η_s) of five driving factors to annual GPP_{EC}.**

2.4 Discussions

2.4.1 Performance of the VPM v3.0 in simulating long-term carbon fluxes

Compared to VPM v2.0, VPM v3.0 predominantly updates the climate data inputs and improves the T_{opt} parameters. Our analysis concludes that VPM v3.0 offers a marked improvement over its previous version, particularly in capturing the seasonal dynamics and interannual variations of GPP. One of the salient factors driving this improvement is the replacement of relatively refined climate data. The coarse spatial resolution (~32 km) of the National Center for Environmental Prediction-North America Regional Reanalysis (NCEP-NARR) dataset utilized by VPM v2.0 isn't its only limitation (Yao

Zhang et al., 2017). Previous research has also highlighted that the NCEP-NARR dataset tends to overestimate radiation by roughly 20% when benchmarked against the eddy flux tower site measurement (Yao Zhang et al., 2016). This discrepancy explains a partial reason for the significant overestimation exhibited by VPM v2.0. Additionally, the quality of the radiation from 2019 was subpar, leading us to exclude the simulations from that year. This exclusion might affect the analysis of interannual variations and decadal trends. Another improvement in VPM v3.0 was the improvement of the T_{opt} input parameter. Given the distinct climatic conditions across the four sites and the thermal acclimation of vegetation (Jin et al., 2015; Niu et al., 2012; Yamori et al., 2014; Yamori et al., 2010), a site-specific T_{opt} should be more efficacious for the ecosystem model than a biome-specific T_{opt} (Bennett et al., 2021; Chang et al., 2021a; Chang et al., 2020; Huang et al., 2019; McCallum et al., 2013).

When benchmarked against GPP_{EC}, VPM v3.0 exhibits acceptable accuracy in capturing both the seasonal dynamics and interannual variations. This robust performance lays a foundational groundwork for tracking interannual variations and decadal trends in deciduous broadleaf forest ecosystems. It should be noted that regarding amplitude, the slopes observed in CA-Cbo, US-Ha1, and US-MMS comfortably reside within the reasonable ranges of model simulation. At the US-WCr, however, GPP_{VPM} is substantially higher (up to 25%) than GPP_{EC}. As the US-WCr site has similar EVI and climatic parameters to the other three sites, we anticipate that it has similar GPP_{EC} and GPP_{VPM} to align with the other sites in terms of GPP magnitude. We compared NEE and R_{eco} data over the four sites, and the R_{eco} at the US-WCr is

significantly lower than that of the other three sites (Figure 2.14), which results in relatively low GPP_{EC} at the US-WCr. Therefore, it is necessary that NEE partitioning at the US-WCr site may need to be re-investigated in the future.

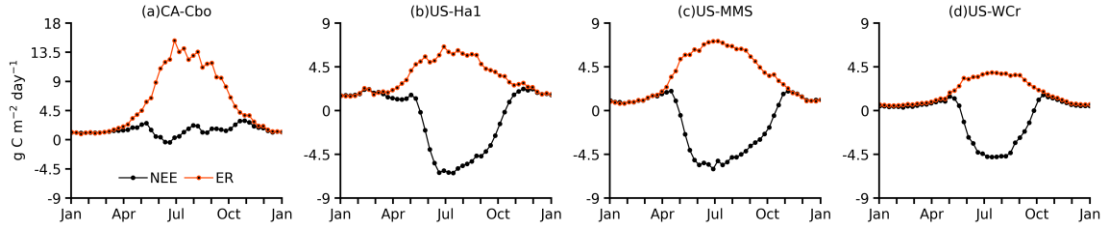

Figure 2.14: The seasonal dynamics of 21-years mean net ecosystem exchange (NEE) and ecosystem respiration (ER).

Considering that this is the first time we applied the VPM model over a continuous span of two decades, whereas previous VPM simulations only encompassed a single year or a few years (Doughty et al., 2018; Kang et al., 2016; Kang et al., 2014; Xiao, Hollinger, et al., 2004; Xiao, Zhang, et al., 2004; Xin et al., 2017), the results demonstrate the effectiveness of VPM v3.0 incorporating the ERA5-Land climate dataset and site-specific T_{opt} in simulating long-term carbon flux. With the accessibility of satellite-derived climate data and surface reflectance data, the next step will be to employ VPM v3.0 in different regions or the globe.

2.4.2 Effects of warm winter and early spring season (WESS) on phenology and GPP

Many studies have reported that climate warming advanced spring phenology (SOS) and delayed autumn phenology (EOS), which then extend the growing season length (GSL) (Dragoni et al., 2011; Finzi et al., 2020; Keenan et al., 2014; Richardson et al.,

2010). According to our results (Figure 2.11, Figure 2.12), in the years marked as hot WESS, SOS is clearly earlier, significantly positively correlated with GDD_{WESS}. However, there is no significant delay in EOS found in hot years, and the response of EOS to GDD_{WESS} is relatively weak. Nevertheless, it can still be confirmed that in hot years there is a corresponding increase in the growing season length due to the high GDD_{WESS}.

In general, the growing season length increase may extend the time period for photosynthesis, leading to a higher annual GPP over the growing season (Finzi et al., 2020). For example, a modeling study reported that annual GPP increased by 5.8 g C m^{-2} $year^{-1}$ for each day the growing season was extended (Piao et al., 2007). However, our results showed clearly that annual GPP (both GPP_{VPM} and GPP_{EC}) did not significantly increase in years with an extended growing season (Figure 2.11, Figure 2.12). Attribution analysis shows poorly contributions of GDD_{WESS} to annual GPP (Figure 2.13), which is similar to a recent study at the Smithsonian Conservation Biology Institute (SCBI) and Harvard Forest sites, which reported that the impact of warm springs on annual stem growth was minimal from 2011 to 2020 (Dow et al., 2022). A previous study on forests in the eastern United States (including US-Ha1 and US-MMS) found that warm springs significantly increased spring GPP (Keenan et al., 2014), and our study came to the same conclusion (Figure 2.15), and simple linear regression results clearly show that warm WESS enhances spring GPP (both GPP_{VPM} and GPP_{EC}) with a significant positive correlation between GDD_{WESS} and spring GPP at CA-Cbo, US-MMS, and US-WCr (***, $p<0.05$). We hypothesize that this positive

effect may be mitigated or offset during the summer. Further analysis supports this hypothesis (Figure 2.15 b, d), there is a negative correlation between GDD_{WESS} and summer GPP for both GPP_{VPM} and GPP_{EC}. For summer GPP_{VPM}, this negative relationship is significant at CA-Cbo (***, $p<0.05$) and US-Ha1 (*, $p<0.15$). For summer GPP_{EC}, the negative correlation is significant at US-Ha1 (*, $p<0.15$), US-MMS (***, $p<0.05$), and US-WCr (***, $p<0.05$). This may be caused by multiple factors, for example, drought stress (Buermann et al., 2013; Buermann et al., 2018; Lian et al., 2020), stomatal closure (Farquhar et al., 1982; Keenan et al., 2013), or leaf senescence (Fu et al., 2014). These factors form negative feedback on climate change. This evidence suggests that over the past two decades, the primary impacts of temperature on deciduous trees have changed. Temperature impacts do not occur during the WESS but rather during the GS (Figure 2.13). Unless vegetation can immediately adapt to climate warming, the hotter WESS is unlikely to have a positive impact on the annual growth of temperate mature deciduous broadleaf forests.

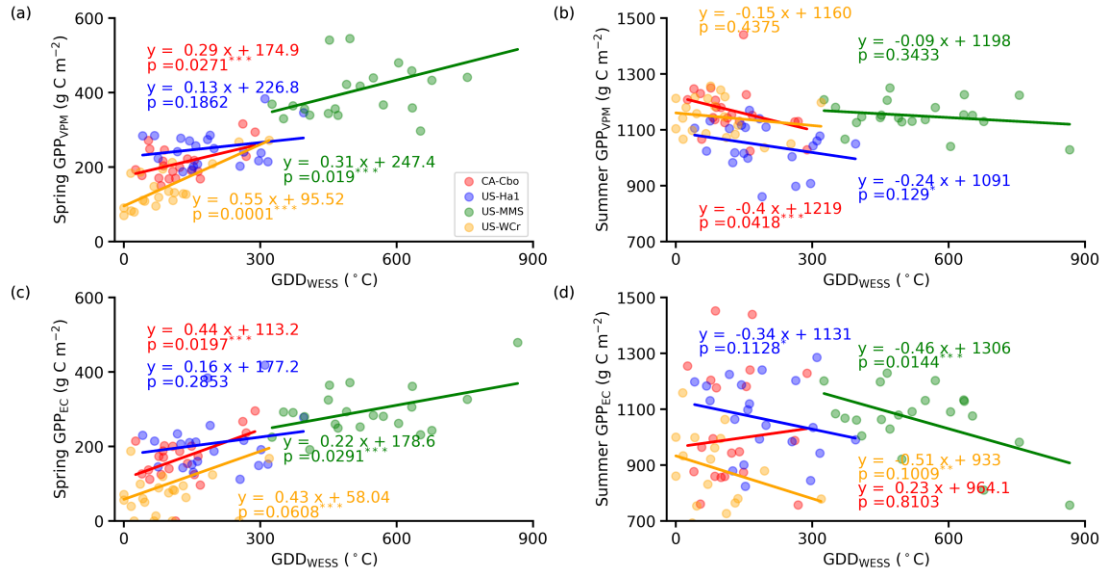

Figure 2.15: The correlations between GPP (GPP_{VPM}, GPP_{EC}) during spring and

summer to GDD_{WESS}. Spring and summer are defined as periods of March to May, and June to August, respectively. *, **, and * represent the significance at 0.15, 0.1, and 0.05 levels.**

2.4.3 Long-term trends in phenology, carbon, and water fluxes

Previous studies of satellite phenology have mostly focused on the last two decades of the twentieth century (Jeong et al., 2011), when global warming was a consensus, however, Cane (2010) reported that the significant warming trend observed during the last two decades of the 20th century ceased from the year 2000 to 2010 (Cane, 2010). This may be caused by the negative feedback of vegetation on climate, the growth of vegetation slows down the rate of air temperature increase (Bounoua et al., 2010). Our trend analysis clearly shows that over the last two decades of the 21st century, the SOS at the four mature deciduous forest sites did not show a significant advance, primarily due to the absence of a significant trend in WESS temperatures (Figure 2.9).

Previous study have reported annual GPP increases due to rising atmospheric CO_2 concentrations or climate warming (Launiainen et al., 2022). Although atmospheric CO_2 concentrations have risen significantly over the last two decades (Sperry et al., 2019), however, air temperature at the four sites shows an insignificant increase. Attribution analysis shows that GDD_{GS} and PAR_{GS} contribute significantly to annual GPP at US-Ha1, US-MMS and US-WCr, so the lack of significant trends in GDD_{GS} and PAR_{GS} at these three sites could explain the stability of GPP at these sites over the past two decades (Figure 2.9, Figure 2.13). CA-Cbo is an exception. At this site, CO_2, GDD_{GS} and PAR_{GS} jointly affect annual GPP. Note in this site, the impact of PAR_{GS} on

annual GPP is higher than the impact of GDD_{GS} on annual GPP, which agrees with a previous study (Gonsamo et al., 2015). Therefore, the significant increase in GPP at this site is attributed to the significant increase in CO_2 and PAR_{GS}. Human management will also affect the trend analysis. In the case of US-WCr, while our analyses show that the decadal trends in GPP are driven solely by GDD_{GS}, however, other events at this site affect attribution and trend analysis. For instance, the severe insect infestation in the late spring of 2001 led to the complete detachment of canopy crown in June, resulting in a particularly low GPP for 2001 (Desai et al., 2022). Moreover, the commercial logging activities during the winters of 2013 and 2014 brought about a significant decline in GPP in the subsequent years (Desai et al., 2022), and it was not until after 2018 that GPP returned to increase. Uncertainty remains regarding the GPP attribution at this site. Therefore, continued observations at US-WCr site are necessary to further explore the site's response to climate change.

2.5 Conclusion

The chapter investigated the skill of VPM v3.0 and the ERA5-Land climate dataset for simulations over the past two decades at four mature deciduous broadleaf forests in the United States and Canada from 2000 to 2020. The results align with long-term measurements conducted at the forest eddy tower sites and support the potential use of the ERA5 climate dataset for regional and global-scale simulations.

Additionally, we also explored the interannual variations of climate, vegetation indices, and carbon fluxes at these sites and assessed the effects of several factors such as atmospheric CO_2 concentration and climate on vegetation indices, phenology, and

carbon and water fluxes. Built upon previous research that used limited and earlier years of data, this study focuses on the last two decades and analyses how phenology and productivity in these forests respond to weather and climate over the years. The findings from this study differ from earlier research, likely due to the complex feedback mechanisms between vegetation adaptation and climate change.

Chapter 3 : Site-specific apparent optimum air temperature for vegetation photosynthesis across the globe

ABSTRACT

The apparent optimum air temperature for vegetation photosynthesis (T_{opt}) is a key temperature parameter in terrestrial ecosystem models estimating daily photosynthesis or gross primary production (GPP, gC m^2 day^{-1}). To date, most models use biome-specific T_{opt} ($T_{opt\text{-}biome}$) parameter values. Given vegetation acclimation and adaptation to local climate, site-specific T_{opt} ($T_{opt\text{-}site}$) is needed to reduce uncertainties in estimating daily GPP across the scales from site to region and the globe. At the site level, VPM v3.0 has demonstrated improved model performance when incorporating site-specific optimum temperature ($T_{opt\text{-}site}$) parameters. Therefore, extending the application of VPM v3.0 to regional or global GPP estimation requires the availability of a spatially explicit, global $T_{opt\text{-}site}$ dataset. Previous studies have demonstrated using the Enhanced Vegetation Index (EVI) derived from Moderate Resolution Imaging Spectroradiometer (MODIS) images and daytime air temperature data to estimate the $T_{opt\text{-}site}$ at the eddy covariance tower sites. In this chapter, we used MODIS-derived EVI and ERA5-Land climate data to estimate and generate global $T_{opt\text{-}site}$ data products. The $T_{opt\text{-}site}$ of individual pixels within a biome has large variation, which clearly cannot be represented accurately by the widely used $T_{opt\text{-}biome}$. Therefore, using this global dataset of $T_{opt\text{-}site}$ estimates might significantly affect GPP simulation in current ecosystem models.

3.1 Introduction

Among the carbon flux components, Gross Primary Production (GPP) represents the amount of carbon dioxide absorbed by vegetation, playing a pivotal role in the global carbon cycle (Anav et al., 2015; Frankenberg et al., 2011). Air temperature (T_{air}, ~2 m above the ground) is one of the key climatic variables influencing the spatiotemporal dynamics of GPP (Anav et al., 2015; Bennett et al., 2021; Jung et al., 2011b). An increase in Tair can boost enzyme activity, leading to a rise in photosynthesis rate, and excessive Tair can result in stomatal closure and enzyme deactivation, causing a decline in photosynthesis (Lloyd et al., 2008; Medlyn et al., 2002). Therefore, the GPP response to Tair follows a parabolic (unimodal) curve (Bennett et al., 2021; Chang et al., 2021b), and the apparent optimum air temperature (T_{opt}) is generally defined as the Tair at which vegetation achieves its peak photosynthesis rate (Figure 3.1).

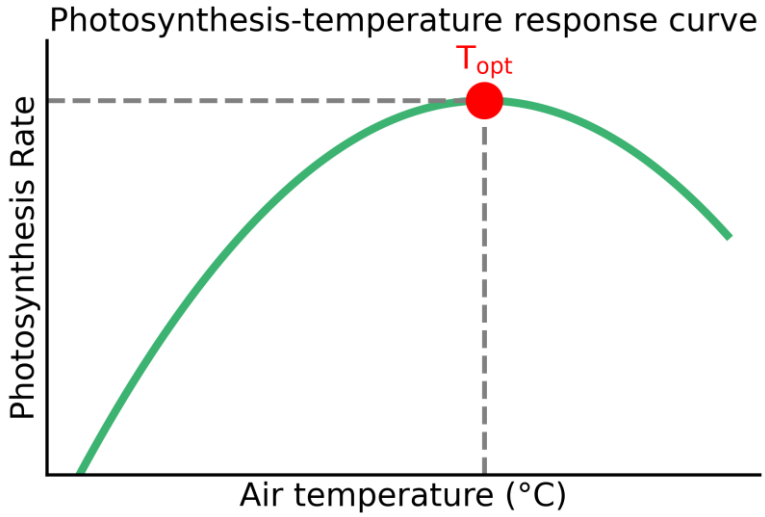

Figure 3.1: The response curve of photosynthetic rate to air temperature.

Almost all terrestrial ecosystem carbon cycle models have temperature response functions for GPP, with T_{opt} being a crucial temperature parameter (Friedlingstein et al.,

2006; Niu et al., 2012). Light Use Efficiency (LUE) models also have the T_{opt} parameter in estimating GPP (Running et al., 2015; Yuan et al., 2007; Yao Zhang et al., 2017). Currently, the T_{opt} parameter values in terrestrial ecosystem models use biome-specific T_{opt} for individual biomes ($T_{opt\text{-}biome}$) (Melillo et al., 1993; Raich et al., 1991). However, recent studies suggest that the $T_{opt\text{-}biome}$ may significantly differ from site-specific T_{opt} ($T_{opt\text{-}site}$) (Chang et al., 2021a; Huang et al., 2019). $T_{opt\text{-}biome}$ parameter values used in the models came from analyses of the limited number of locations for individual biomes (Chang et al., 2021a). Additionally, because of vegetation acclimation and adaption to local climate (Mooney et al., 1978; Niu et al., 2012), the use of biome-specific T_{opt} at the global scale could introduce large errors and uncertainty in global GPP estimation.

GPP and air temperature data from eddy covariance (EC) flux tower sites are widely used to study the response curves of GPP to air temperature and to estimate the $T_{opt\text{-}site}$ at individual sites (ecosystems) (Bennett et al., 2021; Chang et al., 2021a; Chang et al., 2020; Niu et al., 2012; Wang et al., 2023; Yuan et al., 2011). However, the number of EC towers is limited (Baldocchi, 2014), and their footprints only cover a small portion of global land surface (Papale et al., 2006). Additionally, most EC flux tower observations last a few years or a decade, making it challenging to explore the interannual variations of T_{opt} at the sites. Several studies explored the use of remote sensing data to estimate $T_{opt\text{-}site}$ over large geographical domains and longer periods (Yongzhe Chen et al., 2021; Huang et al., 2019; Wang et al., 2023). Since the photosynthesis rate depends on the number of photosynthetic organs (i.e., chloroplasts) in the canopy, it can be directly represented by the total chlorophyll content in the

canopy (Peng et al., 2013; Schlemmer et al., 2013). Many studies have explored the estimation of canopy chlorophyll content from satellite-derived vegetation indices (VIs), such as the Enhanced Vegetation Index (EVI) (Xiao, Hollinger, et al., 2004; Xiao, Zhang, et al., 2004), Normalized Difference Vegetation Index (NDVI) (Xin et al., 2017), and Near-infrared Reflectance of Vegetation (NIRv) (Wu et al., 2020). These VIs have shown a strong relationship with GPP and are therefore used as predictor variables to represent vegetation structure and function (Yongzhe Chen et al., 2021; Gao et al., 2014; Hunt Jr et al., 2013; Peng et al., 2013). Recent studies have demonstrated the feasibility of using VIs-T_{air} response curves to estimate $T_{opt\text{-}site}$ at site, regional, or global scales (Chang et al., 2021b; Chang et al., 2020; A. Chen et al., 2021; Yongzhe Chen et al., 2021; Huang et al., 2019). It is worth noting that these publications differ in terms of VIs variables (e.g., NDVI, EVI, and NIRv), air temperature datasets (e.g., daily mean air temperature), and algorithms, leading to noticeable discrepancies in $T_{opt\text{-}site}$ estimates across these studies. Accurate quantification of $T_{opt\text{-}site}$ and site-year-specific T_{opt} ($T_{opti\text{-}site\text{-}year}$) at global scale remains challenging.

In this chapter, built upon our previous studies that used GPP, EVI, and daytime air temperature data to estimate $T_{opt\text{-}site}$ at the eddy covariance tower sites (Chang et al., 2021b; Chang et al., 2020), we first generated the $T_{opt\text{-}site\text{-}year}$ and $T_{opt\text{-}site}$ dataset across the globe from 2000 to 2019, using MODIS-derived EVI data (500-meter spatial resolution) and daytime air temperature from ERA5-Land climate data (Hersbach et al., 2020; Muñoz-Sabater et al., 2021). We also carried out data analyses of this dataset, which provides basic information on (1) the spatiotemporal patterns of $T_{opt\text{-}site\text{-}year}$ and

$T_{opt\text{-}site}$ across the globe over the past two decades and (2) the variability (frequency distribution) of $T_{opt\text{-}site}$ from all the pixels within individual biomes. Terrestrial ecosystem models could use this global $T_{opt\text{-}site}$ dataset to increase the accuracy of and reduce the uncertainty of GPP data under historical, current, and future climate scenarios. $T_{opt\text{-}site}$ dataset could also be used for further analyses that offer valuable insights into how vegetation has responded to climate change over the past two decades.

3.2 Materials and Methods

3.2.1 ERA5-Land reanalysis climate data

ERA5 is the fifth generation of atmospheric reanalysis products released by the European Centre for Medium-Range Weather Forecasts (ECMWF) (Hersbach et al., 2020). This dataset offers comprehensive historical and near-real-time information on global atmospheric, terrestrial, and oceanic variables (Muñoz-Sabater et al., 2021). ERA5-Land complements the ERA5 by focusing specifically on terrestrial processes. Compared to ERA5, ERA5-Land boasts a higher spatial resolution (0.1°) and a higher temporal resolution (hourly), enabling a more precise depiction of surface processes and characteristics, including air temperature and precipitation.

In this study, we used the air temperature (T_{air}) layer from the ERA5-Land reanalysis climate dataset. We provided an example of the air temperature data from the Harvard Forest site (US-Ha1) in 2010 (Figure 2.5) and illustrate the discrepancies among the three temperature variables: daily maximum air temperature ($T_{air\text{-}max}$), daily daytime mean air temperature ($T_{air\text{-}DT}$), and daily mean air temperature ($T_{air\text{-}mean}$); and

we assessed the appropriateness of these three temperature variables for the Topt estimation algorithm. $T_{air\text{-}DT}$ is defined by averaging $T_{air\text{-}max}$ with $T_{air\text{-}mean}$ (Yao Zhang et al., 2017):

$$T_{air\text{-}DT} = \text{average}(T_{air\text{-}max}, T_{air\text{-}mean}) \quad (3.1)$$

We aggregated these three air temperature variables from daily data into 8-day intervals by averaging the observations over the 8-day period to align with the temporal resolution of MOD09A1

3.2.2 MODIS land surface temperature dataset

The Moderate Resolution Imaging Spectroradiometer (MODIS) is a key instrument for observing changes on the Earth's surface (Justice, Townshend, et al., 2002). The MYD11A2 dataset provides an 8-day and 1-km composite of global land surface temperatures (LST) and emissivity, sourced from the MODIS instrument aboard NASA's Aqua satellite. This dataset provides LST at 1:30 a.m. and 1:30 p.m. In this study, we constrained the analyses of EVI and T_{air} data and T_{opt} algorithm within the thermal growing season (Linderholm et al., 2008), as defined by nighttime LST (Yao Zhang et al., 2016), which helps to mitigate uncertainties from outliers beyond this period (e.g., high EVI caused by snow). For each pixel (1-km spatial resolution), we reconstructed the LST time series using a moving window of three consecutive 8-day periods, calculating the average across them (Figure 3.2a). Adopting the threshold assumption that the LST for the thermal growing season is >=5°C (Dong, Xiao, Kou, et al., 2015), the start of the season (SOS_{LST}) was marked by the LST first surpassing this threshold in winter/spring, while its end of the season (EOS_{LST}) corresponds to the

LST first descending below this threshold in fall/winter (Figure 3.2a). Note this method was applied only to those pixels where the annual peak LST surpasses 5 °C. For areas with an annual peak of LST not reaching 5°C (e.g., high-altitude plateau or boreal forests), we substituted LST with $T_{air\text{-}DT}$.

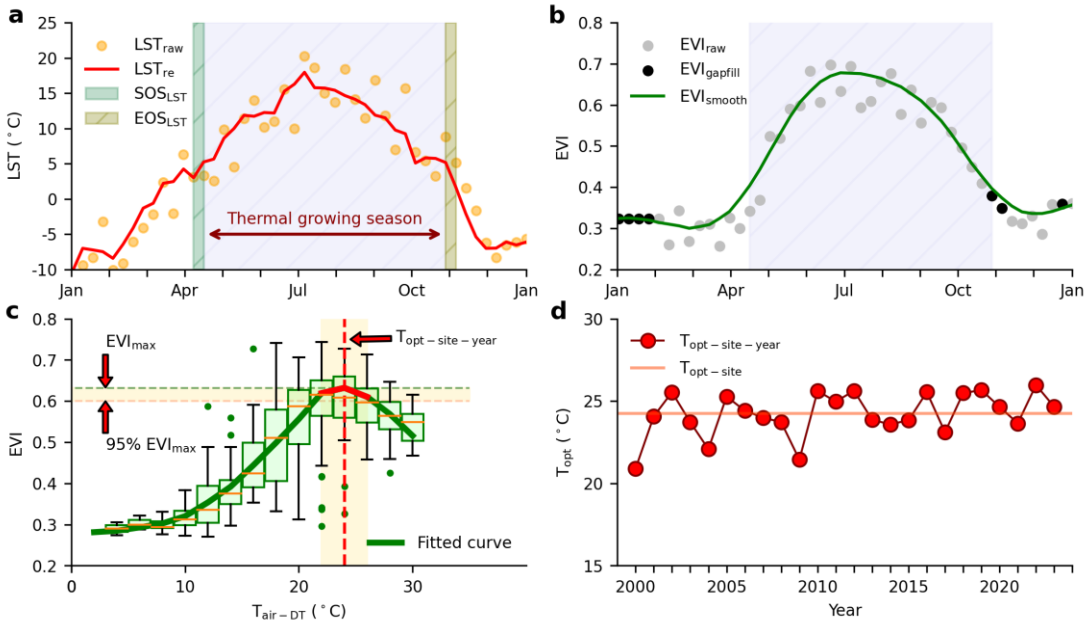

Figure 3.2: The workflow for estimating site-specific apparent optimum temperature ($T_{opt\text{-}site}$) at a deciduous broadleaf forest site in the USA (Harvard Forest, US-Ha1, DBF, 42.5378°N, 72.1715°W). The US-Ha1 site was selected because it is a mature forest subject to long-term observation and research, showing the typical seasonal dynamics of vegetation in mid-latitude areas. The altitude is 340 meters. a. raw LST (LST_{raw}) and reconstructed LST (LST_{re}) time series. The thermal growing season is defined as the period LST_{re} greater than 5°C (light blue filled area). SOS_{LST} and EOS_{LST} represent the start and end of the thermal growing season, respectively; b. raw EVI (EVI_{raw}, only after cloud removal), gap-filled EVI ($EVI_{gapfill}$, linear interpolation), and smoothed EVI

(EVI_{smooth}, S-G filter); c. The curve of EVI-T_{air}. The solid green curve is fitting curves using cubic regression splines. c. also shows a boxplot with points every 2 °C bin; d. interannual variations of $T_{opt\text{-}site\text{-}year}$ from 2000 to 2019, $T_{opt\text{-}site}$ is calculated as the median value from 20 years of $T_{opt\text{-}site\text{-}year}$ data.

3.2.3 MODIS surface reflectance and vegetation indices

The MODIS surface reflectance products are widely used in monitoring global vegetation (Justice et al., 1998). In this study, we utilized the MOD09A1 Surface Reflectance V6.1 product, a dataset of seven spectral bands ranging from 0.459μm to 2.155μm with a 500-m spatial and an 8-day temporal resolution (Didan et al., 2015).

We have processed and analyzed the global MOD09A1 surface reflectance time series data from 2000 to 2019. Three vegetation indices - NDVI, EVI, and NIRv - were calculated. NDVI, utilizing near-infrared and red bands, offers a measure of vegetation greenness and is hence used to identify green vegetation areas (Rouse et al., 1974). EVI, while similar to NDVI, is specifically designed to correct for atmospheric disturbances and background soil effects (Huete et al., 2002). NIRv is derived from NDVI, yet it exhibits a stronger correlation with observed GPP than NDVI (Badgley et al., 2017). Among these vegetation indices, EVI has been reported to be most closely related to leaf and canopy-level chlorophyll content (Gao et al., 2014; Pan, Xiao, Pan, et al., 2024; Xiao, Hollinger, et al., 2004; Xiao, Zhang, et al., 2004; Xin et al., 2017). Additionally, several biophysical studies have shown that EVI is nearly unsaturated and sensitive to canopy changes (Gao et al., 2014; Xiao, Hollinger, et al., 2004). The three VIs are calculated by the Eqs. (3.2) - (3.4):

$$NDVI = \frac{\rho_{nir} - \rho_{red}}{\rho_{nir} + \rho_{red}} \quad (3.2)$$

$$EVI = 2.5 \times \frac{\rho_{nir} - \rho_{red}}{\rho_{nir} + (6 \times \rho_{red} - 7.5 \times \rho_{blue}) + 1} \quad (3.3)$$

$$NIRv = NDVI \times \rho_{nir} \quad (3.4)$$

where ρ_{nir} , ρ_{red}, and ρ_{blue} are the surface reflectance bands of near infrared, red, and blue, respectively. In order to generate a high-quality and continuous surface reflectance time series, the QA-band quality detection approach was employed to retrieve pixels affected by clouds and cloud shadows. Additionally, the Best Index Slope Extraction (BISE) method was used to detect overlooked low-quality observation pixels (Viovy et al., 1992). After two rounds of filtration processes, the low-quality observations were then marked as a mask for the row image (Figure 3.2b). A linear interpolation approach, coupled with high-quality observations, was used to fill the gaps (Liu et al., 2020; J. Wang et al., 2020) (Figure 3.2b). Finally, to further minimize the temporal variation within the time series data, we utilized the Savitzky-Golay (S-G) method for curve smoothing (Savitzky et al., 1964). Note that the smoothing window is set based on the varying lengths of the thermal growing season; for instance, if the thermal growing season of a pixel is 240 days, a sliding window of 31 8-day observations were employed for curve smoothing.

3.2.4 MODIS land cover product

The MODIS Land Cover Type (MCD12Q1) Version 6.1 data product offers annual global land cover classifications from 2001 to the present (Sulla-Menashe et al., 2018). In this study, we utilized the International Geosphere Biosphere Program (IGBP) layer,

which identifies 17 distinct land cover types. Our focus was on the following 14 categories: Evergreen Needleleaf Forests (ENF), Evergreen Broadleaf Forests (EBF), Deciduous Needleleaf Forests (DNF), Deciduous Broadleaf Forests (DBF), Mixed Forests (MF), Closed Shrublands (CSH), Open Shrublands (OSH), Woody Savannas (WSA), Savannas (SAV), Grasslands (GRA), Permanent Wetlands (WET), Croplands (CRO), Urban and Built-up Lands (URB), and Cropland/Natural Vegetation Mosaics (CNV). The spatial delineation of these categories is illustrated in Figure 3.3. In this paper, we explored the variation of $T_{opt\text{-}site}$ within individual biomes for the above-mentioned 14 biomes.

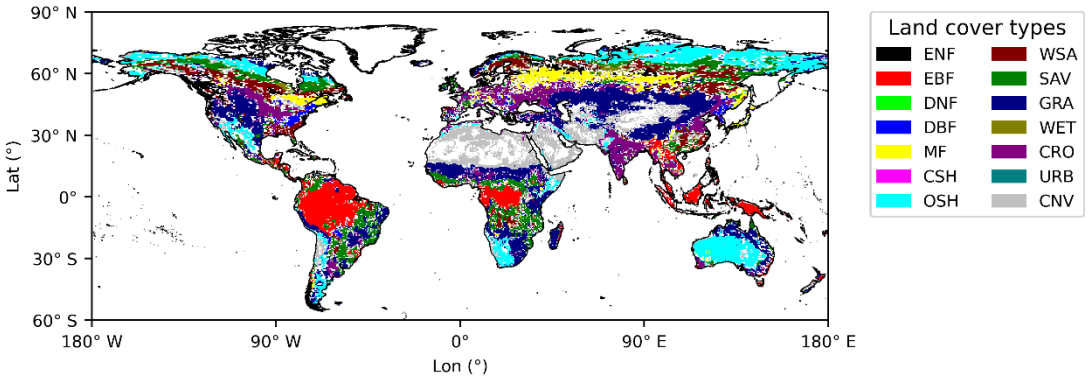

Figure 3.3: Geographical distribution of 14 biome ecosystems in MODIS land cover products (MCD12Q1). This map only shows pixels with constant land cover type from 2000 to 2019. ENF: Evergreen Needleleaf Forests; EBF: Evergreen Broadleaf Forests DNF: Deciduous Needleleaf Forests; DBF: Deciduous Broadleaf Forests; MF: Mixed Forests; CSH: Closed Shrublands; OSH: Open Shrublands; WSA: Woody Savannas; SAV: Savannas; GRA: Grasslands; WET: Permanent Wetlands; CRO: Croplands; URB: Urban and Built-up Lands; CNV: Cropland/Natural Vegetation Mosaics.

3.2.5 Air temperature variables input

We investigated the seasonal dynamics of $T_{air\text{-}max}$, $T_{air\text{-}DT}$, and $T_{air\text{-}mean}$ within one year (Figure 3.4a, the case at Harvard Forest site). The discrepancy between $T_{air\text{-}max}$ and $T_{air\text{-}DT}$ (or between $T_{air\text{-}DT}$ and $T_{air\text{-}mean}$) can be as high as 3°C throughout the whole year.

A further examination of the diurnal dynamics of GPP and T_{air} is presented in Figure 3.4b. Interestingly, the diurnal peaks of GPP and T_{air} were not consistent. GPP reached its peak between 9:00 a.m. and 11:00 a.m., whereas T_{air} peaked later, from 2:00 p.m. to 4:00 p.m. Of particular note is that among the three temperature variables, $T_{air\text{-}DT}$ most closely approximated the temperature of T_{air} at the moment GPP peaked (Figure 3.4c). Given these observations, $T_{air\text{-}DT}$ is regarded as the most appropriate air temperature variable for the algorithm input.

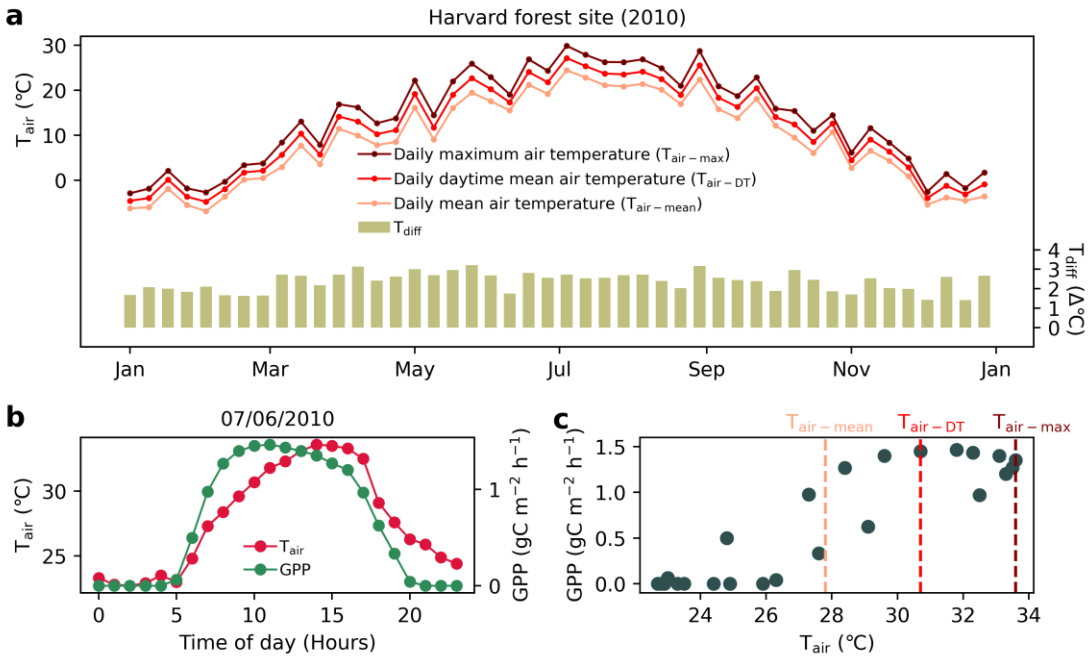

Figure 3.4: Temporal dynamics of air temperature and GPP_{EC} at the Harvard

Forest eddy flux tower site (US-Ha1) in 2010. a. Seasonal dynamics of daily maximum air temperature ($T_{air\text{-}max}$), daily daytime mean air temperature ($T_{air\text{-}DT}$), and daily mean air temperature ($T_{air\text{-}mean}$). This figure also shows the difference between $T_{air\text{-}max}$ and $T_{air\text{-}DT}$ (T_{diff}); b. diurnal dynamics of GPP and T_{air}; c. 2-d scatter plot of GPP and T_{air}.

3.2.6 Algorithm of $T_{opt\text{-}site\text{-}year}$ and $T_{opt\text{-}site}$

$T_{opt\text{-}site\text{-}year}$ is derived from the annual response curve of EVI to $T_{air\text{-}DT}$ (Chang et al., 2021a; Chang et al., 2020). For each year, we plotted the response curve of EVI versus $T_{air\text{-}DT}$ with all observations within the thermal growing season (Figure 3.2c). Then, the curve fitting EVI against $T_{air\text{-}DT}$ was performed using cubic regression splines. The optimum $T_{air\text{-}DT}$ range for vegetation photosynthesis is defined as when EVI exceeds 95% of its maximum value, and $T_{opt\text{-}site\text{-}year}$ is determined from the average of all $T_{air\text{-}DT}$ within that range (Figure 3.2c). $T_{opt\text{-}site}$ was calculated as the median value of $T_{opt\text{-}site\text{-}year}$ across all 20 years (Figure 3.2d).

3.2.7 Algorithm of $T_{opt\text{-}site\text{-}year}$ and $T_{opt\text{-}site}$ from GPP

We selected 137 eddy flux tower sites, encompassing 11 out of 14 biomes (DNF, URB, and CNV were excluded due to their very limited number of sites). The eddy flux tower data were acquired from the AmeriFlux data portal (http://ameriflux.ornl.gov/) and the Fluxnet data portal (https://fluxnet.org/). These sites provide Gross Primary Production (GPP) data at half-hour or hourly intervals. We excluded nighttime GPP data, defining daytime periods as those with Photosynthetic Photon Flux Density (PPFD) greater than

0. Subsequently, GPP data at half-hour or hour intervals were aggregated into daily daytime intervals. To align with the temporal resolution of the EVI and $T_{air\text{-}DT}$, we calculated the average values over 8-day periods as the representative daily average. The $T^{GPP}_{opt\text{-}site\text{-}year}$ was derived from the annual response curves of GPP to $T_{air\text{-}DT}$. The $T^{GPP}_{opt\text{-}site}$ is calculated from the median of all $T^{GPP}_{opt\text{-}site\text{-}year}$.

3.2.8 Statistical analysis

Simple linear regression is a statistical method that models the relationship between two variables by fitting a linear equation to observed data. Performance and fit are often assessed using metrics of the coefficient of determination (R^2), indicating the proportion of the variance in the dependent variable predictable from the independent variable. R^2 without an intercept can be calculated as:

$$R^2 = 1 - \frac{\sum(y_i - \hat{y})^2}{\sum(y_i - \bar{y})^2} \tag{3.5}$$

Where y_i is the i-th value of the independent variable y. $\hat{y}$ is the i-th predicted value. $\bar{y}$ is the mean value. We also calculated the Standard Deviation (S.D.), which is a statistic used to measure the dispersion of a set of data The S.D.can be estimated as:

$$\text{S.D.} = \sqrt{\frac{1}{N}\sum(A_i - \mu)^2} \tag{3.6}$$

Where N is the number of data, A_i is the value of each data, and μ is the mean value.

3.3 Results

3.3.1 Global maps of apparent optimum air temperature and interannual variation

Figure 3.5a shows the global distribution of $T_{opt\text{-}site\text{-}year}$ for the year 2000. From a global perspective, 91% of the vegetation has their $T_{opt\text{-}site\text{-}year}$ within the 10 to 30°C range, while 3% and 6% have their $T_{opt\text{-}site\text{-}year}$ below 10°C and above 30°C, respectively (Figure 3.5a). Across the latitudinal gradient, $T_{opt\text{-}site\text{-}year}$ ranges between 4 to 35°C (Figure 3.5b). The highest $T_{opt\text{-}site\text{-}year}$ is observed in the tropics. The $T_{opt\text{-}site\text{-}year}$ value declines with a northward or southward progression in latitude, decreasing by an average of 0.34°C for each 1° higher latitude, reaching its minimum near the poles. In high-altitude regions, such as the Qinghai-Tibet Plateau and Andes Mountains, the $T_{opt\text{-}site\text{-}year}$ is significantly low.

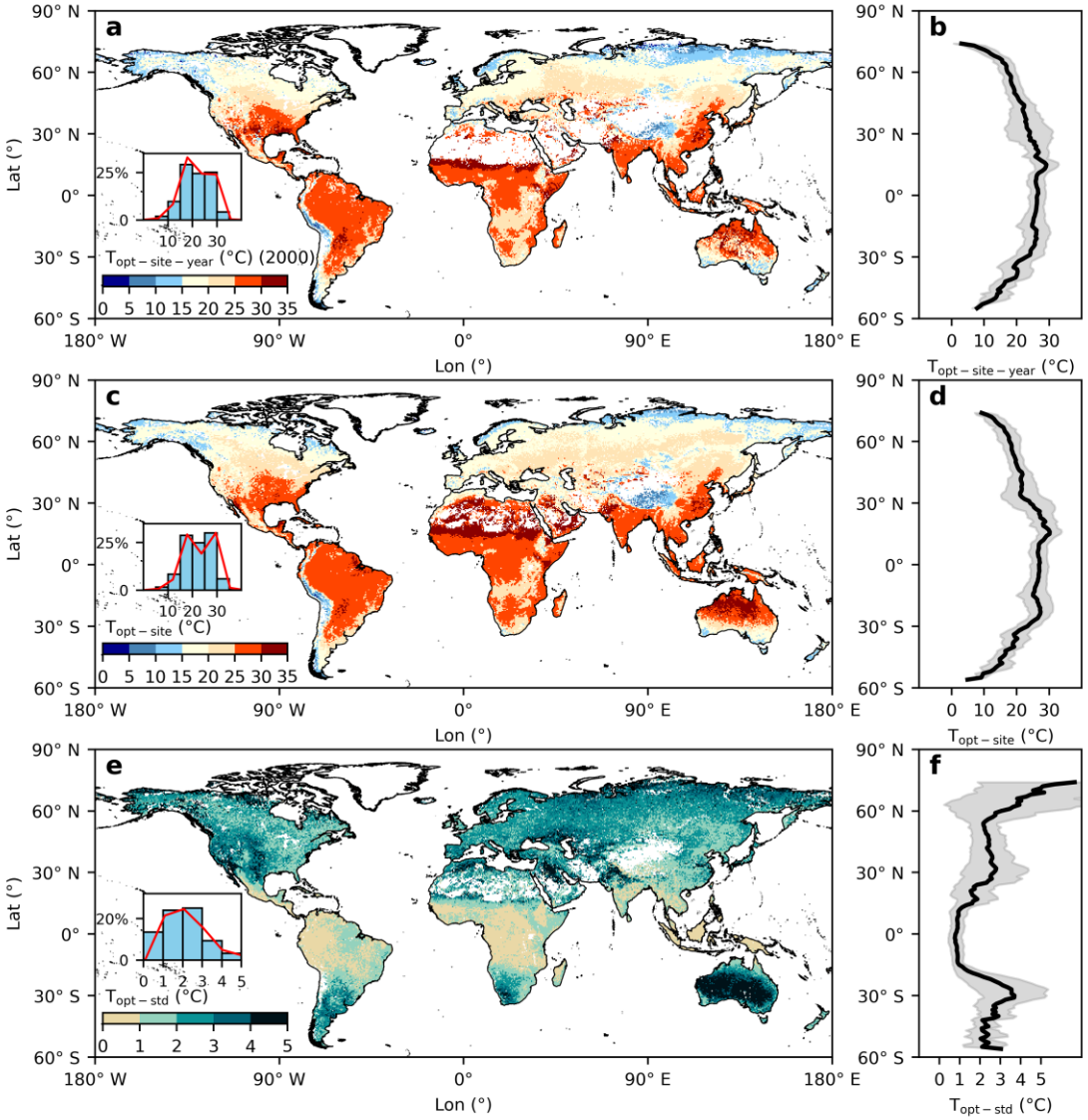

Figure 3.5: Global maps of apparent optimum air temperature and interannual variation. a. global map of $T_{opt-site-year}$ in 2000; c. global map of $T_{opt-site}$, derived from the median value of $T_{opt-site-year}$ from 2000 to 2019; e. $T_{opt-std}$ is calculated as the standard deviation of $T_{opt-site-year}$ during the period. The global map only shows the area where the annual NDVI is larger than 0.1 (The blank areas are pixels where the annual NDVI is less than 0.1). The histogram represents the proportion of pixels within different intervals, as shown on the x-axis. The red line represents

the Kernel Density Estimation (KDE). b, c, and f correspond to the average values across the latitude gradient in a, c, and e, respectively. The solid black lines are calculated as the average value for all pixels within 1° of latitude, and the shadow indicates the standard deviation.

Figure 3.5c shows the global map of $T_{opt\text{-}site}$, derived from the median value of two decades of $T_{opt\text{-}site\text{-}year}$. The spatial distribution and its trend across the latitude gradient mirror the patterns observed for $T_{opt\text{-}site\text{-}year}$ in 2000 (Figure 3.5c, d). Comparing the histograms in Figure 3.5c and Figure 3.5a, the $T_{opt\text{-}site}$ shows a slight increase relative to the $T_{opt\text{-}site\text{-}year}$ from 2000. Notably, between 25°C and 30°C, the proportion of vegetation with this $T_{opt\text{-}site}$ has marginally increased (~approximately 5% pixels higher). We further investigate the trends at five-year intervals (Figure 3.6). The $T_{opt\text{-}site\text{-}year}$ exhibited a slight global increasing trend, predominantly observed in arid regions such as central-northern Australia, North Africa, and southern North America. In these areas, the $T_{opt\text{-}site\text{-}year}$ showed an increase exceeding 5°C.

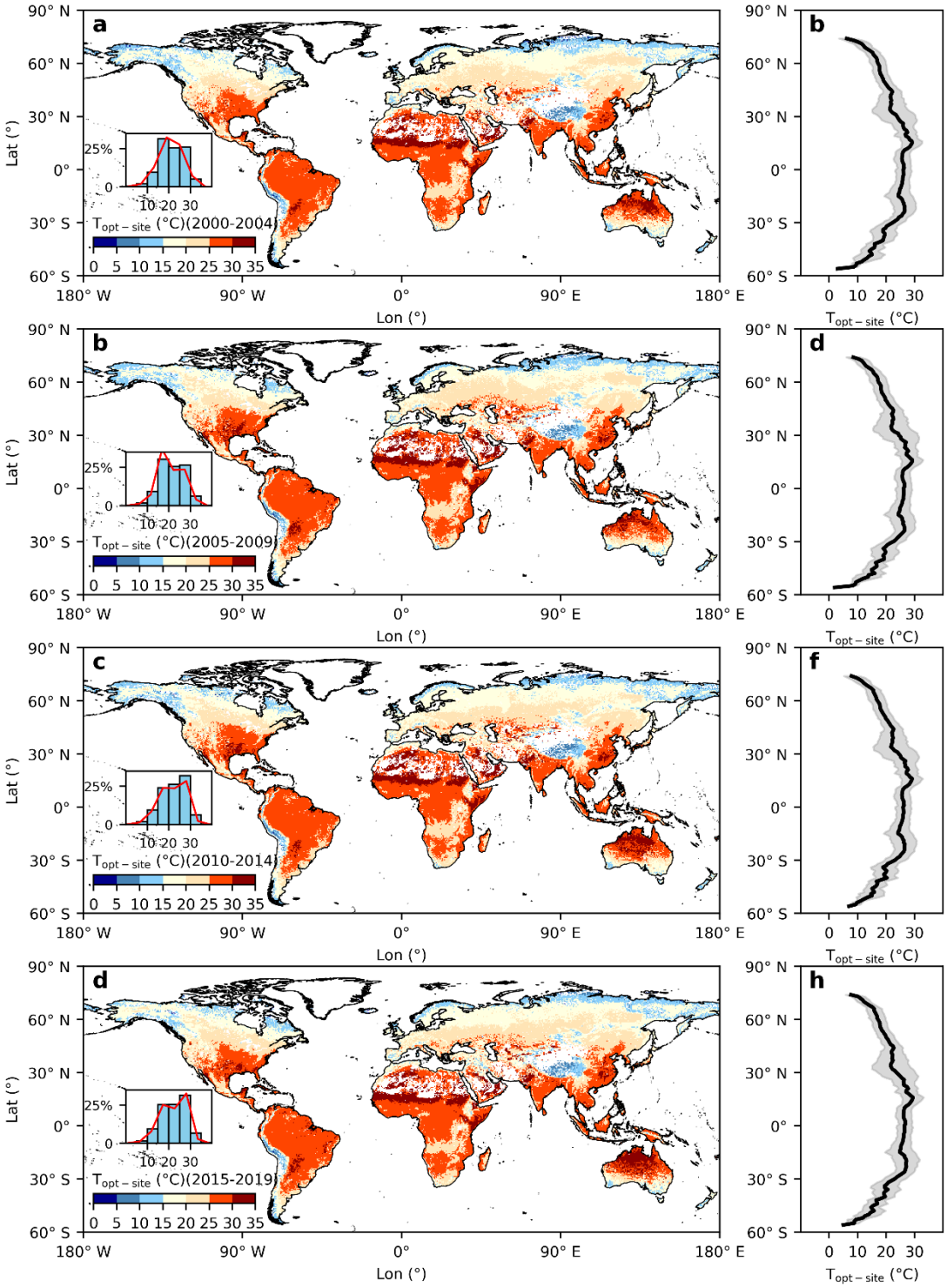

Figure 3.6: Global map of $T_{opt\text{-}site}$ at four period (2000-2004, 2005-2009, 2010-2014, and 2015-2019). Each map is the median value of the $T_{opt\text{-}site\text{-}year}$ during the period.

Figure 3.5e presents the standard deviation of the global $T_{opt\text{-}site\text{-}year}$ ($T_{opt\text{-}std}$) over

the last two decades. Between 2000 and 2019, the histogram shows that $T_{opt\text{-}std}$ primarily fluctuated between 1°C and 3°C for 71% of the vegetation pixels in the globe. Meanwhile, 14% of the vegetation exhibited relative stability with interannual variations of less than 1°C, and 15% of vegetation experienced fluctuations greater than 3°C. Across the latitude gradient (Figure 3.5f), the largest $T_{opt\text{-}std}$ predominantly occurs in the northern boreal and southern temperate zones. Within the northern boreal zone, the $T_{opt\text{-}std}$ increases with latitude, up to 3°C. In the southern temperate zone, Australia manifests the largest $T_{opt\text{-}std}$, up to 5°C. Tropical regions exhibit the smallest $T_{opt\text{-}std}$ with an interannual variability of around 1°C, followed by the northern temperate zone, which shows a moderate fluctuation ranging from 2 to 3°C.

3.3.2 The distribution of $T_{opt\text{-}site}$ across the 14 global biomes.

The histogram in Figure 3.7 shows the range (frequency distribution) of $T_{opt\text{-}site}$ across 14 biomes, revealing significant variation of $T_{opt\text{-}site}$ due to geographical and climatic differences. For instance, the GRA exhibits a wide $T_{opt\text{-}site}$ range from 4°C to 35°C, reflecting their extensive global distribution. In contrast, the DNF, primarily found in colder boreal zones, has a narrower range of 14°C to 21°C.

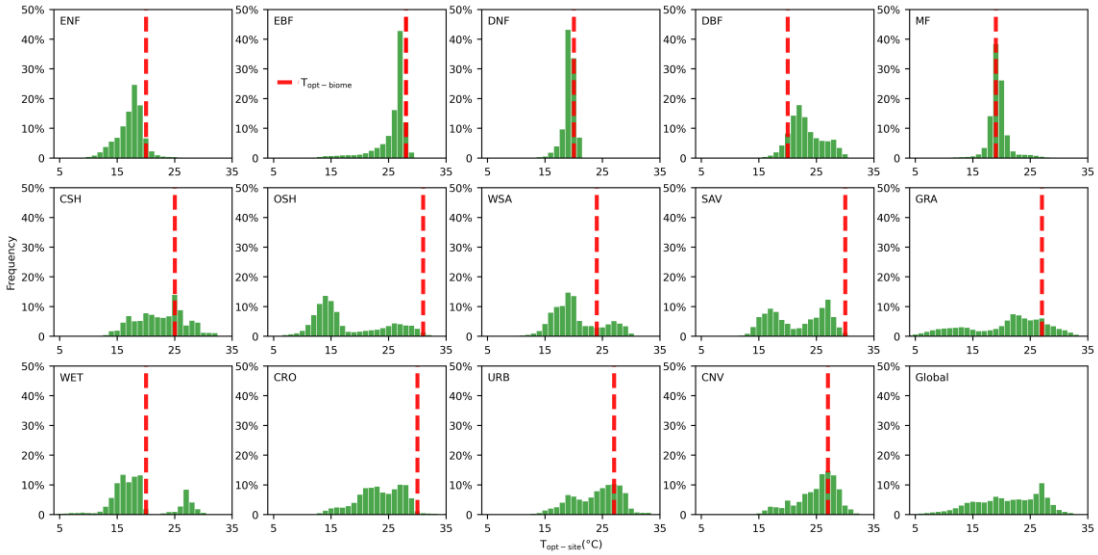

Figure 3.7: Histogram of $T_{opt\text{-}site}$ within 14 biomes. The red line is $T_{opt\text{-}biome}$, a common parameter estimated by Raich et al., 1991 and Melillo et al., 1993, which has been widely used in most ecological models (Melillo et al., 1993; Raich et al., 1991).

3.3.3 Comparison of materials and methods used to estimate $T_{opt\text{-}site}$

We compared the $T_{opt\text{-}site}$ (derived from EVI) with the $T^{GPP}_{opt\text{-}site}$ (derived from GPP) at 137 eddy flux tower sites across 11 out of 14 biomes (DNF, URB, and CNV were excluded due to their very limited number of sites) in the globe (Figure 3.8a). We employed a simple linear regression analysis to investigate the relationship between $T_{opt\text{-}site}$ and $T^{GPP}_{opt\text{-}site}$. The $T_{opt\text{-}site}$ generated in this study showed high consistency with $T^{GPP}_{opt\text{-}site}$ across all 11 biomes (r^2 between 0.80 and 0.95) (Figure 3.8b). The black solid line represents the overall linear fit for all biomes, exhibiting an r^2 of 0.83 (By comparison, the number is 0.52 in Huang et al. 2019 across 125 sites), indicating that the $T_{opt\text{-}site}$ estimated in this study is reliable at the ecosystem scale.

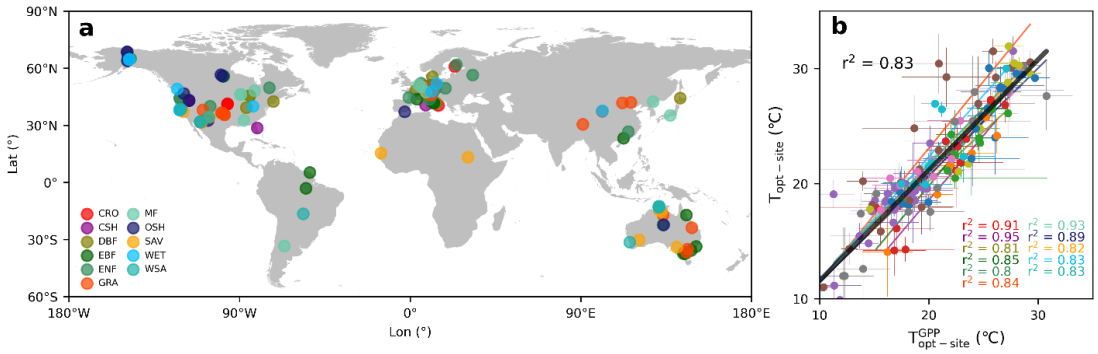

Figure 3.8: The comparison with $T_{opt\text{-}site}$ and $T^{GPP}_{opt\text{-}site}$ across the globe. a. The 137 eddy flux tower sites across the 11 biomes in the globe; b. Relationship between $T_{opt\text{-}site}$ and $T^{GPP}_{opt\text{-}site}$. Error bars indicate ±S.D. from $T_{opt\text{-}site\text{-}year}$ and $T^{GPP}_{opt\text{-}site\text{-}year}$, respectively. Different colors indicate different biomes, and the black solid line indicates all biomes.

3.4 Discussions

3.4.1 Methods widely used in the current literature to estimate $T_{opt\text{-}site}$

We compiled previous studies that utilized GPP/NEE/VIs-T_{air} response curves for estimating $T_{opt\text{-}site}$ (Table 3.1). These studies varied in terms of VIs variables, air temperature variables, and algorithms, leading to noticeable discrepancies in global $T_{opt\text{-}site}$ estimations. For instance, two studies estimated the mean global T_{opt} at 18.8 ± 7.1°C (Wang et al., 2023) and 23 ± 7.8°C (Huang et al., 2019), respectively. In contrast, this study estimates it to be 22 ± 6°C. The discrepancies highlight the necessity and challenges associated with reducing uncertainties in variables, data sources, and algorithms.

Table 3.1: Comparison of variables (vegetation indices, climate), data source,

study area, algorithms, and output in this and previous studies.

Studies	Variables	Data source	Study area	Algorithms	Output
This study	EVI vs. $T_{air\text{-}DT}$	MOD09A1; ERA5-Land	Global	T_{opt} is defined as the $T_{air\text{-}DT}$ at which EVIs exceed 95% of EVI_{max}.	$T_{opt\text{-}site\text{-}year}$, $T_{opt\text{-}site}$
Chang et al. 2020; Chang et al. 2021(Chang et al., 2021b; Chang et al., 2020)	EVI vs. $T_{air\text{-}DT}$ GPP vs. $T_{air\text{-}DT}$	MOD09A1, Eddy flux tower	165 sites, 11 grassland sites	T_{opt} is defined as the $T_{air\text{-}DT}$ at which EVIs exceed 95% of EVI_{max}.	$T_{opt\text{-}site\text{-}year}$, $T_{opt\text{-}site}$
Huang et al. 2019; Chen et al. 2021(A. Chen et al., 2021; Huang et al., 2019)	NIRv vs. $T_{air\text{-}max}$	Climatic Research Unit/National Centers for Environmental Protection (CRU/NCEP)	Global, Tibetan Plateau	T_{opt} is defined as the $T_{air\text{-}max}$ at which the maximum of NIRv occurs	$T_{opt\text{-}site}$
Potter et al. 1993(Potter et al., 1993)	NDVI vs. $T_{air\text{-}mean}$	Monthly NDVI-FASIR; Historical climate data	Global	T_{opt} is defined as the monthly $T_{air\text{-}mean}$ corresponding to the month when the maximum NDVI occurs	$T_{opt\text{-}site}$
Cui et al. 2013(Cui, 2013)	NDVI vs. $T_{air\text{-}mean}$	GIMMS NDVI; 752 meteorological stations over China	China	T_{opt} is defined as the average of the $T_{air\text{-}mean}$ corresponding to the peak NDVI values and the $T_{air\text{-}mean}$ at which NDVI exhibits its maximum rate of increase	$T_{opt\text{-}site}$
Niu et al. 2012; Wang et al. 2023(Niu et al., 2012; Wang et al., 2023)	GPP vs.$T_{air\text{-}mean}$	Eddy flux tower	169 sites, 326 sites, global	T_{opt} is defined as the $T_{air\text{-}mean}$ at which the maximum of GPP occurs	$T_{opt\text{-}site\text{-}year}$, $T_{opt\text{-}site}$
Yuan et al. 2011(Yuan et al., 2011)	NEE vs. $T_{air\text{-}mean}$	Eddy flux tower	72 sites	T_{opt} is defined as the $T_{air\text{-}mean}$ at which maximized carbon uptake is occurs	$T_{opt\text{-}site}$
Bennett et al. 2021(Bennett et al., 2021)	instantaneous GPP vs. T_{air}	Eddy flux tower	17 wooded ecosystem sites in Australia	T_{opt} is defined as the instantaneous T_{air} at which maximized instantaneous GPP occurs	$T_{opt\text{-}site}$

In terms of vegetation index variables used in estimating $T_{opt\text{-}site}$, NDVI, as one of

the earliest and most commonly used vegetation indices (Cui, 2013; Potter et al., 1993), might introduce biases when estimating $T_{opt\text{-}site}$ based on the NDVI- temperature response curve. This bias is attributed to the characteristics of NDVI dynamics in the plant growing season. In those sites of dense forest with high leaf area index (>= 4 m^2 m^{-2}), NDVI may saturate and remain high throughout the summer, which leads to a shift in the T_{opt} window from early summer to mid-summer, causing an overestimation of Topt (Figure 3.9). In the later summer, although NDVI remains high, GPP has already begun to decline (Yongzhe Chen et al., 2021).

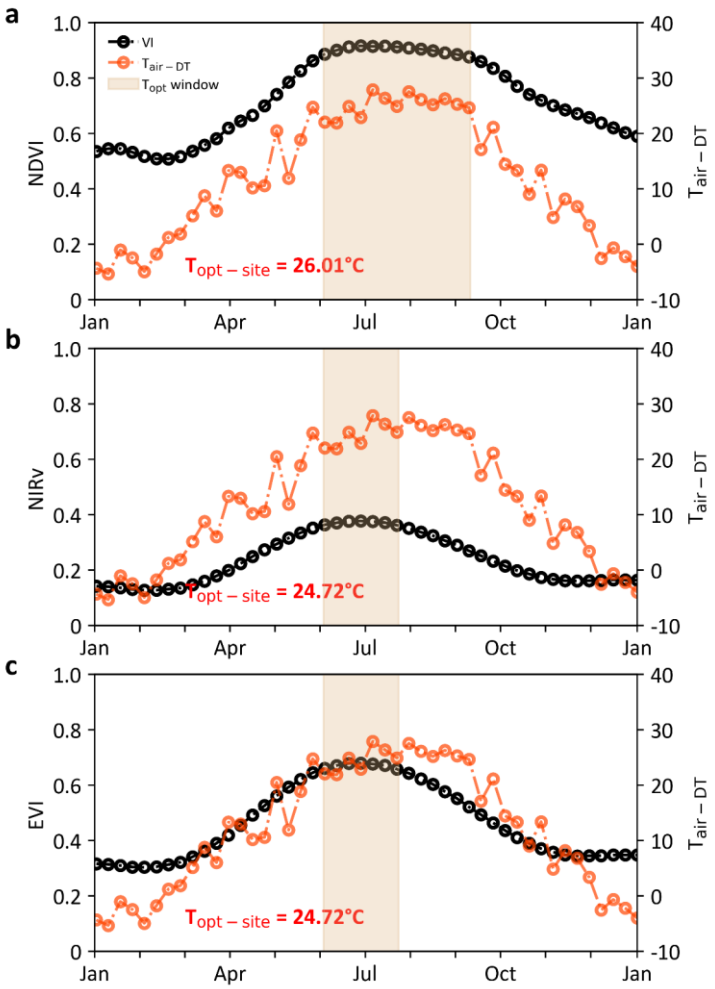

Figure 3.9: The Seasonal dynamics of NDVI, NIRv, EVI and $T_{air\text{-}DT}$ in 2010 at

Harvard Forest site.

The histograms of NDVI-derived $T_{opt\text{-}site}$ map show that pixels with $T_{opt\text{-}site}$ over 20°C make up 64% (Figure 3.10 a), whereas this proportion is 55% in EVI-derived $T_{opt\text{-}site}$ map (Figure 3.6b). Recent studies employed NIRv to generate regional and global $T_{opt\text{-}site}$ maps (A. Chen et al., 2021; Huang et al., 2019). Given that EVI exhibits a higher correlation with GPP than NDVI in most ecosystems like forests (Xiao, Hollinger, et al., 2004; Xiao, Zhang, et al., 2004), crops (Jin et al., 2015; Wagle et al., 2015), and grasslands (Li et al., 2007), it can be regarded as an ideal proxy to study vegetation response to temperature variations. Our findings also show that the $T_{opt\text{-}site}$ map derived from NIRv has similar global patterns and magnitudes with those derived from EVI (Figure 3.10c). This consistency can be attributed to the close correlation of EVI and NIRv, and both of them also have strong correlation with solar-induced chlorophyll fluorescence (SIF), which is the amount of light emitted by plants (Badgley et al., 2017; Huang et al., 2019).

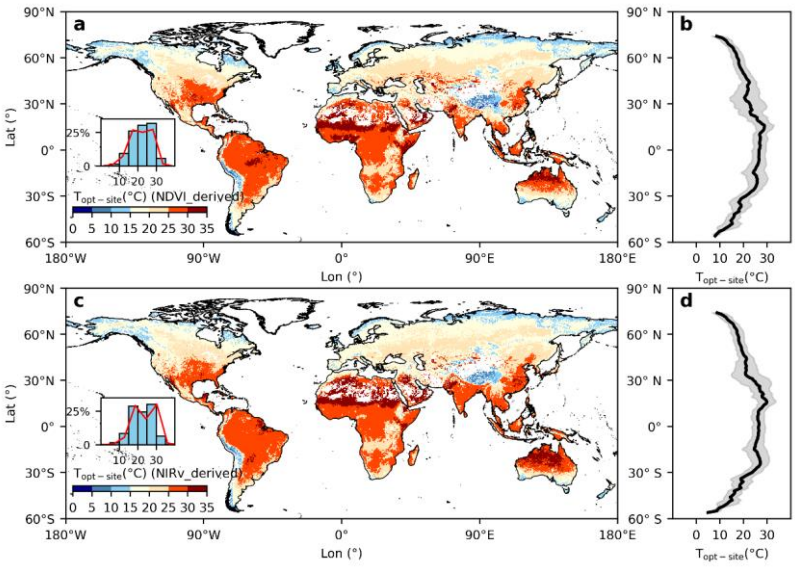

Figure 3.10: Global maps of optimum air temperature derived from different VIs.

a. global map of $T_{opt\text{-}site}$ derived from the NDVI-$T_{air\text{-}DT}$ response curve; c. global map of $T_{opt\text{-}site}$ derived from the NIRv-$T_{air\text{-}DT}$ response curve. The global map only shows the area where annual NDVI is larger than 0.1. The histogram represents the proportion of pixels within different intervals, as shown on the x-axis. The red line represents the Kernel Density Estimation (KDE). b and d correspond to the average values across latitude gradient in and c, respectively. The solid black lines are calculated as the average value for all pixels within 1° of latitude, and the shadow indicates the standard deviation.

In terms of air temperature variables used in estimating $T_{opt\text{-}site}$, most studies employ two types of air temperature variables: $T_{air\text{-}max}$ (A. Chen et al., 2021; Huang et al., 2019) and $T_{air\text{-}mean}$ (Niu et al., 2012; Wang et al., 2023; Yuan et al., 2011). However, the peak of vegetation photosynthesis does not occur at the hottest moment of the day (as shown in Figure 3.4). The maximum GPP typically occurs in the later morning, while $T_{air\text{-}max}$ tends to occur in the earlier afternoon. This renders $T_{air\text{-}max}$ an inappropriate choice for air temperature variables in the analysis of air temperature and GPP relationship, as it tends to overestimate $T_{opt\text{-}site}$ at the higher end, i.e., a bias of higher $T_{opt\text{-}site}$ values. Since photosynthesis only happens during daytime and $T_{air\text{-}mean}$ factors in nighttime temperatures, the use of $T_{air\text{-}mean}$ will introduce a bias of lower $T_{opt\text{-}site}$ values. Previous studies have already demonstrated the potential and feasibility of estimating T_{opt} based on the EVI-$T_{air\text{-}DT}$ response curve at a limited number of sites (Chang et al., 2021b; Chang et al., 2020), and to our knowledge, this study is the first time that $T_{air\text{-}DT}$ was used as variable inputs to estimate global $T_{opt\text{-}site}$.

In terms of algorithms, most studies defined T_{opt} as the air temperature corresponding to the highest point of the VI-T_{air} or GPP-T_{air} response curve with multi-year data (Bennett et al., 2021; A. Chen et al., 2021; Huang et al., 2019; Niu et al., 2012; Wang et al., 2023; Yuan et al., 2011); for example, the recent global $T_{opt\text{-}site}$ estimates by Huang ey al. (Huang et al., 2019). Different with those studies, this study first calculated annual $T_{opt\text{-}site\text{-}year}$ and then estimated $T_{opt\text{-}site}$ as the median of $T_{opt\text{-}site\text{-}year}$ in 20 years. The advantage of this method is that $T_{opt\text{-}site\text{-}year}$ provides the variation information of $T_{opt\text{-}site}$ across years, especially considering the substantial inter-annual variations in climate and land cover in the past two decades in the globe. $T_{opt\text{-}site\text{-}year}$ data would help expand the understanding of how vegetation responds to environmental changes over time. In addition, abnormal vegetation growth caused by extreme climate events in specific years may also introduce uncertainty to the estimation. We use the median value of $T_{opt\text{-}site\text{-}year}$ over multiple years, as the median value is primarily used to eliminate potential outliers and will provide a more balanced perspective of the $T_{opt\text{-}site}$ over time. Additionally, we improved the $T_{opt\text{-}site}$ estimation window based on the thermal growing season defined by LST, which significantly reduced the uncertainty introduced by snow in the algorithm, particularly in high-latitude regions.

3.4.2 Spatial variation of $T_{opt\text{-}site}$ across biomes from this study and its comparison with $T_{opt\text{-}biome}$

The range of $T_{opt\text{-}site}$ highlights the limitations of using a fixed $T_{opt\text{-}biome}$ parameter. $T_{opt\text{-}biome}$ shows a substantial discrepancy when compared with the $T_{opt\text{-}site}$ across biomes. This discrepancy is especially pronounced in biomes as ENF, OSH, SAV, and CRO,

where the $T_{opt\text{-}site}$ is always lower than the $T_{opt\text{-}biome}$. This bias is mainly due to the $T_{opt\text{-}biome}$ being based on limited site data, further introducing significant uncertainty into the GPP estimation (Chang et al., 2021b; Chang et al., 2020; Heinsch et al., 2006; Yan et al., 2015). Our previous research suggests that replacing the $T_{opt\text{-}biome}$ with $T_{opt\text{-}site}$ can significantly improve the accuracy of GPP estimates from the model at site scale by approximately 1% to 34%, especially in the GRA, CRO, and OSH ecosystems (Chang et al., 2021a). This highlights the importance of using the $T_{opt\text{-}site}$ rather than the $T_{opt\text{-}biome}$ for simulations of GPP models across the scales from site to region and the globe.

3.5 Conclusion

This chapter generated a site-specific optimal air temperature parameter for vegetation across the globe over the past two decades (2000–2019) using EVI–$T_{air\text{–}DT}$ response curves. Unlike previous studies, we employed a more appropriate input—daytime means air temperature—to estimate both site-specific-year optimum temperature ($T_{opt\text{-}site\text{-}year}$) and the multi-year average ($T_{opt\text{-}site}$). We examined the interannual variation of $T_{opt\text{-}site\text{-}year}$ during the study period, as well as the influence of interannual climate factors (precipitation and air temperature) on $T_{opt\text{-}site\text{-}year}$. Additionally, this study highlights the potential impact of using biome-level T_{opt} values ($T_{opt\text{-}biome}$) on the errors and uncertainties in GPP estimation by ecosystem models.

The $T_{opt\text{-}site}$ dataset produced in this chapter can be used as an input for most ecosystem models that include temperature parameters. Note that we have masked areas with an annual average NDVI of less than 0.1 (such as deserts, glaciers, or areas with high-density impervious surfaces). Furthermore, $T_{opt\text{-}site}$ is highly related to plant

physiology, ecology, and climatology. The $T_{opt\text{-}site\text{-}year}$ dataset could be used to explore the significant importance of understanding plant growth's environmental dependence, ecosystems' functioning, and their responses to environmental changes.

Chapter 4 : Modeling gross primary production across the globe using Vegetation Photosynthesis Model (VPM v3.0)

ABSTRACT

Accurate estimation of Gross Primary Production (GPP) of terrestrial vegetation is crucial for comprehending the carbon dynamics. To date, there is still no consensus on the magnitude and seasonality of global GPP among the major global GPP products, underscoring the necessity to improve GPP models for higher accuracy of global GPP estimates. Here, we introduce an improved Vegetation Photosynthesis Model (VPM v3.0), which incorporates site-specific apparent optimum temperature for photosynthesis, leaf-trait-based light absorption (flat leaf vs. needle leaf), and improved water stress estimation. The global VPM simulation is driven by Terra/MODIS images and the ERA5-Land climate dataset. We evaluate VPM v3.0 using GPP from 205 eddy flux tower sites across 11 land cover types (1,658 site-years) (GPP_{EC}), as well as the TROPOMI SIF product for 2018-2021. The slope, R^2, and RMSE between GPP from VPM v3.0 ($GPP_{VPM\text{-}v3}$) and GPP_{EC} are 0.97, 0.78, and 1.46 gC $m^{-2}day^{-1}$, respectively. $GPP_{VPM\text{-}v3}$ shows high temporal consistency with TROPOMI SIF. VPM v3.0 provides higher accuracy of GPP estimates at most evaluated sites than VPM v2.0. Comparisons of global GPP from VPM v3.0 with other major global GPP products reveal both spatial-temporal consistency and discrepancies. These findings clearly indicate the improved accuracy of VPM v3.0 in estimating GPP, making it suitable for generating global GPP datasets.

4.1 Introduction

Gross Primary Production (GPP) of terrestrial vegetation plays a critical role in the global carbon cycle (Anav et al., 2015; Frankenberg et al., 2011; Piao et al., 2013). GPP is a crucial indicator of the functionality of Earth's terrestrial ecosystems, influencing climate change, ecosystem function, biodiversity, and global food security through complex feedback mechanisms (Chang et al., 2023; Costanza et al., 2007; Marshall et al., 2018; Migliavacca et al., 2021; Ryu et al., 2019).

To date, GPP is predominantly derived from three primary methodologies: ground-based observations, data-driven ecosystem models, and process-based ecosystem models. Among these, eddy covariance (EC) technology is a widely used method for ground-based observations, providing GPP by measuring carbon fluxes at the ecosystem scales (Chu et al., 2021). However, EC towers are limited in number due to high maintenance costs, and their measurement footprint is restricted, typically spanning only areas ranging from hundreds to thousands of meters (Baldocchi, 2014; Papale et al., 2006). Therefore, the GPP from the eddy flux tower are often used as training and/or validation data to evaluate GPP products from models. Data-driven and process-based ecosystem models offer comprehensive methods to estimate GPP data, including Terrestrial Ecosystem Models (TEM) (Melillo et al., 1993), Light Use Efficiency (LUE) models (Monteith, 1972; Potter et al., 1993; Xiao, Hollinger, et al., 2004), statistical models (Guanter et al., 2014), and machine learning (Alemohammad et al., 2017; Jung et al., 2020). Among these models, LUE models are widely used due to their simple model structure and extensive data availability (e.g., satellite-based data),

making them both applicable and reliable across various ecosystems and regions.

Photosynthesis involves two key stages: the absorption of light energy and the process of carbon fixation. LUE theory assumes that GPP can be estimated as a function of absorbed photosynthetically active radiation (APAR) and light use efficiency (ϵ), which combined environmental factors such as temperature, water, and CO_2:

$$\mathrm{GPP} = \mathrm{APAR} \times \epsilon \tag{4.1}$$

Representative LUE models include MODIS GPP (MOD17) (Running et al., 2000), the Photosynthetic Capacity Model (PCM) (Gao et al., 2014), the Vegetation Photosynthesis Model (VPM) (Cui et al., 2022; Xiao, Hollinger, et al., 2004), the Carnegie-Ames-Stanford Approach (CASA) (Potter et al., 1993), EC-LUE (Yuan et al., 2007), and the Terrestrial Ecosystem Carbon (TEC) flux model (Yan et al., 2015). The accuracy of these models varies substantially due to differences in data inputs, parameter estimation, and model structure.

Most of the models, including VPM (v1.0 and v2.0), use biome-specific apparent optimum air temperature parameters ($T_{opt\text{-}biome}$) for GPP calculation. However, recent studies estimated site-specific apparent optimal air temperatures for GPP ($T_{opt\text{-}site}$) across the biomes, revealing noticeable differences between the biome-specific $T_{opt\text{-}biome}$ and site-specific $T_{opt\text{-}site}$ (Bennett et al., 2021; Chang et al., 2021a; Chang et al., 2020; Huang et al., 2019; Niu et al., 2012; Pan, Xiao, Pan, et al., 2024; Wang et al., 2023; Yuan et al., 2011). These differences raise concerns that using $T_{opt\text{-}biome}$ as a model parameter may negatively affect model performance at regional or global scales.

LUE models use a single equation to calculate light absorption across different leaf traits (e.g., flat leaf and needle leaf) (Running et al., 2000; Yuan et al., 2007; Yao Zhang et al., 2017). Previous studies reported that MODIS-derived FPAR was significantly underestimated in northern boreal forests (dominated by needleleaf trees) (Serbin et al., 2013; Turner et al., 2003). For evergreen needleleaf forest, the GPP estimates from VPM v2.0 were lower than GPP_{EC} by 27% (Yao Zhang et al., 2017). The underestimation of light absorption has been attributed to the shortcomings of the leaf area estimation (Law et al., 2001). As chloroplast in needle leaf is distributed spherically within leaves, the differences of leaf-trait between needle leaf and flat leaf (broadleaf) may also be a reason for those models to underestimate $FPAR_{canopy}$ or $FPAR_{chl}$ in needleleaf forest (Law et al., 2001; Trueba et al., 2022).

Like most LUE models, VPM also considers water stress in its simulation. The water stress estimation equations in VPM v1.0 and v2.0 are sensitive to the water stress from humid to semi-humid but were reported to underestimate the water stress on GPP in arid regions (Dong, Xiao, Wagle, et al., 2015; Wagle et al., 2015; Wagle et al., 2014). This underestimation can be attributed to the relatively weak seasonal variation in water availability in arid areas. Therefore, there is a need to improve the water stress parameter estimation in arid areas.

In this chapter, we developed and ran VPM v3.0 to estimate global GPP using Terra/MODIS images and the ERA5-Land climate dataset. Compared to VPM v2.0 (Zhang et al., 2017), VPM v3.0 has three major improvements: (1) using $T_{opt\text{-}site}$ to replace $T_{opt\text{-}biome}$ (2) the incorporation of leaf traits (flat leaf vs. needle leaf), and (3)

improved estimation of water stress in arid areas and periods. This paper addresses three primary scientific questions. First, to what degree will VPM v3.0 accurately estimate GPP compared to ground GPP observations and satellite-derived SIF data? Second, how large are the differences in global GPP estimates between VPM v3.0 and VPM v2.0? Finally, what are the discrepancies and consistencies between the global GPP estimates from VPM v3.0 and major global GPP products?

4.2 Materials and Methods

4.2.1 MODIS surface reflectance data product (MOD09A1, Version 6.1)

MOD09A1 v6.1 product provides 500-meter and 8-day radiometrically, geometrically, and atmospherically corrected surface reflectance (Vermote, 2021). This dataset has been demonstrated to perform reliable as an input dataset for the VPM model (Yao Zhang et al., 2017). At the global scale, the use of alternative surface reflectance products (e.g., MCD43) as model inputs has shown no significant differences compared to MOD09 (Doughty et al., 2021).

The preprocessing of the MOD09A1 surface reflectance (SR) dataset included several stringent quality control steps. First, the Quality Assurance (QA) band identified observations contaminated by clouds, cloud shadows, and snow, labeled as poor-quality observations, and then removed them from data analyses (Frey et al., 2008). The frequency distribution of good-quality observations showed that the mid-latitudes had more good-quality observations than the tropical and boreal zones (Figure 4.1). On average, the proportion of good-quality observations per pixel across the globe was

71%.

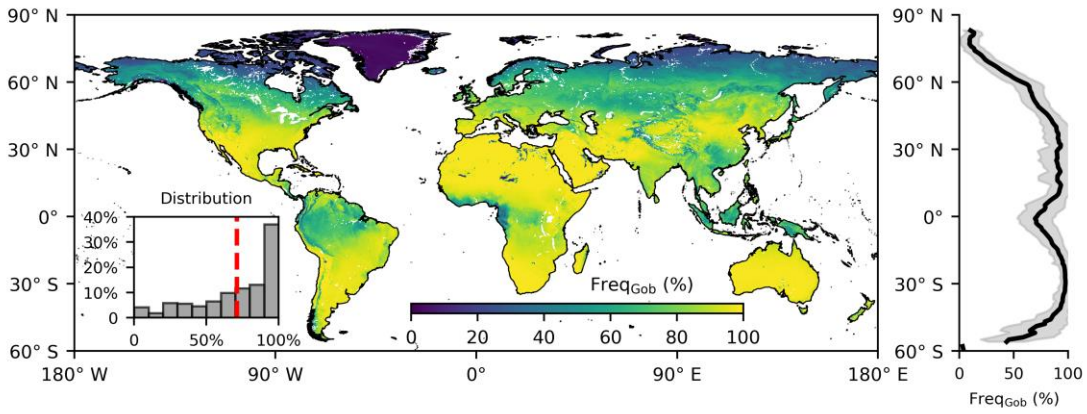

Figure 4.1: The frequency distribution of good-quality EVI observations. The map is 500-meter spatial resolution from 2000 to 2023. The right panel shows the average values of all pixels within 1° latitude bin across the latitude. The red dashed line histogram is the global average value.

Secondly, even after eliminating pixels contaminated by clouds, the time series SR data still exhibited noise that the QA band failed to detect. This noise typically arises from atmospheric factors (such as water vapor and aerosols), surface conditions (like snow), or changes in solar and observation angles (Dozier et al., 2008; Kaufman et al., 1997). The scattering caused by molecules and particles in the atmosphere enhances the reflectance in the blue band (Jensen, 2009). Therefore, blue band larger than 0.2 were used to identify bad-quality observations in the time series SR, i.e., those observations affected by the atmosphere or snow.

Third, given that the surface reflectance of vegetation does not fluctuate dramatically over short periods (e.g., one or two weeks) (Glenn et al., 2008), we employed a biology-based rule to identify bad-quality observations at specific dates (t)

that were substantially larger or smaller than their close neighboring observations (t-1, t+1). Specifically, a three-date moving window was employed over the one-year time series data, calculating the slope between the central observation (t) and both the preceding (t-1) and subsequent (t+1) observations. If the absolute slope exceeded 0.15, the central observation was classified as a low-quality observation. This method helped ensure the time series was more reflective of actual vegetative dynamics, minimizing the impact of abrupt noise unrelated to vegetation growth.

The good-quality SR data were then used to generate the Enhanced Vegetation Index (EVI) and the Land Surface Water Index (LSWI) time series (Huete et al., 2002):

$$EVI = 2.5 \times \frac{\rho_{nir} - \rho_{red}}{\rho_{nir} + (6 \times \rho_{red} - 7.5 \times \rho_{blue}) + 1} \quad (4.2)$$

$$LSWI = \frac{\rho_{nir} - \rho_{swir}}{\rho_{nir} + \rho_{swir}} \quad (4.3)$$

where ρ_{nir} , ρ_{red}, ρ_{blue}, and ρ_{swir} are the surface reflectance bands of near infrared, red, blue, and shortwave infrared, respectively. To generate continuous VI time series, reference curves and linear interpolation were utilized to fill data gaps in the EVI and LSWI time series (Yao Zhang et al., 2017). For the EVI time series, we generated site-specific EVI reference curves, where the value for a specific date within the EVI reference curve was derived from the average of all good-quality observations from all years, subsequently smoothed using Savitzky-Golay (S-G) filtering (Press et al., 1990). The reference curve was applied to fill missing values on the corresponding dates in the EVI time series. For the LSWI time series, given the sensitivity of LSWI to moisture (e.g., rainfall events) and the challenges in predicting vegetation water conditions and precipitation over different periods (Yao Zhang et al., 2017), we used a straightforward

method of linear interpolation, using high-quality observations before and after the gaps to fill in the LSWI time series (Liu et al., 2020).

4.2.2 MODIS land cover type data product (MCD12Q1, Version 6.1)

MCD12Q1 v 6.1 product provides global land cover classifications at 500-meter spatial resolution (Friedl et al., 2022). Here, we utilized the land cover types identified by the International Geosphere-Biosphere Programme (IGBP), in which we focused on the following 11 IGBP land cover types: Croplands (CRO), Closed Shrublands (CSH), Deciduous Broadleaf Forests (DBF), Evergreen Broadleaf Forests (EBF), Evergreen Needleleaf Forests (ENF), Grasslands (GRA), Mixed Forests (MF), Open Shrublands (OSH), Savannas (SAV), Permanent Wetlands (WET), and Woody Savannas (WSA).

4.2.3 MODIS land surface temperature data product (MYD11A2, Version 6.1)

MYD11A2 v 6.1 product provides land surface temperature (LST) data at an 8-day and 1-kilometer resolution (Wan, 2021). This dataset provides LST measurements at 1:30 AM (nighttime) and 1:30 PM (daytime). Here, we utilized the nighttime LST (LST_{night}) to delineate the thermal growing season (TGS). For each pixel, the LST_{night} time series was reconstructed using a three-date moving window. Each observation was replaced by the average value within the window. Based on the threshold assumption that the LST_{night} >= 5°C for the TGS (Dong, Xiao, Kou, et al., 2015), the start of the season (SOSTGS) was defined as the first date in late winter or spring when LST exceeds this threshold, while the end of the season (EOS_{TGS}) was identified as the first date in autumn or winter when LST falls below this threshold.

4.2.4 ERA5-Land reanalysis climate data

The European Centre for Medium-Range Weather Forecasts (ECMWF) offers the global climate reanalysis product ERA5, spanning from 1979 to the present. This product offers approximately 25-km and hourly intervals meteorological data, encompassing atmospheric, surface, and oceanic (Hersbach et al., 2020). ERA5-Land, developed based on ERA5 data, focuses on the surface and offers global maps at approximately 11-km (Muñoz-Sabater et al., 2021). Compared to ERA5, ERA5-Land is specifically optimized for terrestrial processes, enhancing data quality for simulating surface processes, and assessing surface states with finer spatial resolution.

Since photosynthesis does not occur at night, we used daytime climate variables from the ERA5-Land reanalysis climate dataset as model input. Daytime is defined by shortwave radiation (SW_{rad}), where periods within the day when $SW_{rad} > 0$ is considered as daytime. Based on this definition, hourly air temperature and radiation data are aggregated into daytime daily values. Daytime air temperature ($T_{air\text{-}DT}^{ERA5}$) was calculated as the average for daytime, and daytime radiation ($SW_{rad\text{-}DT}^{ERA5}$) was calculated as the sum for daytime. These values were then averaged every 8 days (Figure 4.2a). $SW_{rad\text{-}DT}^{ERA5}$ (J m^{-2}) was converted into PAR_{DT}^{ERA5} (mol m^{-2}) to meet the model's input standards (Pan, Xiao, Pan, et al., 2024; Ryu et al., 2018):

$$PAR_{DT}^{ERA5} = SW_{rad\text{-}DT}^{ERA5} \times r_{SW\_PAR} \times \beta \quad (4.4)$$

where $r_{SW\_PAR} = 0.45$ is the ratio of SW to PAR (Ma et al., 2014; Meek et al., 1984), and $\beta = 4.56$ μmol J^{-1} is the energy-quanta conversion factor (Dye, 2004). We compared in-situ climate data from 205 global flux towers with the processed ERA5-Land climate

dataset. The climate variables ($T_{air\text{-}DT}$, PAR_{DT}) from the EC towers and those from ERA5-Land had high consistency, suggesting that it is okay to use ERA5-Land climate data for VPM simulation at the global scale (Figure 4.2c).

Since the ERA5-Land dataset primarily focuses on terrestrial surfaces, there are uncertainties in the classifications of land or ocean near coastlines, leading to jagged boundaries and missing data on some terrestrial surfaces. To fill these gaps, we employed a 3x3 pixel window for edge buffering outward from the image boundaries, where each newly generated pixel was calculated as the average value within this 3x3 pixel window (Figure 4.2b). Subsequently, we used the bicubic method to resample the imagery from 11-kilometer to 500-meter. Finally, a terrestrial surface mask (derived from MCD12Q1) was applied to clip the imagery accordingly.

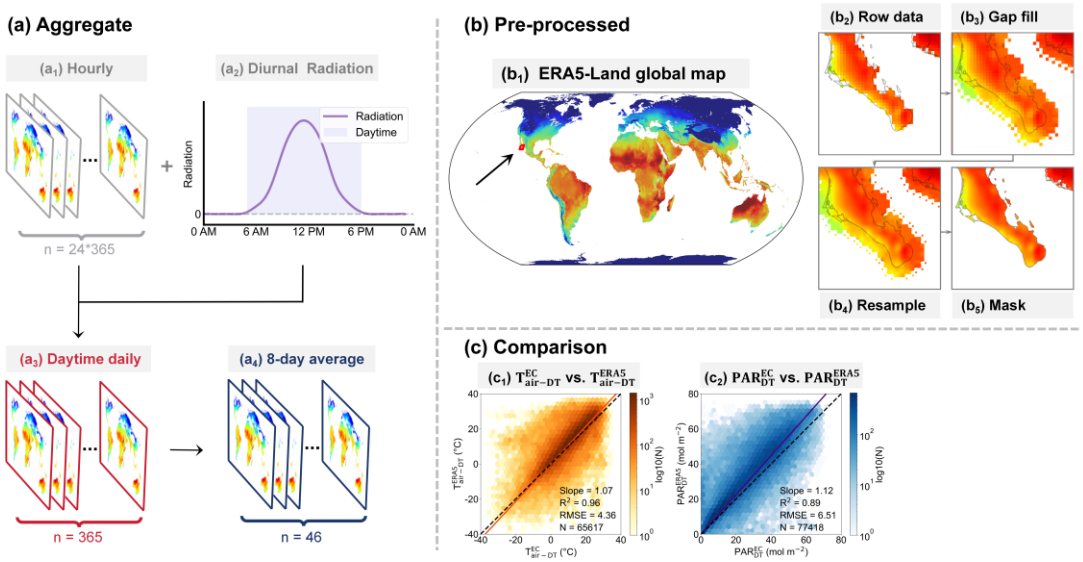

Figure 4.2: Preprocessing workflow of the ERA5-Land reanalysis climate dataset and comparison with climate variables from the eddy flux tower. (a) Schematic illustration of data aggregation from hourly to 8-day; (b) Preprocessing of climate variable maps, including gap-fill, resample, and mask; (c) Simple linear regression

between $T_{air\text{-}DT}^{ERA5}$ and PAR_{DT}^{ERA5} from the ERA5-Land reanalysis climate dataset and $T_{air\text{-}DT}^{EC}$ and PAR_{DT}^{EC} from the eddy flux towers.

4.2.5 C_4 percentage for cropland and natural vegetation

C_3 and C_4 plants have different photosynthetic mechanisms and light use efficiencies (Sage et al., 2007). C_3 plants, which dominate global ecosystems, can perform photosynthesis at lower temperatures and are predominantly found in temperate and boreal regions, including crops, trees, shrubs, and grasses. Conversely, C_4 plants, less widely distributed globally, can perform photosynthesis with high efficiency under high temperature, high radiation, and drought conditions. It is predominantly found in tropical and subtropical areas, including maize, sugarcane, and many grasses. Because of their differences, it is necessary to have C_3 and C_4 plant function types within the LUE models (Collatz et al., 1992; Yan et al., 2015).

We utilized the global ISLSCP II C_4 natural vegetation map (1-degree) to estimate the percentage of C_4 vegetation in grasslands and savannas (the ratio of C_4 vegetation area to whole pixel area) (Still, 2009). Additionally, we used the EarthStat 2000 global crop type map (0.083-degree) to estimate the percentage of C_4 crops, including maize, sugarcane, sorghum, and millet (Ramankutty, 2008). Despite both maps having limitations such as low spatial resolution and the omission of interannual variations, they provide a relatively reliable distribution of C_4 vegetation (Yao Zhang et al., 2017). These two maps were then resampled to 500-meter using the bicubic method (Figure 4.3), and the area-weighted average of the C_4 percentage within individual pixels were

calculated.

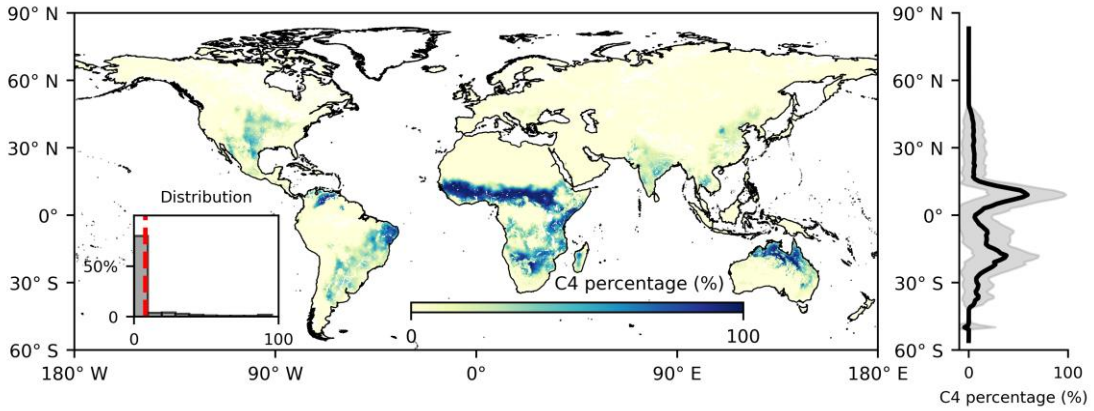

Figure 4.3: Spatial distribution of C_4 plant percentage (%) within individual gridcells. The right panel shows the average values of all gridcells within 1° latitude bin across the latitude. The red dashed line histogram is the global average value of C_4 plant percentage. The C_4 plant percentage dataset comes from ISLSCP II C_4 natural vegetation map and Earth Stat 2000 global crop type map (Ramankutty, 2008; Still, 2009).

4.2.6 In-situ data from the eddy flux tower sites

FLUXNET and AmeriFlux provide continuous measurements of terrestrial–atmosphere carbon and water exchange, as well as climate data, through eddy flux towers distributed around the world (Chu et al., 2021).

We downloaded eddy flux tower data from FLUXNET and AmeriFlux, collected from towers spanning the 11 IGBP land cover types. Initially, we selected 274 sites that contain carbon flux and climate data. We filtered these sites in two steps.

First, we calculated the average GPP observations (GPP_{EC}) of carbon flux variables (GPP_NT_VUT_REF, GPP_DT_VUT_REF) for each time interval (hourly or half-hourly, depending on the specific eddy flux tower). Then, we calculated the

mean and standard deviation (σ) of GPP_{EC} for all the years at each time interval to generate a mean reference curve (Figure 4.4). The mean reference curve was compared with the observations from each year. Observations exceeding the mean by over three standard deviations ($\pm 3\sigma$) were marked as bad-quality observations. If a site had more than 30% of its observations identified as bad-quality, it was excluded.

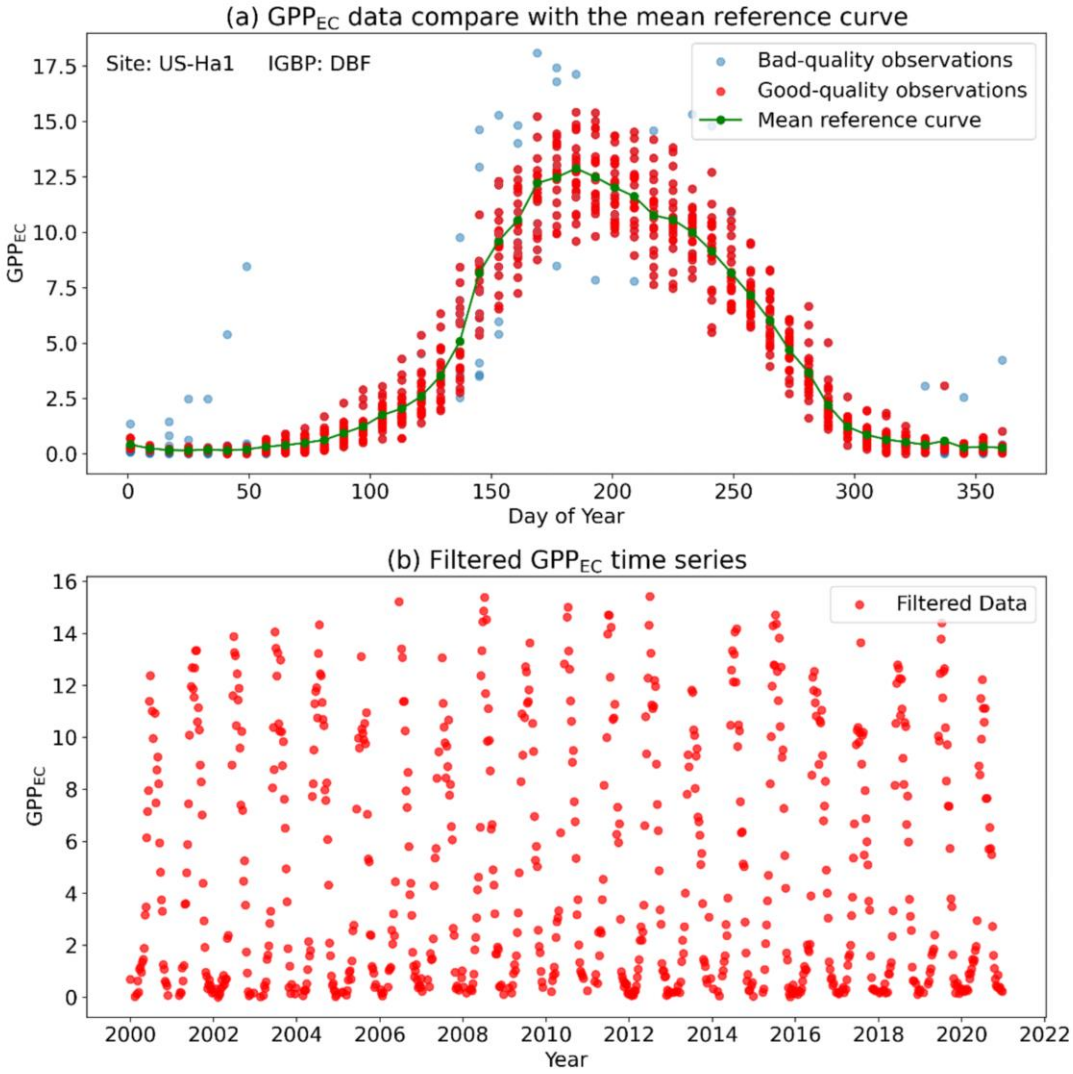

Figure 4.4: GPP_{EC} data quality control, taking US-Ha1 as an example. (a) GPP_{EC} data compared with the mean reference curve; (b) Filtered GPP_{EC} data for model evaluation.

Second, we compared the IGBP classification provided by FLUXNET or AmeriFlux with that from the MODIS land cover type data. Sites with inconsistencies IGBP were excluded. After this two-step quality-check and site-scope, we finally selected 205 eddy flux sites with a total of 1,658 site-years of data. Their distribution is shown in Figure 4.5.

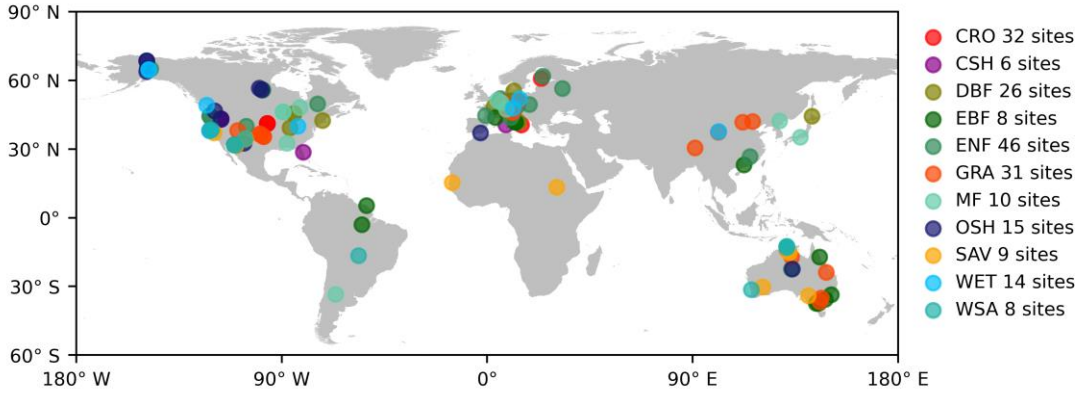

Figure 4.5: Spatial distribution of 205 eddy flux tower sites across 11 biomes in this study. In the figure, the sites are consistent with the IGBP classifications defined by FLUXNET, AmeriFlux and MCD12Q1.

For the selected sites, GPPEC observations marked as bad-quality were excluded from the validation sample used to evaluate VPM v3.0. Subsequently, the hourly or half-hourly data were converted to daily, with GPPEC and the climate variable of radiation (PPFD_IN) as daily sums, and the climate variable of air temperature (TA_F) as the daytime average, where daytime is defined as the periods when PPFD_IN > 0. Then, this daily data was averaged every 8 days. Climate variables were used to evaluate the ERA5-Land reanalysis climate dataset. The unit of PPFD_IN was converted to compare with the PAR_{DT}^{ERA5} obtained from ERA5-Land reanalysis climate

data:

$$PAR_{DT}^{EC} = \frac{1800 \times PPFD\_IN}{1000000} \quad (4.5)$$

$$PAR_{DT}^{EC} = \frac{3600 \times PPFD\_IN}{1000000} \quad (4.6)$$

The unit of PPFD_IN is μmol Photon m^{-2} s^{-1}, and the unit of PAR_{DT}^{EC} is mol m^{-2}. Eq. (4.5) and Eq. (4.6) were applied for half-hourly and hourly interval data, respectively.

4.2.7 Solar-induced fluorescence (SIF) data from TROPOspheric Monitoring Instrument (TROPOMI)

The amounts of $APAR_{chl}$ are determined by the amounts of incoming PAR, the chlorophyll content in the canopy, and the canopy structure. These amounts are generally used in three pathways: photochemical quenching, non-photochemical quenching, and emitted fluorescence. Therefore, SIF is closely linked with $APAR_{chl}$ and the canopy structure that affects reabsorption and the so-called "escaping factor."(Zhang et al., 2023)

Here, we utilized L2 SIF from TROPOMI to compare with $APAR_{chl}$ and GPP (Guanter et al., 2021; Köhler, Frankenberg, et al., 2018). The data were selected from the 743-758 nm retrieval window due to its lower sensitivity to atmospheric disturbances than the 735-758 nm retrieval window (Guanter et al., 2021).

We employed a weighted mean oversampling method that accounts for the proportion of the instrument's detection footprint within each 0.25-degree pixel to map the global SIF (Figure 4.6). As a result, SIF for each 0.25-degree pixel represents the weighted average of daily-averaged SIF detection footprints within that pixel over an 8-day period. The selection of an 8-day aggregation period was designed to synchronize

with TROPOMI's 16-day orbital repeat cycle and MOD09A1's 8-day cycle, thereby minimizing discrepancies due to changes in observational geometry (Doughty et al., 2021). This method reduces retrieval errors inherent in single detections and standardizes the effects of differences in the geometrical positions of the sun and sensor (Guanter et al., 2021).

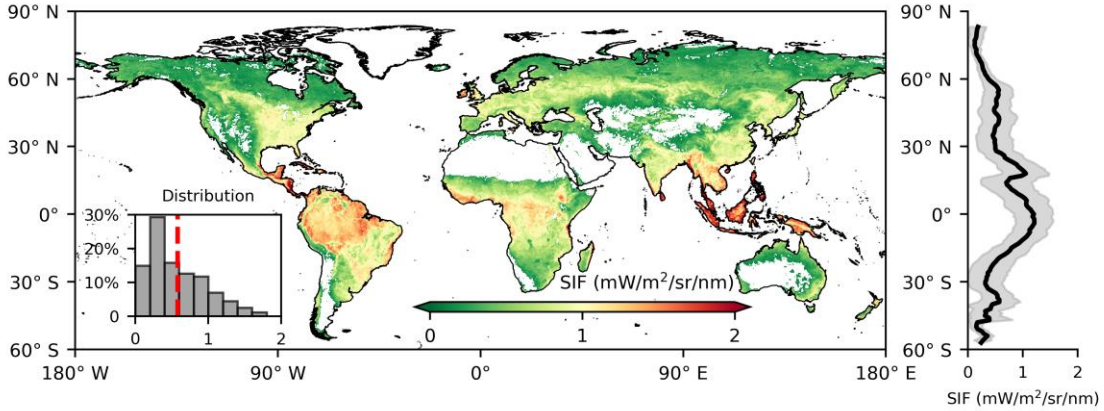

Figure 4.6: Spatial distribution of annual means TROPOMI SIF in 2020. The right panel shows the average values of all pixels within 1° latitude bin across the latitude. The red dashed line histogram is the global average value.

4.2.8 GPP products from previous version of VPM (VPM v2.0) and other models

For comparison with this new GPP product from VPM v3.0 and TROPOMI SIF, we selected GPP from remote sensing (RS)-based machine learning, data-driven, and process-based models, including VPM v2.0 (version of Zhang. 2017) (Yao Zhang et al., 2017) and other five global GPP products: BEPS GPP (Leng et al., 2023), BESS GPP (B. Li et al., 2023), FLUXCOM GPP (Jung et al., 2020), GOSIF GPP (Li et al., 2019), and MOD17 GPP products (Running et al., 1999). We obtained the above products from all available years within the period from 2018 to 2021, all products are converted to

an 8-day temporal resolution for comparison. Detailed information about these products can be found in Table 4.1.

Table 4.1: Basic information of VPM v2.0 and other five major global GPP products. Note that the spatial resolution and temporal resolution only list the spatiotemporal resolutions used in this study, and do not represent all the spatiotemporal resolutions provided by the dataset.

GPP product	Spatial resolution	Temporal resolution	Availability	Reference
VPM v2.0	500-meter	8-day	2018-2020	(Yao Zhang et al., 2017)
BEPS GPP	0.5-degree	Daily	2018-2020	(Leng et al., 2023)
BESS GPP	0.05-degree	Daily	2018-2019	(B. Li et al., 2023)
FLUXCOM GPP	0.5-degree	Daily	2018-2020	(Jung et al., 2020)
GOSIF GPP	0.05-degree	Daily	2018-2021	(Li et al., 2019)
MOD17 GPP	500-meter	8-day	2018-2021	(Running et al., 1999)

4.2.9 Vegetation Photosynthesis Model (VPM v3.0)

VPM estimate GPP as the product of $APAR_{chl}$ and LUE (ε_g) (Xiao, Hollinger, et al., 2004; Xiao, Zhang, et al., 2004):

$$GPP_{VPM} = APAR_{chl} \times \varepsilon_g \quad (4.7)$$

where $APAR_{chl}$ is product of PAR and the fraction of PAR absorbed by chlorophyll ($FPAR_{chl}$):

$$APAR_{chl} = PAR \times FPAR_{chl} \quad (4.8)$$

In VPM v2.0, $FPAR_{chl}$ was calculated as a linear function with EVI across all the land

cover types (Yao Zhang et al., 2017):

$$FPAR_{chl} = a + b \times EVI \quad (4.9)$$

Where a and b are set to be -0.1 and 1.0, respectively. Note that chloroplasts in needleleaf species are distributed in a ring, while chloroplasts in broadleaf (flat leaf) species are usually spread out on the surface of the leaves (Trueba et al., 2022). This structural difference between needleleaf and broadleaf species implies that the radiation absorption area of chloroplasts in needleleaf species differs from that in broadleaf species. VPM v3.0 adjusted the radiation absorption area of chloroplasts in needleleaf species to represent the photosynthetic efficiency of the ring-shaped distribution of chloroplasts more accurately. Specifically, we applied a ratio (γ_E) based on the comparison between the area of the annular and the area of the concentric circles, to approximate the actual area of chloroplasts involved in photosynthesis in needleleaf species. The improved equation for $FPAR_{chl}$ is as follows:

$$FPAR_{chl} = \begin{cases} a + \gamma_E \times b \times EVI, \text{ if needleleaf} \\ a + b \times EVI, \text{ if broadleaf} \end{cases} \quad (4.10)$$

where γ_E = 1.25 is the ratio of the area of the annular area and the area of concentric circles (Law et al., 2001; Trueba et al., 2022). Needleleaf forests can be found in lands classified as ENF, Deciduous Needleleaf Forests (DNF), and MF in the MCD12Q1 dataset. According to the official documentation of MCD12Q1, the pixel proportion of broadleaf and needleleaf forests within MF ranges between 40% and 60%. Thus, we used a needleleaf pixel proportion of 50% and an area-weighted average method to estimate the $FPAR_{chl}$ for MF pixels.

LUE (ε_g) includes the temperature (T_{scalar}) and water (W_{scalar}) stress:

$$\varepsilon_g = \varepsilon_0 \times W_{scalar} \times T_{scalar} \quad (4.11)$$

where ε_0 = 0.53 (g C mol^{-1} PAR) for C3 and 0.79 (g C mol^{-1} PAR) for C4 are the maximum light use efficiency (Xiao, 2006). For a pixel with a mix of C3 and C4 plant, we used an area-weighted average method to estimate the ε_0 (ε_0 = 0.53*C3% + 0.79*C4%).

The W_{scalar} of VPM v2.0 is calculated as follows:

$$W_{scalar} = \frac{1 + LSWI}{1 + LSWI_{max}} \quad (4.12)$$

where $LSWI_{max}$ is the maximum LSWI during the TGS (Yao Zhang et al., 2016). In VPM v3.0, the impact of drought and non-drought within the temporal profile on W_{scalar} is considered (He et al., 2014):

$$W_{scalar} = \begin{cases} \frac{1 + LSWI}{1 + LSWI_{max}}, \text{ if } LSWI \geqslant -0.1 \\ 0.5 + LSWI, \text{ if } LSWI < -0.1 \end{cases} \quad (4.13)$$

T_{scalar} is calculated as follows:

$$T_{scalar} = \frac{(T - T_{max}) \times (T - T_{min})}{(T - T_{max}) \times (T - T_{min}) - (T - T_{opt})^2} \quad (4.14)$$

where the T_{max}, T_{min}, and T_{opt} are the maximum, minimum, and optimum temperatures for photosynthesis activities. T_{max} and T_{min} are derived from the look-up table (Yao Zhang et al., 2017).

In VPM v2.0, the input for T_{opt} was defined by biome-specific T_{opt} ($T_{opt\text{-}biome}$), as estimated by Raich et al. (1991) and Melillo et al. (1993). In VPM v3.0, $T_{opt\text{-}biome}$ was replaced with site-specific T_{opt} ($T_{opt\text{-}site}$), which is derived from site-specific-year T_{opt} ($T_{opt\text{-}site\text{-}year}$), and used as the T_{opt} parameter input into the model. $T_{opt\text{-}site\text{-}year}$ is obtained from the annual EVI-$T_{air\text{-}DT}^{ERA5}$ response curve. The response curve within the TGS was

generated and fitted by cubic regression splines for each year (Figure 4.7 a). The optimal $T_{air\text{-}DT}^{ERA5}$ range for vegetation photosynthesis is defined as the set of air temperatures corresponding to when EVI surpasses 95% of EVI_{max}. Subsequently, the $T_{opt\text{-}site\text{-}year}$ is calculated as the mean of all $T_{air\text{-}DT}^{ERA5}$ falling within this specified range. $T_{opt\text{-}site}$ was then calculated as the median value of $T_{opt\text{-}site\text{-}year}$ (Figure 4.7 b). Figure 4.7 c shows the global map of $T_{opt\text{-}site}$. Along the latitudinal gradient, $T_{opt\text{-}site}$ ranges between 4°C to 35°C. The highest values are found in tropical regions, gradually decreasing along the latitudinal gradient, and reaching their lowest near the poles. Further details on the global $T_{opt\text{-}site}$ dataset are provided in another manuscript (Pan, Xiao, Yao, et al., 2024).

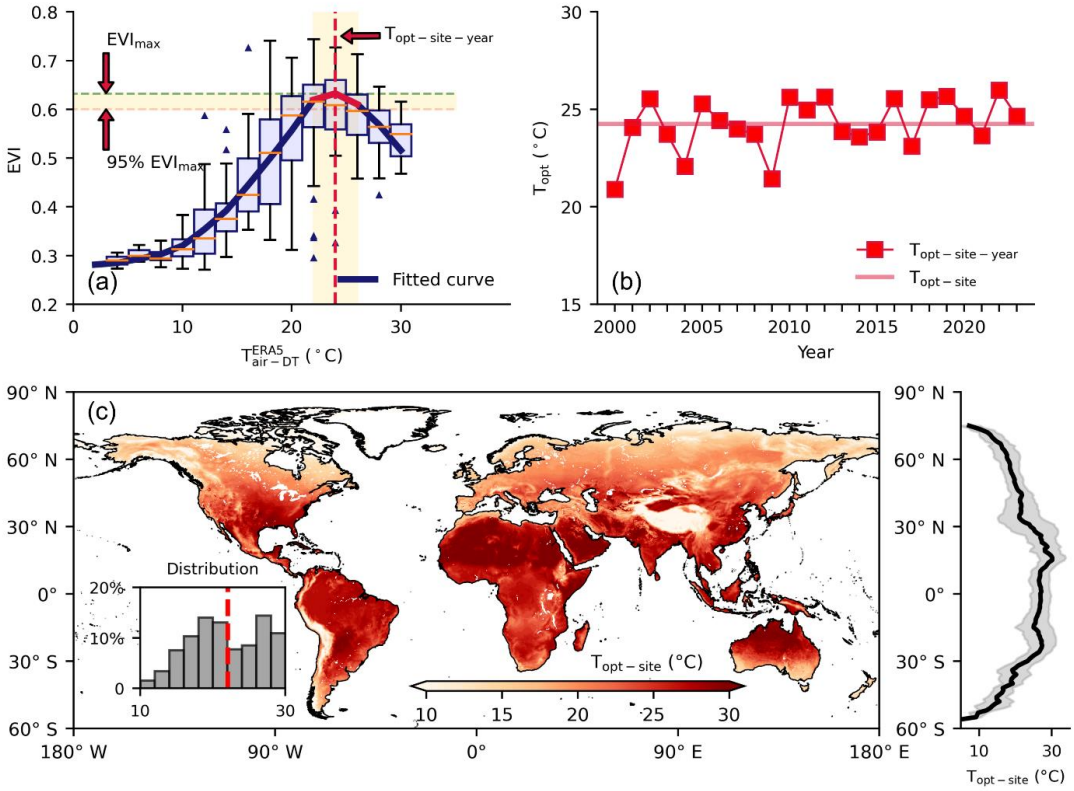

Figure 4.7: Global site-specific apparent optimal air temperature for photosynthesis ($T_{opt\text{-}site}$) dataset. (a) The response curve of EVI to $T_{air\text{-}DT}^{ERA5}$, using the

US-Ha1 site (Harvard Forest, DBF, 42.5378, -72.1715) as an example. The solid dark blue line represents curve fit using cubic regression splines. The boxplot shows points every 2°C bin; (b) $T_{opt\text{-}site\text{-}year}$ from each year; and (c) global map of $T_{opt\text{-}site}$. The red dashed line in the histogram is the global average value. The black solid line is the average value of all pixels within 1-degree across the latitude.

We ran VPM v3.0 and estimated the global $GPP_{VPM\text{-}v3}$, with the main workflow and input data illustrated in Figure 4.8. Additionally, we set up various scenarios to run the VPM model (Table 4.2): S (VPM v3.0), S0 (VPM v2.0), S1 (VPM v2.0 with $T_{opt\text{-}site}$ parameter), S2 (VPM v2.0 with improved $FPAR_{chl}$ parameter), S3 (VPM v2.0 with improved W_{scalar} parameter).

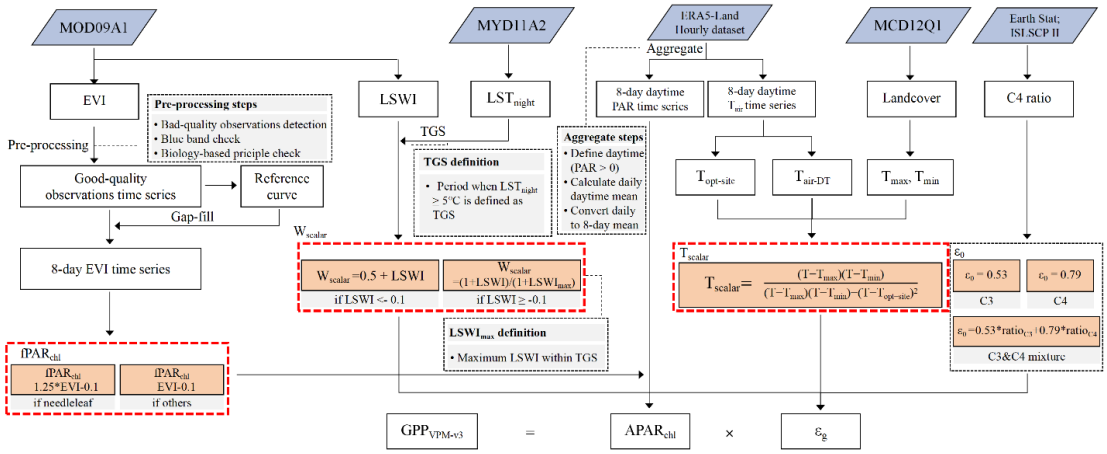

Figure 4.8: Workflow and input data of VPM v3.0 to simulate global GPP ($GPP_{VPM\text{-}v3}$).

Table 4.2: The VPM model under various scenarios. $T_{opt\text{-}site}$ and $T_{opt\text{-}biome}$ represent the T_{opt} in VPM v2.0 and VPM v3.0, respectively. All other parameters across these scenarios are consistent.

Scenarios	T_{opt}	$FPAR_{chl}$	W_{scalar}
S	$T_{opt\text{-}site}$	VPM v3.0	VPM v3.0
S0	$T_{opt\text{-}biome}$	VPM v2.0	VPM v2.0
S1	$T_{opt\text{-}site}$	VPM v2.0	VPM v2.0
S2	$T_{opt\text{-}biome}$	VPM v3.0	VPM v2.0
S3	$T_{opt\text{-}biome}$	VPM v2.0	VPM v3.0

4.2.10 Statistical analysis

We evaluated VPM v3.0 using GPP derived from eddy flux towers and TROPOMI SIF at site and global scales. Simple linear regression was utilized to compute three key indicators: slope, the coefficient of determination (R^2), and the root mean square error (RMSE). The application of simple linear regression served two primary purposes in our assessment: (1) comparing $GPP_{VPM\text{-}v3}$ with GPP_{EC} from 205 eddy flux tower sites, and (2) comparing $GPP_{VPM\text{-}v3}$ with other major GPP products, including $GPP_{VPM\text{-}v2}$, BEPS, MOD17, GOSIF, BESS, and FLUXCOM GPP products. Simple linear regression is a statistical method that models the relationship between two variables by fitting a linear equation to observed data (Zou et al., 2003). In this study, we calculated the linear equation without intercept ($y = \alpha * x$). The primary aim was to estimate the slope and the determination coefficient (R^2). The slope of the linear regression model without intercept can be calculated by the following formula:

$$\alpha = \frac{\sum x_i y_i}{\sum {x_i}^2} \tag{4.15}$$

Where x_i and y_i are the i-th values of the two independent variables, respectively. R^2

can be calculated as:

$$R^2 = 1 - \frac{\sum(y_i - \alpha x_i)^2}{\sum(y_i - \bar{y})^2} \quad (4.16)$$

Where $\bar{y}$ is the mean values of the independent variables y. The RMSE can be estimated as:

$$RMSE = \sqrt{\frac{1}{n}\sum\left(y_i - \bar{y_i}\right)^2} \quad (4.17)$$

The Pearson correlation coefficient was calculated to evaluate temporal consistency at the pixel level. This method was used to evaluate: (1) the temporal consistency between the TROPOMI SIF time series with the $APAR_{chl}$ and the $GPP_{VPM\text{-}v3}$ time series; (2) the temporal consistency between the $GPP_{VPM\text{-}v3}$ and other major GPP time series; and (3) the temporal consistency between the TROPOMI SIF time series and other major GPP time series products. The Pearson correlation coefficient (*r*) is a statistical indicator of the linear correlation between two variables, with its value ranging from -1 to 1 (Cohen et al., 2009). Negative and positive values indicate negative and positive correlations, respectively. The magnitude of the *r* absolute value signifies the extent of correlation between the two variables, with 0 indicating no linear correlation. The formula for calculating *r* is as follows:

$$r = \frac{\sum_{i=1}^{n}(x_i - \bar{x})\left(y_i - \bar{y}\right)}{\sqrt{\sum_{i=1}^{n}(x_i - \bar{x})^2\left(y_i - \bar{y}\right)^2}} \quad (4.18)$$

Where x_i and y_i are the i-th values of the two independent variables, respectively, $\bar{x}$ and $\bar{y}$ are the mean values of the variables, respectively, and n is the number of each variable.

4.3 Results

4.3.1 Evaluation of GPP_{VPM} from VPM v3.0 with GPP_{EC} from eddy flux tower

We compared the relationship between time series $GPP_{VPM\text{-}v3}$ and GPP_{EC} data (g $C/m^2/day$) across 11 land cover types and 205 eddy flux tower sites with 1,658 site-years on an 8-day temporal resolution by using simple linear regression (Figure 4.9). According to the slope, the magnitude of $GPP_{VPM\text{-}v3}$ is consistent with GPP_{EC} for most land cover types, such as CRO, CSH, ENF, GRA, MF, WET, and WSA, ranging between 0.85 and 1.02. $GPP_{VPM\text{-}v3}$ slightly overestimates in DBF (slope = 1.12) and OSH (slope = 1.18), and underestimates in EBF (slope = 0.72) and SAV (slope = 0.79). According to the R^2 values, EBF (R^2 = 0.55) and SAV (R^2 = 0.69) had moderate agreement, and the remaining nine land cover types had high agreement between $GPP_{VPM\text{-}v3}$ and GPP_{EC}, with R^2 ranging from 0.72 to 0.90. RMSE across all 11 biomes ranged from 0.87 to 2.19 gC m^{-2} day^{-1}, with most biomes showing RMSE below 2 gC m^{-2} day^{-1}, except for EBF, which had an RMSE of 2.19 gC m^{-2} day^{-1}. Aggregated data from all 205 sites (1,658 site-year), the slope, R^2, and RMSE between $GPP_{VPM\text{-}v3}$ and GPP_{EC} are 0.97, 0.78, and 1.46 gC m^{-2} day^{-1}, respectively. The high degree of consistency demonstrates that $GPP_{VPM\text{-}v3}$ reasonably tracks the magnitude and seasonal dynamics of GPP_{EC} at these eddy flux tower sites.

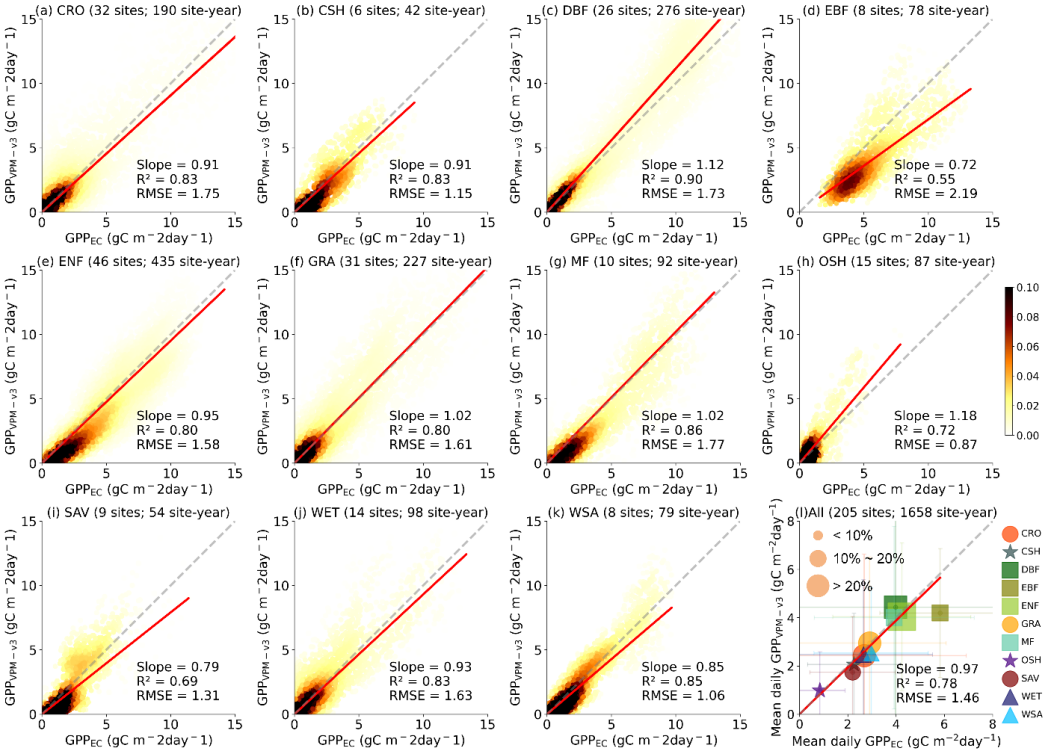

Figure 4.9: Comparisons between $GPP_{VPM\text{-}v3}$ and GPP_{EC}. (a)–(k) compare GPP estimated from VPM v3.0 ($GPP_{VPM\text{-}v3}$) with observed GPP (GPP_{EC}) across 11 biomes, using statistical metrics slope, R^2, and RMSE (see Supplementary Method 1). The red dashed line is regression curve between $GPP_{VPM\text{-}v3}$ and GPP_{EC}, while the gray dashed line is the 1:1 line. (l) reports mean daily GPP_{EC} and mean daily $GPP_{VPM\text{-}v3}$ across all sites within each biome, with error bars indicating the standard deviations across sites. The amounts of available GPP_{EC} observations (from eddy flux towers) varies across biomes. Point size represents the proportion of GPP_{EC} observations in specific biome relative to the total observations.

4.3.2 Evaluation of $APAR_{chl}$ and GPP_{VPM} with SIF

Time series TROPOMI SIF and $APAR_{chl}$ data during 2018-2021 were strongly correlated in most areas, such as North America and large parts of Europe, Asia, and

Africa (Figure 4.10a). The correlation is relatively lower in tropical forest regions between 20°S and 20°N, such as the Amazon basin, Congo basin, Southern Asia, and part of Australia, in part driven by small seasonal dynamics of PAR, VIs, $APAR_{chl}$, and SIF in tropics. We explored a site with little land cover and land use change, ATTO, in Manaus, Brazil (Figure 4.11). Inconsistencies appeared in the seasonal dynamics between SIF, GPP, and $APAR_{chl}$ in this site. We also noticed that the correlation is relatively low in high-latitude regions, such as the boreal forests and tundra areas of North America and Russia. Despite these regional variations, TROPOMI SIF and $APAR_{chl}$ exhibit a high positive correlation across most parts of the world, with more than 55% of grid cells having $r > 0.8$. This suggests that the estimated $APAR_{chl}$ is an effective indicator reflecting the radiation utilized by vegetation chlorophyll for photosynthesis.

The temporal consistency between $GPP_{VPM\text{-}v3}$ and TROPOMI SIF aligned well with those between $APAR_{chl}$ and TROPOMI SIF (Figure 4.10b). $GPP_{VPM\text{-}v3}$ and TROPOMI SIF exhibit a slightly higher positive correlation across most regions of the globe, with an average r of 0.81 (Figure 4.10b).

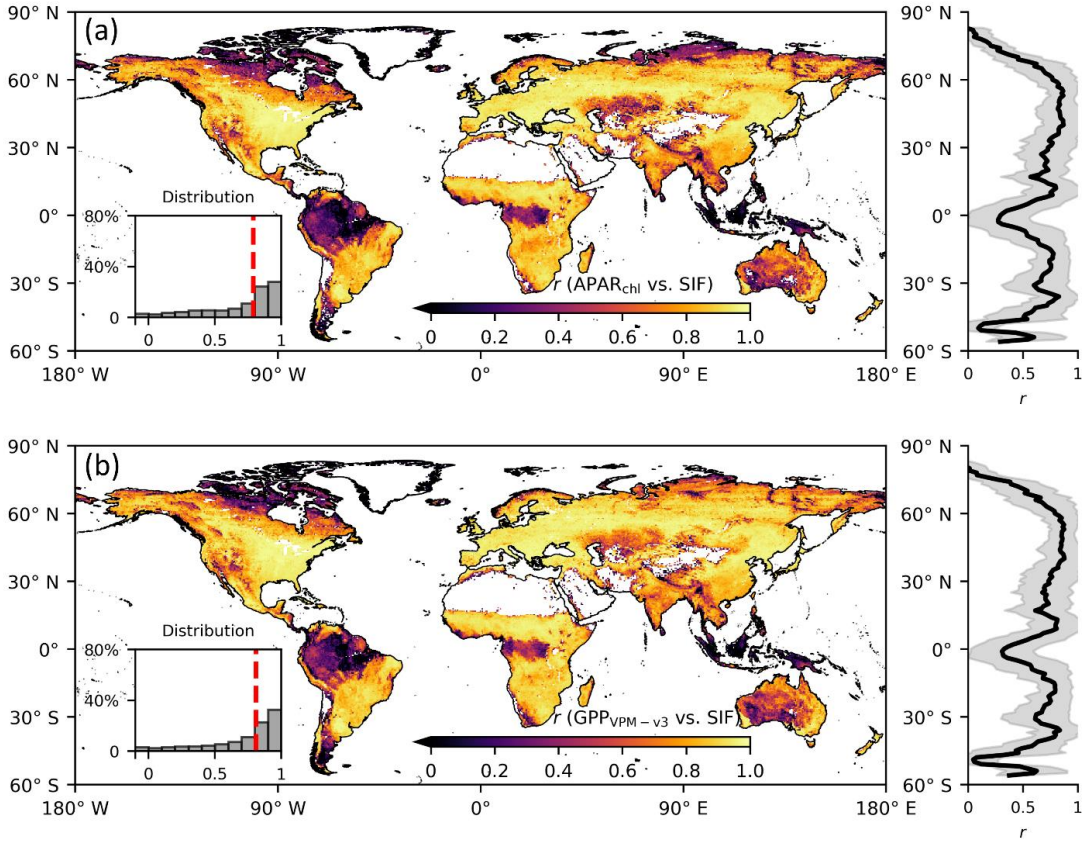

Figure 4.10: Temporal consistency of $APAR_{chl}$ and GPP_{VPM} with TROPOMI SIF at the pixel-to-pixel level. The comparison period spans from May 1, 2018, to December 31, 2021, totaling 169 images. *r* denotes the Pearson correlation coefficient. The red dashed line in the histogram is the global average value. The black solid line is the average value of all pixels within 1° across the latitude. All data were aggregated to 0.25-degree and 8-day.

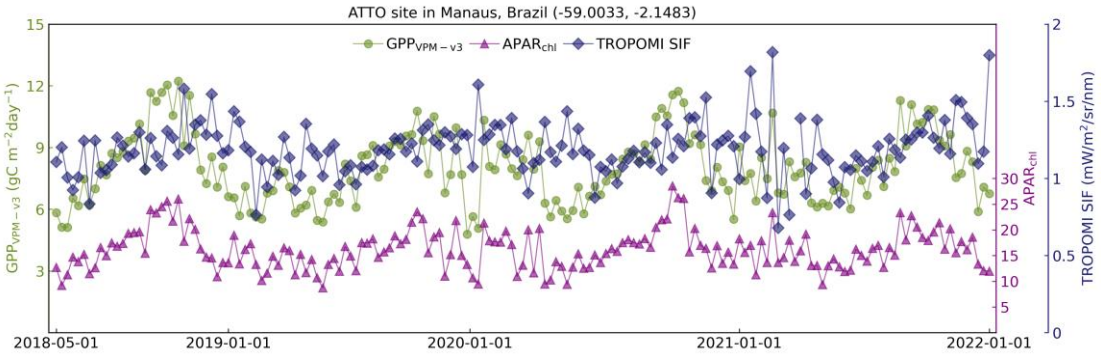

Figure 4.11: Seasonal dynamics of TROPOMI SIF, $APAR_{chl}$, and $GPP_{VPM\text{-}v3}$ in the grid cell covering the ATTO tower site in Manaus, Brazil (-59.0033, -2.1483).

4.3.3 The effects of model parameter changes (T_{opt}, $FPAR_{chl}$, and W_{scalar}) on GPP estimation in VPM (v3.0) at the global scale

We conducted simple linear regressions between GPP_{VPM} under various scenarios and GPP_{EC}. Figure 4.12 shows the statistical results comparing GPP_{VPM} with all GPP_{EC} observations (205 sites, 1,658 site-years).

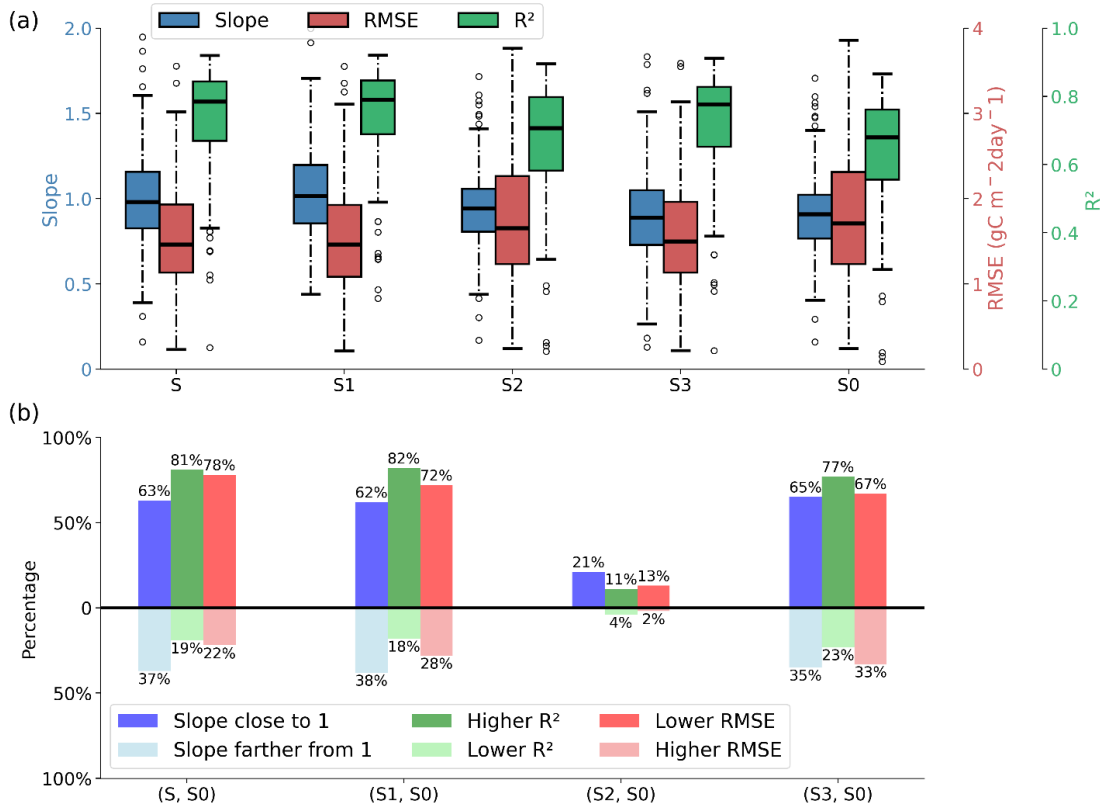

Figure 4.12: Simple linear regression between GPP_{VPM} under various scenarios (S, S1, S2, S3, S0) and GPP_{EC} in 205 eddy flux tower sites with 1,658 site-year across 11 land cover types. S: VPM v3.0; S1: VPM v2.0 plus improved T_{opt} parameter; S2: VPM v2.0 plus improved $FPAR_{chl}$ parameter; S3: VPM v2.0 plus improved W_{scalar} parameter; S0: VPM v2.0. (a) The blue, red, and green boxes represent the

slope, RMSE, and R^2 between GPP_{VPM} and GPP_{EC} for all sites, respectively. (b) The differences in simple linear regression between GPP_{VPM} and GPP_{EC} were evaluated across various scenarios (S, S1, S2, S3) relative to scenario S0. For instance, (S, S0) denotes comparison between scenario S and scenario S0. Dark-colored bars indicate the percentage of sites where model performance improved relative to scenario S0 (VPM v2.0), while light-colored bars indicate poorer model performance. Improved model performance specifically refers to a slope closer to 1, higher R^2, and lower RMSE.

Under Scenario S0 (VPM v2.0), an overall slope, R^2, and RMSE of 0.90, 0.69, and 1.71 $gCm^{-2}day^{-1}$, respectively (Figure 4.12). Across 11 land cover types, specifically, the range of slopes was from 0.62 to 1.11, RMSE was from 0.63 to 2.21 $gCm^{-2}day^{-1}$, and R^2 ranged from 0.47 to 0.87 (Figure 4.13, Figure 4.14).

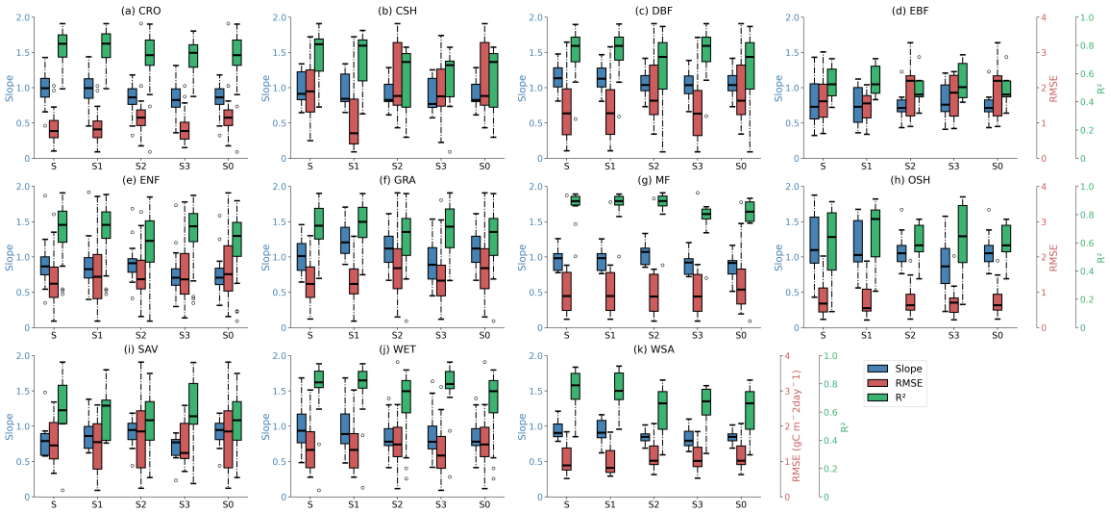

Figure 4.13: Simple linear regression between GPP_{VPM} under various scenarios (S, S1, S2, S3, S0) and GPP_{EC} in specific land cover types. S: VPM v3.0; S1: VPM v2.0 plus improved T_{opt} parameter; S2: VPM v2.0 plus improved $FPAR_{chl}$ parameter;

S3: VPM v2.0 plus improved W_{scalar} parameter; S0: VPM v2.0. The blue, red, and green boxes represent the slope, RMSE, and R^2 between GPP_{VPM} and GPP_{EC} for all sites, respectively.

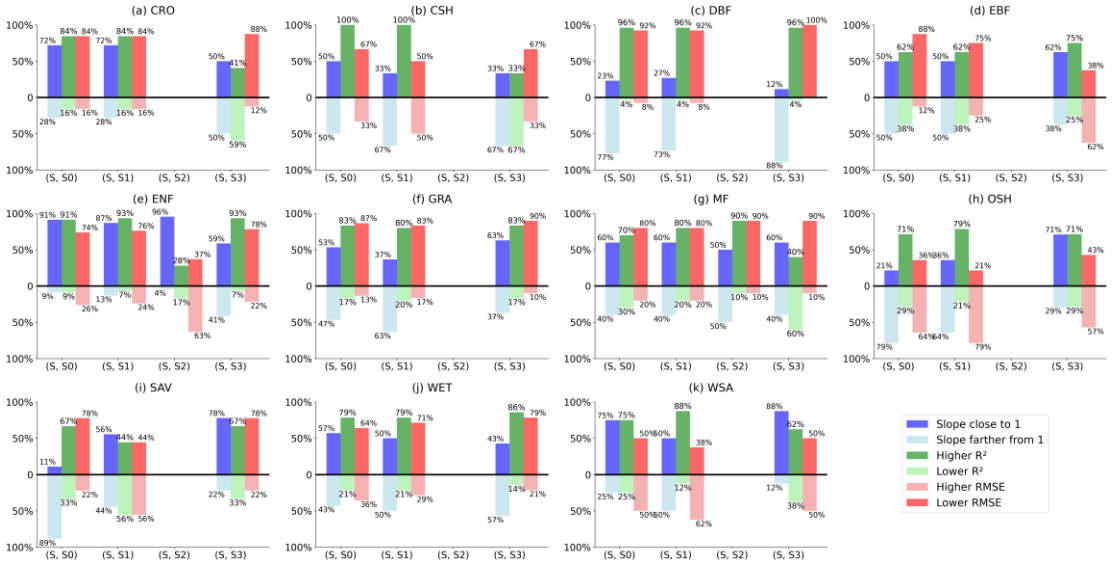

Figure 4.14: The differences in simple linear regression between GPP_{VPM} and GPP_{EC} were evaluated across various scenarios (S, S1, S2, S3) relative to scenario S0 in specific land cover types. For instance, (S, S0) denotes comparison between scenario S and scenario S0. Dark-colored bars indicate the percentage of sites where model performance improved relative to scenario S0 (VPM v2.0), while light-colored bars indicate poorer model performance. Improved model performance specifically refers to a slope closer to 1, higher R^2, and lower RMSE.

Compared to scenario S0, the three scenarios (S1, S2, S3) varied by land cover type but overall showed improved model performance (slope closer to 1, higher R^2, and lower RMSE) (Figure 4.12a, Figure 4.13). Specifically, scenario S1 improved modeling performance across most sites, with 62%, 82%, and 72% of sites showing higher model

performance (Figure 4.13, Figure 4.14). Scenario S2 effectively addressed the underestimation of GPP at ENF and MF sites, achieving a slope closer to 1, lower RMSE, and increased R^2 at some sites (Figure 4.12b, Figure 4.13, Figure 4.14). Evidence from several ENF sites with over 10 years of observations indicates that the improvement of $FPAR_{chl}$ in Scenario S2 notably improved VPM's model performance during the growing season, whereas Scenario S0 was pronounced underestimated (Figure 4.15). Under scenario S3, the slopes are closer to 1 at GRA, OSH, and SAV sites, which are mostly in arid/semi-arid regions (Figure 4.13, Figure 4.14).

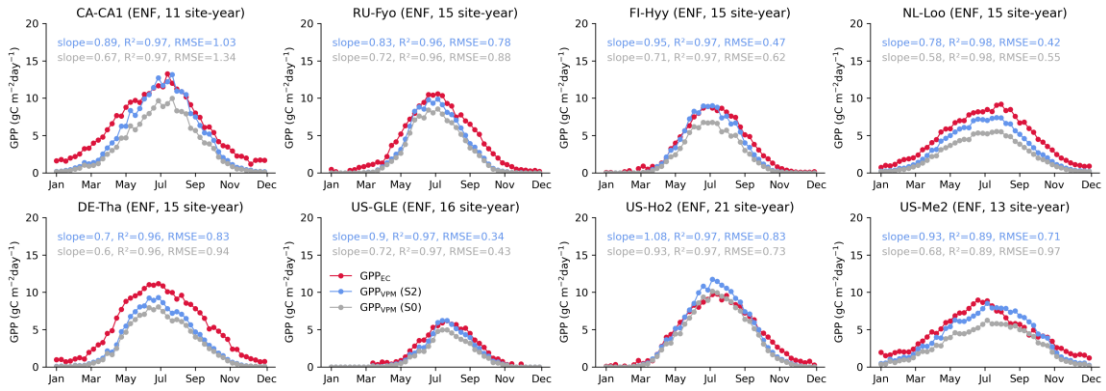

Figure 4.15: The seasonal comparison of GPP at eight typical ENF (coniferous tree) sites includes data from VPM (scenario S2), VPM (scenario S0), and the eddy flux tower. These sites were selected for providing over 10 site-years of observations. Red, blue, and gray dashed lines represent GPP_{EC}, GPP_{VPM} (S2), and GPP_{VPM} (S0), respectively. The blue and gray text denote the linear regression between GPP_{EC} and GPP_{VPM} (S2), and between GPP_{EC} and GPP_{VPM} (S0), respectively. Data shown in the figure represents mean value across all years.

We also selected several typical arid sites to show the model performance improvements in Scenario S3 compared to Scenario S0 (Figure 4.16). Scenario S0 was

overestimated at these sites, while the improvement in W_{scalar} in Scenario S3 effectively mitigated this overestimation.

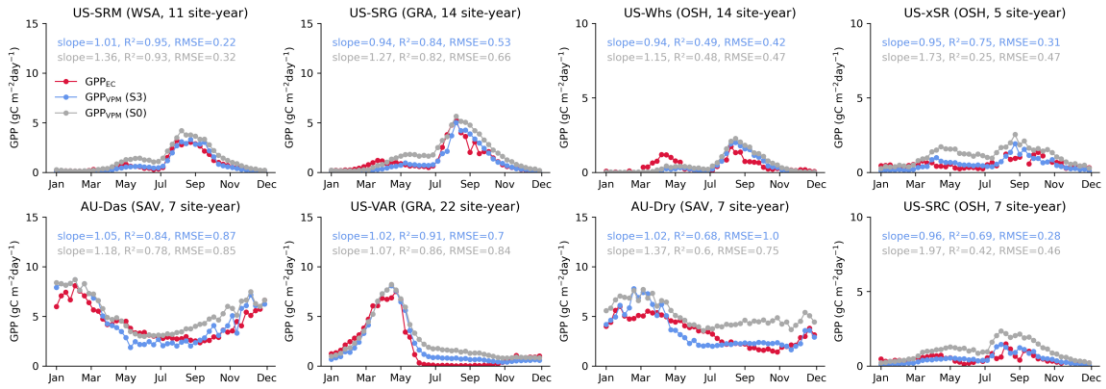

Figure 4.16: The seasonal comparison of GPP at eight typical arid sites includes data from VPM (scenario S3), VPM (scenario S0), and the eddy flux tower. These sites were selected because they are located in arid regions or have experienced severe drought events. Red, blue, and gray dashed lines represent GPP_{EC}, GPP_{VPM} (S3), and GPP_{VPM} (S0), respectively. The blue and gray text denote the linear regression between GPP_{EC} and GPP_{VPM} (S3), and between GPP_{EC} and GPP_{VPM} (S0), respectively. Data shown in the figure represents mean value across all years.

Integrating these three improvements, scenario S (VPM v3.0) demonstrated higher model performance relative to scenario S0 (VPM v2.0), with 63% of sites showing a slope closer to 1, 81% of sites achieving higher R^2, and 76% of sites exhibiting lower RMSE (Figure 4.12). The results clearly demonstrate the positive impact of combining three parameters T_{opt}, $FPAR_{chl}$, and W_{scalar} improvements on the VPM modeling performance. Among these, the T_{opt} parameter improved modeling performance across most ecosystems, while $FPAR_{chl}$ and W_{scalar} parameters showed varying effectiveness depending upon the land cover type.

4.3.4 Comparisons between global GPP products from VPM v3.0 and other major models

The relationship between the mean daily GPP from $GPP_{VPM\text{-}v3}$ and various major GPP products was compared. The comparison between $GPP_{VPM\text{-}v3}$ and the previously released $GPP_{VPM\text{-}v2}$ shows a slope of 1.08, an R^2 of 0.91, and an RMSE of 0.71 g C m^{-2} day^{-1} (Figure 4.17a). This suggests that $GPP_{VPM\text{-}v3}$ generally continues the performance of the $GPP_{VPM\text{-}v2}$ product, with the improvement introducing estimation variations in magnitude. Among other GPP products with differences in model structure and data input, $GPP_{VPM\text{-}v3}$ exhibits good consistency with those GPP products, such as BEPS, GOSIF, and BESS. The slopes ranged from 0.98 to 1.06, R^2 ranged from 0.83 to 0.88, and RMSE ranged from 0.82 to 0.97 g C m^{-2} day^{-1} (Figure 4.17b, d, and e). Despite the MOD17 and FLUXCOM GPP products having reasonable R^2 values compared to $GPP_{VPM\text{-}v3}$, they tended to underestimate GPP by 31% and 12% compared to $GPP_{VPM\text{-}v3}$, respectively (Figure 4.17c, f).

Overall, $GPP_{VPM\text{-}v3}$ provides GPP estimates consistently aligned with those from various major GPP products within a reasonable error range, thereby confirming VPM v3.0 as a reliable model for global long-term GPP estimation.

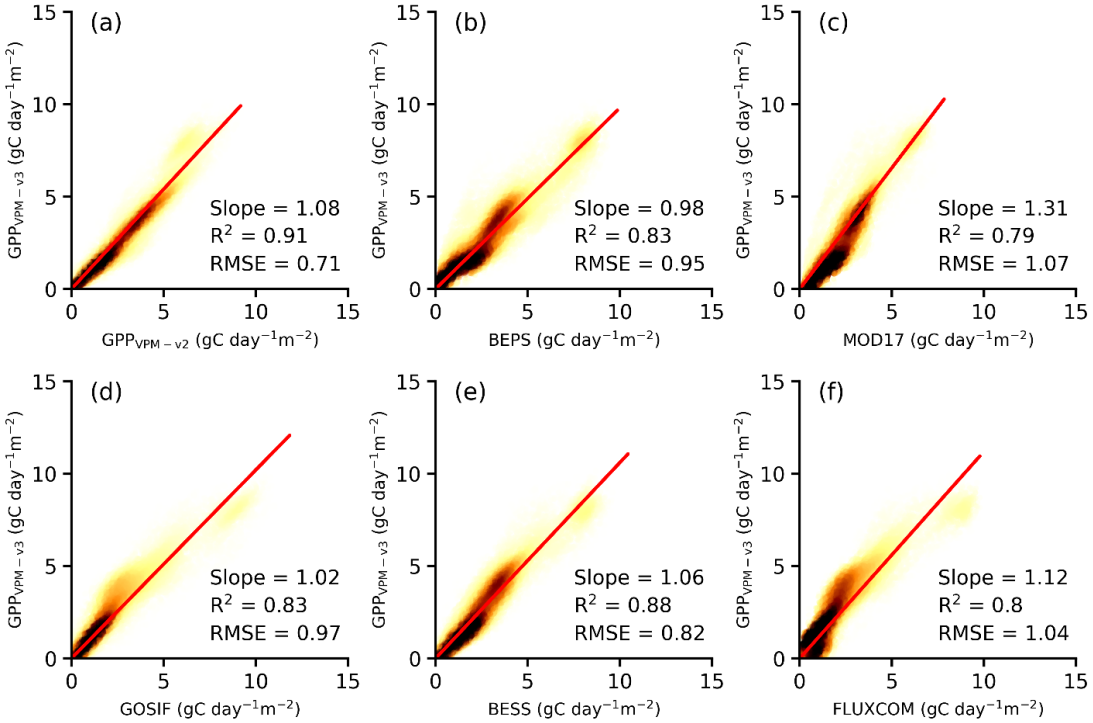

Figure 4.17: Comparison of mean daily GPP between $GPP_{VPM\text{-}v3}$ and other GPP products. $GPP_{VPM\text{-}v3}$ refers to the estimation of VPM v3.0 in this study, while $GPP_{VPM\text{-}v2}$ refers to the estimation of VPM v2.0 from the version of Zhang et al. (2017). BEPS, MOD17, GOSIF, BESS, and FLUXCOM GPP refer to the other major GPP products. All GPP products selected data available from May 1, 2018, to December 31, 2021, and were aggregated to 0.25 degrees and 8-day.

We also analyzed the temporal correlation between $GPP_{VPM\text{-}v3}$ and other major GPP products during 2018-2021 at the pixel-to-pixel scale (Figure 4.18). $GPP_{VPM\text{-}v3}$ and $GPP_{VPM\text{-}v2}$ showed a very strong correlation, with r exceeding 0.8 in more than 90% of pixels, indicating consistent seasonal dynamics between the two versions (Figure 4.18a). However, the correlation between $GPP_{VPM\text{-}v3}$ and other GPP products varies by region. In North America and most parts of Europe, Asia, and Africa, $GPP_{VPM\text{-}v3}$ strongly

correlates with other GPP products (Figure 4.18b, c, d, e, and f).

The correlation is relatively low in tropical regions, including the Amazon rainforest, the Congo Basin, Southeast Asia, and Australia, primarily due to persistent cloud cover, which result in small number of good-quality satellite observations and significantly impacts the performance of models in these areas. Additionally, the tropical forests are dominated by evergreen plants with small seasonal dynamics, making it challenging to achieve statistical consistency across different products. This weak correlation in the tropical regions is particularly significant when compared to process-based and machine learning models such as BEPS, BESS, and FLUXCOM GPP, where the correlation is close to zero or even negative (Figure 4.18b, e, and f). Data-driven models like MOD17 and GOSIF showed slightly better correlations with $GPP_{VPM\text{-}v3}$ (Figure 4.18c, d). Overall, $GPP_{VPM\text{-}v3}$ exhibits strong correlations with these GPP products in most parts of the world, with a global average *r* ranging from 0.88 to 0.95.

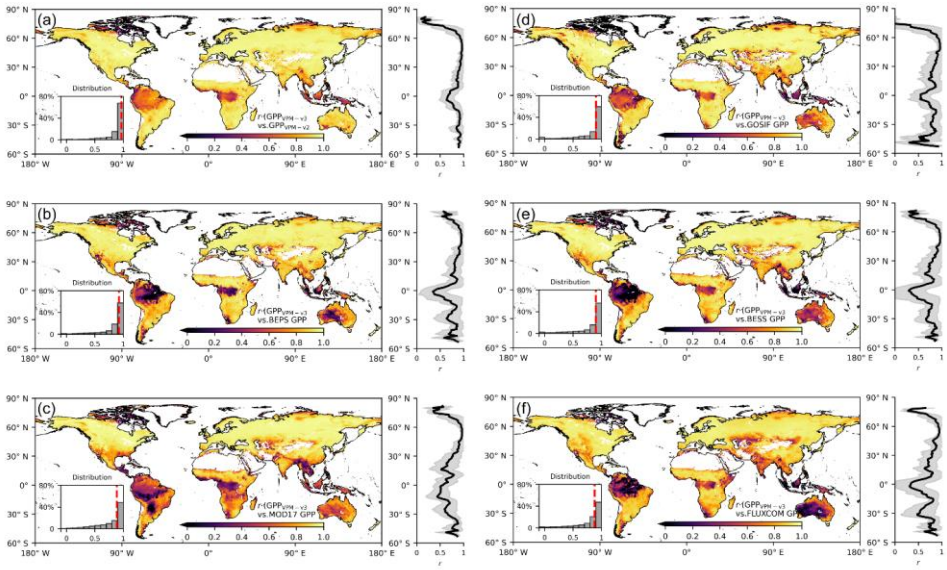

Figure 4.18: Temporal consistency between $GPP_{VPM\text{-}v3}$ and other GPP products at

the pixel-to-pixel level. $GPP_{VPM\text{-}v3}$ refers to the estimation of VPM v3.0 in this study, while $GPP_{VPM\text{-}v2}$ refers to the estimation of VPM v2.0 from the version of Zhang, et 2017. BEPS, MOD17, GOSIF, BESS, and FLUXCOM GPP refer to the other GPP products. All GPP products selected data available from May 1, 2018, to December 31, 2021, and were aggregated to 0.5 degrees and 8-day.

We used TROPOMI SIF data as a common reference to compare the temporal correlation at the pixel scale between these major GPP products and TROPOMI SIF. The correlations between these seven GPP products (including $GPP_{VPM\text{-}v3}$) and SIF showed a globally consistent geographic pattern (Figure 4.10b, Figure 4.19). North America and most parts of Europe, Asia, and Africa show relatively strong correlations, while tropical and high-latitude regions exhibit low correlations. Notably, MOD17 shows almost no correlation with TROPOMI SIF throughout the Amazon rainforest (Figure 4.19c). Similarly, FLUXCOM shows almost no correlation with TROPOMI SIF in central Australia (Figure 4.19f).

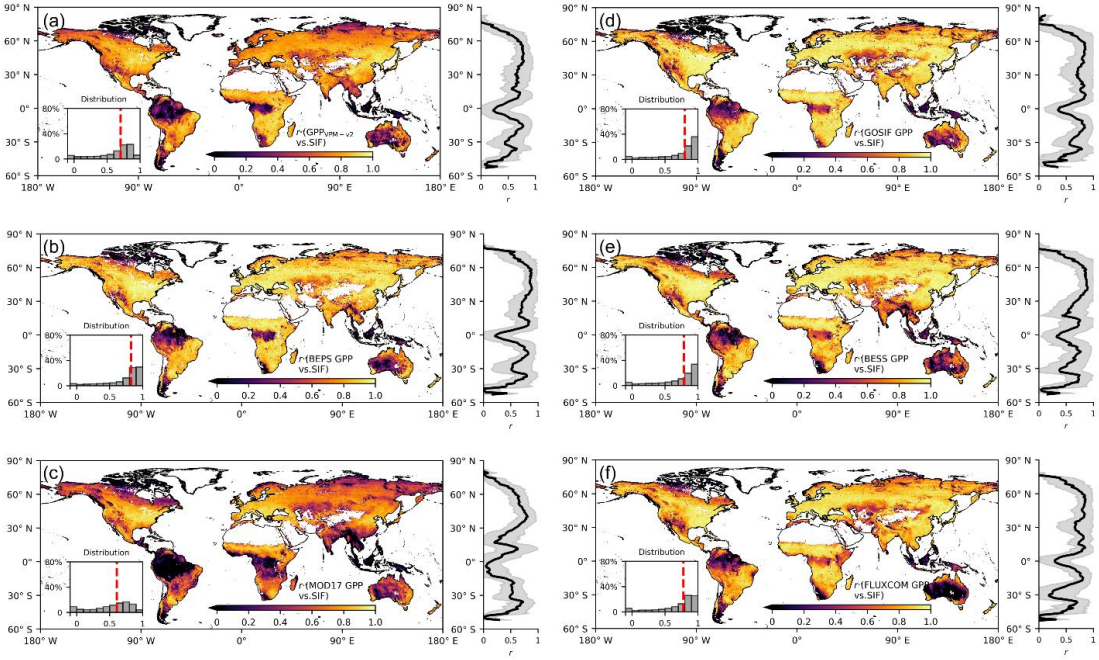

Figure 4.19: Temporal consistency between SIF and other GPP products at the pixel-to-pixel level. In this figure, $GPP_{VPM\text{-}v2}$ refers to the estimation of VPM v2.0 from the version of Zhang, et 2017. BEPS, MOD17, GOSIF, BESS, and FLUXCOM GPP refer to the other GPP products. All GPP products selected data available from May 1, 2018, to December 31, 2021, and were aggregated to 0.5 degrees and 8-day.

The cumulative frequency of the Pearson correlation coefficient among these global GPP products shows that MOD17 has the lowest correlation with SIF, while BEPS, BESS, GOSIF, and $GPP_{VPM\text{-}v3}$ have a relatively high correlation with SIF (Figure 4.20).

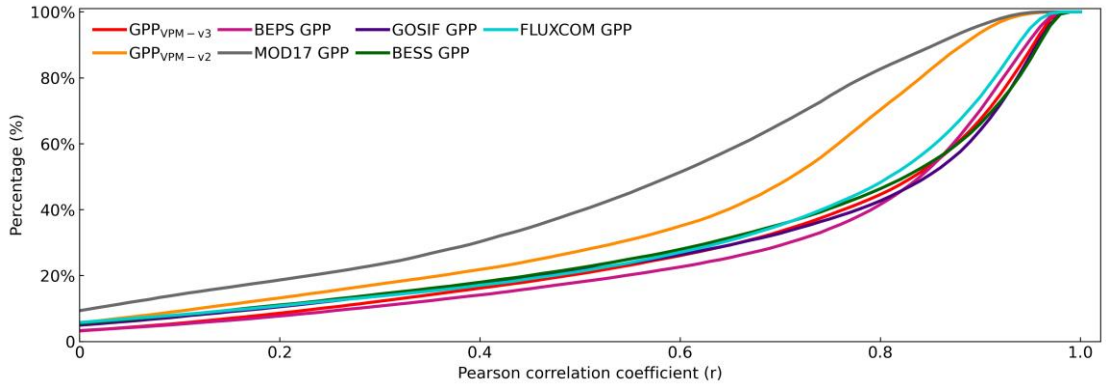

Figure 4.20: Cumulative frequency of the Pearson correlation coefficient for the comparison among the global GPP products.

4.4 Discussions

4.4.1 Improved GPP estimation from VPM v3.0

VPM v2.0 and various ecosystem models use a biome-specific $T_{opt\text{-}biome}$ parameter to represent the influence of air temperature on GPP (Running et al., 2000; Yan et al., 2015; Yuan et al., 2007; Yao Zhang et al., 2017). However, biome-specific $T_{opt\text{-}biome}$ does not account for vegetation physiological adaptation and acclimatization under different geographic locations and climatic conditions (Figure 4.21) (Melillo et al., 1993; Niu et al., 2012; Raich et al., 1991; Wang et al., 2023).

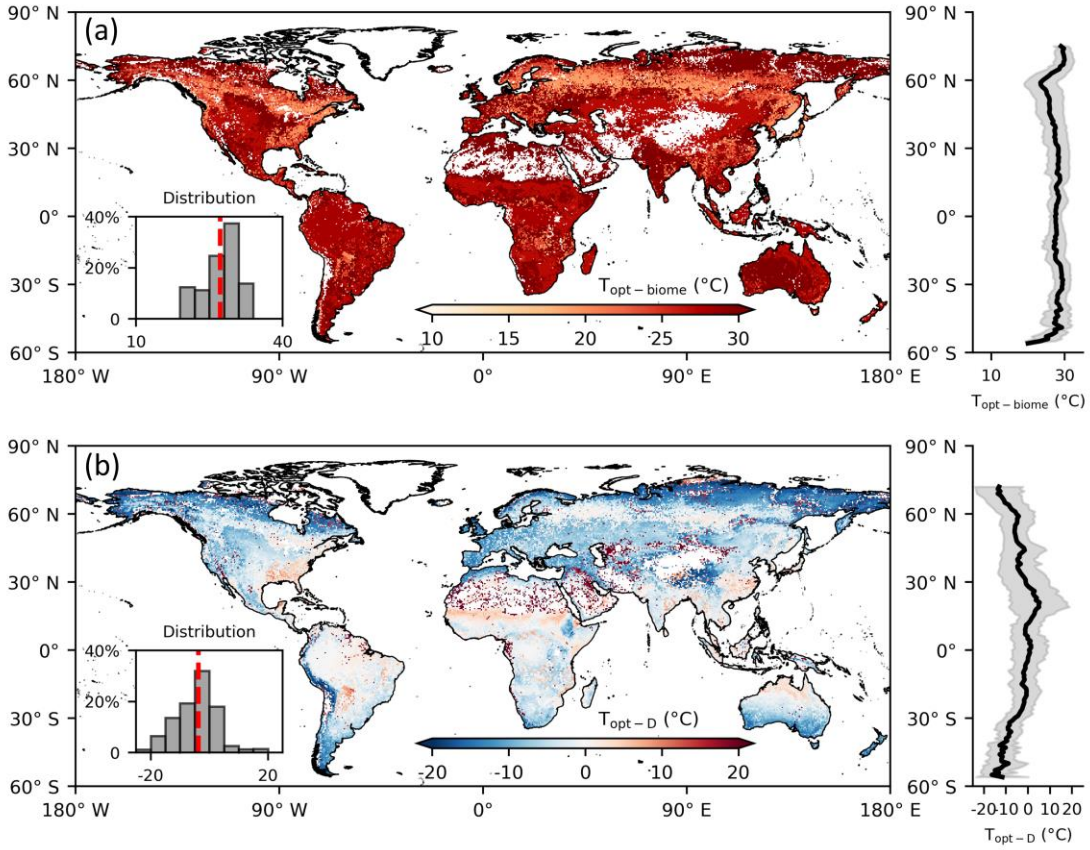

Figure 4.21: Spatial distributions of biome-specific ($T_{opt-biome}$) and site-specific ($T_{opt-site}$) apparent optimal air temperature for photosynthesis. (a) Global map of $T_{opt-biome}$ used in VPM v2.0, derived from MCD12Q1 and look-up table (Melillo et al., 1993; Raich et al., 1991; Yao Zhang et al., 2017). (b) The difference between $T_{opt-site}$ and $T_{opt-biome}$ ($T_{opt-D} = T_{opt-site} - T_{opt-biome}$). The red dashed line in histogram is the global average value. The black solid line is the average value of all pixels within 1-degree across the latitude.

One study in 11 grassland sites reported significant variations in T_{opt} among these sites, highlighting substantial uncertainties when the biome-specific $T_{opt-biome}$ parameter was used for estimating GPP at these sites (Chang et al., 2020). The global map of site-specific $T_{opt-site}$ shows that $T_{opt-site}$ varies substantially within a biome, and furthermore,

$T_{opt\text{-}biome}$ does not match the mean or median values of the $T_{opt\text{-}site}$ over all the pixels within a biome (Figure 4.22). Recent studies assessed the performance of site-specific $T_{opt\text{-}site}$ for GPP estimation at multiple sites across diverse land cover types and have demonstrated that replacing biome-specific $T_{opt\text{-}biome}$ with site-specific $T_{opt\text{-}site}$ in the VPM model substantially improves the accuracy of GPP estimates (Chang et al., 2021a; Pan, Xiao, Pan, et al., 2024). Our results further confirm that, on a global scale, using Topt-site as an input can significantly enhance model accuracy. This improvement is crucial before conducting global GPP estimates. VPM v3.0 also introduces new equations to estimate W_{scalar} and $FPAR_{chl}$, and the results indicate these improvements are necessary, as they show better consistency with GPP_{EC} measurements from flux towers than VPM v2.0.

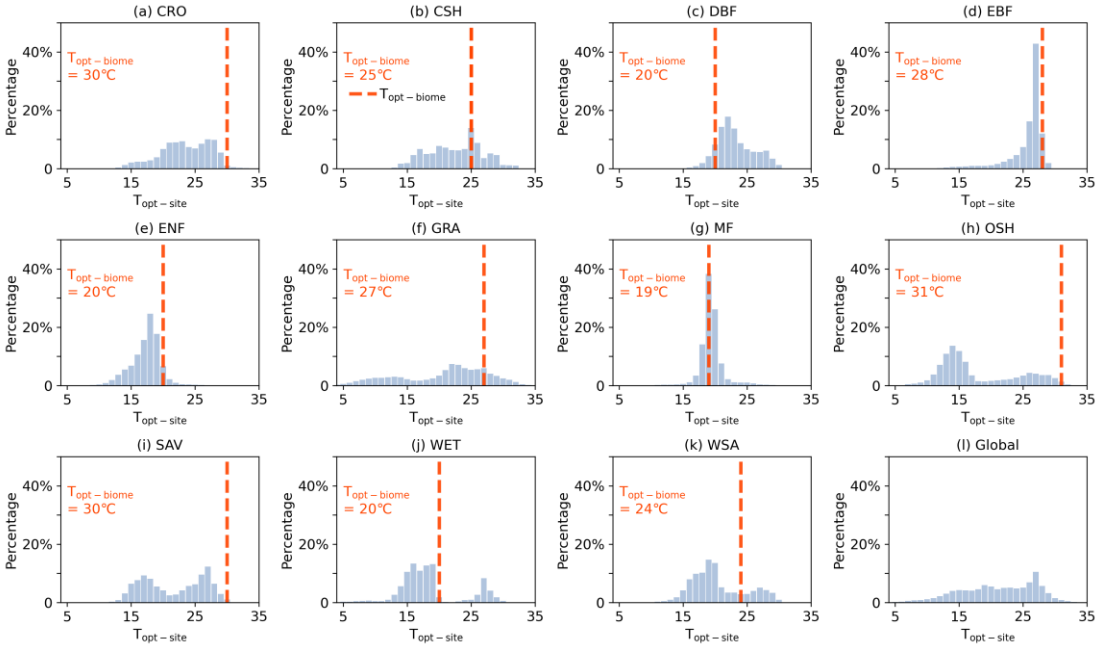

Figure 4.22: Histogram of site-specific apparent optimal air temperature for photosynthesis ($T_{opt\text{-}site}$) and its comparison with $T_{opt\text{-}biome}$. This histogram is obtained based on the $T_{opt\text{-}site}$ of specific biomes across the globe. The classification

of biomes is from MODIS Land Cover Type (MCD12Q1).

The improvements in the above-mentioned model variables and parameters ($T_{opt\text{-}site}$, W_{scalar}, and $FPAR_{chl}$) in VPM v3.0 are pivotal for enhancing the model's accuracy in estimating GPP. The comparison between GPP_{VPM} from VPM v3.0 and GPP_{EC} from 205 eddy covariance tower sites encompassing 1,658 site-years achieves a slope of 0.97, an R^2 of 0.78, and an RMSE of 1.46 gC m^{-2} day^{-1} with GPP_{EC}, which is reasonable and commendable. Previous model studies on GPP estimates over the eddy flux tower sites typically reported R^2 ranging from 0.6 to 0.8 between GPP_{model} and GPP_{EC} (Leng et al., 2023; B. Li et al., 2023; Li et al., 2019; Yao Zhang et al., 2017). In addition, the relationship between GPP_{VPM} from VPM v2.0 and GPP_{EC} at these tower sites had a slope of 0.91, an R^2 of 0.67, and an RMSE of 1.71 gC m^{-2} day^{-1}. VPM v3.0 exhibited higher performance at over 80% of the sites than VPM v2.0. These results highlight the substantial advancements, and the critical necessity of the improvements implemented in VPM v3.0. VPM v3.0 is now a more robust and reliable model for global GPP estimation and paves the way for developing new, long-term global GPP products.

4.4.2 Evaluation between TROPOMI SIF data and model estimation at global scale

Previous studies have compared SIF and APAR, as both serve as crucial energy indicators in the photosynthetic process. At individuals' site, ground-observed APAR and SIF exhibit a significant positive correlation and consistent seasonal dynamics (Yang et al., 2018; Yang et al., 2015). Furthermore, some studies have identified that

APAR is the predominant factor influencing the relationship between GPP and SIF (Miao et al., 2018; Yang et al., 2015). Satellite-derived SIF has demonstrated strong linear temporal correlations with ground-based SIF observations (Yang et al., 2015). Consequently, SIF is used to evaluate its large-scale association with APAR. For instance, one study showed consistent seasonal dynamics and spatial variations between SIF and APAR across North America (Yao Zhang et al., 2016). This study shows that satellite-derived SIF closely aligns with the $APAR_{chl}$ estimates from VPM v3.0 on a global scale. This high correlation highlights the robust performance of VPM v3.0 in estimating $APAR_{chl}$, effectively capturing the seasonal variability of photosynthetic activity across various ecosystems worldwide. Recent studies indicate that the relationship between SIF and APAR is stronger than that between SIF and GPP at the site scale (Miao et al., 2018; Yang et al., 2018). This insight is crucial for global estimates of GPP and emphasizes the importance of accurately estimating APAR within the VPM v3.0 framework.

Many publications have consistently demonstrated a strong correlation between SIF and GPP (Li et al., 2019; Yang et al., 2018; Yang et al., 2015; Yongguang Zhang et al., 2016; Yao Zhang et al., 2016). Our results corroborate these observations, showing a high correlation between SIF and GPP on the global scale. The correlation coefficients of SIF vs. $APAR_{chl}$ and SIF vs. GPP varied noticeably across regions, ranging from weak in arid and tropical regions to strong in temperate regions. Tropical forest areas in the Amazon and Congo basins exhibit relatively low correlations. In these moist and dense forest areas, frequent cloud cover substantially affects satellite-based SIF and

surface reflectance data quality. High cloud optical thickness, water vapor content, and dense aerosol properties lead to a scarcity of good-quality satellite observations, negatively affecting the estimation and evaluation of data-driven models (Martin et al., 2010).

The correlation coefficients of SIF vs. $APAR_{chl}$ and SIF vs. GPP are also relatively low over high-latitude regions with evergreen boreal forests. Conversely, in temperate regions where both vegetation canopy and climate have strong seasonal dynamics, the correlation coefficients of SIF vs. $APAR_{chl}$ and SIF vs. GPP are very high. These findings emphasize the need to account for regional variations when using TROPOMI SIF as a proxy for estimating GPP, as environmental factors and satellite data quality could affect the correlation between TROPOMI SIF and GPP. These findings also call for more in-situ SIF measurements over evergreen broadleaf forests in the tropical zone and evergreen needleleaf forests in the boreal zone.

4.4.3 Consistency and discrepancy among the major global GPP data products

The comparison of GPP data products between VPM v3.0 and major global GPP models, including machine learning, LUE, and process-based models, demonstrates consistent global seasonal dynamics (R^2 from 0.8 to 0.9). Note all models we selected are RS-based GPP models. This consistency in seasonal dynamics arises from the coherence of seasonality in variables derived from satellite, including meteorological parameters, vegetation indices, and other environmental variables, as well as the strong emergent constraints among these variables (Chen et al., 2024; Doughty et al., 2021; Zhao et al., 2021).

Despite the high consistency in seasonal dynamics within different models, there are significant discrepancies in the annual global total GPP (Figure 4.23). The global annual total GPP from these major global GPP products ranges from 105 Pg C $year^{-1}$ to 142 Pg C $year^{-1}$. FLUXCOM GPP product, based on machine learning model, estimates a relatively low global annual total GPP of 118 Pg C $year^{-1}$. MOD17 model also significantly underestimates global GPP, with the total annual global GPP being 105 Pg C $year^{-1}$. These underestimations arise result from uncertainties in model structure, parameter settings, and data inputs. For example, FLUXCOM does not differentiate between C3 and C4 vegetation types, potentially leading to an underestimation of C4 vegetation (Tramontana et al., 2016). MOD17 model is widely recognized for underestimating the maximum light use efficiency (Turner et al., 2006), FPAR product (Turner et al., 2003), and atmospheric forcing data (Ryu et al., 2019; Turner et al., 2006; Turner et al., 2003; Xin et al., 2017). In contrast, the global annual total GPP estimate of VPM v3.0 is 141 Pg C $year^{-1}$, which is highly consistent with BEPS (142 Pg C $year^{-1}$), BESS (137 Pg C $year^{-1}$), and GOSIF (141 Pg C $year^{-1}$). Historically, the trajectory of LUE model development has focused on reconciling the magnitude of APAR and light use efficiency parameter estimates (Ryu et al., 2019). The high consistency between VPM v3.0 and process-based GPP models reflects relatively reasonable estimates of these two key parameters in VPM v3.0.

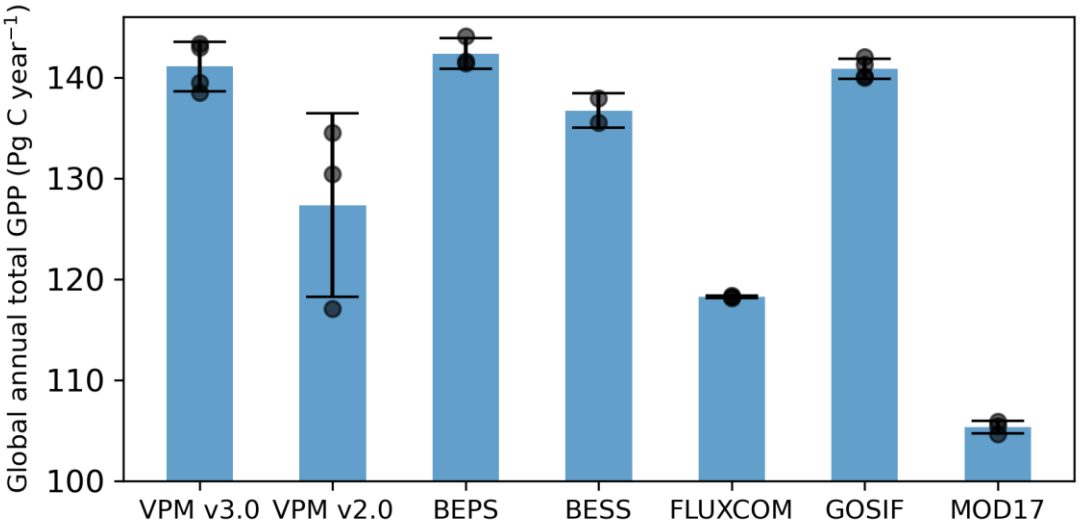

Figure 4.23: Global annual total GPP estimates from major global GPP products. Error bars indicate the standard deviation from 2018 to 2021, and black dots represent the values for each year.

The interannual variability among different GPP products also shows significant differences. For example, FLUXCOM exhibits almost no interannual variability, with a multi-year standard deviation of 0.11 Pg C year^{-1} over two decades. This is likely attributed to the limited distribution of eddy flux towers worldwide, particularly their scarcity in tropical regions (Fu et al., 2018; Jung et al., 2020). Given that tropical regions are the largest contributors to global GPP, FLUXCOM's heavy reliance on extensive interpolation fails to accurately capture the long-term dynamics (Jung et al., 2019; Jung et al., 2020). VPM v3.0 replaced NCEP with ERA5-Land from VPM v2.0 because we found significant uncertainties in the radiation data from NCEP in 2019, which resulted in an underestimation of annual GPP by more than 10%. The update to meteorological data resolved this issue, and the interannual variability of VPM v3.0 is

2.34 Pg C, slightly higher than BEPS (1.5 Pg C $year^{-1}$), BESS (1.7 Pg C $year^{-1}$), and GOSIF (0.72 Pg C $year^{-1}$).

The comparison of six global GPP datasets over the period of 2018-2021 from machine learning models, data-driven models, and process-based models shows that the global GPP estimates provided by VPM v3.0 fall within a reasonable and acceptable range of GPP estimates across major GPP models. These findings demonstrate that VPM v3.0 has reasonable robustness and capability to integrate MODIS data and ERA5-Land climate data effectively and can be used to generate a global GPP product over many years.

4.4.4 Future work of LUE models

Many LUE models do not include the CO_2 fertilization effect on LUE, these LUE models are not able to accurately capture interannual variations and changes in carbon flux when compared with ground GPP measurement (Anav et al., 2015; B. Li et al., 2023; Schaefer et al., 2012). To date, widely used RS-based GPP models do not incorporate the impact of the CO_2 fertilization effect on GPP estimations, potentially resulting in underestimations of interannual variations and changes (trends) in global GPP. A recent study that included atmospheric CO_2 concentration in the MODIS GPP model found that interannual variability doubled relative to the original (Keenan et al., 2023). The impact of atmospheric CO_2 concentration on model simulations may need further consideration in future model development.

LUE models primarily use vegetation indices as inputs, which are highly sensitive to the quality of surface reflectance products. An improved method could involve using

SIF to estimate $APAR_{chl}$, as SIF is less affected by sun-sensor geometry and cloud cover than surface reflectance and vegetation indices (Doughty et al., 2019; Du et al., 2022). Unlike vegetation indices, SIF also does not saturate (Köhler, Guanter, et al., 2018), making it a promising tool for refining $APAR_{chl}$ estimates in the future. Additionally, canopy saturation with radiation has been widely observed in tropical regions (Doughty et al., 2021); LUE models estimating light absorption and GPP at daily temporal resolution typically omit this saturation effect as they assume a linear relationship between radiation and $APAR_{chl}$ at daily temporal resolution. Since SIF does not saturate under high radiation, future VPM models could integrate SIF or introduce non-linear models to estimate these effects at hourly temporal resolution (Hu et al., 2020; Mahadevan et al., 2008).

4.5 Conclusion

In this chapter, we developed an improved version of VPM v3.0, which incorporates three key enhancements over VPM v2.0, and conducted global simulations using Terra/MODIS imagery and the ERA5-Land. We evaluated the performance of GPP estimates from VPM v3.0 using ground GPP measurements (GPP_{EC}) from 205 eddy flux tower sites, which collectively represent 1,658 site-years across 11 land cover types. Additionally, the relationships among SIF, $APAR_{chl}$, and GPP were analyzed globally from 2018 to 2021. The results showed that GPP from VPM v3.0 exhibited high consistency with GPP_{EC} and TROPOMI SIF at site and global scales, respectively. VPM v3.0 significantly improved the accuracy of GPP estimates at the majority of eddy flux tower sites compared to its predecessor, VPM v2.0. Furthermore, VPM v3.0

strongly agreed with major global GPP products, such as BEPS, BESS, and GOSIF. Our results suggest that VPM v3.0 could serve as a new, reliable, and accurate tool for global GPP estimation, supporting the production of long-term global GPP datasets and advancing studies on the carbon cycle and climate change.

Chapter 5 : Incorporating CO_2 into VPM to improve global gross primary production estimates

ABSTRACT

Terrestrial gross primary production (GPP) is a major flux in the carbon cycle, and estimates of global annual GPP vary substantially, ranging from 120 Pg C yr^{-1} (Beer et al., 2010) to 157 ± 8.5 Pg C yr^{-1} (Lai et al., 2024). Here we use Vegetation Photosynthesis Model (VPM v4.0), satellite images, ERA5-Land climate, and atmospheric CO_2 concentration data to estimate global GPP during 2000-2023. VPM v4.0 considers (1) light absorption by chlorophyll and leaf traits (broad leaf vs. needle leaf) and (2) CO_2 fixation by plant function types (C_3 and C_4) and site-specific effects of air temperature, water and atmospheric CO_2 concentration. At the site scale, VPM v4.0 accurately tracks annual GPP, interannual variability (IAV) and trends as observed by eddy covariance towers over 777 site-years. At the global scale, global annual GPP from VPM v4.0 varies from 145 Pg C yr^{-1} in 2000 to 166 Pg C yr^{-1} in 2023, with a mean of 155 ± 6 Pg C yr^{-1}, which falls within the range of annual GPP from carbonyl sulfide (OCS)-based method (157 Pg C yr^{-1}, 2000-2010) (Lai et al., 2024), respiration-based method (149 Pg C yr^{-1}) (Jian et al., 2022), and ^{18}O-based method (150–175 Pg C yr^{-1}) (Lisa R. Welp et al., 2011b). Annul GPP from VPM v4.0 increased substantially during 2000-2023, with a trend of 0.78 Pg C yr^{-2}, higher than that from most models. The direct CO_2 effect is high in tropical and subtropical forests and contributes substantially to continued increase of global GPP during 2000-2023. Our findings show that as a

diagnostic model, VPM v4.0 has improved global GPP estimation and offers useful GPP data products for benchmark of other terrestrial biosphere models.

5.1 Introduction

Terrestrial gross primary production (GPP) is the largest carbon flux in the global carbon cycle (Anav et al., 2015; Beer et al., 2010; Ryu et al., 2019). Accurately quantifying GPP is essential for us to understand how terrestrial ecosystems respond to and regulate the effects of climate change and atmospheric CO_2 concentration and to formulate carbon emission reduction and ecological protection policies (Ciais et al., 2014; Gampe et al., 2021). Many prognostic and diagnostic terrestrial biosphere models (TBM) have been developed and applied to estimate global GPP over the years. In addition to different input datasets used in simulations, these models vary in terms of model (processes, variables, algorithms, and parameters), ranging from complex and prognostic Earth system models incorporating detailed physiological processes (e.g., dynamic global vegetation models; DGVMs) to simple, diagnostic, data-driven models that combine remote sensing data and statistical methods (Guanter et al., 2014; Jung et al., 2019; Leng et al., 2023; B. Li et al., 2023; Monteith, 1972; Sitch et al., 2003). For several decades, the estimates of global annual GPP were ~120 Pg C yr^{-1} (Beer et al., 2010), which has been widely used in the study of the global carbon cycle and budget. Recent studies reported that global annual GPP could be as high as ~157±8.5 Pg C yr^{-1} by carbonyl sulfide (OCS) flux method (Lai et al., 2024), ~149 Pg C yr^{-1} by soil respiration method (Jian et al., 2022), and 150–175 Pg C yr^{-1} by ^{18}O method (Lisa R. Welp et al., 2011b). The large discrepancies among these estimates call for the further

development of TBMs.

Plant photosynthesis has light absorption process and CO_2 fixation (Calvin cycle) process, which are represented differently in TBMs (Farquhar et al., 1980; Sellers, 1985). Among the data-driven TBMs, one group of models explicitly calculate light absorption and use light use efficiency (LUE) to approximate the complex CO_2 fixation process (Monteith, 1972). The basic assumption of the LUE models is that photosynthesis is directly related to absorbed photosynthetically active radiation (APAR) and light use efficiency (ϵ_g):

$$\mathrm{GPP} = \mathrm{APAR} \times \epsilon_g \tag{5.1}$$

ϵ_g is a parameter related to the maximum light use efficiency (ϵ_{max}), which represents the theoretical maximum light use efficiency that vegetation can attain under stress-free or optimal growth conditions (Monteith, 1972, 1977). Multiple environmental factors, such as air temperature, water availability (e.g., vapor pressure deficit, soil moisture, leaf water content), and atmospheric CO_2 concentration, are used to constrain ϵ_{max}, thus obtaining the actual light use efficiency (ϵ_g) under prevailing conditions:

$$\epsilon_g = \epsilon_{max} \times \mathrm{f(Environmental\ factors)} \tag{5.2}$$

It is important to note that most LUE models do not explicitly account for the effect of atmospheric CO_2 concentration (c_a) on ϵ_{max}. According to the classic FvCB biochemical model of photosynthesis, which uses maximum rate of RuBisCo carboxylase activity (Vc_{max}) parameter, increasing c_a enhances the CO_2 supply within leaves (c_i) and increases the relative contribution of Rubisco carboxylation compared to photorespiration, thereby directly improving photosynthetic efficiency (Ainsworth et

al., 2007; Chen et al., 2022; Farquhar et al., 1980). This "direct CO_2 effect" is theoretically critical (Keenan et al., 2023) and it is independent of the "indirect effect," whereby increasing atmospheric CO_2 concentration led to greater leaf area or vegetative cover, allowing plants to intercept more photosynthetically active radiation (PAR) (Donohue et al., 2013; Keenan et al., 2013). Because most LUE models use leaf area index (LAI) or vegetation indices derived from satellite data to estimate light absorption, they can partially capture the indirect CO_2 effect but lack an explicit representation of its direct physiological enhancement.

Due to the absence of an explicit representation of the direct CO_2 effect, current LUE models may systematically underestimate the global magnitude of photosynthesis (Anav et al., 2015; De Kauwe et al., 2016). Global annual GPP estimates from these LUE models are in the range of 120–140 Pg C yr^{-1} (Beer et al., 2010; Li et al., 2019; Running et al., 2004; Yao Zhang et al., 2017). Underestimation of GPP is particularly severe in high-productivity regions such as tropical rainforests (Lai et al., 2024; Zhang-Zheng et al., 2024). Since the CO_2 effect often interacts with temperature and radiation conditions (Chen et al., 2022; Keenan et al., 2023), failing to incorporate it into LUE models explicitly may be closely linked to this pronounced underestimation of GPP.

In addition to the magnitudes of global annual GPP estimates from these models, a large range and considerable uncertainty also persists in interannual variability (IAV) and trends of global annual GPP estimates from the LUE models (Anav et al., 2015; Ryu et al., 2019). A review of multiple satellite-based GPP products indicates that CO_2-exclusive LUE models (e.g., MTE and MODIS) show weaker interannual

variability and trends than most process-based models (Anav et al., 2015). Recent work suggests that rising atmospheric CO_2 concentration explains approximately 44% of the global GPP increase (Chen et al., 2022), with about 13.5% contributed by direct CO_2 effects (Keenan et al., 2023). This implies that at least one-third of the GPP increase is underestimated by current LUE models (Chen et al., 2022). Moreover, different GPP products vary substantially in their sensitivities of IAV to atmospheric CO_2 concentration increase (Sun et al., 2019; Walker et al., 2021), yet overall, these sensitivities remain underestimated (Anav et al., 2015; Keenan et al., 2023; Kolby Smith et al., 2016). Current improvements to LUE models have primarily focused on refining model parameters and environmental constraints (L. Pan et al., 2025; Pan, Xiao, Pan, et al., 2024), with few studies systematically incorporating CO_2 as an independent factor (Prentice et al., 2024, Nature Reviews Earth & Environment).

In this study, we use the new version of Vegetation Photosynthesis Model (VPM v4.0), which is built upon a previous version (VPM v3.0) (Meng et al., 2025; L. Pan et al., 2025; Pan, Xiao, Pan, et al., 2024) and explicitly incorporate the direct CO_2 effect based on the FvCB biochemical photosynthetic CO_2 assimilation theory (Farquhar et al., 1980). The VPM v4.0 explicitly considers (1) light absorption by chlorophyll and leaf traits (broad leaf or flat leaf vs needle leaf) and (2) carbon fixation by plant functional types (C_3 and C_4 plants) and the effects of air temperature, water, and atmospheric CO_2 concentration (see Materials and Methods). Through simulations of VPM v4.0 and VPM v3.0, driven by atmospheric CO_2 concentration, ERA5-Land climate data, and satellite images, we have three specific objectives in this study. First,

we assessed the direct effect of atmospheric CO_2 concentration on GPP at the scale of eddy covariance tower sites by evaluating annual GPP and its IAV and trends from VPM v4.0, VPM v3.0 and eddy covariance observations. Second, we calculated global annual GPP during 2000-2023 from VPM v4.0 and VPM v3.0 and assessed the direct effect of atmospheric CO_2 concentration on GPP at the global scale. Third, we compared the global annual GPP, IAV and trend as well as their sensitivity to CO_2 (β_R^{GPP}) between VPM v4.0, VPM v3.0 and other models. This study will report new global annual GPP dynamics during 2000-2023 after incorporating the direct CO_2 effect into LUE models, and the findings could help lay a foundation for improving global GPP estimates, which can be used to evaluate terrestrial carbon sink potential under climate change scenarios

5.2 Materials and Methods

5.2.1 MOD09A1 v6.1 surface reflectance dataset

MOD09A1 v6.1 is a composite product derived from NASA's Terra MODIS sensor, providing surface reflectance data for seven bands at a 500-meter spatial resolution and an 8-day temporal resolution after correcting for atmospheric effects such as gases, aerosols, and Rayleigh scattering (Vermote, 2021). We did preprocess of surface reflectance by removing observations flagged by quality assurance (QA) as contaminated by clouds, snow, or cloud shadows (Frey et al., 2008), applying a blue-band threshold of 0.2 to filter out residual noise caused by atmospheric scattering (Jensen, 2009). In addition, we did temporal consistency check by using a moving

window (t−1, t, t+1) to eliminate abrupt reflectance changes inconsistent with normal vegetation dynamics (Pan, Xiao, Pan, et al., 2024). Specifically, if the absolute slope between the middle and adjacent time steps exceeded 0.15, we deemed the observation anomalous and removed it. The Enhanced Vegetation Index (EVI) and the Land Surface Water Index (LSWI) were then calculated as inputs to the VPM model, defined respectively as:

$$EVI = 2.5 \times \frac{\rho_{nir} - \rho_{red}}{\rho_{nir} + (6 \times \rho_{red} - 7.5 \times \rho_{blue}) + 1} \quad (5.3)$$

$$LSWI = \frac{\rho_{nir} - \rho_{swir}}{\rho_{nir} + \rho_{swir}} \quad (5.4)$$

Where ρ_{nir} , ρ_{red}, ρ_{blue}, and ρ_{swir} are the surface reflectance bands of near infrared, red, blue, and shortwave infrared, respectively. Here, we applied the reference curves and linear interpolation to fill gaps in the vegetation index time series (L. Pan et al., 2025; Yao Zhang et al., 2017).

5.2.2 MCD12Q1 v6.1 land cover type dataset

MCD12Q1 v6.1 provides 500-meter global land cover classification layers starting from 2001, generated by machine learning algorithms and time-series smoothing techniques (Sulla-Menashe et al., 2018). In this study, we employed the land cover types identified by the International Geosphere-Biosphere Programme (IGBP) and focused on the following 11 categories: Croplands (CRO), Closed Shrublands (CSH), Deciduous Broadleaf Forests (DBF), Evergreen Broadleaf Forests (EBF), Evergreen Needleleaf Forests (ENF), Grasslands (GRA), Mixed Forests (MF), Open Shrublands (OSH), Savannas (SAV), Permanent Wetlands (WET), and Woody Savannas (WSA).

5.2.3 ERA5-Land reanalysis climate dataset

The ERA5-Land reanalysis climate dataset, developed by the European Centre for Medium-Range Weather Forecasts (ECMWF), is specifically designed for land surface variables (Muñoz-Sabater et al., 2021; Muñoz Sabater, 2019). It has a 0.1-degree spatial resolution and an hourly temporal resolution, allowing for a more refined representation of local climate conditions and their short-term fluctuations than ERA5. A previous study comparing ground-based climate measurements at 205 global flux towers with ERA5-Land data showed strong agreement (L. Pan et al., 2025). In this study, we selected air temperature (T) and shortwave radiation (SW) from ERA5-Land as model inputs, with SW converted to PAR (W m^{-2}) as follows:

$$PAR = SW \times r_{SW\_PAR} \times \alpha \quad (5.5)$$

where $r_{SW\_PAR} = 0.45$ is the ratio of SW to PAR (Ma et al., 2014; Meek et al., 1984; L. Pan et al., 2025; Pan, Xiao, Pan, et al., 2024), and $\alpha = 4.56$ μmol J^{-1} is the energy-quanta conversion factor (Dye, 2004; L. Pan et al., 2025; Pan, Xiao, Pan, et al., 2024).

In addition, we calculated the vapor pressure deficit (VPD) from air temperature (T) and dew point temperature (T_d) using:

$$VPD=0.6108 \times \exp\left(\frac{17.27 \times T}{T + 237.3}\right) - 0.6108 \times \exp\left(\frac{17.27 \times T_d}{T_d + 237.3}\right) \quad (5.6)$$

5.2.4 Atmospheric CO_2 concentration

The annual atmospheric CO_2 concentration (c_a) data is sourced from the National Oceanic and Atmospheric Administration (NOAA). Based on globally averaged marine surface measurements from multiple monitoring stations, this dataset captures long-

term variations in atmospheric CO2 levels. We obtained annual atmospheric CO2 concentration spanning from 2000 to 2023 from https://doi.org/10.15138/9N0H-ZH07 (Lan, 2025).

5.2.5 Global multi-resolution terrain elevation dataset

The Global Multi-resolution Terrain Elevation Data 2010 (GMTED2010) dataset provides globally distributed elevation data at approximately 250-meter spatial resolution, compiled from multiple sources (Danielson et al., 2011). The primary data source for GMTED2010 is the National Geospatial-Intelligence Agency's (NGA) SRTM Digital Terrain Elevation Data. To extend coverage beyond SRTM's geographic limits and to fill remaining gaps in the SRTM data, additional sources were incorporated, including non-SRTM DTED®, Canadian Digital Elevation Data (CDED) at two resolutions, Satellite Pour l'Observation de la Terre (SPOT 5) Reference3D, the National Elevation Dataset (NED) for the continental United States and Alaska, the GEODATA 9-second digital elevation model (DEM) for Australia, as well as satellite radar and laser altimeter DEMs for Antarctica and Greenland.

5.2.6 In-situ climate and carbon flux data from the eddy flux tower sites

We used in-situ GPP data from eddy covariance (EC) towers to compare predicted GPP with VPM estimations. These site data were obtained from AmeriFlux and the FLUXNET portals. To evaluate long-term GPP IAV, we selected sites with at least 10 years of observations (site-year ≥ 10) and high data quality (i.e., >90% high-quality observations). Given the spatial distribution of the CO_2 fertilization effect, we further

restricted sites to latitudes between 60°N and 60°S. We also compared the IGBP ecosystem classifications provided by FLUXNET or AmeriFlux with those from the MODIS land cover data product, excluding any sites with mismatched classifications. After screening, 59 sites were retained, spanning 11 biome types and totaling 777 site-years. Detailed IGBP ecosystem classifications and data availability for these sites are provided in Figure 5.1.

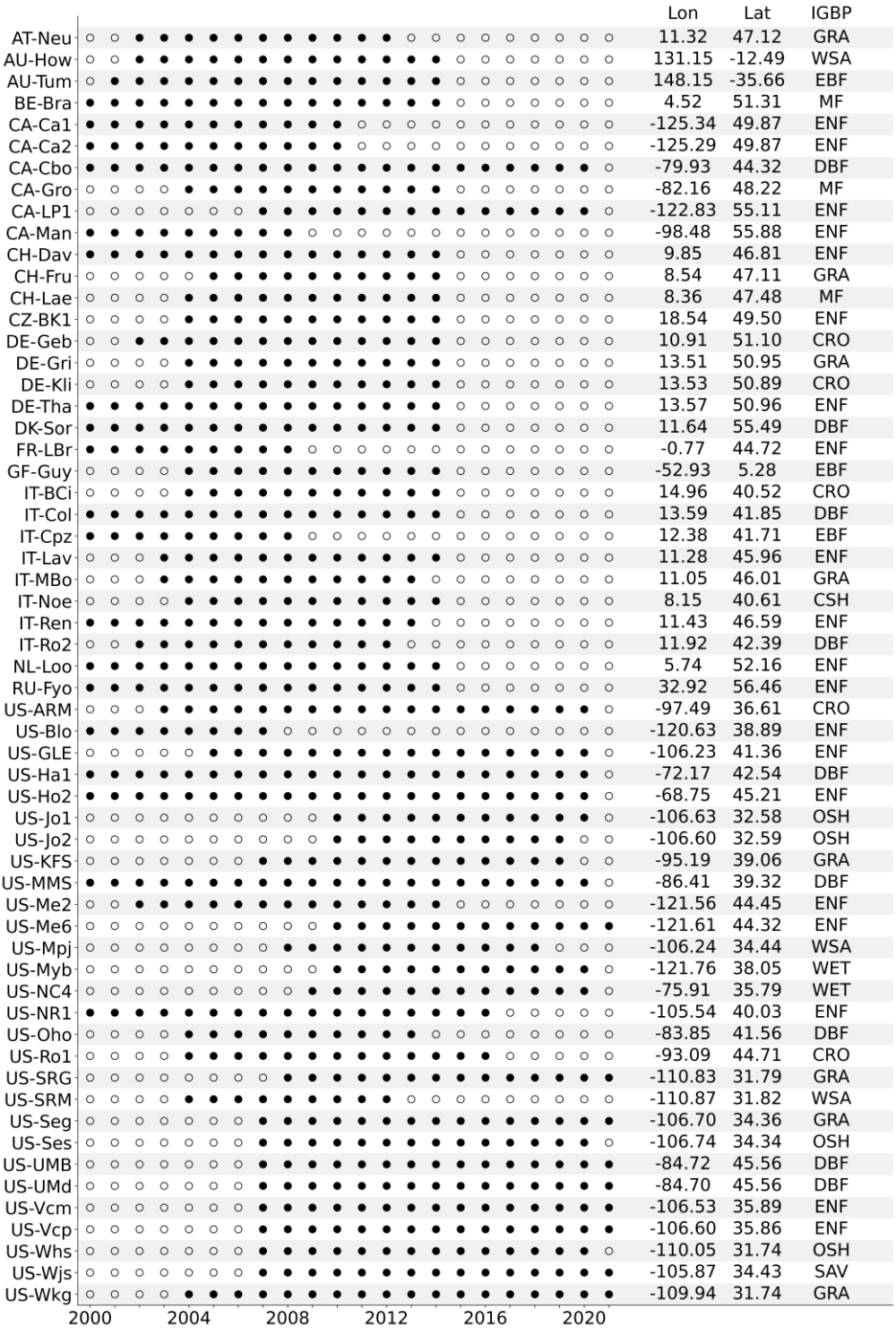

Figure 5.1: Basic information of all sites used in this study. Data availability spans from 2000 to 2021, with white and black dots indicating years without and with

available data, respectively. A total of 59 sites (777 site-years) were included, distributed across biomes as follows: 5 CRO sites (66 site-years), 1 CSH site (11 site-years), 9 DBF sites (142 site-years), 3 EBF sites (34 site-years), 20 ENF sites (266 site-years), 8 GRA sites (102 site-years), 3 MF sites (36 site-years), 4 OSH sites (49 site-years), 1 SAV site (15 site-years), 2 WET sites (22 site-years), and 3 WSA sites (33 site-years).

5.2.7 GPP dataset from other models

We selected and compared multiple global GPP estimates derived from various models. These models are grouped by their methods. First, newly proposed methods based on OCS offer relatively higher confidence intervals (Lai et al., 2024), complemented by oxygen isotope (^{18}O) techniques (Lisa R. Welp et al., 2011b) and soil respiration-based estimates (Jian et al., 2022)—each independently tracking ecosystem or isotopic signals to derive GPP values. Second, we included a group of Dynamic Global Vegetation Models (DGVMs), including 13 DGVMs from the latest Trendy-GCB2024 (v13) dataset, which encompass CO_2-inclusive scenario (S2) as well as CO_2-exclusive scenario (S2 − S1 + S0) (Sitch et al., 2015). Third, we selected the PR, BESS, and BEPS models, which simulate ecophysiological processes to estimate GPP (Keenan et al., 2016; Leng et al., 2023; B. Li et al., 2023). Fourth, we selected data-driven remote sensing empirical models (e.g., SIF, NIRv), which rely on statistical relationships between satellite-derived vegetation indices and ground observations to infer global GPP (Badgley et al., 2019; Li et al., 2019). Fifth, we selected a set of simulation results (including results from six models) from the machine learning-based upscaling

FLUXCOM (RS+METEO), which combines flux tower observations and CRUNCEP climate data for GPP estimation (Jung et al., 2019; Tramontana et al., 2016). Sixth, we selected LUE models, including the newly developed VPM v4.0 (w/ CO_2) in this study, alongside VPM v3.0 (w/o CO_2), GLASS, EC-LUE, LRF, and MOD17 (Liang et al., 2021; Tagesson et al., 2021; Zhao et al., 2005; Zheng et al., 2020a). Additional details and corresponding citations can be found in Table 5.1 and Table 5.2

Table 5.1: Basic information and literature of all models used in this study. Including the method used (category), averaged global GPP magnitude (PgC yr^{-1}), and the year the data was available.

Model	Method	Year	Global GPP (PgC yr^{-1})	Citation
VPM v4.0 (w/ CO_2)	**Satellite-based model using ϵ_{max}**	**2000-2023**	**155±6**	**This study**
VPM v3.0 (w/o CO_2)		**2000-2023**	**143±4**	
OCS	estimated by carbonyl sulfide	2000-2010	157±8.5	(Lai et al., 2024)
^{18}O	estimated by oxygen isotopes	1980-2009	150-175	(Lisa R. Welp et al., 2011a)
Soil respiration	estimated by soil respiration	1980-2022	149^{+29}_{-23}	(Jian et al., 2022)
DGVMs ensemble (S2, w/ CO_2)	DGVM model using Vc_{max}	2000-2023	139±16	(Sitch et al., 2015)
DGVMs ensemble (S2-S1+S0, w/o CO_2)	DGVM model using Vc_{max}	2000-2023	113±18	
GOSIF	Statistical models using EC and RS data	2001-2023	138±3	(Li et al., 2019)
NIRv	Statistical models using EC and RS data	2003-2015	147±16	(Badgley et al., 2019)
PR	Satellite-based model using Vc_{max}	1982-2011	133±3	(Keenan et al., 2016)
BESS		1982-2019	125±5	(B. Li et al., 2023)
BEPS		2001-2020	137±3	(Leng et al., 2023)
FLUXCOM ensemble	Statistical models using EC and RS data	2000-2013	124±7	(Jung et al., 2019; Tramontana et al., 2016)
GLASS	Satellite-based model using ϵ_{max}	1981-2022	127±3	(Liang et al., 2021)
EC-LUE		1982-2017	106±3	(Zheng et al., 2020b)
LRF		1982-2015	121±4	(Tagesson et al., 2021)
MOD17		2001-2022	101±3	(Zhao et al., 2005)

Table 5.2: Global GPP estimates for 2001 to 2011 across models. The table is calculated based on publicly available products or from literature. The period

2001 to 2011 was chosen as the overlap between the models to obtain comparable results.

Model	CO_2	Year	Global annual GPP				
			Start year (2001) (PgC yr^{-1})	End year (2011) (PgC yr^{-1})	Mean (PgC yr^{-1})	IAV (PgC yr^{-1})	Trend (PgC yr^{-2})
VPM v4.0	**w/ CO_2**	2001-2011	**147**	**158**	**151**	**1.0931**	**0.8874**
VPM v3.0	**w/o CO_2**		**137**	**145**	**140**	**0.9863**	**0.6358**
DGVMs ensemble (S2, w/ CO_2)	w/ CO_2		135±16	140±16	136±16	0.7852± 0.2409	0.571± 0.1065
DGVMs ensemble (S2-S1+S0, w/o CO_2)	w/o CO_2		113±17	114±18	112±17	0.7288± 0.2839	0.1688± 0.1102
GOSIF	w/o CO_2		132	139	135	0.6164	0.6602
PR	w/ CO_2		136	140	136	0.9635	0.4090
BESS	w/ CO_2		130	132	129	1.2153	0.3583
BEPS	w/ CO_2		134	139	135	0.893	0.4591
FLUXCOM ensemble	w/o CO_2		125±8	125±7	125±8	0.2365± 0.1228	0.061± 0.0204
GLASS	w/o CO_2		132	129	129	0.9345	-0.354
EC-LUE	w/ CO_2		110	108	108	0.9136	-0.2484
LRF	w/o CO_2		124	128	124	1.2751	0.2735
MOD17	w/o CO_2		94	101	98	1.2055	0.4745

5.2.8 Biochemical photosynthetic CO_2 assimilation theory

In C_3 plants, Rubisco limitation and electron transport limitation are the two dominant processes controlling the rate of photosynthesis (Farquhar et al., 1980). However, when external light intensities are low to moderate and CO_2 concentrations are high, the carboxylation capacity of Rubisco is often in relative surplus, making the limitation imposed by electron transport (light reactions) the primary bottleneck (Keenan et al., 2023). Based on this observation, this study employs only the "electron transport-limited" biochemical expression to characterize gross photosynthetic rate, temporarily excluding mitochondrial dark respiration as an optional process. According to the FvCB model, the gross photosynthetic rate (A_{gross}) is defined as:

$$A_{gross} = V_c - 0.5V_o \quad (5.7)$$

Where V_c is the rate of carboxylation and V_o is the rate of oxygenation. This expression

reflects that, in the photosynthetic redox cycle, when the enzyme catalyzes the reaction of RuBP with one mole of O_2, 0.5 mole of CO_2 is released. Here, we define $\Phi = V_o/V_c$, so that Eq. (5.7) can be rewritten as:

$$A_{gross} = V_c(1 - 0.5\Phi) \tag{5.8}$$

When RuBP regeneration is limited by electron transport, the rate of NADPH supply determines the upper limit of carboxylation. In the light reactions, the production of 1 mol NADPH requires 2 mol electrons; if the electron transport rate is denoted by J (mol e^- m^{-2} s^{-1}), then the rate of NADPH production is:

$$\text{NADPH production} = \frac{J}{2} \tag{5.9}$$

According to the FvCB model, the rate of NADPH consumption is related to the production rate of 3-phosphoglycerate (PGA) and the refixation rate of ammonia in the photorespiratory cycle. Based on the formulation provided by Farquhar et al. (1980):

$$\text{NADPH consumption} = (2V_c + 1.5V_o) + 0.5\ V_o \tag{5.10}$$

Substituting $\Phi = V_o/V_c$ into Eq. (5.10) yields:

$$\text{NADPH consumption} = (2 + 2\Phi) \cdot V_c \tag{5.11}$$

By equating NADPH production (Eq. (5.9)) and consumption (Eq. (5.11)):

$$(2 + 2\Phi) \cdot V_c = \frac{J}{2} \tag{5.12}$$

Which can be rearranged to yield:

$$V_c = \frac{J}{4(1 + \Phi)} \tag{5.13}$$

Substituting Eq. (5.13) into Eq. (5.8) yields:

$$A_{gross} = \frac{J}{4(1 + \Phi)}(1 - 0.5\Phi) \tag{5.14}$$
$$= \frac{J}{4}\frac{(1 - 0.5\Phi)}{(1 + \Phi)}$$

Due to oxygenation, the CO_2 fixed by carboxylation is partially offset by the CO_2 released during photorespiration. When considering only photorespiratory losses (excluding dark respiration), if the leaf-internal CO_2 concentration (c_i) falls to a critical value Γ^* (the CO_2 compensation point), such that $c_i = \Gamma^*$, then the CO_2 fixed via carboxylation exactly equals the CO_2 released by photorespiration (i.e., $A_{gross} = 0$). Setting $A_{gross} = 0$ in Eq. (5.14) yields $\Phi = 2$. As Φ decreases from 2—indicating increased CO_2 fixation and reduced photorespiratory CO_2 release—the c_i correspondingly increases from Γ^* to higher levels. This relationship can be expressed as the following fractional mapping:

$$\frac{(1 - 0.5\Phi)}{(1 + \Phi)} = \frac{(c_i - \Gamma^*)}{(c_i + 2\Gamma^*)} \tag{5.15}$$

Substituting this mapping into Eq. (5.14) links the photosynthetic rate directly to c_i:

$$A_{gross} = \frac{J}{4} \frac{(c_i - \Gamma^*)}{(c_i + 2\Gamma^*)} \tag{5.16}$$

Letting $c_i = \chi c_a$, where c_a is the atmospheric CO_2 concentration and χ is the ratio of leaf internal to external CO_2, Eq. (5.16) becomes:

$$A_{gross} = \frac{J}{4} \frac{(\chi c_a - \Gamma^*)}{(\chi c_a + 2\Gamma^*)} \tag{5.17}$$

The CO_2 compensation point Γ^* varies with temperature and can be described by an Arrhenius-type function:

$$\Gamma^*(T) = \Gamma^*_{25} \exp\left[\frac{\Delta H\ (T\text{-}298.15)}{298.15RT}\right] \tag{5.18}$$

Where Γ^*_{25} = 4.22 Pa is the reference CO_2 compensation point at 25 °C. ΔH = 37.83kJ mol^{-1} is the activation energy for Γ^*. T is the temperature in Kelvin. R = 8.314 J mol^{-1} K^{-1} is the molar gas constant. These parameters were obtained from the

literature (Farquhar et al., 1980; Keenan et al., 2023).

In most current terrestrial ecosystem models, χ is described as an empirically derived parameter; however, it is highly sensitive to environmental conditions. Based on the least-cost hypothesis, a theoretical dependence of χ on air temperature (T), VPD, and elevation can be derived, and this dependence can be expressed in a linear form (Wang et al., 2017):

$$\ln\left[\frac{\chi}{1-\chi}\right] = 0.0545\ (\text{T-25}) - 0.5 \ln \text{VPD} - 0.0815\text{z} + \text{C} \tag{5.19}$$

where T and VPD are obtained from the ERA5-Land reanalysis climate dataset, z is the elevation derived from GMTED2010, and C=1.189 (Wang et al., 2017).

The equations derived above establish the relationship between gross photosynthetic rate and CO_2 concentration, thereby providing a framework for calculating gross photosynthesis under different years or scenarios.

5.2.9 Incorporating direct effect of CO_2 on GPP into the VPM Model

VPM (VPM v3.0) is a typical LUE model, and its general formulations are as follows:

$$\text{GPP}_{\text{VPM-v3}} = \text{PAR} \times \text{FPAR}_{\text{chl}} \times \varepsilon_0 \times \text{f(T)} \times \text{f(W)} \tag{5.20}$$

$$\text{FPAR}_{\text{chl}} = \begin{cases} \text{a} + \gamma_{\text{E}} \times \text{b} \times \text{EVI, if needleleaf} \\ \text{a} + \text{b} \times \text{EVI, if broadleaf} \end{cases} \tag{5.21}$$

$$\text{f(T)} = \frac{(\text{T} - \text{T}_{\text{max}}) \times (\text{T} - \text{T}_{\text{min}})}{(\text{T} - \text{T}_{\text{max}}) \times (\text{T} - \text{T}_{\text{min}}) - (\text{T} - \text{T}_{\text{opt}})^2} \tag{5.22}$$

$$\text{f(W)} = \frac{1 + \text{LSWI}}{1 + \text{LSWI}_{\text{max}}} \tag{5.23}$$

Where PAR is photosynthetically active radiation (W m^{-2}). FPAR_{chl} is calculated as a linear function across all land cover types, with the coefficients a and b set to –0.1 and 1.0, respectively, and γ_{E} = 1.25 representing the ratio between the annular area and the

area of concentric circles (L. Pan et al., 2025). The apparent quantum yield or maximum light use efficiency, ε_0 is set at 0.53 (g C mol^{-1} PAR) for C_3 plants and 0.79 (gC mol^{-1} PAR) for C_4 plants (Xiao, 2006). The temperatures T_{max}, T_{min}, and T_{opt} are the maximum, minimum, and optimum temperatures for photosynthetic activity, where T_{max} and T_{min} were obtained from a look-up table, and T_{opt} was obtained from a global site-specific T_{opt} dataset (Pan, Xiao, Yao, et al., 2024). EVI and LSWI were calculated from MOD09A1 multispectral surface reflectance data.

Previous studies have demonstrated that the sensitivity of ecosystem-scale GPP to CO_2 is consistent with the sensitivity of electron transport-limited gross photosynthetic rate (A_{gross}) (Baig et al., 2015; Keenan et al., 2023). Hence, the influence of CO_2 on photosynthetic rate can be incorporated into the VPM as an additional environmental factor. VPM v4.0 estimates GPP as:

$$GPP_{VPM\text{-}v4} = PAR \times FPAR_{chl} \times \varepsilon_0 \times f(T) \times f(W) \times f(CO_2) \quad (5.24)$$

Note that $f(CO_2)$ is applied only to C_3 plant. $f(CO_2)$ can be estimated through the following steps. To highlight that this gain is “additional” or relative to pre-industrial levels, we establish a baseline assumption: pre-industrial atmospheric CO_2 concentrations were maintained at a relatively stable, low value. As atmospheric CO_2 concentrations increased over time, the model compares simulation results between two CO_2 scenarios (or different observation years) to quantify the additional carbon fixed at the biochemical level in the leaves. Thus, $f(CO_2)$ is quantified as a relative gain compared to the pre-industrial era:

$$f(CO_2) = \frac{A^{t}_{gross}}{A^{baseline}_{gross}} \quad (5.25)$$

In this study, we estimate the pre-industrial baseline ($A^{baseline}_{gross}$) using an atmospheric CO_2 concentration of 278 ppm (c_a= 278 ppm) and climate data from 1951 to 1960 (Friedlingstein et al., 2024). Then, for each year from 2000 to 2023, we estimate A^{t}_{gross} using the corresponding CO_2 concentration and climate data. Finally, $f(CO_2)$ is calculated as the ratio of A^{t}_{gross} to $A^{baseline}_{gross}$. Our results indicate that, from a global perspective, regions with higher $f(CO_2)$ values are predominantly located in the low-latitude tropics and subtropics (Figure. 5.2a, b, c). Moreover, the long-term trend shows a significant increase in $f(CO_2)$ in these regions, suggesting that the CO_2 effect is most pronounced in tropical and subtropical regions and diminishes with increasing latitude (Figure. 5.2d).

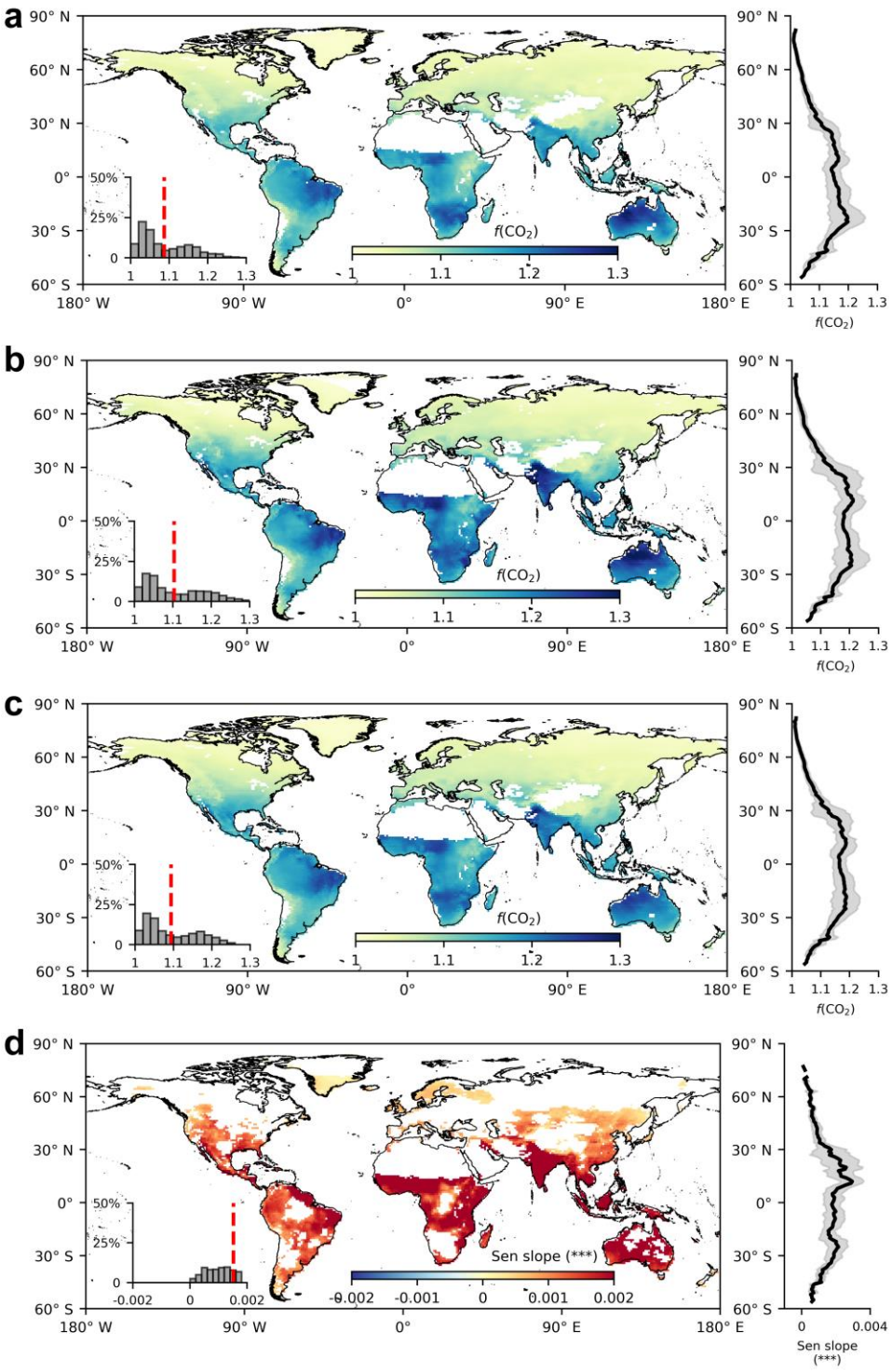

Figure 5.2: Spatial distribution of f(CO_2) and its long-term trend from 2000 to 2023. f(CO_2) is estimated annually from 2000 to 2023. (a) shows the distribution of f(CO_2) in the year 2000, (b) shows that of 2023, (c) shows the multi-year average,

and (d) shows the long-term trend. In (d), only pixels with statistically significant trends ($p < 0.01$*, as determined by the Mann–Kendall test) are shown, and the magnitude of the trend is represented by the Sen slope.**

5.2.10 Statistical analysis

At the site scale, we compared GPP estimates from the VPM with eddy flux tower observations. The comparison focused on two aspects: GPP IAV and the annual total GPP magnitude. For GPP IAV, we calculated the mean IAV for each site over all available years for three data sources (EC tower, VPM v4.0, and VPM v3.0). We computed the slope of the linear trend to assess differences among these sources. For the annual total GPP magnitude, annual GPP was aggregated, and simple linear regression was used to compare GPP from VPM v4.0, VPM v3.0, and EC tower. Evaluation metrics included the zero-intercept slope, the coefficient of determination (R^2), and the relative root-mean-square error (rRMSE).

Subsequently, we estimated the global total GPP from VPM v4.0 and VPM v3.0 for the period 2000–2023 and analyzed their respective linear trends as well as the differences between them. In addition, we compared the GPP from VPM models with other global GPP models, with a primary focus on global total GPP and the sensitivity of GPP to CO_2. Global total GPP and their uncertainties for the other models were obtained from published literature and data products. A propagation of uncertainty method to calculate the standard deviation (σ) for each category of GPP models:

$$\sigma = \sqrt{\frac{\sum_i^n \sigma_i^2}{n}} \tag{5.26}$$

For the DGVMs, we selected three scenarios (S0, S1, S2, S3): the baseline scenario (S0), the scenario considering only CO_2 effects (S1), and the scenario considering both climate and CO_2 effects (S2). The global GPP estimate without CO_2 effects was then derived as S2−S1+S0, while S2 was used directly to represent the global GPP estimate with CO_2 effects.

We computed the interannual change rates (Δ, %) for atmospheric CO_2 concentration (c_a) and GPP for the period 2000 to 2023 as follows:

$$\Delta c_a = \frac{c_a(t) - c_a(t_0)}{c_a(t_0)} \times 100\% \quad (5.27)$$

$$\Delta GPP = \frac{GPP(t) - GPP(t_0)}{GPP(t_0)} \times 100\% \quad (5.28)$$

where GPP(t) and $c_a(t)$ are the GPP (in Pg C) and atmospheric CO_2 concentration (in ppm) in year t, respectively, and GPP(t_0) and $c_a(t_0)$ are the GPP and atmospheric CO_2 concentration in the baseline year 2000. To mitigate the influence of anomalies on GPP interannual variability, we reconstructed the GPP time series via linear regression fitting of GPP(t) following methods used in previous studies (Keenan et al., 2023). Finally, the sensitivity coefficient of GPP to c_a (β_R^{GPP}) was calculated for VPM v4.0, VPM v3.0, and the DGVMs, and the results were compared with relevant literature:

$$\beta_R^{GPP} = \frac{\Delta GPP}{\Delta c_a} \quad (5.29)$$

5.3 Results

5.3.1 Direct effect of CO_2 on GPP at the EC tower sites

At the site scale, we compared GPP_{EC} from 59 EC tower sites with GPP from VPM v4.0 (w/ CO_2) and VPM v3.0 (w/o CO_2) over 777 site-years (Figure 5.3). The

comparison focused on annual GPP and its interannual variability (IAV) and trend. Annual GPP from the EC tower sites shows an increasing GPP trend from 2000 to 2023 with a rate of 6.0 gC m^{-2} yr^{-2} (Figure 5.3a). Annual GPP from VPM v4.0 also shows an increasing GPP trend over the years with a rate of 5.3 gC m^{-2} yr^{-2}, which is slightly (12%) lower than that from the EC tower sites. Annual GPP from VPM v3.0 did have an increasing trend but with much smaller rate of 3.8 gC m^{-2} yr^{-2}. The sites that have a higher f(CO_2) also exhibit larger GPP IAV, and the sensitivity of GPP IAV to f(CO_2) in VPM v4.0 is closer to that from the EC tower sites than VPM v3.0 (Figure 5.4). These results suggest that incorporating f(CO_2) into the VPM v4.0 model enhances its ability to capture IAV and trend of annual GPP at EC tower sites accurately. This improved tracking of GPP IAV by VPM v4.0 is evident across most biomes, including CRO, CSH, EBF, ENF, GRA, MF, and WSA (Figure 5.5).

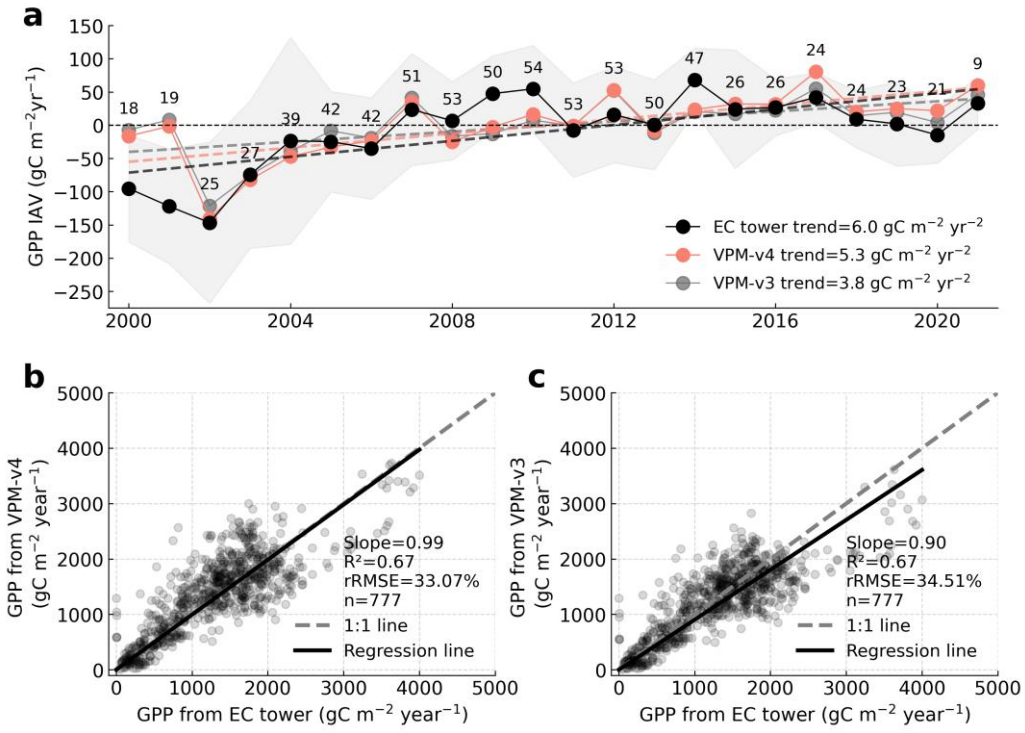

Figure 5.3: Comparison of GPP estimates from EC tower measurements and the

VPM model (VPM v4.0 and VPM v3.0). (a) compares the GPP IAV, where IAV was calculated as the deviation of each year's GPP from the multi-year average. Each point in the time series represents the mean GPP IAV across all site-years, with the number annotated on each point indicating the total number of site-years for that year. The grey buffer represents the GPP range derived using covariance techniques from both nighttime- and daytime-partitioning methods. (b) and (c) compare the annual GPP magnitude, with (b) showing the relationship between GPP from VPM v4.0 and EC tower, and (c) showing the relationship between GPP from VPM v3.0 and EC tower. The annual GPP magnitude was calculated as the total GPP over a year, and these comparisons are conducted using simple linear regression.

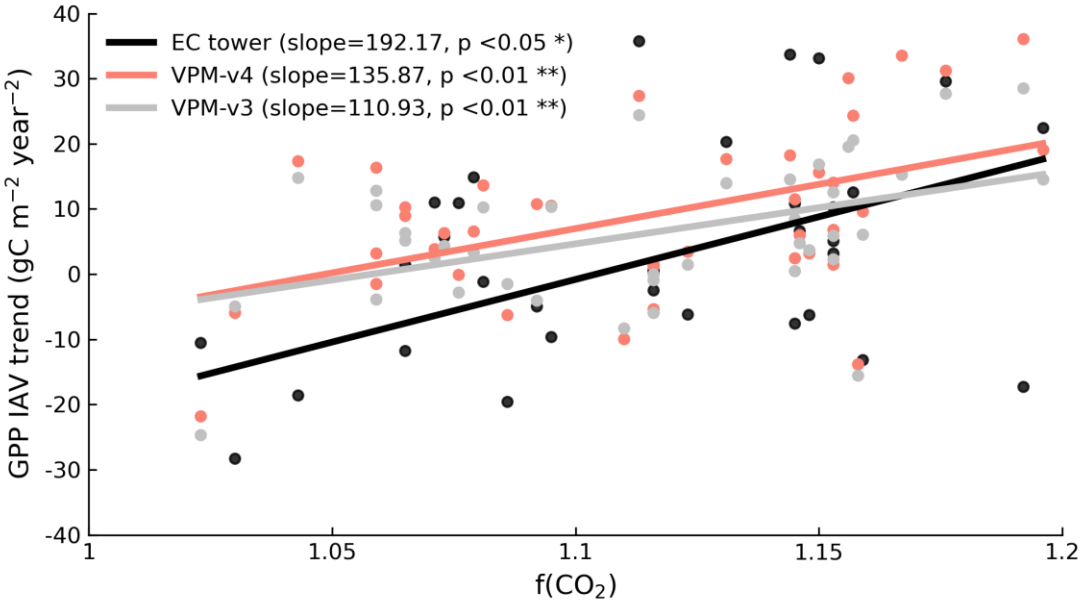

Figure 5.4: Relationship between the GPP IAV trend and f(CO_2). The GPP IAV trend is estimated as the slope of a linear regression fitted to the GPP IAV time series at each EC tower site, with a higher trend indicating greater GPP IAV. f(CO_2)

is a dimensionless parameter representing the magnitude of the direct CO_2 effect at each site.

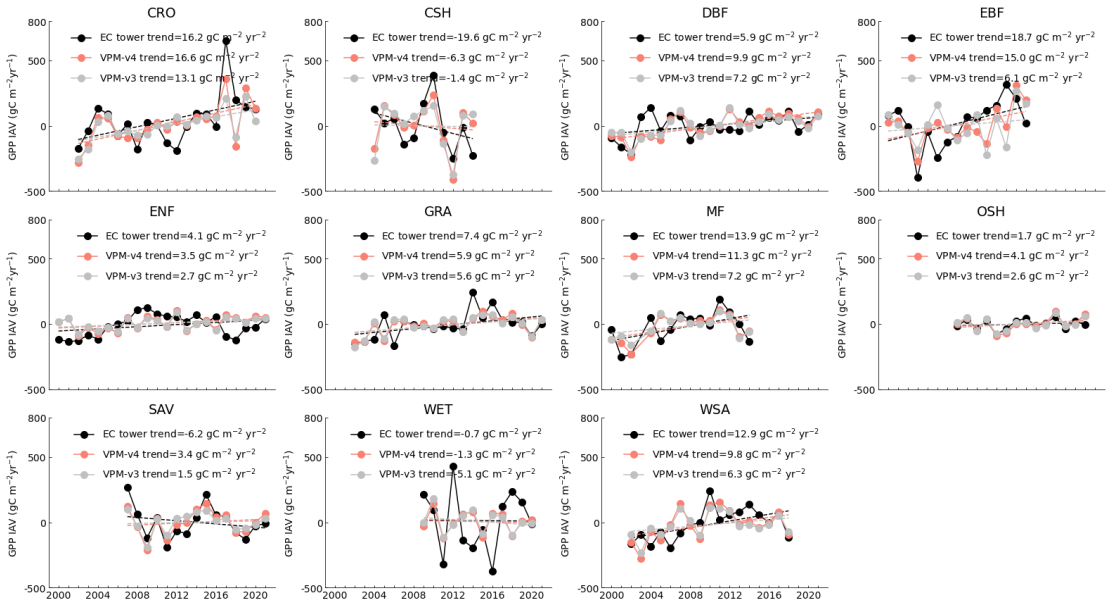

Figure 5.5: Comparison of GPP IAV from EC tower measurements and the VPM model (VPM v4.0 and VPM v3.0) across all biomes. IAV was calculated as the deviation of each year's GPP from the multi-year average. Each point in the time series represents the mean GPP IAV across all site-years.

With regards to annual GPP, a linear regression analysis (without an intercept) between VPM v4.0 estimates and EC tower observations yielded a slope of 0.99 (R^2 = 0.67, rRMSE = 33.07%) (Figure 5.3b), whereas the regression for VPM v3.0 resulted in a slope of 0.90 (R^2 = 0.67, rRMSE = 34.51%) (Figure 5.3c). The closer-to-unity (1:1 line) slope for VPM v4.0 indicates that It does not underestimate GPP at the site scale after we incorporate the direct effect of atmospheric CO_2 concentration on GPP. This improvement of VPM v4.0 over VPM v3.0 is also observed in biomes such as EBF, ENF, SAV, and CRO (Figure 5.6).

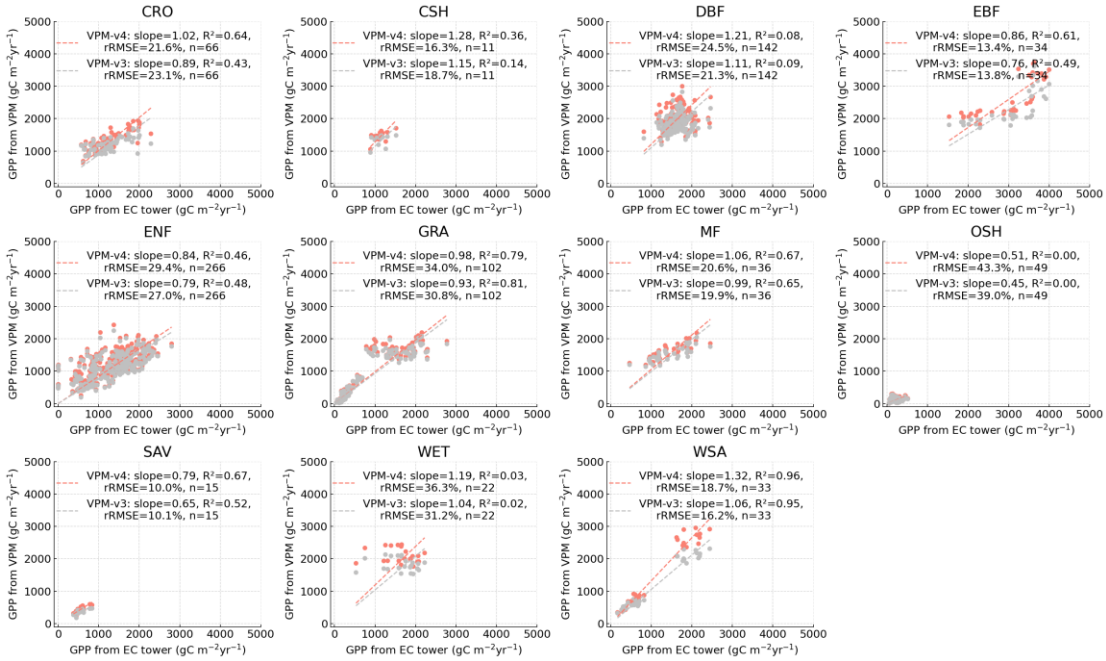

Figure 5.6: Comparison of annual GPP estimates across sites by biomes. Red dots show the relationship between GPP from VPM v3.0 and EC tower, and gray dots show the relationship between GPP from VPM v3.0 and EC tower.

5.3.2 Direct effect of CO_2 on GPP at the glob scale from 2000 to 2023

Global annual GPP estimates during 2000–2023 from VPM v4.0 (w/ CO_2) range from 145 Pg C yr^{-1} in 2000 to 166 Pg C yr^{-1} in 2023, with an average estimate of 155 ± 6 Pg C yr^{-1} and an annual increase rate of 0.78 Pg C yr^{-2} (Figure 5.7a). Global annual GPP estimates from VPM v3.0 (w/o CO_2) range from 135 Pg C yr^{-1} in 2000 to 151 Pg C yr^{-1} in 2023, with an average estimate of 143 ± 4 Pg C yr^{-1} and an annual increase rate of 0.57 Pg C yr^{-2} (Figure 5.7a). On average, the direct CO_2 effect results in an increase of mean global annual GPP (12 Pg C yr^{-1}; ~9%). The spatial differences between these two GPP data products are most pronounced in the tropical and subtropical regions (Figure 5.7 c, d), where vegetation is dominated by evergreen broadleaf forest (EBF),

grassland (GRA), woody savanna (WSA), savanna (SAV) and cropland (CRO) (Figure 5.8, Figure 5.9). Mid-to-high latitude regions are dominated by deciduous broadleaf forest (DBF), evergreen needleleaf forest (ENF), mixed forest (MF), and open shrubland (OSH) exhibit relatively smaller differences (Figure 5.8, Figure 5.9). At the scale of biomes (Figure 5.10), the largest difference between these models occurred in EBF, where mean annual GPP from VPM v4.0 was 38.46 Pg C yr^{-1}, approximately ~3.19 Pg C yr^{-1} (~9%) higher than the estimate from VPM v3.0 (35.26 Pg C yr^{-1}). Biomes such as GRA, SAV, CRO, and WSA also exhibit varying degrees of GPP increase in VPM-v4. In contrast, DBF, ENF, MF, and OSH show small differences between VPM v4.0 (w/ CO_2) and VPM v3.0 (w/o CO_2).

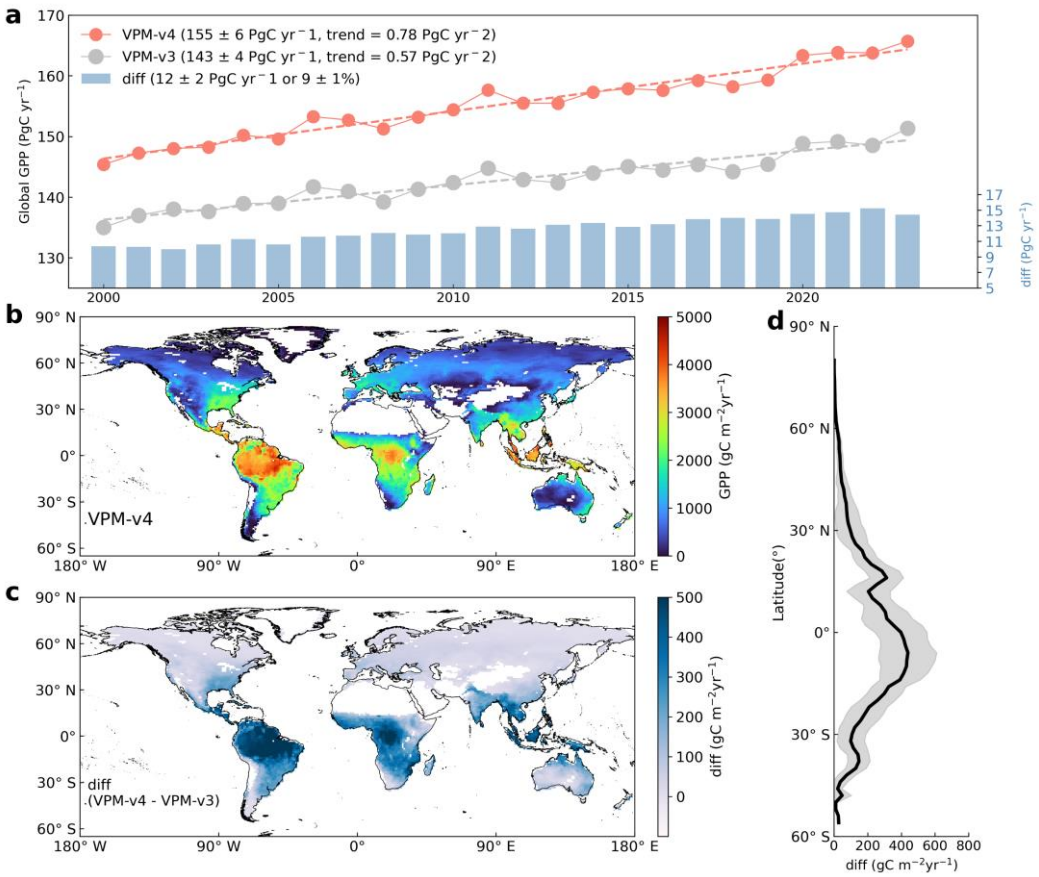

Figure 5.7: Comparison of global GPP estimates from VPM v4.0 and VPM v3.0.

(a) shows the global GPP estimated by VPM v4.0 and VPM v3.0 from 2000 to 2023, where the difference (diff) is calculated as the difference between VPM v4.0 and VPM v3.0. (b) shows the spatial distribution of the annual GPP magnitude estimated by VPM v4.0, while (c) shows the spatial distribution of the diff in annual GPP magnitude between VPM v4.0 and VPM v3.0. (d) shows the latitudinal gradient of the diff, with the curve representing the average of all pixels within each 2°. Data analysis was carried out at a 500-meter spatial resolution and visualized at a 1° spatial resolution.

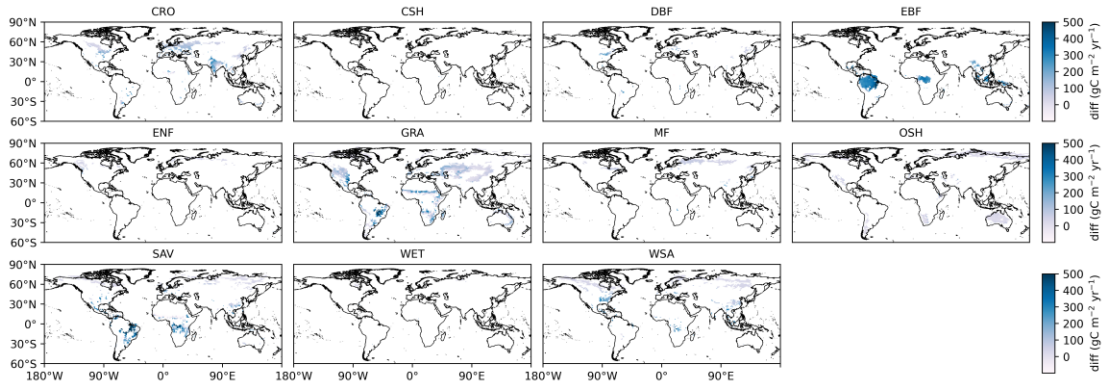

Figure 5.8: The spatial distribution of the diff in annual GPP magnitude between VPM v4.0 and VPM v3.0 across all biomes. Data was visualized at a 1° spatial resolution.

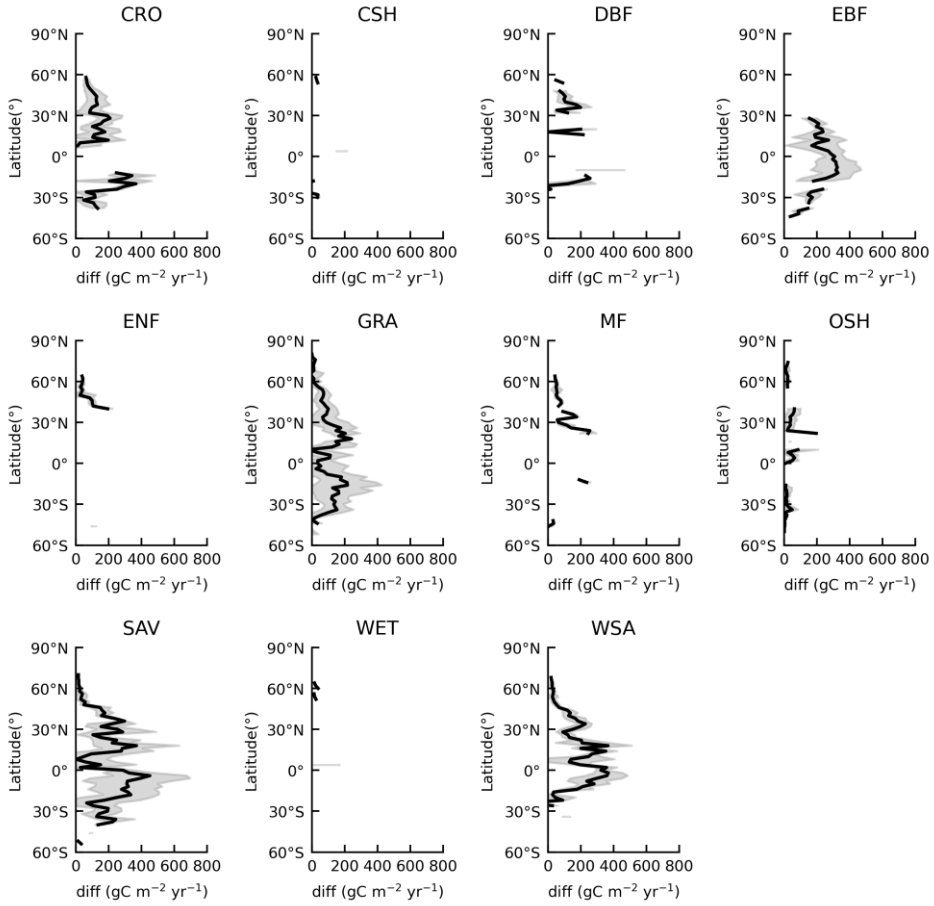

Figure 5.9: The latitudinal gradient of the diff (VPM v4.0 – VPM v3.0) across all biomes. The curve represents the average of all pixels within each 2°.

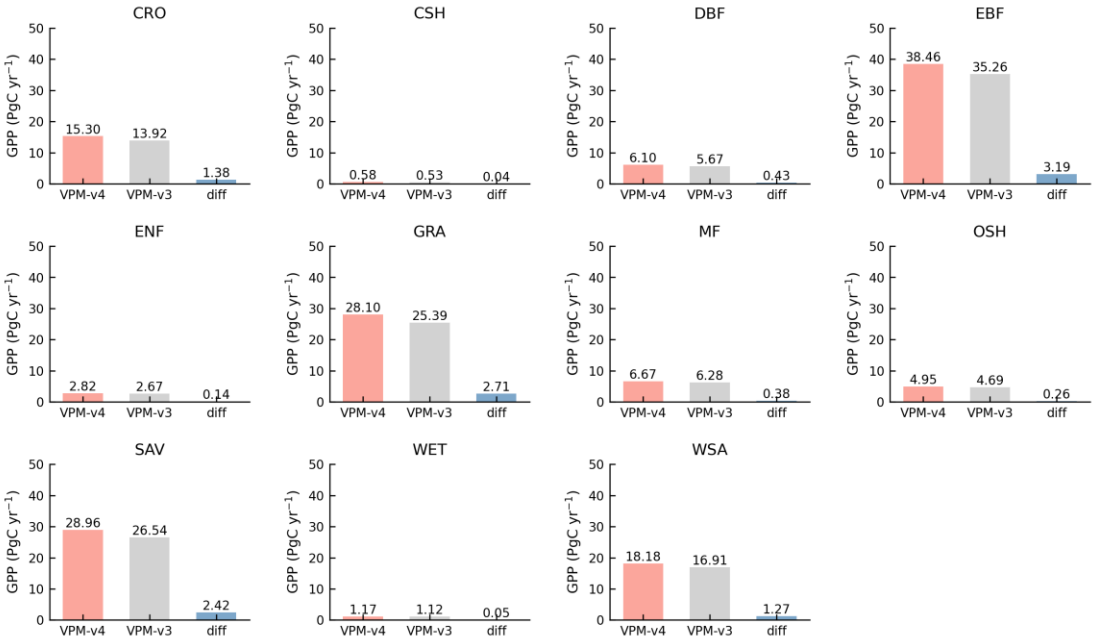

Figure 5.10: The magnitude of global annual GPP across all biomes.

5.3.3 Comparison of global annual GPP from VPM and other GPP models

We compared the global annual GPP estimates from the VPM model with those from other models in terms of annual GPP magnitude and interannual trends. The models in the comparison are grouped into four categories: (1) DGVMs, including 13 models that run simulations with CO_2 or without CO_2, (2) satellite-based models using Vc_{max} parameter for CO_2 fixation , including BESS, BESP, and PR; (3) satellite-based model using ϵ_{max} parameter for CO_2 fixation with CO_2 effect or without CO_2 effect, including VPM (v4.0, v3.0), MOD17, LRF, EC-LUE, and GLASS, and (4) statistical models trained with EC data and satellite data (FPAR, NIRv and SIF), including FLUXCOM, NIRv, and GOSIF models.

As shown in Figure 5.11a, the mean global annual GPP estimate during 2000-2023 from VPM v4.0 (155 ± 6 Pg C yr^{-1}) is very close to the estimate from the OCS method (157 ± 8.5 Pg C yr^{-1}, 2000-2010) (Lai et al., 2024), and falls within the range of 150–175 Pg C yr^{-1} from ^{18}O methods (Lisa R. Welp et al., 2011b), and slightly exceeds the 149 Pg C yr^{-1} from soil respiration (Jian et al., 2022). A latitudinal profile comparison of annual GPP from VPM with that from the OCS method reveals a high degree of consistency along the latitude gradient (Figure 5.11b). In tropical regions, annual GPP from VPM v3.0 is smaller than that from the OCS method, whereas annual GPP from VPM v4.0 is closer to that from the OCS method. VPM v4.0 GPP magnitude closely matches that from the OCS method between 0° and 10°S latitudinal zone. Note that annual GPP from VPM v4.0 is slightly higher than that from the OCS method between

10°S and 20°S latitudinal zone, where vegetation in Africa is dominated by C_4 grasses. Our VPM v4.0 model simulations employed an updated and detailed C_4 vegetation distribution map (see Materials and Method section for more details), note that C_4 plants have higher maximum light use efficiency parameter value than C_3 plants.

Mean global annual GPP estimates from various models are compared (Figure 5.11, Figure 5.12, Table. 5.1). Mean global annual GPP from three satellite-based models using Vc_{max} parameter (PR, BESS, and BEPS) was 132 ± 6 Pg C yr^{-1} (Figure 5.12 a). Mean global annual GPP from four satellite-based models using ϵ_{max} (MOD17, LRF, EC-LUE, and GLASS) is 114 ± 12 Pg C yr^{-1}, ranging from 98 to 130 Pg C yr^{-1}. Mean global annual GPP from three statistical models (FLUXCOM, NIRv, GOSIF) vary from 124 ± 7 Pg C yr^{-1} (FLUXCOM) to 135 ± 9 Pg C yr^{-1} (NIRv) and 147 ± 16 Pg C yr^{-1} (GOSIF), respectively. Mean global annual GPP from 13 models in the CO_2-inclusive DGVMs ensemble varied substantially, and four of them (CLM5.0, iMAPLE, LPJml, and LPJwsl) have comparable annual GPP with VPM v4.0 (Figure 5.12b). It is clear that most of the models without CO_2 effect have lower annual GPP than the models with CO_2 effect and are noticeably lower than the global GPP estimates from the OCS method.

Interannual variability (IAV) and trend of global annual GPP from various models are compared (Figure 5.13, Figure 5.14, Table 5.2, Table 5.3). The global annual GPP from 2000 to 2023 from these models have substantial differences in both IAV and trend over years. We conducted two sets of comparisons to evaluate interannual trend of global annual GPP, based on the data availability among the models. The first

comparison covers the period from 2001 to 2011, during which period data from all selected models were available (Figure 5.11c, e, Table 5.2). The CO_2-inclusive DGVMs ensemble has an interannual trend of 0.57 Pg C yr^{-2}. The CO_2-exclusive DGVM ensemble has a small trend of 0.17 Pg C yr^{-2}. The satellite-based models using Vc_{max} paramter (PR, BESS and BEPS) have moderate trends of 0.36 to 0.46 Pg C yr^{-2}. The satellite-based models using ϵ_{max} parameter have a wide range of trends (Pg C yr^{-2}), varying from 0.89 (VPM v4.0) to 0.64 (VPM v3.0), 0.47 (MOD17), 0.27 (LRF), -0.25 (EC-LUE) and -0.35 (GLASS). The statistical models (FLUXCOM and GOSIF) also have a large range of trends (Pg C yr^{-2}), varying from 0.06 (FLUXCOM) to 0.66 (GOSIF). The second comparison covers the period of 2000-2023 (Figure 5.15, Table 5.3). VPM v4.0 (w/ CO_2) had the largest trend (0.78 Pg C yr^{-2}), followed by VPM v3.0 (w/o CO_2, 0.57 Pg C yr^{-2}), the CO_2-inclusive DGVM ensemble (0.43 Pg C yr^{-2}) and the CO_2-exclusive DGVM ensemble (0.03 Pg C yr^{-2}). The interannual trends of global annual GPP from VPM simulations are consistently larger than those from DGVMs. Among the 13 DVGM models, CO_2-inclusive simulations have large (0.64 Pg C yr^{-2} in iMAPLE) to moderate (0.28 Pg C yr^{-2} in CLASSIC) increasing trend of global annual GPP, while CO_2-exclusive simulations have interannual trends of global annual GPP from small (0.18 Pg C yr^{-2} in LPJm1) increase to a loss (-0.04 Pg C yr^{-2} in CABLE-POP).

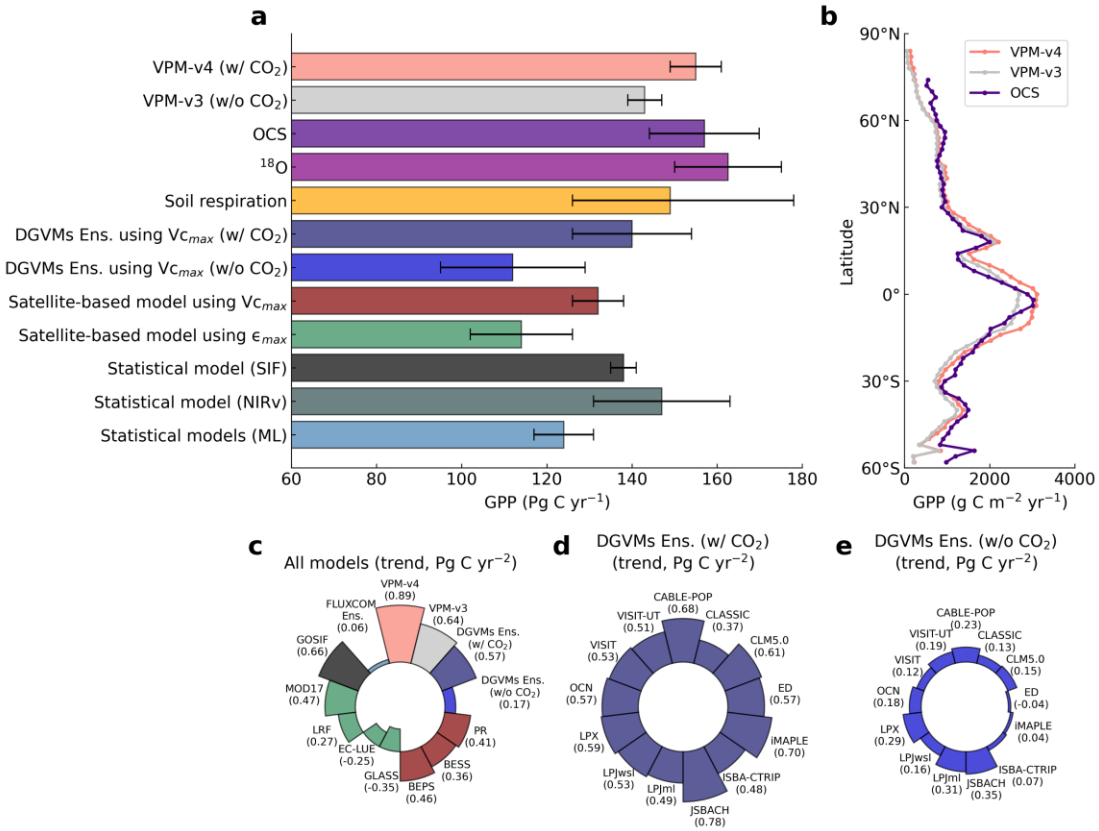

Figure 5.11: Intercomparison of GPP estimates from multiple models. (a) Global GPP and its ranges are presented for all models and grouped by category. VPM v4.0 and VPM v3.0 are the estimates from this study, while estimates for other models are derived from historical literature or published datasets, and detailed estimates for each model can be found in Figure 5.12. The range for each category is calculated across all models within that category using the propagation of uncertainty method. (b) The latitudinal distribution of GPP is shown for VPM v4.0, VPM v3.0, and the OCS method, with curves estimated as the average of all pixels within each 2°. (c), (d) and (e) show the interannual trends (Pg C yr^{-2}) in the selected models from 2001 to 2011. These models were selected because the data provided by these models overlap during 2001-2011. (c) is the trend of all models,

(d) and (e) are two estimates (CO_2-inclusive, CO_2-exclusive) of the 13 models in DGVMs ensemble, respectively.

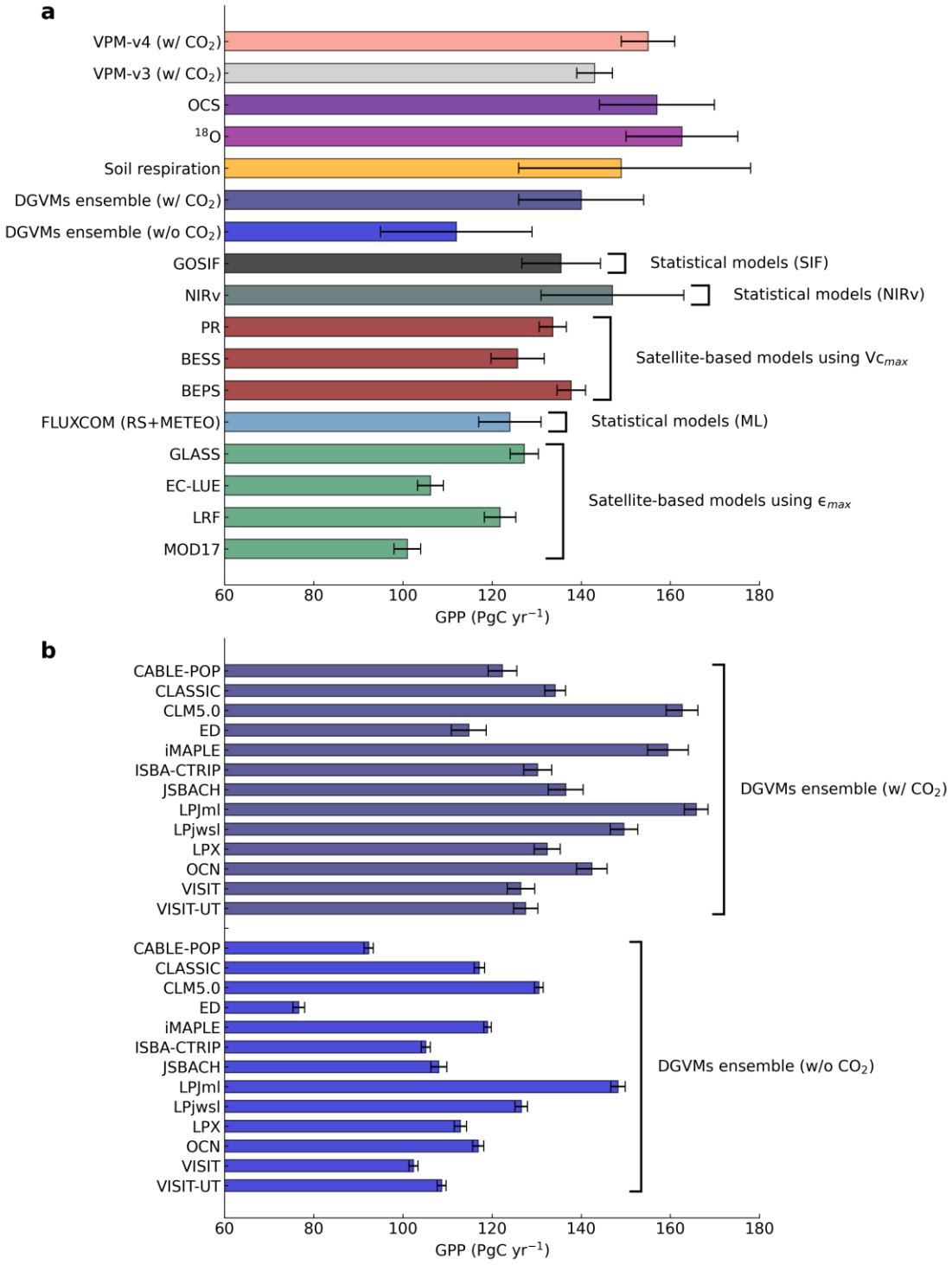

Figure 5.12: Global annual GPP magnitude across all models. (a) shows the annual

GPP magnitude for all models grouped by category. (b) shows the annual GPP magnitude for the 13 CO_2-inclusive and CO_2-exclusive DGVMs.

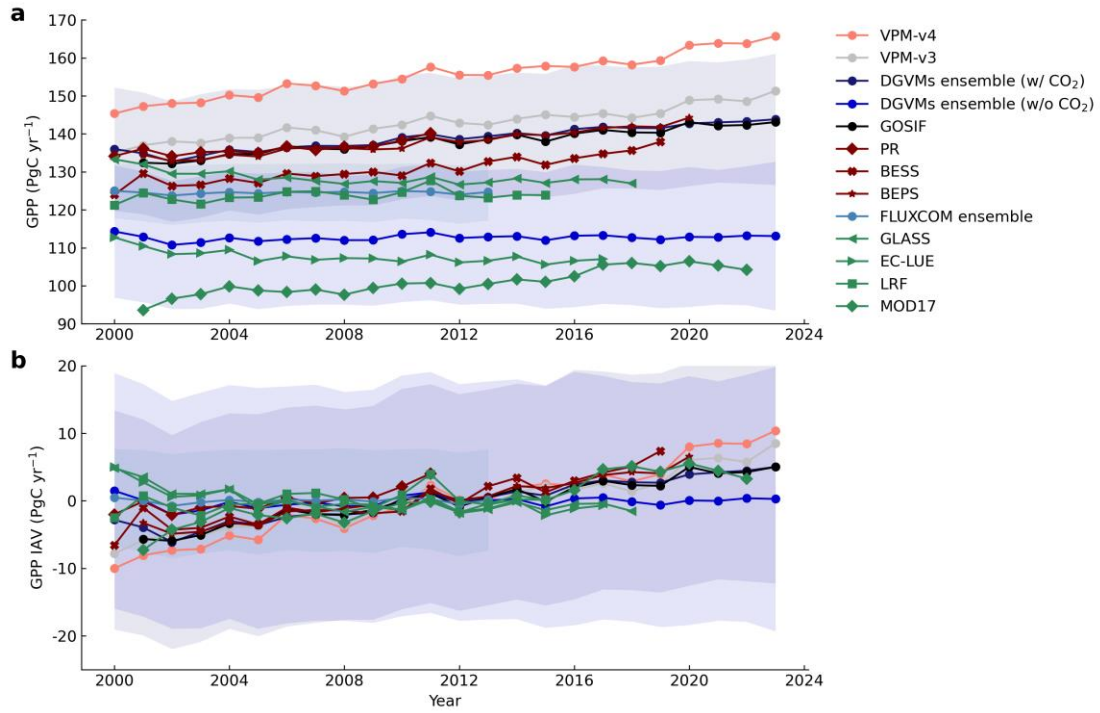

Figure 5.13: Global annual GPP from 2000 to 2023 across all models. This figure selected models for which data were publicly available or accessible from published literature. (a) Global annual GPP from 2000 to 2023. (b) Interannual variability (IAV) of global GPP over the same period, calculated as the anomaly of each year's GPP from the multi-year mean. The shaded areas represent the ranges of different model ensembles: CO_2-inclusive DGVMs ensemble (w/ CO_2), CO_2-exclusive DGVMs ensemble (w/o CO_2), and the FLUXCOM ensemble.

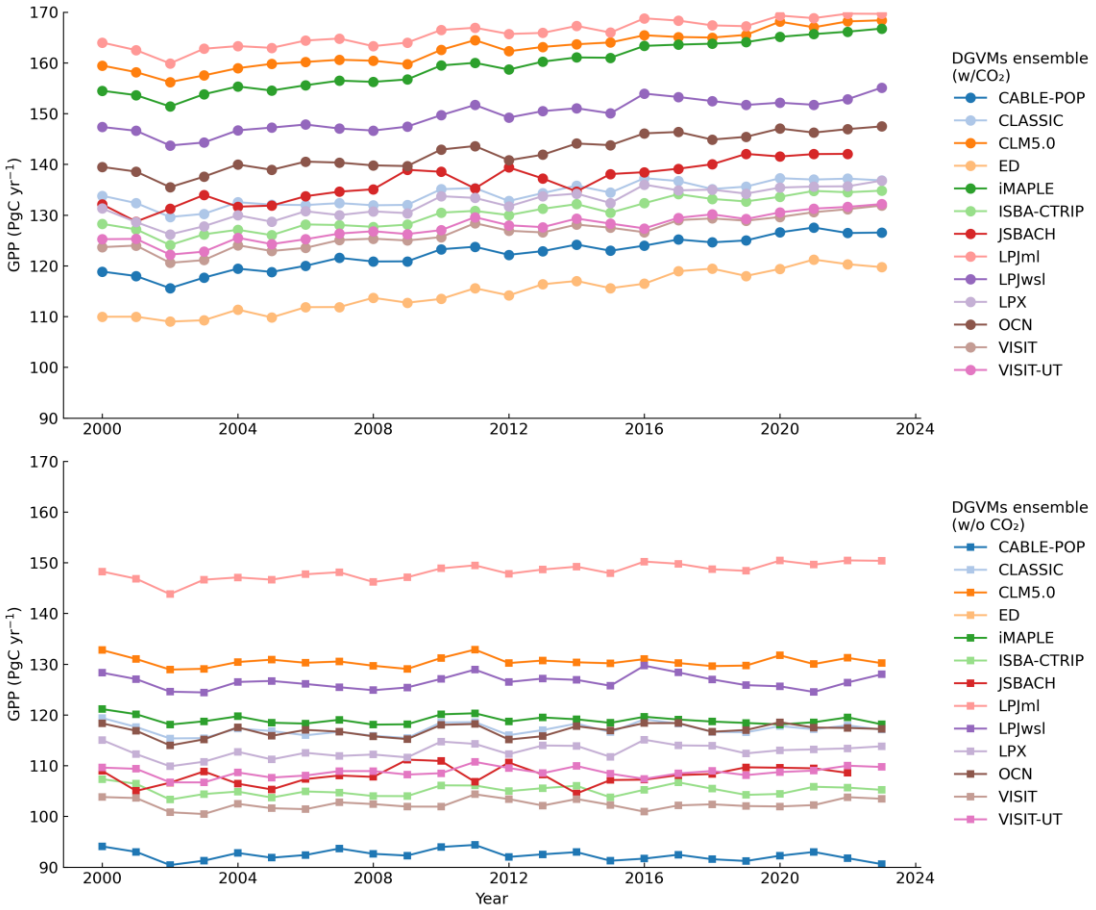

Figure 5.14: Global annual GPP from 2000 to 2023 across all DGVMs under two scenarios: S2 (w/ CO_2) and S2-S1+S0 (w/o CO_2).

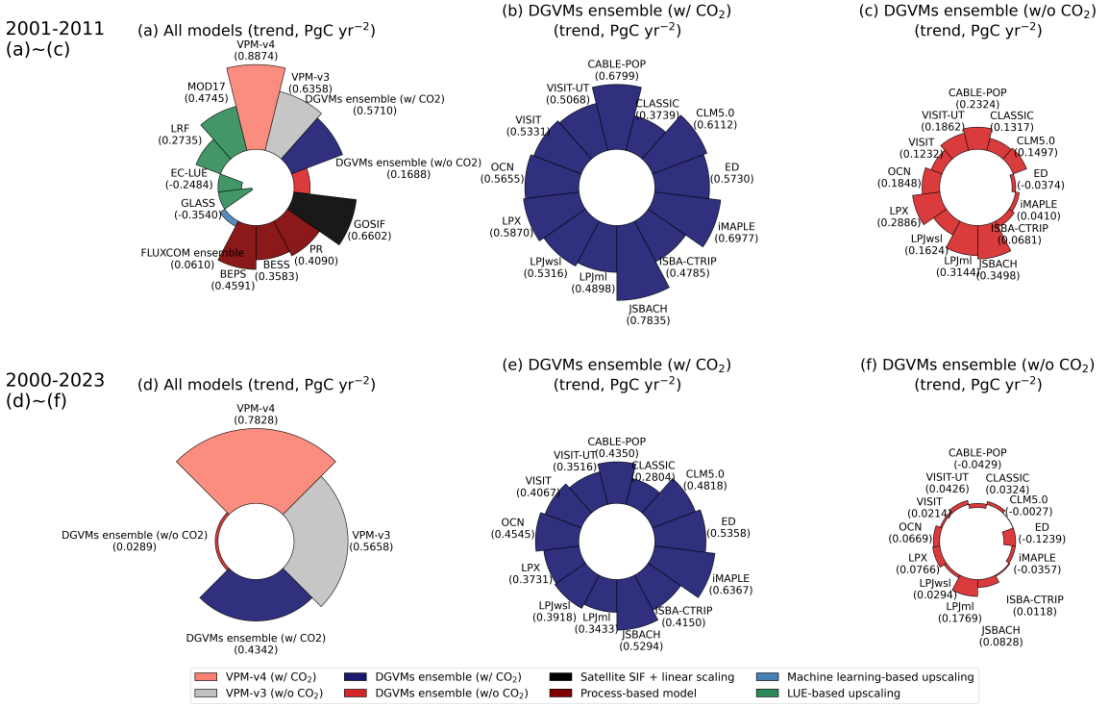

Figure 5.15: Global annual GPP trends across all models. Here, we conducted two sets of comparisons based on the years of data availability for different models. The first row is a comparison from 2001 to 2011, where (a) is the trend of all the models involved in this comparison, and (b) and (c) are the 13 CO_2-inclusive and 13 CO_2-exclusive DGVMs, respectively. The second row is a comparison from 2000 to 2023, where (d) is the trend of VPM v4.0, VPM v3.0, and DGVMs, and (e) and (f) are the 13 CO_2-inclusive and 13 CO_2-exclusive DGVMs, respectively.

Table 5.3: Global GPP estimates for 2000 to 2023 across VPM and DGVMs. The table is calculated based on publicly available products or from literature.

Model	CO_2	Year	Global annual GPP				
			Start year (2001) (PgC yr^{-1})	End year (2011) (PgC yr^{-1})	Mean (PgC yr^{-1})	IAV (PgC yr^{-1})	Trend (PgC yr^{-2})
VPM v4.0	**w/ CO_2**		**145**	**166**	**155**	**1.1826**	**0.7828**
VPM v3.0	**w/o CO_2**		**135**	**151**	**143**	**1.1521**	**0.5658**
DGVMs ensemble (S2, w/ CO_2)	w/ CO_2	2000-2023	136±16	144±16	139±16	1.1033 ± 1.1829	0.4342 ± 0.0951
CABLE-POP			119	127	122	0.9631	0.435
CLASSIC			134	137	134	1.1891	0.2804
CLM5.0			159	168	163	0.974	0.4818
ED			110	120	115	0.9077	0.5358
iMAPLE			154	167	159	0.8855	0.6367
ISBA-CTRIP			128	135	130	1.0595	0.415
JSBACH			132	142	137	1.528	0.5294
LPJml			164	170	166	1.013	0.3433
LPjwsl			147	155	150	1.3149	0.3918
LPX			131	137	132	1.2472	0.3731
PCN			139	147	142	1.1875	0.4545
VISIT			124	132	126	1.0462	0.4067
VISIT-UT			125	132	128	1.0242	0.3516
DGVMs ensemble (S2-S1+S0, w/o CO_2)	w/o CO_2		114±17	113±19	113±18	1.0829 ± 0.2234	0.0289 ± 0.0722
CABLE-POP			94	91	92	0.9834	-0.0429
CLASSIC			119	117	117	1.1205	0.0324
CLM5.0			133	130	131	0.9839	-0.0027
ED			79	73	77	0.9482	-0.1239
iMAPLE			121	118	119	1.7816	-0.0357
ISBA-CTRIP			107	105	105	1.0105	0.0118
JSBACH			109	109	108	1.6519	0.0828
LPJml			148	150	148	0.994	0.1769
LPjwsl			128	128	127	1.3601	0.0294
LPX			115	114	113	1.2215	0.0766
PCN			118	117	117	1.1164	0.0669
VISIT			104	103	102	0.9807	0.0214
VISIT-UT			110	110	109	0.9253	0.0426

5.3.4 Comparison of GPP sensitivity to increased CO_2 concentration

We compared the sensitivity of global annual GPP during 2000-2023 from VPM and DGVMs to the increase of atmospheric CO_2 concentration (c_a) (Figure 5.16a). Global annual GPP from VPM v4.0 (slope = 0.90, R^2 = 0.95, $p < 0.01$), the CO_2-inclusive DGVM ensemble (slope = 0.53, R^2 = 0.93, $p < 0.01$), and VPM v3.0 (slope = 0.70, R^2

= 0.92, $p < 0.01$) significantly increase with rising c_a. As anticipated, global annual GPP from the CO_2-exclusive DGVM ensemble had little to no changes with rising c_a (slope = 0.04, $R^2 = 0.05$, $p = 0.31$). We further calculated a dimensionless coefficient, β_R^{GPP}, to represent the sensitivity of GPP to historical changes in c_a during 2000-2023 (Figure 5.16 b, Table 5.4). Our method for calculating β_R^{GPP} is based on previous literature and is anticipated to yield a metric that can be directly compared with other studies (Keenan et al., 2023). The β_R^{GPP} is 0.59 ± 0.16 for the CO_2-inclusive DGVMs and 0.03 ± 0.03 for the CO_2-exclusive DGVM (Figure 5.16b, Figure 5.17). The β_R^{GPP} is 0.97 ± 0.07 for VPM v4.0 and 0.76 ± 0.05 for VPM v3.0, respectively (Figure 5.16b). In both DGVMs and VPM v4.0, explicitly including CO_2 markedly enhances the sensitivity of GPP to c_a changes. At the scale of biome, after incorporating the CO_2 into VPM v4.0, the sensitivity of annual GPP to c_a increases across all biomes, with the largest increases in EBF (Figure 5.18). The β_R^{GPP} values are large for EBF, moderate for CRO, CSH, SAV, and WSA, and small for CSH, OSH, and WET.

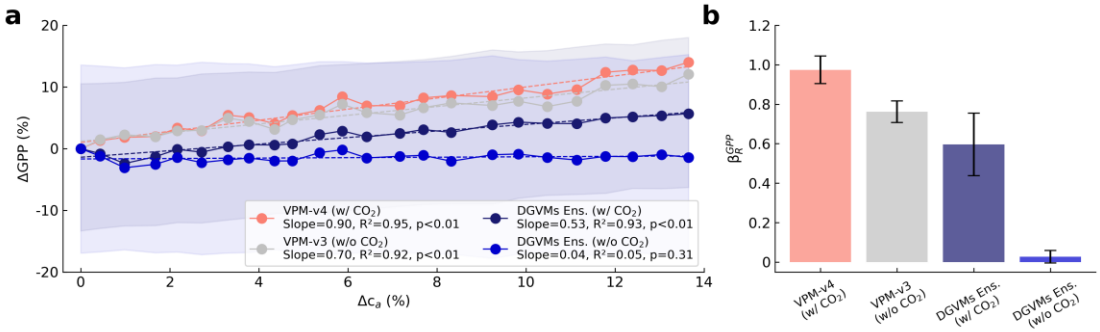

Figure 5.16: Sensitivity of GPP to atmospheric CO_2 concentration (c_a). (a) compares the changes in GPP (ΔGPP) against changes in atmospheric CO_2 concentration (Δc_a) using data from both the VPM models (VPM v4.0 and VPM

v3.0) and a DGVM ensemble (CO_2-inclusive, CO_2-exclusive). These two sets of models—yielding four estimates in total—were chosen because they provide continuous global GPP estimates from 2000 to 2023. Slope, R^2, and significance (p) are calculated from simple linear regression. (b) shows the magnitude and range of the sensitivity coefficient (β_R^{GPP}) for these four estimates.

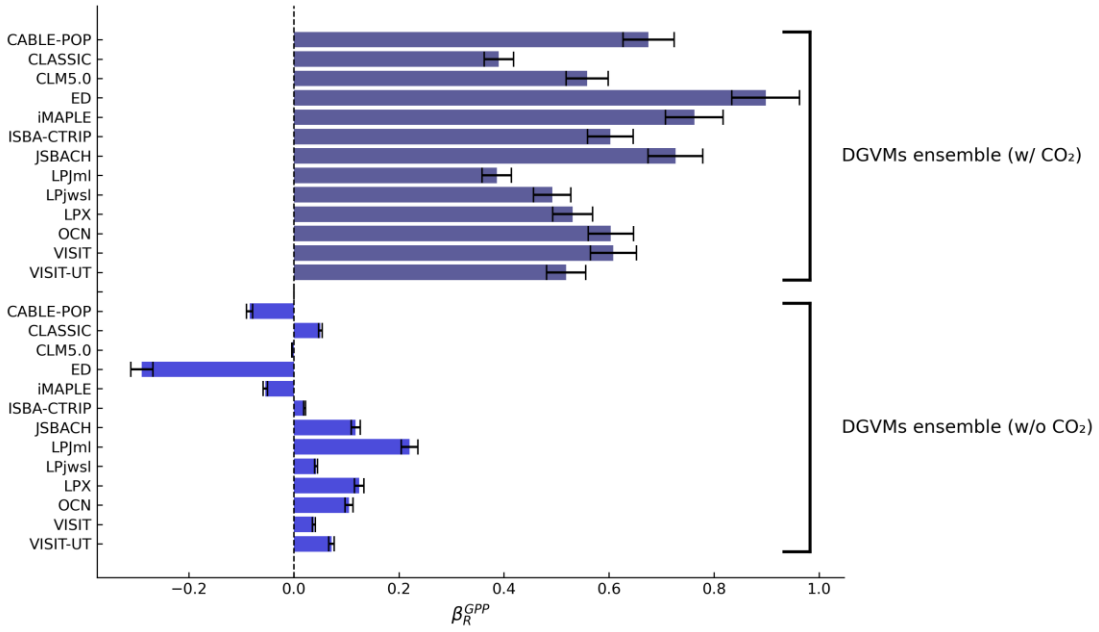

Figure 5.17: The sensitivity of GPP to c_a for the 13 CO_2-inclusive and 13 CO_2-exclusive DGVMs.

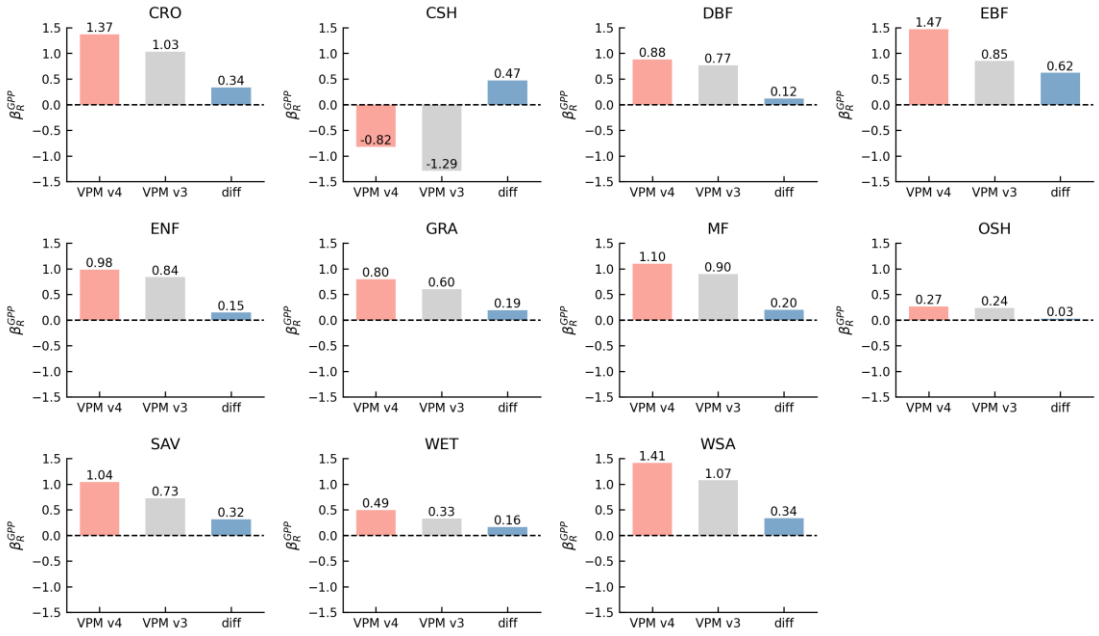

Figure 5.18: The sensitivity of GPP to c_a for the VPM (VPM v4.0, VPM v3.0) across all biomes.

Table 5.4: Magnitude of sensitivity of GPP to c_a in VPM (VPM v4.0, VPM v3.0) and DGVMs (w/ CO_2, w/o CO_2). The number in this table corresponds to Figure 5.16 in the main text.

Model	CO_2	Year	β_R^{GPP}
VPM v4.0	**w/ CO_2**		**0.97±0.07**
VPM v3.0	**w/o CO_2**		**0.76±0.05**
DGVMs ensemble (S2, w/ CO_2)	w/ CO_2	2000-2023	0.59±0.16
CABLE-POP			0.68±0.05
CLASSIC			0.39±0.03
CLM5.0			0.56±0.04
ED			0.90±0.06
iMAPLE			0.76±0.05
ISBA-CTRIP			0.60±0.04
JSBACH			0.73±0.05
LPJml			0.39±0.03
LPjwsl			0.49±0.04
LPX			0.53±0.03
PCN			0.60±0.04
VISIT			0.61±0.04
VISIT-UT			0.52±0.04
DGVMs ensemble (S2-S1+S0, w/o CO_2)	w/o CO_2		0.03±0.03
CABLE-POP			-0.08±0.01
CLASSIC			0.05±0.00
CLM5.0			-0.00±0.00
ED			-0.29±0.02
iMAPLE			-0.05±0.00
ISBA-CTRIP			0.02±0.00
JSBACH			0.12±0.01
LPJml			0.22±0.02
LPjwsl			0.04±0.00
LPX			0.12±0.01
PCN			0.10±0.01
VISIT			0.04±0.00
VISIT-UT			0.07±0.01

5.4 Discussions

5.4.1 Global annual GPP estimates

The effects of increased atmospheric CO_2 concentration on plants are well recognized but are very difficult to be quantified, as it has direct effects (e.g., photosynthesis and evapotranspiration) and indirect effects (e.g., leaf traits, leaf area index, water) (Keenan et al., 2023). An increase of leaf area index (LAI) due to rising CO_2 is often considered as one of indirect CO_2 effects, which leads to more light absorption and increased GPP (Donohue et al., 2013; Keenan et al., 2013). Most satellite-based models used LAI and

vegetation indices (e.g., NDVI, EVI), which is related to LAI, to estimate the fraction of light absorbed by canopy, thus partially accounting for the indirect CO_2 effect. This is evidenced by the fact that on average, those models using remote sensing data (VPM v3.0, GOSIF) have noticeably larger global annual GPP estimates and interannual variability and trends than those from the CO_2-exclusive DVGM models (112 ± 17 Pg C;). It is also clear that solely incorporating the indirect CO_2 effects is not sufficient for accurate GPP estimation (Anav et al., 2015; Ryu et al., 2019). Estimates from the 13 DGVM models: the average global GPP under CO_2-inclusive scenarios is 140 ± 11 Pg C yr^{-1}, which is approximately 28 Pg C y^{-1} (25%) larger than average global GPP under CO_2-exclusive scenarios (112 ± 17 Pg C yr^{-1}). Therefore, it is imperative to incorporate direct CO_2 effects into those satellite-based models using light use efficiency (ϵ_{max}) in CO_2 fixation (Prentice et al., 2024).

In this study, we introduced an environmental factor, f(CO_2), to represent the direct CO_2 effect in VPM v4.0. The spatio-temporal distribution of f(CO_2) reveals that the CO_2 direct effect follows a clear spatial pattern, smaller in high latitude but larger in high-productivity tropical and subtropical regions. This distribution pattern is primarily attributable to dynamic representation of χ (c_i/c_a), which integrates the influences of c_a, air temperature, vapor pressure deficit, and elevation (Wang et al., 2017). Previous studies have shown that warm and humid regions typically exhibit a marked CO_2 effect (Piao et al., 2020). According to the least-cost hypothesis, when air temperatures are relatively high and water supply is adequate (i.e., when VPD is low), plants can afford to increase or maintain an optimal stomatal aperture (Medlyn et al., 2011; Prentice et

al., 2014), thereby sustaining higher c_i as c_a rises (Ainsworth et al., 2007). This enhances the relative advantage of carboxylation over photorespiration, leading to a more pronounced net carbon fixation (Ainsworth et al., 2007; Farquhar et al., 1980). Conversely, under conditions of low temperature or significant drought stress, increases in c_a do not translate into comparable increments in c_i (Chaves et al., 2009; Sage et al., 2007). These phenomena have been confirmed by multiple ground-based observational studies (Ainsworth et al., 2007; Collatz et al., 1991; Farquhar et al., 1982; Piao et al., 2013; Sun et al., 2019; Wang et al., 2017), and help explain the particularly strong direct CO_2 effects observed in rainforests, grasslands, and savanna ecosystems in the tropical and subtropical regions. Altogether, these results underscore the substantial and non-negligible influence of the direct CO_2 effect on photosynthesis at the global scale.

In addition to explicitly modeling both direct and indirect effects of CO_2, VPM v4.0 also inherits critical improvement on several environmental and biological factors in VPM v3.0 (L. Pan et al., 2025). The VPM v3.0 considers (1) leaf traits (broadleaf vs. needleleaf) on light absorption by chlorophyll (Pan et al. 2025, AFM), (2) plant function types (C_3 and C_4 photosynthesis payways) on maximum light use effleciency (LUE_{max}, ϵ_{max}) (L. Pan et al., 2025; Yao Zhang et al., 2017), (3) site-specific optimum air temperature parameter ($T_{opt\text{-}site}$) on LUE_{max} (Chang et al., 2021a; Meng et al., 2025; L. Pan et al., 2025; Pan, Xiao, Pan, et al., 2024), and (4) site-specific water scalar on LUE_{max} under dry and normal conditions (Meng et al., 2025; L. Pan et al., 2025). In comparison to those LUE models that use biome-specific optimum temperature parameters ($T_{opt\text{-}biome}$) for photosynthesis, these site-specific parameters have

substantially improved GPP estimates from individual sites to the global level (L. Pan et al., 2025).

VPM v4.0 incorporates the direct CO_2 effect and uses satellite images as input data, representing a major improvement in diagnostic and data-driven TBMs. We selected OCS-derived GPP as a reference because previous research reported that OCS flux-based GPP correlates well with flux tower observations in tropical regions (e.g., eastern Amazonia), providing a relatively robust estimate of tropical GPP (Lai et al., 2024). This consistency highlights the considerable improvement in tropical GPP estimations achieved by VPM v4.0. Given the critical role of tropical rainforests in the global carbon cycle and the widespread underestimation of GPP in these regions by most LUE models (L. Pan et al., 2025; Running et al., 2004; Yao Zhang et al., 2017; Zheng et al., 2020b), this improvement is particularly important. VPM v4.0 emerges as a relatively robust tool for GPP estimation, offering a more reliable foundation and global GPP data product for subsequent research. Further work should integrate other factors such as soil nutrient availability, extreme climatic events, and community ecological processes (Chaves et al., 2009; Norby et al., 2016), which may yield a more comprehensive understanding and quantification of the spatiotemporal variability and underlying uncertainties of global GPP.

5.4.2 Interannual variability and trend of global annual GPP

Many studies have investigated interannual variation and trends of LAI and vegetation greenness (as measured by NDVI or EVI), using time series AVHRR data during 1982-2009 (Zhu et al., 2016) and MODIS data since 2000 (Chen et al., 2019; Gui et al., 2025;

Li et al., 2024). The NDVI anomaly analysis showed continuous increase of NDVI during 2000-2023 in the global land surface (Gui et al., 2025).One publication compared global annual GPP in 1990-2009 from (1) statistical models using flux tower data, FPAR, and climate data, (2) satellite-based models, and (3) DGVMs, and reported a large range of IAV, varying from 0.8 Pg C yr^{-1} in MOD17 to 4.4 Pg C yr^{-1} in JULES, and a large range of trend, varying from 0.005 Pg C yr^{-2} in MOD17 to 0.62 Pg C yr^{-2} in JULES (Anav et al., 2015). In comparison to the DGVMs, most satellite-based models have smaller interannual variability and trends, primarily because they do not explicitly incorporate CO_2 (Anav et al., 2015; Piao et al., 2013).

The interannual variability and trends of global annual GPP are affected by many factors, including increased atmospheric CO_2 concentration, climate change (rainfall, air temperature, PAR, VPD, soil moisture), land use change, and disturbances (fire, insect outbreak) (Beer et al., 2010; Keenan et al., 2016; Kurz et al., 2008; Zhu et al., 2016). Time series GPP data from the EC tower sites were used to evaluate the satellite-based GPP products, including temporal agreement of IAV and trends between them (Pan, Xiao, Pan, et al., 2024; Schaefer et al., 2012). In this study, our comparisons among the models show large ranges of IAV and trend of global annual GPP during 2000–2023 (Table 5.2, Table 5.3). The IAV and trend of global annual GPP differ during 2001-2011 among the four groups of models (DGVMs, satellite-based models using Vc_{max}, satellite-based models using ϵ_{max}, statistical models) (Table 5.2). Although they do not explicitly incorporate CO_2, VPM v3.0, GOSIF, and MOD17 have moderate increasing trends of global annual GPP, which can be attributed to the fact that these

models include vegetation indices and/or SIF data that can partially capture the indirect CO_2 effects. The neglible trend of 0.06 Pg C yr^{-2} in FLUXCOM and negative trends of -0.25 Pg C yr^{-2} in EC-LUE and -0.35 Pg C yr^{-2} in GLASS suggest that further investigations is needed for these models, as they fail to reflect the increases of vegetation greenness and atmospheric CO_2 concentration during 2001-2011.

The CO_2-exclusive DGVMs ensemble has a small interannual trend of 0.17 Pg C yr^{-2} during 2001-2011 (Table 5.2) and 0.03 Pg C yr^{-2} during 2000-2023 (Table 5.3), which reflects the increased negative effect of climate changes on GPP in 2010s. The CO_2-inclusive DGVMs ensemble has a moderate trend of 0.57 Pg C yr^{-2} during 2001-2011 and 0.43 Pg C yr^{-2} during 2000-2023, which also reflects the increased negative effect of climate change on GPP in 2010s. VPM v4.0 reported an interannual trend of 0.89 Pg C yr^{-2} during 2001-2011 and 0.78 Pg C yr^{-2} during 2000-2023. Global annual GPP from VPM v4.0 increased 21 Pg C yr^{-1} from 2000 to 2023. We reviewed the CO_2 sensitivity of GPP (β_R^{GPP}) estimates from previous publications in searching for evidence that may support the estimates of the GPP interannual variability and trends estimated by VPM v4.0. Previous publications reported that β_R^{GPP} varies across the studies but generally falls within a relatively moderate range from 1.3 ± 2.3 from the ice core measurements of atmospheric O_2 isotopes (Ciais et al., 2012) to 1.12 from an analysis framework based on photosynthetic optimization theory at 68 EC tower sites (Chen et al., 2022), 1.1 ± 0.5 from the satellite-derived evapotranspiration with ecosystem water use efficiency models (Cheng et al., 2017), and 0.95 ± 0.2 from the OCS-based methods (Campbell et al., 2017). VPM v4.0 estimates β_R^{GPP} of 0.97, which

falls within this historical estimate range of 0.9 to 1.3 but is higher than 13 models in the CO_2-inclusive DGVMs ensemble (0.39 to 0.90, Table 5.4).

As atmospheric CO_2 concentration has continued to rise, global GPP is expected to increase, especially in tropical regions where the direct CO_2 effect is particularly pronounced (Huntingford et al., 2013). Driven by rising CO_2 concentrations and climate change, global greening, as measured by LAI and GPP, was well documented (Zhu et al., 2016). VPM v4.0 predicts a significantly increasing trend of global annual GPP over 2000-2023, which is considerably higher than the trends reported in many models. The global annual GPP data product from the VPM v4.0 provides more reliable prior data for inversion of terrestrial–atmospheric carbon cycle models.

5.5 Conclusion

The large range of global annual GPP estimates from various models can be attributed to a number of factors, ranging from model structure, variables, algorithms, and parameters as well as input datasets. This study, based on classical biochemical CO_2 assimilation theory in photosynthesis, incorporates the direct CO_2 effect into the VPM model and compares the performance of the CO_2-inclusive version (VPM v4.0) with the CO_2-exclusive version (VPM v3.0) from eddy flux tower sites to the globe. The results indicate that explicitly incorporating the direct CO_2 effect enhances VPM's model performance regarding annual GPP, interannual variability and trend as well as sensitivity to CO_2 of GPP. This improvement is particularly evident in low-latitude, high-productivity regions, where most satellite-based models tend to underestimate GPP. Annual GPP from the CO_2-inclusive VPM v4.0 aligns more closely with EC tower

observations and recent global annual GPP estimates (Lai et al., 2024). The large annual GPP and continued increase of annual GPP during 2000-2023, as predicted by VPM v4.0, shed new light on how to improve accuracy of and reduce uncertainty of GPP across the scales from individual eddy flux tower sites to the globe, which will have significant implications for stablishing a more robust modeling framework for assessing terrestrial carbon fluxes and sink potential under elevated CO_2 conditions.

Chapter 6 : Application of GPP dataset: a case study of post-fire recovery of vegetation productivity in Australia

ABSTRACT

Fires disrupt ecosystems, release carbon, and reduce carbon uptake, which increases atmospheric CO_2 concentration, warms the atmosphere, and fosters more frequent and intense fires. Quantifying post-fire recovery is crucial for understanding the adaptability and resilience of ecosystems to fire disturbances. Observations from satellite-derived active fire (~1-km) and Gross Primary Productivity (GPP) products reveal that Australia experiences extensive fires annually, reducing vegetation productivity. Here we analyze the post-fire GPP recovery trajectories of 1.7×10^6 fire-affected pixels (or 1.5×10^6 km^2) in Australia between 2011 and 2019, of which 1.3 × 106 pixels (1.2×10^6 km^2) experienced a single fire (single-fire pixels), and 0.4×10^6 pixels (0.3×10^6 km^2) experienced two or more fires (multiple-fire pixels). We found that Australia's post-fire GPP recovery was strong and rapid. 88% of single-fire pixels recovered to 135% of the pre-fire level in an average of 2.3 years, while 86% of multiple-fire pixels recovered to 115% of the pre-fire level in an average of 1.2 years. NonForest ecosystems (e.g., grasslands, shrublands, and savannas) exhibited a higher post-fire recovery magnitude (138% for single-fire pixels and 115% for multiple-fire pixels) compared to Forest (110% for single-fire pixels and 108% for multiple-fire pixels). This rapid and robust post-fire GPP recovery is significantly influenced by post-fire precipitation, fire (i.e., fire frequency, intensity) and fire severity (damage, impacts;

a metric of resistance of terrestrial ecosystems to fire). Specifically, higher fire severity and higher post-fire precipitation have a positive impact on post-fire recovery, whereas increased fire frequency has a negative impact. Furthermore, fire dynamics has a smaller role in the long-term interannual continental GPP changes than climate or land-use changes, as strong and rapid GPP recovery offsets the short-term fire-induced GPP losses.

6.1 Introduction

Wildfires are becoming increasingly frequent globally, driven by climate variability (and trends) (Canadell, Meyer, et al., 2021; Jones et al., 2022). Fires directly alter terrestrial ecosystems by disrupting their structure and function, altering soil composition, reducing biodiversity, and impairing vegetation recovery, which can lead to ecosystem degradation (Canadell & Jackson, 2021). Additionally, fire emissions reduce terrestrial carbon stocks and increase the atmospheric carbon dioxide concentration, triggering feedback effects on the climate system that further escalate fire risk, resulting in fire cycles (van der Velde et al., 2021; J. Zhao et al., 2024; Zheng et al., 2023).

Australia experiences frequent and intense fires that profoundly shape its ecosystems and carbon cycling (van der Velde et al., 2021; Villalobos et al., 2023). Large-scale fire events directly affect the release of terrestrial carbon in Australia (Burton et al., 2024). One study estimates that fires in Australian grasslands emitted around 280 Tg CO_2 per year between 1997 and 2013 (Beringer et al., 2015). During the extreme 2019 southeastern Australia forest fire event, results from five inventories

indicate total carbon emissions of approximately 275 Tg CO_2, however, these figures may still be conservative, as alternative assessments based on atmospheric CO measurement suggest that emissions could have reached 517–867 Tg CO_2 (van der Velde et al., 2021), underscoring the vast scale of fire-induced carbon release in Australia.

Beyond the direct effect of carbon emissions, biomass mortality and the loss of functional leaf area due to fire significantly weaken the capacity of ecosystems to sequester carbon (Beringer et al., 2007; Cernusak et al., 2006). In a northern Australian savanna, for instance, fire transformed the ecosystem from a carbon sink into a carbon source, primarily because of the marked decline in post-fire productivity—an impact on the carbon balance comparable to direct fire emissions (Beringer et al., 2007). Similarly, in a semiarid woodland in southern Australia, GPP decreased by 65% following a fire (Sun et al., 2016). These considerable carbon emissions and the associated reduction in carbon uptake can sharply diminish aboveground biomass, and in certain years, their influence on the carbon balance even surpasses that of climatic factors. For example, one study indicates that the 2019 southeastern Australia forest fire event was responsible for 85% of the total annual biomass loss (Qin et al., 2022), with the remainder attributed to drought and land clearing. Overall, existing research suggests that fires are a primary driver of high interannual variability in carbon fluxes across the Australian continent.

Carbon losses from fires are offset by post-fire vegetation recovery (Bartels et al., 2016; Qin et al., 2022). The post-fire recovery trajectory reflects the natural fire-

adaptation mechanisms that Australian ecosystems have developed over long-term evolutionary processes (Karavani et al., 2018; Nolan et al., 2021). These processes are influenced by various factors, including fire behavior (e.g., intensity and frequency), climatic conditions (e.g., precipitation), and biome characteristics (Nolan et al., 2021; Sun et al., 2016; Turner, 2010), such that at large spatial scales, different regions and biomes with varying biomass densities may exhibit divergent post-fire recovery trajectories. This spatial and biome-specific heterogeneity shapes post-fire carbon dynamics, encompassing spatiotemporal patterns of carbon fluxes, carbon sinks, biomass, and atmospheric CO_2. To date, current studies on post-fire vegetation recovery in Australia mainly focus on individual fire events or short-term impacts (Beringer et al., 2007; Byrne et al., 2021; Cernusak et al., 2006; Driscoll et al., 2024; Sun et al., 2016), leaving a gap in our comprehensive understanding of recovery trajectories over broader temporal and spatial scales. Systematically and comprehensively quantifying post-fire recovery processes is therefore critical for deepening our understanding of ecosystem resilience to fire disturbances and the positive feedback mechanisms linking fires and climate (Byrne et al., 2021; Williams et al., 2004). In addition, considerable uncertainty remains regarding fire-induced carbon anomalies and vegetation dynamics simulations in current regional-scale ecosystem models (Hantson et al., 2016; Quegan et al., 2011; Van Der Werf et al., 2017). If the terrestrial ecosystem response to wildfires can be accurately captured through long-term observations, it will furnish ecosystem process models with more robust parameters and algorithms, thereby enhancing the capacity to evaluate carbon budgets, fire risk, and climate change across broader spatial

and temporal scales.

In this chapter, we analyzed the short-term post-fire GPP recovery of all pixel-fire events (i.e., fires in forests, savannas, shrublands, and grasslands) across Australia from 2011 to 2019, using GPP data from 07/2000 to 06/2023. The analyses included all 1.7 × 10^6 fire-affected pixels (1.5 × 10^6 km^2) across Australia during the study period, comprising 1.3 × 10^6 single-fire pixels (1.2 × 10^6 km^2) and 0.4 × 10^6 multiple-fire pixels (0.3 × 10^6 km^2), the two categories being distinguished because fire frequency influences post-fire recovery. We investigated three scientific questions: (1) What are the post-fire GPP recovery trajectories (i.e., recovered/unrecovered, magnitude, slope, and time) in single-fire and multiple-fire pixels? (2) How do post-fire precipitation and fire severity influence recovery? and (3) What are the relative roles of fire on the long-term interannual GPP change? The multi-year record of active fire and GPP products derived from satellites enables a comprehensive understanding of post-fire recovery trajectories to an extent not previously possible (Bao et al., 2024; Qin et al., 2022; Woodgate et al., 2025; Xu et al., 2024). A deeper understanding of post-fire GPP recovery trajectories and their long-term impacts is essential for assessing ecosystem resilience, anomalies in atmospheric CO_2, and climate change dynamics.

6.2 Materials and Methods

6.2.1 Forest and NonForest map

Differences in biomass (herbaceous and woody) and ecosystem structure (understory and overstory vegetation, canopy, cover, and leaf area) among various land cover and

plant functional types may result in differing responses to fire and post-fire recovery. Therefore, we separately analyzed post-fire recovery in Forest and NonForest (grassland, savanna, scrublands, etc.). We used the forest map in 2010 year developed by Qin et al. (2021), which employed PALSAR imagery and Moderate Resolution Imaging Spectroradiometer (MODIS) imagery to generate a 50-meter spatial resolution forest map of Australia (Figure 6.1). This map used the forest definition (areas exceeding 0.5 hectares with a tree canopy cover greater than 10% and trees reaching a height of over 5 meters) provided by the United Nations Food and Agriculture Organization (FAO). It is important to note that the Australian government has its unique definition of forest (areas exceeding 0.2 hectares with a tree canopy cover greater than 20% and trees reaching a height of over 2 meters), which includes shrubs and short trees. Different forest maps lead to varying statistical conclusions (Pan., et al 2025, GCB). In this study, our primary objective in distinguishing between Forest and NonForest is to explore the differences in post-fire recovery between pixels dominated by trees and pixels dominated by grasses and shrubs. Therefore, we used the FAO definition forest maps (Qin et al., 2021).

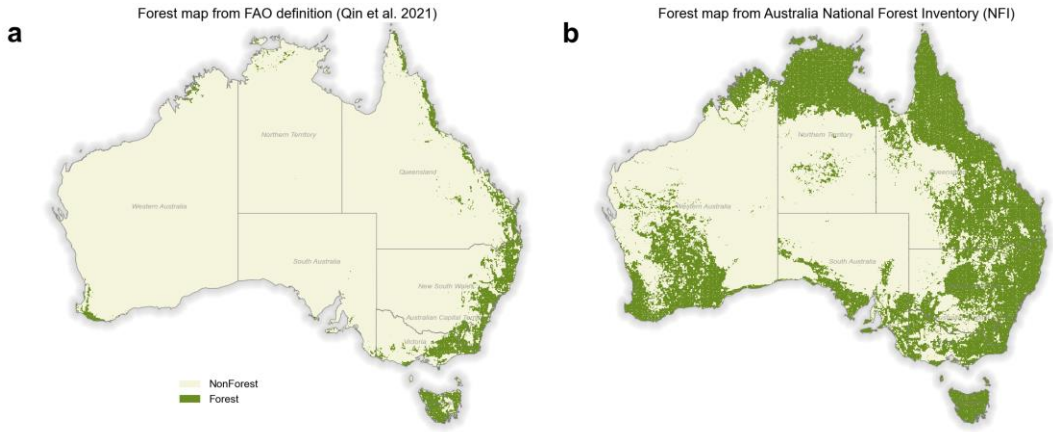

Figure 6.1: Forest maps in Australia. a. The 50-meter forest map (2010) derived from the FAO definition was reported by Qin et al. (2021), b. The 100-meter forest map based on the Australian official NFI definition was reported by Australia's State of the Forests Report (2018, 2023).

6.2.2 Fire pixels

MODIS provides the MCD64A1 500-meter global burned area product and the MOD14A1 1-km global active fire product. MCD64A1 has been reported to have significant omission errors (~90%) and commission errors (~50%) in the tropics (Boschetti et al., 2019). Burned area (BA) products (e.g., MCD64A1 and CCI Fire) do not align well with active fire products in Australia, primarily due to the omission of small fires (Boschetti et al., 2019). Active fire products offer absolute detection of sufficiently intense fires and identify weaker, easily missed fire spots by comparing thermal infrared and brightness temperature anomalies with surrounding pixels. The active fire product has been reported to effectively reduce fire omission errors in the tropics (Giglio et al., 2003; Justice, Giglio, et al., 2002; Masocha et al., 2018). Previous studies have reported that MOD14A1 can detect small fire patches in grasslands, savannas, and forests that are difficult to identify by MCD64A1 (Devineau et al., 2010; Yin, 2020). Additionally, active fire products directly record high thermal radiation signals from fire-affected areas, thereby avoiding the complexities and potential errors associated with burned area algorithms. Therefore, in this study, we mainly used the 1-km MOD14A1 v6.1 daily active fire product to define fire events (Giglio, 2015), while the 500-meter MCD64A1 v6.1 (Giglio, 2021) and the 250-meter CCI Fire v5.1

(Lizundia-Loiola et al., 2020) BA dataset served as references for cross-comparison with MOD14A1 v6.1.

Annual active fire pixel maps are generated based on the timing of the fire and the growing season (GS). The annual active fire search period was defined from July (year) to June (year+1) to cover the entire growing season. We then examined the temporal sequence of active fire occurrences relative to the growing season, categorizing them into three types: Fire before GS, Fire within GS, and Fire after GS. Fire before GS and Fire within GS are the predominant fire types in Australia, accounting for 58% and 38% of total fires, respectively (Pan., et al 2025, GCB). These two fire types directly influenced productivity for that year; therefore, all Fires before GS and Fires within GS were included in that year's analysis. Fire after GS constitutes a small portion (4%) and primarily affects productivity in the subsequent year, thus being incorporated into the next year's analysis. These criteria generated 1-km annual active fire pixel maps from 2011 to 2019 (nine years). Fires were subsequently classified into Forest-fire (Forest) and NonForest-fire (NonForest) using the forest map.

Each active fire pixel for each year is considered a pixel-fire event (f_i). The fire frequency (ω_f) of individual events was then stacked as:

$$\omega_f = \sum_{i=1}^{n} f_i \quad (6.1)$$

Where *n* is the total number of years, f_i =1 if a pixel-fire event was detected in the i-th year, and f_i = 0 if not.

6.2.3 Fire severity

We calculated the 500-meter and 8-day Normalized Burn Ratio (NBR), an index widely

used to describe vegetation-related fire severity due to its sensitivity to green vegetation and moisture (García et al., 1991; Miller et al., 2007):

$$\mathrm{NBR} = \frac{\rho_{\mathrm{nir}} - \rho_{\mathrm{swir2}}}{\rho_{\mathrm{nir}} + \rho_{\mathrm{swir2}}} \tag{6.2}$$

Where ρ_{nir} and ρ_{swir2} are the surface reflectance values of near infrared (841-876 nm) and short-wave infrared (2105-2155 nm) bands from the MOD09A1 v6.1 surface reflectance product (500-meter, 8-day) (Vermote, 2015). We generated the NBR time series for fire events at an 8-day temporal resolution annually. Differenced NBR (dNBR) represents the absolute vegetation loss caused by the fire and is calculated as the difference between the pre-fire and post-fire NBR:

$$\mathrm{dNBR} = \mathrm{NBR}_{\text{pre-fire}} - \mathrm{NBR}_{\text{post-fire}} \tag{6.3}$$

Where $\mathrm{NBR}_{\text{pre-fire}}$ is the mean of two observations (16-day) taken before the fire, while $\mathrm{NBR}_{\text{post-fire}}$ is the mean of two observations (16-day) taken after the fire. Given the diverse landscape types the study area covers, we used the Relative dNBR (RdNBR) to quantify fire impacts on vegetation across temporal and spatial scales (Miller et al., 2007):

$$\mathrm{RdNBR} = \frac{\mathrm{dNBR}}{\sqrt{\mathrm{NBR}_{\text{pre-fire}}}} \tag{6.4}$$

The fire severity defined by RdNBR mainly reflects the relative change in vegetation loss before and after the fire. Reference values for fire severity are currently based on literature review (Botella-Martínez et al., 2017; Miller et al., 2007), where RdNBR above 0.8 is considered high, RdNBR between 0.4 and 0.8 is considered moderate, and RdNBR below 0.4 is considered low.

6.2.4 Gross primary productivity data

We used the global GPP dataset estimated by the Vegetation Photosynthesis Model (VPM v3.0) in Chapter 4. In this study, post-fire recovery analyses are reported primarily using GPP from VPM in the main text.

6.2.5 Leaf area index data

Leaf Area Index (LAI) data is from the MCD15A3H v6.1 LAI product (500-meter, 4-day) (Myneni et al., 2015). LAI was then aggregated by annual means from July (year) to June (year + 1) to match the fire years as described in Australia.

6.2.6 Vegetation index data

Vegetation indices, including Normalized Difference Vegetation Index (NDVI), Enhanced Vegetation Index (EVI), and Near-Infrared Reflectance of Vegetation (NIRv), were calculated using reflectance bands from the MOD09A1 v6.1 surface reflectance product (500-meter, 8-day) (Vermote, 2015). EVI, NDVI, and NIRv were then aggregated by annual means from July (year) to June (year + 1).

6.2.7 Analysis of post-fire recovery of GPP during 07/2000 to 06/2023

We used the time series data of fire events within individual pixels during 07/2000 – 06/2023 to count the number of fire events for each pixel (fire frequency, ω_f), and those fire-affected pixels are grouped into two categories: single-fire pixels ($\omega_f = 1$) and multiple-fire pixels ($\omega_f > 1$). Time series GPP data of each fire-affected pixel is divided into two periods based on the year the fire occurred: the baseline period (pre-fire) and the transition period (post-fire).

The baseline period was defined as spanning from 2000 to the year before the fire, ensuring a minimum of 11 years of data for reference and extending over multiple years. The GPP during the baseline period is used to represent the undisturbed state of the ecosystem. Years during the baseline period with extreme environmental conditions, such as fires, floods, or droughts, were excluded. The filtering process specifically involves (1) excluding fire years, the wettest year, and the driest year; (2) calculating the mean and standard deviation (σ) of the GPP for the remaining years and excluding any years where GPP fell outside the range of mean ± σ; and (3) estimated the mean of the remaining years as the baseline.

The transition period is the period following the fire year, during which vegetation either transitions toward recovery or remains unrecovered. This period was generally defined as the period from the fire year until the final year of the study period (fire year - 2023 in single-fire pixels), or until the next fire disturbance (fire year - next fire year in multiple-fire pixels). We used the following criteria to determine whether a pixel-fire event had recovered during the transition period:

$$\begin{cases} \text{recovered} & \text{if } t \in T\ (GPP_{(t)} \geqslant GPP_{baseline}) \\ \text{unrecovered} & \text{otherwise} \end{cases} \tag{6.5}$$

where T represents the entire transition period, t denotes a specific year within T, and $GPP_{(t)}$ refers to the value of GPP for the year t. A fire event was considered recovered if GPP exceeded the baseline in any year t within the transition period; otherwise, it was marked as unrecovered. Each year, all pixel-fire events were classified into a binary map as either recovered or unrecovered. ω_r is defined as the recovery frequency within the fire-affected pixels:

$$\omega_r = \frac{\sum_{i=1}^{\omega_f} r_i}{\omega_f} \quad (6.6)$$

With $r_i = 1$ if the pixel-fire event was recovered in the i-th fire year and $r_i = 0$ otherwise. ω_f is fire frequency. $\omega_r = 1$ indicates that the pixel has recovered from all fire events in the pixel, while $\omega_r = 0$ indicates that the pixel is unrecovered from any of the pixel-fire events. For multiple-fire pixels, $0 < \omega_r < 1$ indicates that the pixel has partially recovered. Three metrics were calculated to quantify the post-fire recovery trajectories at one pixel-fire event: relative recovery magnitude (φ_{rec}) of a pixel, relative recovery slope (β_{rec}) of a pixel, and the number of years required for recovery (Y_{rec}) of a pixel. Specifically:

φ_{rec} is calculated as the percentage of GPP in the recovery year relative to the baseline during the transition period, in case of complete recovery:

$$\varphi_{rec} = \frac{GPP_{rec}}{GPP_{baseline}} \times 100\% \quad (6.7)$$

Where GPP_{rec} is GPP in the first year in which GPP exceeds the baseline GPP. In cases where recovery does not occur (unrecovered pixels), φ_{rec} is defined as the percentage of the maximum GPP observed during the transition period (GPP_{max}) relative to the baseline:

$$\varphi_{rec} = \frac{GPP_{max}}{GPP_{baseline}} \times 100\% \quad (6.8)$$

β_{rec} is the regression coefficient (slope) of the linear regression of the annual net GPP recovery percentage relative to baseline GPP during the transition period. t is the year during the transition period:

$$\beta_{rec} = \frac{1}{t} \frac{GPP_{t+1} - GPP_t}{\text{Baseline GPP}} \times 100\% \quad (6.9)$$

Y_{rec} is estimated in recovered fire-affected pixels. Generally, Y_{rec} ranged from 1 to 11 years. In some cases, Y_{rec} equaled 0, indicating recovery occurred within the same year. One metric was calculated to quantify the post-fire recovery trajectory for all pixel-fire events in Australia: ratio of recovered pixel-fire events relative to the pixel-fire events ($Ratio_{rec}$) in Australia:

$$Ratio_{rec} = \frac{\sum_{i=1}^{m} \omega_r \times \omega_f}{\sum_{i=1}^{m} \omega_f} \times 100\% \quad (6.10)$$

Where *m* is the count of fire-affected pixels. $Ratio_{rec}$ was calculated at single-fire pixels and multiple-fire pixels separately.

6.2.8 Analysis for attribution of driving factors of post-fire recovery

Australia's ecosystem productivity is predominantly driven by precipitation (Byrne et al., 2021). We explored the effects of precipitation and fire severity on recovery. Here, we used precipitation data from the ERA5-Land reanalysis climate dataset (Muñoz Sabater, 2019), which has a spatial resolution of 0.1° and an hourly temporal resolution and was aggregated by annual sums spanning from July (year) to June (year+1). Post-fire precipitation was quantified by precipitation anomaly (Δ mm):

$$\text{Precipitation anomaly} = \overline{p_{max}} - \overline{p_{mean}} \quad (6.11)$$

For a recovered fire event, $\overline{p_{max}}$ is defined as the maximum annual precipitation from the fire year to the recovered year. For an unrecovered fire event, $\overline{p_{max}}$ is the maximum annual precipitation for the entire transition period. $\overline{p_{mean}}$ is the multi-year mean annual precipitation from the year 2000 to the fire year.

All fire events were then categorized into subgroups based on different intervals of precipitation anomalies and fire severity (RdNBR). Subgroups with sufficient fire

events were selected to ensure statistical significance. For the All and NonForest categories, subgroups with at least 1000 fire events were selected, while subgroups with at least 100 fire events were selected for the Forest category.

$Ratio_{rec}$, φ_{rec}, and β_{rec} were calculated within each subgroup. In each subgroup, $Ratio_{rec}$ was calculated using Eq. (6.10), while φ_{rec} and β_{rec} were calculated as the mean values of all fire-affected pixels within the subgroup. We then used the logarithmic model to explore the relationship between $Ratio_{rec}$, φ_{rec}, and β_{rec} with precipitation anomalies under various fire severities and calculated the significance.

For the recovered fire event, the timing and amount of precipitation may impact Y_{rec}. Here, we used an index to quantify the temporal distribution of precipitation, the Normalized Precipitation Timing Index (NPTI), which integrates the temporal variation characteristics of post-fire precipitation (Pan, et al 2025):

$$NPTI = \frac{\sum_{i=1}^{n} e^{-\lambda i} \times \frac{p_i}{\overline{p_{mean}}}}{\sum_{i=1}^{n} e^{-\lambda i}} \quad (6.12)$$

Where λ is the decay constant. We used λ=0.5 because when n = 11 (maximum recovery years), $e^{-\lambda i}$ tends to 0. i represents the i-th year after the fire, n is Y_{rec}, and p_i is the annual precipitation for the i-th year. The exponential decay parameter was designed to adjust the sensitivity to both the timing and amount of precipitation, giving more weight to early precipitation and less to later precipitation. The index is normalized by the multi-year mean precipitation ($\overline{p_{mean}}$), allowing for comparison across regions with varying precipitation conditions.

We analyzed the distribution of NPTI values across all recovered pixels under

various precipitation scenarios, as well as the NPTI values for four representative precipitation scenarios (Figure 6.2). NPTI values were categorized into four scenarios based on different post-fire precipitation patterns between the fire year and the recovery year: consistently low precipitation (consistently low), low early precipitation followed by high late precipitation (late high), high early precipitation followed by low late precipitation (early high), and consistently high precipitation (consistently high). High and low precipitation were defined relative to the multi-year mean precipitation, with the early and late corresponding to the first and second half of the period. When post-fire precipitation was consistently low, all NPTI values were below 1, with an interquartile range of 0.67 to 0.88. Under late high precipitation, NPTI values increased slightly, though most remained below 1, with an interquartile range of 0.77 to 1.05. When precipitation was early high, most NPTI values exceeded 1, with an interquartile range of 0.99 to 1.23. For consistently high precipitation, all NPTI values exceeded 1, with an interquartile range of 1.09 to 1.34. Four representative fire events show specific NPTI values under four post-fire precipitation scenarios, indicating that NPTI effectively captures the influence of precipitation timing and amount, with higher values when precipitation occurs earlier and in greater magnitudes.

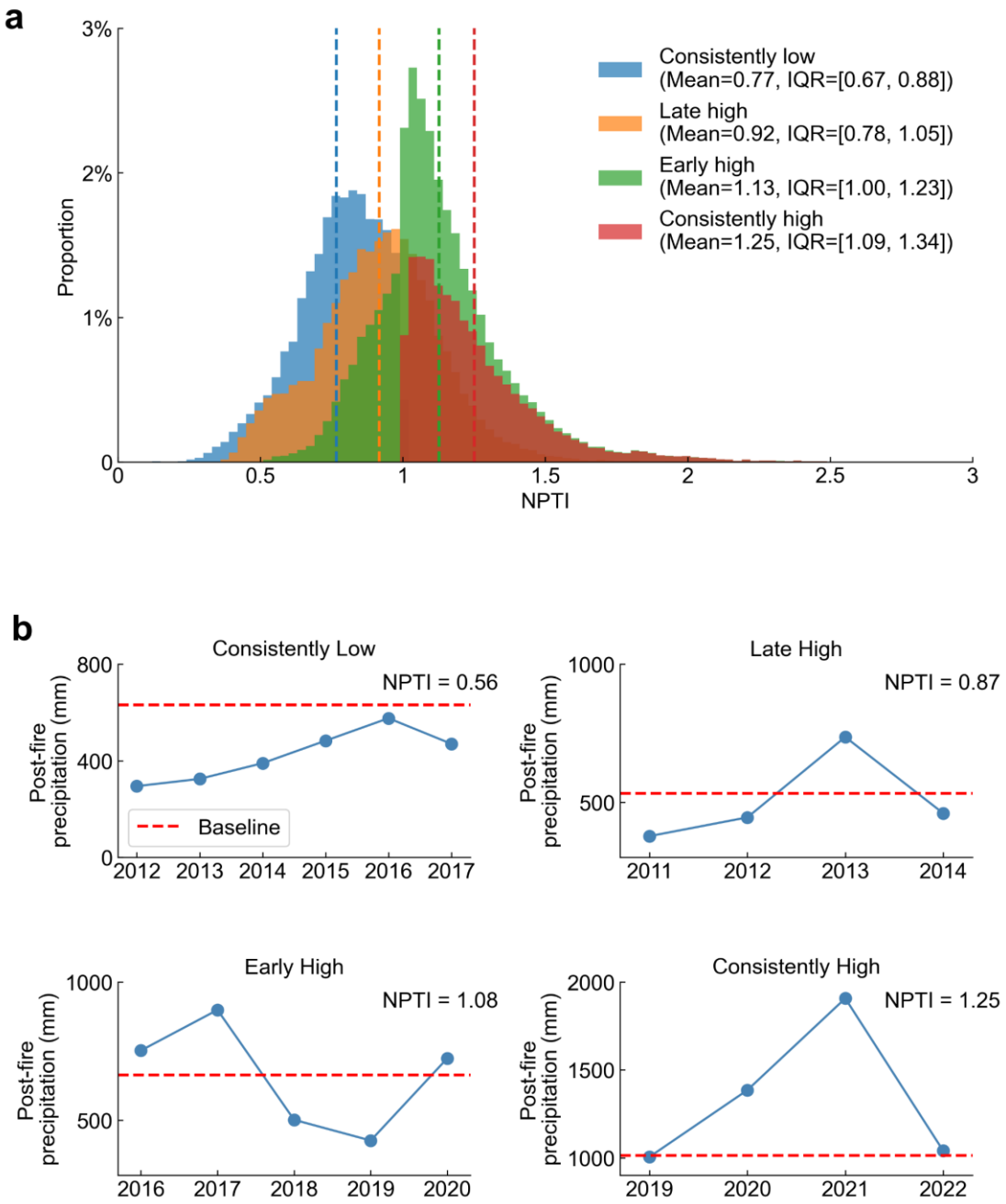

Figure 6.2: The distribution of NPTI values across different post-fire precipitation scenarios. a. The distribution of NPTI under four precipitation scenarios: consistently low (consistently low), low early followed by high late (late high), high early followed by low late (early high), and consistently high (consistently high). b

selected four representative sites to show specific NPTI values under four post-fire precipitation scenarios.

6.2.9 Impacts of fire on interannual GPP change

We explored the components of interannual GPP change (ΔGPP) over the long term (from 2000 to 2022). ΔGPP was calculated as the difference between year *t* and year *t*-1. For each fire-affected pixel, ΔGPP can be decomposed into four subcategories:

$$\Delta GPP = \Delta GPP_{NN} + \Delta GPP_{FN} + \Delta GPP_{NF} + \Delta GPP_{FF} \quad (6.13)$$

where ΔGPP_{NN} refers to the ΔGPP of the fire occurred in consecutive years (year t and year t-1) with no fire, driven primarily by climate change and land use change. ΔGPP_{FN} refers to the ΔGPP of the fire occurred in the year *t*-1, representing the annual climate-induced GPP recovery. ΔGPP_{NF} refers to the ΔGPP of the fire occurred in the year *t*, and ΔGPP_{FF} refers to the ΔGPP of the fire occurred in consecutive years (year *t* and year *t*-1). ΔGPP_{NF} and ΔGPP_{FF} are fire-induced GPP losses. We selected a representative pixel to illustrate the analytical process (Figure 6.3).

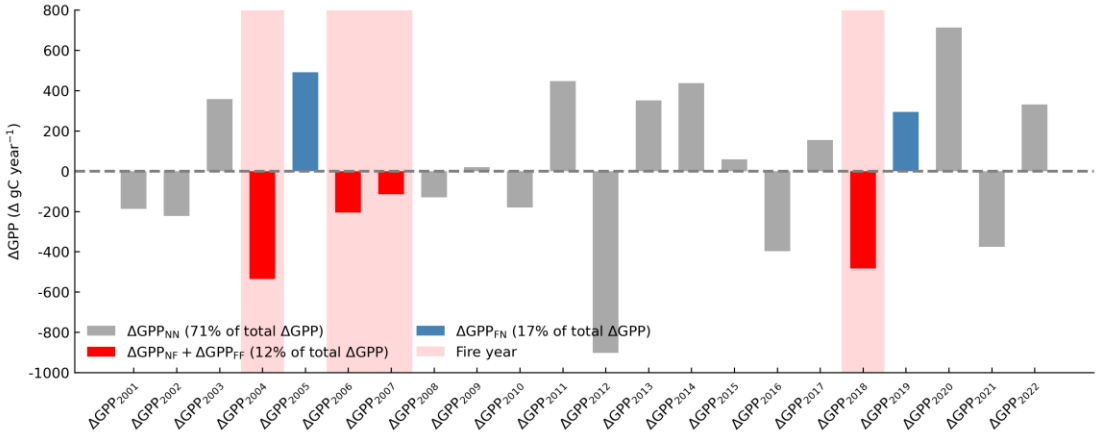

Figure 6.3: Analysis of impacts of fire on interannual GPP change at a selected fire pixel (133.9206, -16.0256). ΔGPP was calculated as the difference between year *t*

and year *t*-1. ΔGPP_{NN} refers to the ΔGPP of the fire occurred in consecutive years (year t and year t-1) with no fire, driven primarily by climate change and land use change. ΔGPP_{FN} refers to the ΔGPP of the fire occurred in the year *t*-1, representing the annual climate-induced GPP recovery. ΔGPP_{NF} refers to the ΔGPP of the fire occurred in the year *t*, and ΔGPP_{FF} refers to the ΔGPP of the fire occurred in consecutive years (year t and year t-1). ΔGPP_{NF} and ΔGPP_{FF} are fire-induced GPP losses. The numbers in parentheses in the legend indicate the contribution to the total ΔGPP.

The contribution of each subcategory ($|\Delta GPP_i|$) to the total ΔGPP is estimated as:

$$\text{Contribution to } \Delta GPP = \frac{|\Delta GPP_i|}{\sum |\Delta GPP_i|} \times 100\% \quad (6.14)$$

Here, we quantified the contribution of ΔGPP_i on ΔGPP at fire-affected pixels and the contribution of ΔGPP_i on ΔGPP at the entire Australian.

6.3 Results

6.3.1 Characteristics of fires in Australia during 2011-2019

Observations of active fire from satellite products (MOD14A1, 1-km resolution) reveal that from 2011 to 2019, 1.7×10^6 pixels (1.5×10^6 km^2) were affected by active fires, covering 19% of Australia's land area (Figure 6.4a, b). We found that 1.3×10^6 pixels (1.2×10^6 km^2) experienced only one fire event since 2011 (single-fire pixels), distributed over temperate forests and savanna fire-prone zones, covering 15% of Australia's land area. Of these, the number of extreme fire pixels in 2019 was 0.2×10^6. Conversely, 0.4×10^6 pixels (0.3×10^6 km^2) experienced two or more fire events

(multiple-fire pixels), primarily within the savanna fire-prone biome, covering 4% of Australia's land area. The annual fire-affected pixels (or area) varied across years, ranging from 0.1×10^6 (0.1×10^6 km^2) to 0.4×10^6 pixels (0.4×10^6 km^2) during the study period, covering 2-5% of Australia's land area (Figure 6.4c). Non-forest fire (NonForest), including savannas, shrublands, and grasslands, were dominant, accounting for 94% of total fire-affected pixels and are the primary contributors to the interannual variability of burned areas over the years (Figure 6.4c). Forest-fire (Forest) comprised only 6% of total fire-affected pixels and had small interannual variability except for the extreme southeastern "Black Summer" forest fires of 2019 (Figure 6.4c).

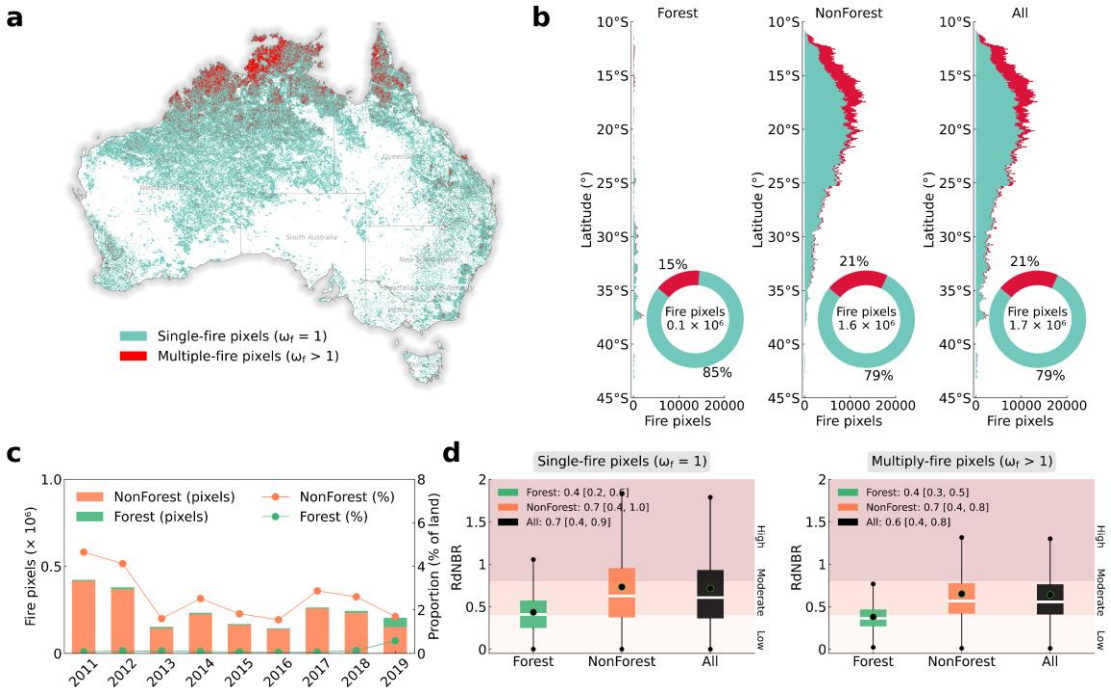

Figure 6.4: Fire pixels and events in Australia from 2011 to 2019. a show the spatial distribution of single-fire pixels ($\omega_f = 1$) and multiple-fire pixels ($\omega_f > 1$) (1-km) during the study period. b summarizes the fire events and proportion of fire pixels for Forest, NonForest, and all (Forest and NonForest) along the latitude gradient

in 0.1° bins. c reports the interannual variability in pixel-fire events and the corresponding proportion of Australia's land area for NonForest and Forest. d reports the fire severity (RdNBR) for pixel-fire events in single-fire pixels ($\omega_f = 1$) and in multiple-fire pixels ($\omega_f > 1$). Severity categories: Low (RdNBR≤0.4), moderate (0.4<RdNBR≤0.8), and High (RdNBR>0.8). Black solid dots and white solid lines are the mean and median values in boxplot. The numbers in the legend are the mean values and interquartile range (mean [interquartile range]).

Fire severity, defined by the RdNBR, shows a gradient from low to high in NonForest pixels, and a gradient from low to moderate in Forest (Figure 6.4 d). Higher RdNBR in NonForest indicates that fires generally cause more severe damage to non-forests than forests. 81% of NonForest had minimum daily GPP after fire below 1 gC m^{-2} day^{-1} (Figure 6.5d), which means that NonForest lost their photosynthetic capacity just after fires. While Forest experienced higher daily GPP instant losses after fires (Figure 6.5b), the minimum daily GPP after fire averages 2.2 gC m^{-2} day^{-1} (Figure 6.5d), suggesting that fires did not kill all the trees, and these pixels kept a limited amount of photosynthesis activities.

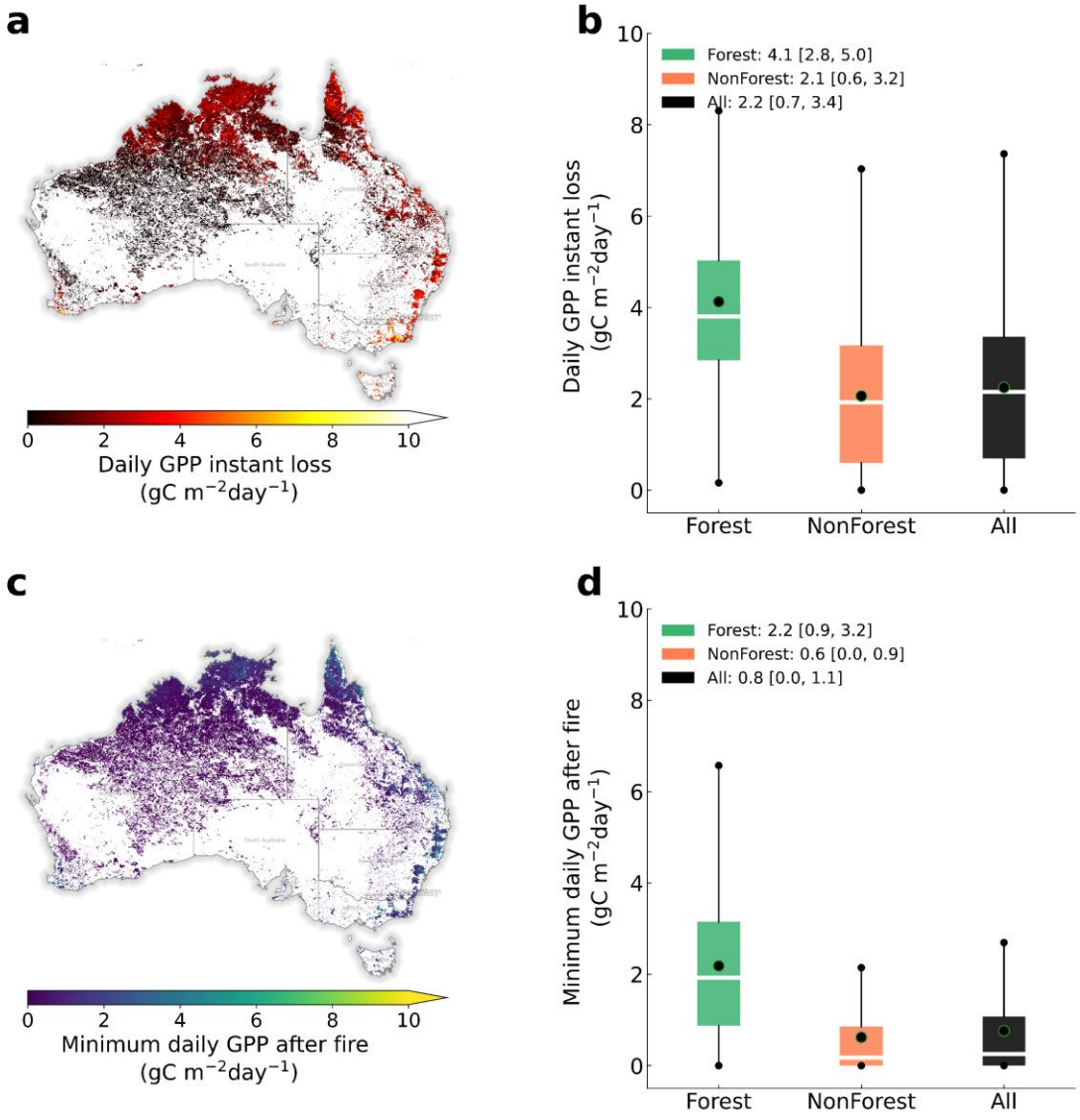

Figure 6.5: The impact of fire on instantaneous daily GPP. Daily GPP instant loss was calculated using a time window of three GPP observations (24-day) following fire events. Minimum daily GPP after fire is minimal GPP among the three GPP observations (24-day period) following the fire. a shows the spatial distribution of daily GPP instant loss, while b is the distribution of GPP instant loss for Forest, NonForest, and All. c shows the spatial distribution of minimal daily GPP after fire, while d is the distribution of minimal daily GPP after fire for Forest,

NonForest, and All. Black solid dots and white solid lines are the mean and median values in boxplot. The numbers in the legend are the mean values and interquartile range (mean [interquartile range]).

6.3.2 Post-fire recovery in single-fire pixels (1-km spatial resolution)

Of the 1.3×10^6 single-fire pixels (1.2×10^6 km^2), the post-fire recovery ratio (Ratiorec) is 88% (Figure 6.6a, b), indicating that 88% of pixel-fire events recovered to pre-fire level and are distributed across the entire latitudinal gradient. 12% of pixel-fire events have remained unrecovered yet and are predominantly distributed in central and southwestern Australia's arid desert regions. Both Forest and NonForest show high Ratiorec, with the NonForest recovery ($Ratio_{rec}^{NonForest}$ = 88%) being slightly higher than the Forest recovery ($Ratio_{rec}^{Forest}$ = 83%). The average Yrec of single-fire pixels is 2.3 years (Figure 6.6c). Y_{rec} varied across years, with a general pattern of shorter Yrec for NonForest than Forest. The mean and range of relative recovery magnitude (φ_{rec}) for single-fire pixels are 135% [110%, 156%], showing a widespread pattern of overcompensation (Figure 6.6d). Specifically, NonForest has a higher mean value and broader range of φ_{rec} (138% [111%, 160%]) than Forest (110% [103%, 117%]). The mean and range of relative recovery slope (β_{rec}) for single-fire pixels are 8% [2%, 13%]. Forest (10% [4%, 15%]) was slightly higher than NonForest (8% [2%, 12%]) (Figure 6.6e). It is noteworthy that in the 12% of pixel-fire events have remained unrecovered, 10% of pixel-fire events have β_{rec} very low (β_{rec} <1%), indicating that these unrecovered areas have experienced degradation, while 2% of pixel-fire events are due to without enough time to recover.

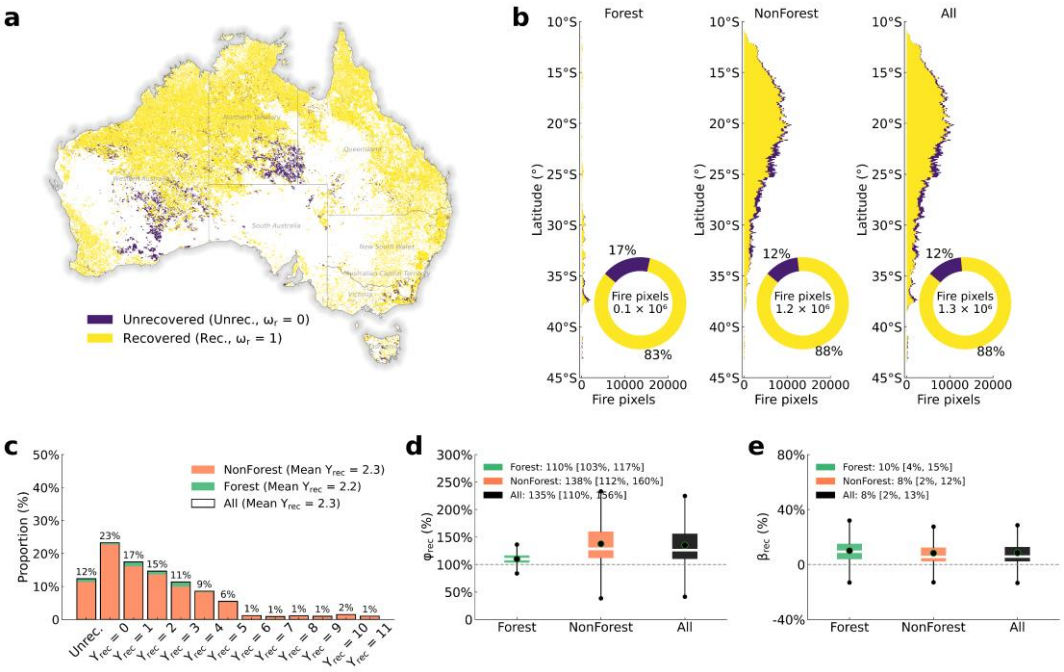

Figure 6.6: Post-fire recovery of single-fire pixels. a show the spatial distribution of unrecovered and recovered fire-affected pixels. b summarizes the counts of fire-affected pixels and proportion of unrecovered and recovered pixel-fire events for Forest, NonForest, and all (Forest and NonForest) along the latitude gradient in 0.1° bins. c shows the proportion of pixels with different Y_{rec} values among all fire-affected pixels. d and e show the distribution of the GPP recovery magnitude in pixels with complete recovery (φ_{rec}) and the temporal slope of annual relative GPP recovery (β_{rec}) for Forest, NonForest, and All. Black solid dots and white solid lines are the mean and median values in boxplot. The numbers in the legend are the mean values and interquartile range (mean [interquartile range]).

6.3.3 Post-fire recovery in multiple-fire pixels (1-km spatial resolution)

Of the 0.4 × 10^6 multiple-fire pixels (or 0.3 × 10^6 km^2), 71% fully recovered, 1%

remained unrecovered, and 27% partially recovered (Figure 6.7a, b). Using Eq. (6.10), the average $Ratio_{rec}$ was 86%, which is only 2% lower than that in single-fire pixels. The NonForest recovery ratio ($Ratio_{rec}^{NonForest}$ = 86%) is higher than the one of Forest ($Ratio_{rec}^{Forest}$ = 80%). Notably, under similar $Ratio_{rec}$, multiple-fire pixels had notably shorter Y_{rec} (1.2 years) than single-fire pixels (2.3 years). NonForest has shorter Y_{rec} than Forest, consistent with observations in single-fire pixels (Figure 6.7c). The mean and range of φ_{rec} for multiple-fire pixels show overcompensation (115% [105%, 123%]) as well but lower than in single-fire pixels (135% [110%, 156%]), indicating that increased fire frequency negatively impacts the recovery magnitude in both Forest and NonForest (Figure 6.7d). β_{rec} in multiple-fire pixels was slightly higher than in single-fire pixels (Figure 6.7e). The higher recovery slope highlights the adaptability of ecosystems to high-frequency fires.

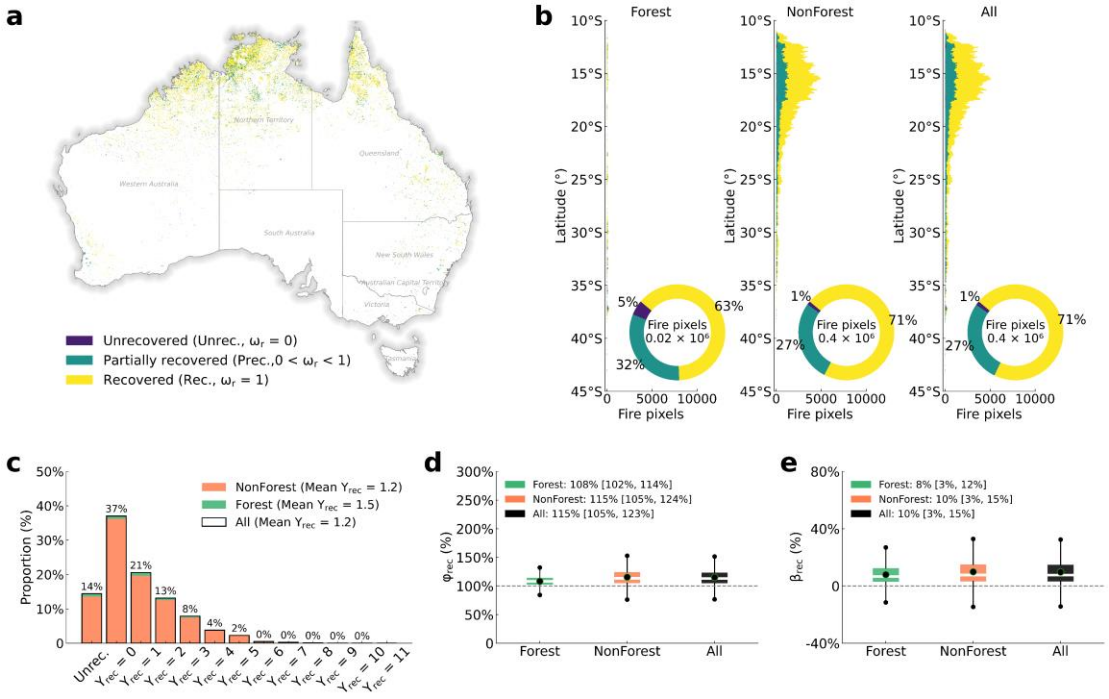

Figure 6.7: Post-fire recovery of fire events in multiple-fire pixels. a show the

spatial distribution of unrecovered, partially recovered and recovered fire pixels. b, c, d, and e are the same as Figure 6.6 but focus on multiple-fire pixels.

6.3.4 Impacts of precipitation on post-fire recovery under various levels of fire severity

Most ecosystems in Australia are water-limited, making post-fire recovery closely linked to water availability and fire severity. Across the gradient of fire severity, we applied a logarithmic regression model (y=alog(x)+b) to explore the relationship between post-fire recovery ($Ratio_{rec}$) and precipitation. The overall response of $Ratio_{rec}$ to precipitation (Δ mm) exhibited a significant positive correlation, characterized by an initial increase in $Ratio_{rec}$ with rising precipitation, and a saturation above a specific threshold (Figure 6.8a-c). Accordingly, the response of $Ratio_{rec}$ to precipitation can be divided into two stages: rapid increase and saturation. In the rapid stage of increase, $Ratio_{rec}$ gradually increases with precipitation but levels off once the response to precipitation reaches saturation. During this stage, fire severity and precipitation jointly influence the $Ratio_{rec}$, with fire severity impacting negatively and precipitation impacting positively. In the saturation regime, $Ratio_{rec}$ remains stable at its peak, indicating that additional precipitation is no longer necessary and that recovery can proceed irrespective of fire severity. Notably, the saturation point for NonForest is relatively low, $Ratio_{rec}$ reaching peak at Δ mm > 50 mm, whereas it is higher for Forest, $Ratio_{rec}$ reaching peak at Δ mm > 150 mm.

The response mechanism of $Ratio_{rec}$ to precipitation is fundamentally driven by the recovery magnitude (φ_{rec}) and slope (β_{rec}) (Figure 6.8d-i). Similarly, the logarithmic

model indicates a significant positive correlation between φ_{rec}, β_{rec}, and precipitation. After precipitation saturation, excessive precipitation tends to slightly weaken or halt this effect, but it still maintains relatively high levels, keeping $Ratio_{rec}$ at its peak. This response pattern is more pronounced in NonForest than in Forest, highlighting the rapid rebound of NonForest and its sensitivity to water availability. The responses of φ_{rec} and β_{rec} to precipitation are particularly noteworthy under varying fire severities. Fire severity positively correlates with φ_{rec} and β_{rec} under wet conditions (Δ mm > 0). This indicates that when water is sufficient, larger fire-induced damage leads to higher recovery magnitudes and slopes. These findings reveal the high adaptability of Australia's ecosystems to fire and the dominant role of precipitation in their recovery.

In recovered fire pixels, we further explored Y_{rec} with factors associated with precipitation amount and timing (Figure 6.8j-l). We used the Normalized Precipitation Timing Index (NPTI) as an indicator to simulate scenarios with varying precipitation amounts and timings. NPTI is generally negatively correlated with Y_{rec} and positively correlated with RdNBR, which means earlier and greater precipitation results in shorter recovery times, whereas higher fire severity prolongs recovery times. This pattern is clear and direct in NonForest but not significant in Forest, although Forest exhibits a similar overall trend. It is important to clarify that, although fire severity negatively impacts Y_{rec}, this does not conflict with the positive correlation of fire severity with φ_{rec} and β_{rec}. Higher fire severity is typically associated with greater GPP loss, making a longer Y_{rec} reasonable.

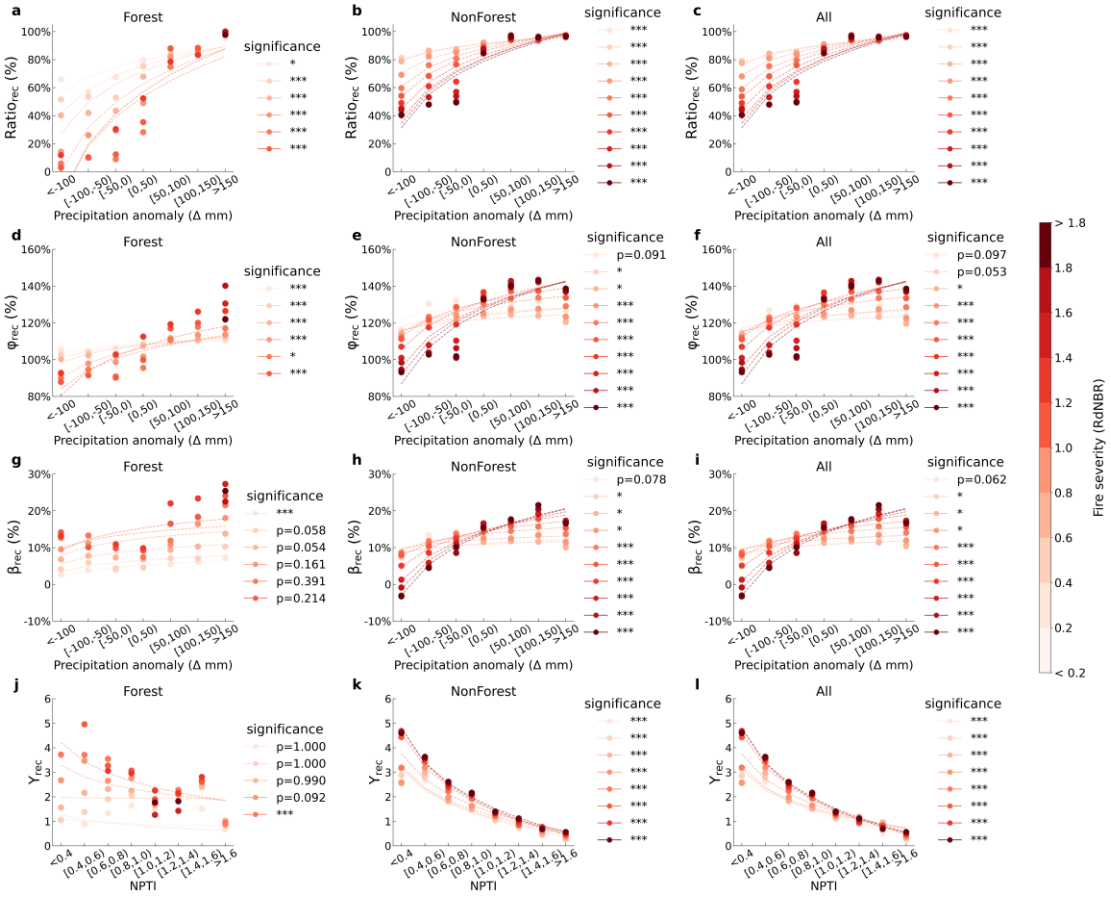

Figure 6.8: The relationship between post-fire recovery trajectories and precipitation varies under different levels of fire severity. Post-fire precipitation was quantified using precipitation anomalies (Δ mm), and fire severity was quantified using RdNBR. Each point represents the mean value in subgroup (see Methods). Each panel in a~i presents statistical metrics under varying precipitation anomaly and fire severity: $Ratio_{rec}$ (a~c), recovery magnitude (φ_{rec}) (d~f), and recovery slope (β_{rec}) (g~i). j~l shows Y_{rec} under different Normalized Precipitation Timing Index (NPTI) and fire severity (see Methods). Three columns correspond to Forest, NonForest, and All, respectively. The curves are the fitted regression line of the logarithmic model (y=alog(x)+b), with significance

determined based on the F-test. $p<0.01$ (***) and $p<0.05$ (*) indicate confidence levels of 99% and 95%, respectively.

6.3.5 Impacts of fire on interannual GPP change

We extended the GPP data to cover the period from 2000 to 2022 to explore the contribution of fire-related GPP to the long-term interannual GPP change (ΔGPP). Within fire-affected pixels, single-fire pixels, ΔGPP_{NN} dominated ΔGPP, accounting for 89% [85%–94%] of ΔGPP. ΔGPP_{FN} accounting for 6% [3%, 9%] of ΔGPP, and ΔGPP_{NF} accounting for 5% [2%, 7%] (Figure 6.9a). For multiple-fire pixels, we merged the ΔGPP_{NF} and ΔGPP_{FF} into one category as both are related to fire-induced GPP loss (Figure 6.9b). Multiple-fire pixels exhibited similar patterns to single-fire pixels, but with a relatively larger contribution of fire to ΔGPP. ΔGPP_{NN}, ΔGPP_{FN}, and $\Delta GPP_{NF}+\Delta GPP_{FF}$ accounting for 77% [70%,87%], 12% [6%,16%], and 11% [5%,15%] of ΔGPP.

We then extended the analysis to the entire Australia, exploring the contribution of total fire-related GPP to the continent's total GPP. Over the two decades, total ΔGPP in Australia ranged from -1.07 GtC $year^{-1}$ to 1.12 GtC $year^{-1}$ (Figure 6.9c). ΔGPP_{FN} ranged from -0.95 GtC $year^{-1}$ to 1.08 GtC $year^{-1}$ and served as the primary contributors to the ΔGPP, explaining 82% [74%, 90%] of the ΔGPP over years (Figure 6.9d). ΔGPP_{FN} ranged from -0.01 GtC $year^{-1}$ to 0.10 GtC $year^{-1}$, with most of the years show positive values, explaining 11% [5%, 17%] of the ΔGPP over years. $\Delta GPP_{NF}+\Delta GPP_{FF}$ ranged from -0.07 GtC $year^{-1}$ to 0.01 GtC $year^{-1}$, explaining 7% [4%, 10%] of the ΔGPP over years. $\Delta GPP_{NF}+\Delta GPP_{FF}$ were generally negative as fires directly reduce GPP.

However, in some years, such as 2003, 2010, and 2020, they turned positive, reflecting climate-driven recovery within the year.

Fire-related GPP loss ($\Delta GPP_{NF} + \Delta GPP_{FF}$) accounts for 7% of ΔGPP (Figure 6.9d). This proportion is non-negligible, as the fire-affected areas are much smaller than the areas without fire-affected. The key point is that the annual climate-driven GPP recovery (11%) can fully offset the fire-related GPP loss, a similar pattern also observed at the pixel scale (Figure 6.9a, b). These findings suggest that the long-term impact of fires on ΔGPP in Australia is significantly smaller than that of climate change or land use changes, primarily due to the offset effect of rapid post-fire recovery.

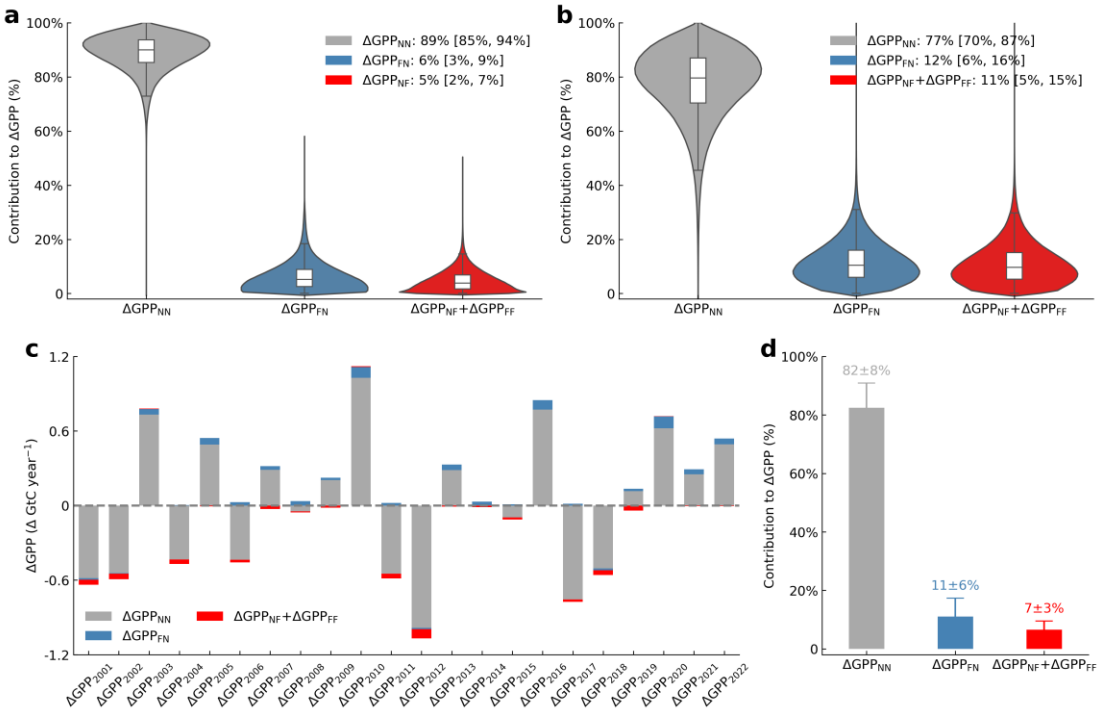

Figure 6.9: Interannual GPP change (ΔGPP) across fire-affected pixels and whole Australia. ΔGPP is defined as: $\Delta GPP_{(t)} = GPP_{(t)} - GPP_{(t-1)}$. ΔGPP is divided into four subcategories: $\Delta GPP = \Delta GPP_{NN} + \Delta GPP_{FN} + \Delta GPP_{NF} + \Delta GPP_{FF}$. ΔGPP_{NN} refers to the ΔGPP of the year with no fire, driven primarily by climate change and land

use change. ΔGPP_{FN} refers to the ΔGPP of the year fire that occurred in the previous year, representing the annual climate-induced GPP recovery. ΔGPP_{NF} refers to the ΔGPP of the years with fire, and ΔGPP_{FF} refers to the ΔGPP of the years with fire occurring in consecutive years. a and b show the distributions of each subcategory contribution to ΔGPP for fire-affected pixels, with a for single-fire pixels and b for multiple-fire pixels. c shows the annual time series of Australia's total ΔGPP. Each bar is stacked by the sum of ΔGPP across all pixels in that subcategory. The positive and negative signs of ΔGPP represent increases and decreases in interannual anomalies. d shows the contribution of each subcategory to total Australia's interannual GPP difference by mean and 95% confidence interval (mean ± 95% CI) across all years.

6.4 Discussions

6.4.1 Strong and rapid post-fire recovery in Australia

As shown by the post-fire recovery dynamics in GPP (together with multiple satellite-derived products) across 1.7×10^6 fire-affected pixels (1.5×10^6 km^2) from 2011 to 2019, Australian ecosystems demonstrate strong and rapid post-fire recovery in the carbon uptake capacity in response to fire disturbances. This recovery is characterized by high recovery ratios, overcompensation, and rapid recovery. NonForest ecosystems are worth highlighting as they exhibit an extraordinarily strong and rapid recovery. This highlights NonForest in Australia as fire-adapted ecosystems, attributed to the rapid resprouting of herbaceous and shrub species, along with their lower resource

requirements (Driscoll et al., 2024; Xu et al., 2024). Note that we did not differentiate between grasslands, shrubs, and savannas here, as savannas are typically composed of grass and trees. Further refinement is needed to distinguish between understory and overstory fires in the future, as savannas, which involve a more dominant grass layer, are expected to recover more quickly. Forest are relatively stable, as indicated by recovery metrics showing narrower response ranges to fire (Woodgate et al., 2025). Most forest species have adapted to fire over millions of years, with the dominant eucalyptus species in Australia having evolved fire resilience by vigorously resprouting after fire or by releasing large quantities of seeds that rapidly germinate after burning (Woodgate et al., 2025). The stronger and more rapid post-fire recovery observed in NonForest compared to Forests could be attributed to the higher fire-induced GPP instant loss in forests, as well as the higher post-fire demands of radiation, water, and nutrients (Bond et al., 2001; Crisp et al., 2011).

6.4.2 Precipitation and fire drives post-fire recovery in Australia

With these traits that promote resilience, we find that strong and rapid post-fire recovery is largely driven by subsequent precipitation and fire severity. Consistent with previous studies, precipitation in water-limited Australian ecosystems is the dominant factor driving post-fire GPP recovery (Byrne et al., 2021), as it provides essential water resources for resprouting and germination, while also accelerating soil nutrient cycling (Li et al., 2009). Precipitation directly determines whether vegetation can recover and shape the recovery trajectories. The spatial patterns of post-fire recovery indicate that unrecovered fire pixels were concentrated in arid areas. In these regions, insufficient

precipitation and high fire severity fail to counterbalance fire-induced soil warming and reduce soil moisture (Baur et al., 2024; J. Zhao et al., 2024), resulting in ecosystem degradation or desertification (Armstrong McKay et al., 2022; Driscoll et al., 2024; Feng et al., 2021). One key finding is that the precipitation threshold needed to support post-fire recovery is relatively modest—in most cases, slightly exceeding the long-term mean precipitation is sufficient to facilitate recovery (Figure 6.8). This finding leads to the conclusion that ecosystems in Australia are highly sensitive to water availability, which is particularly significant for Australia, given that its ecosystems are predominantly arid and semi-arid. When precipitation is sufficient, vegetation can recover from any fire event. A prime example is the extensive southeastern forest fires in 2019, where early and abundant post-fire precipitation greatly accelerated recovery (Qin et al., 2022). Moreover, it is easy to understand that earlier and higher precipitation would shorten recovery times. However, the complex response pattern of Forest to NPTI may arise from variations in soil types, which could influence how precipitation impacts the ecosystem (Fernandez-Going et al., 2012). Additionally, early precipitation may trigger microbial flushes, altering soil microbial diversity and functionality (DeBano et al., 1978), which warrants further investigation.

Fire influences post-fire recovery in GPP in two ways: fire frequency and fire severity. In general, an increasing fire frequency negatively affects post-fire GPP recovery, most directly by reducing the level of recovery and shortening the time window for recovery. This prevents ecosystems from fully regaining their maximum carbon uptake capacity. On the positive side, our results indicate that these increases in

fire frequency have a minimal effect on the post-fire recovery ratio. Most vegetation in Australia, especially NonForest, can still return to baseline levels despite repeated fire disturbances. However, as fire frequency has increased over the recent decades, and intervals between fires continue to shorten, the negative impacts are likely to intensify.

Fire severity reveals an interesting pattern: under wet conditions, vegetation affected by higher fire severity exhibits a stronger recovery response, i.e., higher level of GPP recovery than pre-fire and steeper slopes. Our findings also align with a previous grassland study, which reported a 30–60% increase in productivity following fire (Santos et al., 2003). In our analyses, productivity increased by 38% for single-fire events and 15% for multiple-fire events. Our results also corroborate a North American boreal fire study, which reported an 8–40% increase in SIF following fires (Kim et al., 2024). This phenomenon can be attributed to several complementary mechanisms. First, intense burning returns the nutrients in dead plant matter to the soil, providing a short-term pulse of nutrient inputs or fertilization effect (Caon et al., 2014; Certini, 2005). Second, the removal of pre-existing plant species creates space that reduces competition for fire-adapted or pioneer species (Driscoll et al., 2024; Xu et al., 2024), such as many eucalypts and shrubs, which can rapidly occupy (Clarke et al., 2002; Crisp et al., 2011). Third, these fire-adapted species possess strong resprouting and germination capacities (Knox et al., 2006), as well as high photosynthetic efficiencies (Clemente et al., 2005). Finally, large post-fire precipitation maximizes the positive effects from nutrient release and reduced competition (Blanco-Rodríguez et al., 2023; Davis et al., 2023), thereby producing the high recovery magnitudes and slopes after fires. In comparison, under

drought conditions, fire severity exerts a generally negative influence. These findings indicate fire regulates and constrains recovery processes by altering initial conditions. However, the high sensitivity of vegetation to water drives strong resilience and adaptability in response to fire impacts.

Australia's ecosystems are mainly composed of water-limited and fire-dependent ecosystems (Byrne et al., 2021), which guided our continental-scale post-fire recovery analysis focusing on precipitation and fire severity. More potential drivers need to be considered in the future to conduct post-fire recovery analysis at a finer scale (Beringer et al., 2015). For example, as mentioned, in grassland and savanna fire zones, intense fires can trigger rapid species turnover, with pioneer fire-adapted species supplanting pre-existing species (Driscoll et al., 2024; Xu et al., 2024), and in extreme cases, driving ecosystem extinction and changes in land use (Armstrong McKay et al., 2022; Driscoll et al., 2024; Feng et al., 2021). In relatively complex forest ecosystems, such as those in the southeastern Australian eucalypt forests, radiation is as critical a driver of post-fire recovery as precipitation (Woodgate et al., 2025). Furthermore, forest ecosystems demand attention to vertical structural complexity. Evidence from a recent study suggests that the overstorey and understory follow distinct post-fire recovery trajectories, with a substantial loss of overstorey biomass and a concurrent increase in understory biomass (Woodgate et al., 2025), a pattern that optical sensors cannot capture accurately and that underscores the need to incorporate active remote-sensing datasets capable of resolving three-dimensional canopy structure, such as GEDI LiDAR (Potapov et al., 2021). Moreover, biophysical interactions, such as hydrothermal

coupling and soil microbial community dynamics, also modulate post-fire recovery trajectories and should be incorporated into analyses at finer scales (Certini, 2005; DeBano, 2000).

6.4.3 Fire has a small role in long-term carbon uptake dynamics in Australia

Because of this strong and rapid post-fire recovery, the fire-induced GPP losses are unlikely to have solely long-term effects on the interannual GPP difference, thereby explaining the previously observed limited impacts of fire on the interannual variability of biomass and carbon sinks (Beringer et al., 2007; Qin et al., 2022). Even during the devastating forest fires of 2019, the strong and rapid precipitation-induced intra-annual recovery resulted in the GPP losses from that year's fires not being significant at the interannual scale. In the subsequent three years (2020-2022), GPP continued to increase significantly due to above mean rainfall, particularly in Forest. This evidence suggests that vegetation recovery might have reabsorbed a large fraction or the totality of the 2019 forest emissions from burned biomass, contrary to what some studies had suggested (Abram et al., 2021; van der Velde et al., 2021). Furthermore, these findings help explain a recent study on Australia's carbon budget, where net fire emissions (9.9 TtC yr^{-1}) are significantly lower than total gross fire emissions (158 TtC yr^{-1}) (Villalobos et al., 2023).

Other work tracking aboveground biomass change after fires suggests that the impact of fires on Australia's living carbon stock currently remains within the bounds of ecosystem self-repair (Byrne et al., 2021; Qin et al., 2022). We acknowledge that our study and those cited above are restricted to post-fire vegetation carbon uptake

dynamics and do not quantify other fire-induced carbon fluxes, including the combustion and respiration of carbon in soils and litter, and increased erosion and carbon transport into inland waters and coastal zones.

We also note that increased fire frequency in forests and total burned area in the whole of Australia have already been observed over the past three decades (Canadell, Meyer, et al., 2021). With a warming climate and rainfall becoming more variable, Earth System models suggest an increase in fire intensity and a lengthening of the fire season in many regions of the world, including Australia (Jones et al., 2022). We acknowledge that our results are based on a decade of fires and GPP postfire recovery in a country where the climate and fire occurrence is highly variable in time frames of years to decades.

Future research can further investigate the role of this GPP recovery pattern in atmospheric CO_2 dynamics to comprehensively quantify the impact of fires on carbon dioxide anomalies in Australia. That will need to include the incorporation of post-fire recovery into simulations of Earth system models (e.g., CESM's CLM5, ORCHIDEE, LP-GUESS, JSBACH) (Lawrence et al., 2019; Yue et al., 2014), as we found that a large portion of fire pixels recover their GPP within a year, which may lead to models overestimating fire-induced losses if they ignore such a fast recovery process. Other processes, such as full biomass and soil carbon dynamics, and the ultimate fate of carbon transported into inland water bodies and coastal zones are also needed.

6.5 Conclusion

This chapter systematically analyzed Australia's post-fire GPP recovery trajectories of

all fires from 2011 to 2019. The findings reveal a strong and rapid post-fire recovery in Australian ecosystems, highlighting the GPP resilience and adaptability to fire disturbances. Climate intensification is expected to exacerbate fires and heighten the risk of terrestrial carbon sink loss, making it essential to deepen understanding of this climate-driven post-fire recovery (Burton et al., 2024; Stevens-Rumann et al., 2018). Our results provide new insights into the long-term impacts of fire on ecosystem functionality and carbon anomaly in Australia. Future research should further investigate the dynamics of biomass and soil carbon dynamics, the role of land use changes, hydrothermal coupling, soil microbial dynamics, and shifts in ecosystem structure as driving factors to comprehensively assess the potential mechanisms of this recovery pattern and the associated risks of carbon loss under future warming scenarios.

Chapter 7 : Application of GPP dataset: a case study of first-year post-fire recovery of vegetation productivity in northern high latitude forests

ABSTRACT

Forests in high northern latitudes (north of 40°N) constitute one of the largest terrestrial carbon reservoirs in the world. In recent years, climate change has exacerbated forest fires, which result in forest area loss and forest degradation. Here, we assessed the spatiotemporal distribution of the recovery of forest CO_2 uptake (gross primary production, GPP; 500-meter spatial resolution) after the first-year since fire in the region from 2002 to 2022. We show that, on average, GPP recovered to 85% of its pre-fire levels within one year, with a large spatial variation driven by tree species. First-year post-fire GPP recovery in needleleaf forests (80%) was lower than broadleaf forests (88%). First-year post-fire GPP recovery decreased over time since late 2000s. The decline was primarily driven by increasing fire intensity and severity, coupled with higher vapor pressure deficit (VPD) and air temperature, as well as reduced soil moisture. The results from this study elucidate the spatiotemporal patterns of post-fire CO_2 uptake recovery in high-latitude forests and identify the key factors governing that recovery. These findings could be used to improve Terrestrial Biosphere Models and Earth system models that simulate carbon fluxes and their net impact on the atmospheric CO_2 concentration.

7.1 Introduction

Forests in northern high latitudes (north of 40°N) are a crucial component of the biosphere (Esseen et al., 1997) and are characterized by deep organic soil layers and large vegetation biomass (Magnani et al., 2007; Tagesson et al., 2020). Northern high-latitude forests are recognized as one of the largest terrestrial carbon reservoirs in the world (Harden et al., 2000; Lorenz, 2010), storing approximately 32% of the total carbon in the terrestrial biosphere (861 ± 66 Pg C) and contributing around 21% of the global terrestrial carbon sink (Magnani et al., 2007; Pan et al., 2011).

Wildfires have significant impacts on forests in northern high latitudes, ranging from forest area loss to various degrees of damage (forest degradation), depending on wildfire intensity and severity (Bond et al., 2005; Flannigan et al., 2009). Wildfires result in large losses of plant biomass (leaf, stem and trunk), corse woody debris, litterfall, and soil organic matter (Boby et al., 2010; Fan et al., 2023). Between 2010 and 2019, Siberian forests had substantial losses of aboveground biomass, predominantly attributed to wildfires (Fan et al., 2023). CO_2 emissions from forest wildfires in northern high latitudes have been increasing since 2000, reaching a record high in 2021 (Zheng et al., 2023). Driven by wildfires, some boreal forest regions had shifted from carbon sinks to carbon sources, despite their historically stable role as carbon sinks over the past millennia (Brovkin et al., 2016). Wildfires have been considered a major driver of the forest carbon balance (Bond-Lamberty et al., 2007; Harden et al., 2000; Tagesson et al., 2020; Virkkala et al., 2025; Walker et al., 2019; Wilkinson et al., 2023)

Quantifying post-fire recovery by years provides a critical measure of forest ecosystem resilience (Tepley et al., 2018). Many in-situ studies have reported post-fire recovery of deforested stands and degraded forest stands (Barlow et al., 2008; Bond-Lamberty et al., 2007; Johnstone et al., 2004; Johnstone et al., 2010; Kim et al., 2024). Most of these studies have examined the long-term post-fire recovery trajectory (Johnstone et al., 2004; Johnstone et al., 2010). However, assessing resilience of forest in northern high-latitudes to wildfires through long-term recovery remains challenging, as the recovery of forests often spans decades and is influenced by multiple external factors, including climate-induced shifts in hydrothermal conditions and various anthropogenic management interventions (Bao et al., 2024; Bartels et al., 2016; Gitas et al., 2012; Meng et al., 2015). In the past decades, the boreal zone experienced large and continued rise in air temperature (Bekryaev et al., 2010), which may affect post-fire recovery. The post-fire recovery in early years (e.g., first-year after the fire) is also important, which involves pioneer seed germination, soil property modifications, and microbial community structural and functional reorganization, all of these processes collectively determine the initial post-fire carbon flux and lay the foundation for recovery in subsequent years (Bartels et al., 2016; Holden et al., 2016; Yakun Zhang et al., 2017). To date, most studies have focused on specific years or local areas in northern high latitudes (Boby et al., 2010; Bond-Lamberty et al., 2007; Gauthier et al., 2015), and consequently, the spatial and temporal dynamics of forest post-fire recovery in the early years remain poorly understood. In addition, most studies using time series satellite images at moderate spatial resolutions to track post-fire recovery have not fully

investigated the relative effects of wildfire intensity and severity on temporal variations in CO_2 uptake (Hermosilla et al., 2018). Therefore, an assessment of post-fire recovery of forests in early years across the entire northern high latitudes is needed, which are likely to be affected by global warming and climate variation.

Post-fire recovery of vegetation has been measured by the temporal changes of several variables. Many publications used time series vegetation index data derived from satellite images with high (tens of meters, HSR) and moderate (hundreds of meters, MSR) spatial resolutions to assess the wildfire impacts (resistance) and post-fire recovery (resilience) (Bao et al., 2024; Qin et al., 2022; Woodgate et al., 2025; Xu et al., 2024). Some publications used vegetation aboveground biomass to assess fire impacts and post-fire recovery (Qin et al., 2021). Vegetation photosynthesis or gross primary production (GPP) is a crucial component of the carbon budget (Anav et al., 2015; Frankenberg et al., 2011), and has also served as one of the major indicators of post-fire recovery (Woodgate et al., 2025; Xu et al., 2024).

In this chapter, we conduct a comprehensive analysis of the spatial-temporal characteristics of forest fires and the first-year post-fire GPP recovery of forests across the northern high latitudes (north of 40°N) from 2002 to 2022. Specifically, we aim to address the following three scientific questions: (1) What are the spatial-temporal characteristics of forest fires in northern high latitudes (i.e., fire intensity, fire severity, burned areas, fire-induced forest loss (deforestation) and degradation) during 2002 to 2022? (2) How much does CO_2 uptake recover in the first year after fire (the first-year post-fire GPP recovery)? (3) What are the decadal trends and drivers in the first-year

post-fire GPP recovery during 2002 to 2022? Addressing these scientific questions will help reveal the mechanisms by which wildfires impact forest GPP in the region, providing critical insights for accurately assessing the carbon budget in the region, improving terrestrial ecosystem models, and formulating effective wildfire prevention, mitigation, and ecological restoration strategies.

7.2 Materials and Methods

7.2.1 Study area

The study area encompasses all terrestrial regions north of 40° N, spanning a mosaic of biomes that includes evergreen needleleaf and deciduous needleleaf forests, deciduous broadleaf forests, etc. Contiguous needleleaf forests dominate, while broadleaf stands along the southern margin zones. In North America, fire-prone taxa such as black spruce (*Picea mariana*), white spruce (*Picea glauca*), and balsam fir (*Abies balsamea*) are dominant, whereas Eurasian forests are dominated by larch (*Larix*), Scots pine (*Pinus sylvestris*), Siberian spruce (*Picea obovata*), and Siberian fir (*Abies sibirica*). The region's climate transitions from a continental subarctic to a tundra climate, characterized by long, severe winters (mean temperatures below –10°C) and short, cool summers (mean temperature around 15°C). Annual precipitation ranges from 300 to 800 mm.

7.2.2 Fire intensity data

Fire intensity information was obtained from the MOD14A1 v6.1 product (1-km resolution) and quantified using the maximum fire radiative power (MaxFRP) as an

indicator (Giglio et al., 2021). MOD14A1 v6.1 estimates the total radiative energy released per unit time using brightness temperatures from the 4 μm spectral band. As MaxFRP represents the peak radiative flux from the most intensely burning areas, it is widely used as an effective proxy for fire intensity (Jie Zhao et al., 2024). Given that the active fire detections in MOD14A1 v6.1 do not always spatially overlap with the burned area pixels in MCD64A1 v6.1, we assigned an FRP value to each burned area pixel by selecting the nearest active fire pixels.

7.2.3 Burn area data

Burned area information was obtained from the MCD64A1 v6.1 product (500-meter resolution). MCD64A1 v6.1 integrates multi-source data sources—including surface reflectance, active fire, and land cover type—to comprehensively detect burned areas. Compared to its predecessor, MCD45A1, MCD64A1 significantly improves the accuracy of detecting small burned patches, reduces uncertainties in burn date estimation, and effectively minimizes unmapped areas (Giglio et al., 2018). Previous studies have evaluated the reliability of the MCD64A1 product. For instance, comparisons between MCD64A1 and 30-meter resolution Landsat reference data indicate that, at the global scale, the estimated error of MCD64A1 is approximately 40%. However, this error is primarily attributed to tropical forests, temperate forests, and Mediterranean biomes, where errors exceed 50%. In contrast, within the Northern high-latitude biome, MCD64A1 exhibits a lower omission error of only 27%, which is partially offset by an estimated commission error of approximately 24% (Boschetti et al., 2019; Giglio et al., 2018). Therefore, in the context of Northern high-latitude forests,

the accuracy of MCD64A1 for burn area detection can be considered within an acceptable range. Here, we aggregated all burned area pixels from MCD64A1 annually from 2002 to 2022.

7.2.4 Fire severity data

Fire severity is a measurement on the impacts of fire on vegetation (fire-induced loss of vegetation structure or function) and the resistance of vegetation to fire. In this study, fire severity was quantified using the widely applied index, the Relative Differenced Normalized Burn Ratio (RdNBR). RdNBR calculates the difference in vegetation surface reflectance before and after fire events, with relative normalization, to quantify the severity of vegetation damage in burned areas. RdNBR was calculated by near-infrared (NIR) and shortwave infrared (SWIR2) bands (Miller et al., 2007):

$$\mathrm{NBR} = \frac{\rho_{\mathrm{nir}} - \rho_{\mathrm{swir2}}}{\rho_{\mathrm{nir}} + \rho_{\mathrm{swir2}}} \tag{7.1}$$

$$\mathrm{dNBR} = \mathrm{NBR}_{\text{pre-fire}} - \mathrm{NBR}_{\text{post-fire}} \tag{7.2}$$

$$\mathrm{RdNBR} = \frac{\mathrm{dNBR}}{\sqrt{\mathrm{NBR}_{\text{pre-fire}}}} \tag{7.3}$$

Where ρ_{nir} and ρ_{swir2} are the surface reflectance of the NIR and SWIR2 bands from the MOD09A1 v6.1 product (Vermote, 2015). The Differenced NBR (dNBR) quantifies the absolute vegetation loss caused by fire and was calculated as the difference between pre-fire and post-fire NBR values (Alonso-González et al., 2021; Miller et al., 2007). Here, we applied a five-observation time window centered on the fire occurrence date. The pre-fire NBR ($\mathrm{NBR}_{\text{pre-fire}}$) was calculated as the mean of two 16-day observations preceding the fire, while the post-fire NBR ($\mathrm{NBR}_{\text{post-fire}}$) was calculated as the mean of

two 16-day observations following the fire.

7.2.4 Forest cover data

Forest map information was obtained from the MCD12Q1 v6.1 dataset (500-meter resolution). MCD12Q1 v6.1 provides global land cover classification layers since 2001, generated using machine learning algorithms and time-series smoothing techniques (Sulla-Menashe et al., 2018). We selected the LAI/fPAR (Leaf Area Index/Fraction of Absorbed Photosynthetically Active Radiation) classification scheme, as LAI/fPAR is closely linked to vegetation CO_2 uptake. In the MCD12Q1 classification, forest pixels are defined based on a minimum tree height of ≥2 m and a canopy cover of ≥60%. This product categorizes forests into four major types: evergreen broadleaf forest (EBF), deciduous broadleaf forest (DBF), evergreen needleleaf forest (ENF), and deciduous needleleaf forest (DNF). Based on these four categories, we further classified forest types for each year from 2002 to 2022 as follows: forest (composed of EBF, DBF, ENF, and DNF), needleleaf forest (NF, composed of ENF and DNF), and broadleaf forest (BF, composed of EBF and DBF).

7.2.5 ERA5-Land reanalysis climate data

The ERA5-Land reanalysis climate data (~0.1-degree, hourly), developed by the European Centre for Medium-Range Weather Forecasts (ECMWF), is specifically designed for land surface variables (Muñoz-Sabater et al., 2021; Muñoz Sabater, 2019). In this study, we used ERA5-Land air temperature, surface solar radiation, and volumetric soil water content in the 0 to 7 cm layer to examine interannual variability

in climate and near-surface moisture. Vapor pressure deficit (VPD) was also calculated by using air temperature and dewpoint temperature.

7.2.6 Gross primary productivity data

We used the global GPP dataset estimated by the Vegetation Photosynthesis Model (VPM v3.0) in Chapter 4. Here, we utilized data from the global VPM estimation spanning from 2000 to 2023 for analysis.

7.2.7 Post-fire GPP recovery analyses

First-year post-fire GPP recovery is assessed by comparing pre-fire and post-fire GPP. Pre-fire GPP serves as a reference (reference GPP), representing the normal state of productivity before wildfire disturbance. The ratio of GPP in the first-year post-fire to the reference GPP (denoted as β) indicates the first-year post-fire GPP recovery. There are typically three methods (Figure 7.1): (1) comparing the relative change in total annual GPP pre- and post-fire, (2) comparing the relative change in total GPP in the growing season (GS) pre- and post-fire, and (3) analyzing the regression slope of an 8-day GPP time series pre- and post-fire. While the first two methods provide a rapid assessment of the overall impact of fire on productivity, they lack insights into the seasonal dynamics of post-fire recovery, e.g., fire may disrupt the onset of spring phenology, suppress summer growth peaks, or induce premature autumn senescence. In contrast, the third method uses an 8-day pre-fire GPP time series as a reference and applies linear regression to assess recovery rates over 46 consecutive 8-day windows in the first post-fire year. This method integrates both recovery magnitude and seasonal

dynamics, offering a comprehensive characterization of post-fire recovery processes.

We applied this regression-based method to quantify first-year post-fire GPP recovery (Figure 7.1). For each burned forest pixel (500-meter resolution), the pre-fire GPP reference curve ($GPP_{pre\text{-}fire,\,i}$) was constructed using GPP data from the three years preceding the fire, considering only years without fire. This reference curve was based on an 8-day interval GPP time series, consisting of 46 GPP values corresponding to each 8-day period in the year (DOY: i = 1, 9, 17, …). Each value in the reference curve was calculated as the means of the corresponding 8-day period across the three pre-fire years. To assess relatively post-fire GPP changes, we compared the pre-fire reference curve with the 8-day interval GPP time series for the first year after the fire event ($GPP_{post\text{-}fire,\,i}$). A simple linear regression model without intercept was applied to obtain the regression slope (β_{GPP}):

$$GPP_{post\text{-}fire,\,i} = \beta \cdot GPP_{pre\text{-}fire,\,i} \tag{7.4}$$

$$\beta_{GPP} = \beta \times 100\% \tag{7.5}$$

Then, we calculated the mean, median and standard deviation of β_{GPP} for all burned forest pixels within each 2° grid cell, and report and use the mean values for further analyses in this chapter.

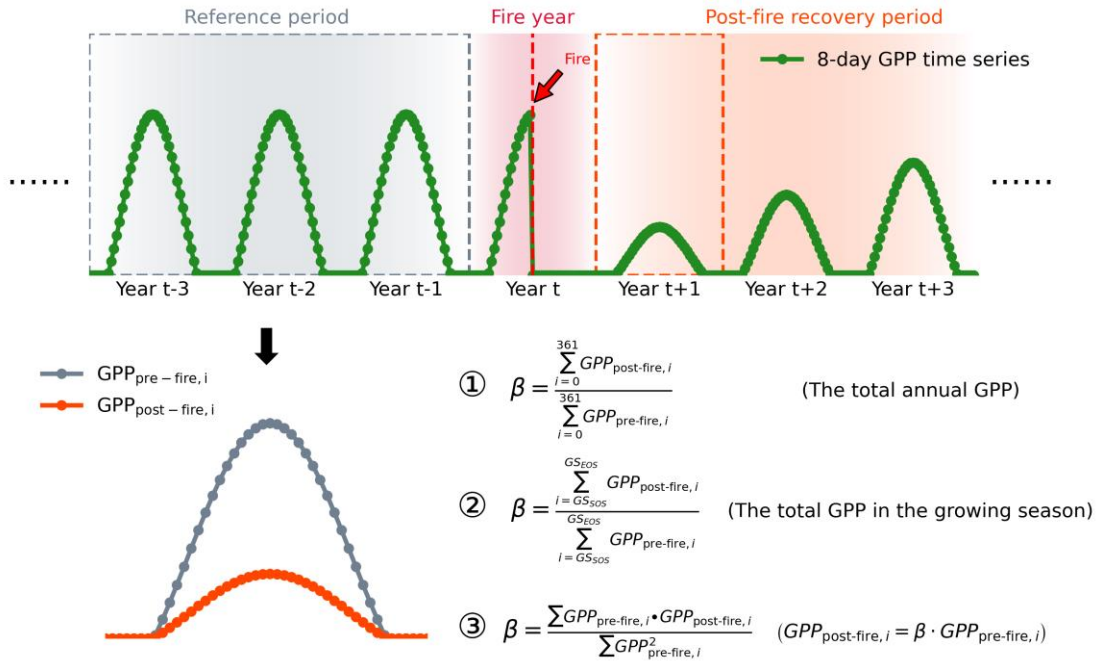

Figure 7.1: Post-fire GPP recovery analyses. The framework was analyzed using an 8-day GPP time series within a continuous five-year window. For the fire year *t*, the three years preceding the fire year (*t*-3, *t*-2, *t*-1) were designated as the reference period, during which the reference GPP ($GPP_{pre\text{-}fire,i}$) was calculated as the mean GPP for each 8-day interval across the three years (*i* = 1, 9, 17, ...). The first year following the fire year (year *t*+1) was defined as the post-fire GPP ($GPP_{post\text{-}fire,i}$). Recovery ratio (β) was calculated to quantify post-fire GPP recovery using three equations: (1) the ratio of total annual post-fire GPP to total annual pre-fire GPP, (2) the ratio of total growing season post-fire GPP to total growing season pre-fire GPP, and (3) the regression slope between $GPP_{post\text{-}fire,i}$ and $GPP_{pre\text{-}fire,i}$. In this study, we employed the third equation to quantify post-fire recovery.

7.2.8 Statistical analysis

We explored the long-term trend of β_{GPP} across the Northern high-latitude forests and

within each 2° grid cell from 2002 to 2022 using simple linear regression. The regression coefficients were used to quantify the long-term trend of β_{GPP} over the study period, including its direction and rate of change. We attributed inter-annual changes in β_{GPP} with ridge regression that incorporated fire intensity, fire severity, burn area, air temperature, VPD, soil water, and radiation as drivers. For each driver, we calculated a contribution score by dividing the absolute value of its ridge coefficient by the sum of the absolute values of all coefficients, while retaining the coefficient sign to indicate the direction of influence.

7.3 Results

7.3.1 Forest fires in northern high latitudes (north of 40°N) during 2002-2022

Fire intensity in northern high latitudes during 2002 to 2022 had large spatial variation (Figure 7.2a). The regions with the highest fire intensity were primarily concentrated in northeast Siberia and northern North America, whereas central North America, Europe, and northeast Asia exhibited relatively lower fire intensities (Figure 7.2a). Fire severity showed a highly consistent spatial pattern with fire intensity, with severe fire-induced damage observed in northeast Siberia and northern North America, while central Siberia, central North America, Europe, and northeast Asia experienced moderate to low damage Figure 7.2b). These findings suggest that wildfire disturbances had more severe impacts on forests at higher latitudes within the Northern high-latitude forests.

The annual burned area across forests in northern high latitudes during 2002-2022 ranged from 1.6 to 6.6 × 10^4 km^2, with a mean of 3.5 × 10^4 km^2. The spatial distribution

of burned areas (Figure 7.2c) indicates that wildfires predominantly occurred in Siberia, northeast Asia, and northern North America, with relatively few occurrences in Europe. The spatial distribution of the burned area, fire intensity, and fire severity does not fully align with each other. The regions experiencing lower-intensity fire disturbances tend to exhibit faster biomass accumulation, making them more prone to frequent fire recurrence.

Based on the distribution of forest types across the northern high latitudes (Figure 7.2d), the regions with higher fire intensity and severity are predominantly covered by needleleaf forests (NF), while the regions with relatively lower fire intensity and severity are predominantly covered by broadleaf forests (BF). This finding suggests that different forest types exhibit distinct responses to wildfire disturbances, warranting further investigation into their fire resilience and recovery dynamics.

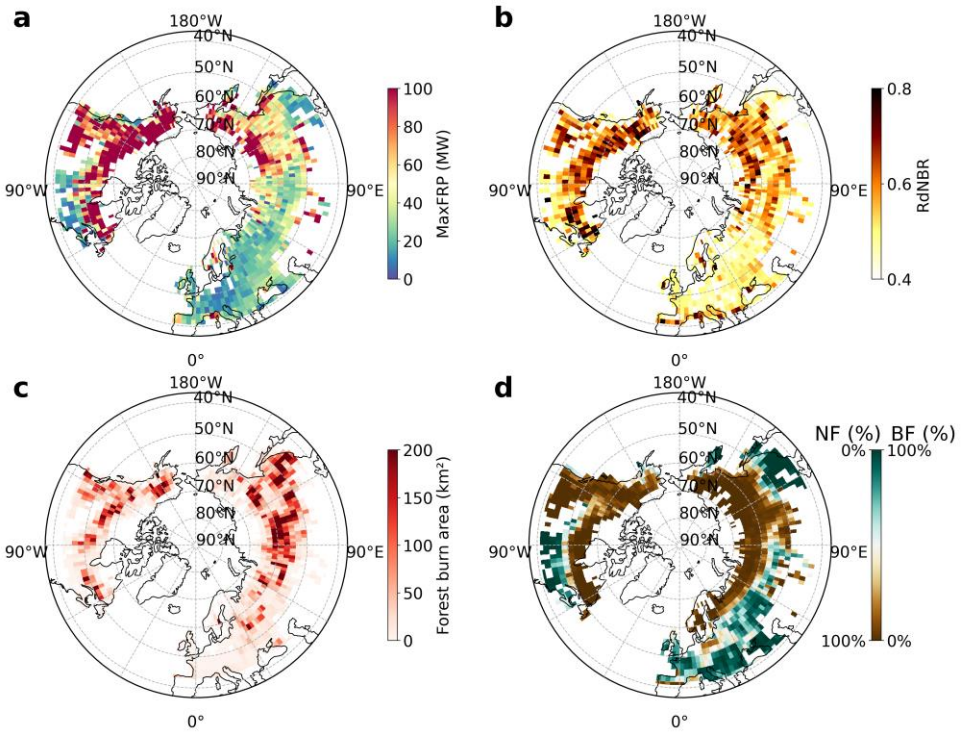

Figure 7.2: Overview of forest fires in the northern high latitudes (north of 40°N)

from 2002 to 2022. The maps show multi-year averages, with all datasets resampled to a 2° resolution. a. Forest fire intensity (maximum fire radiative power (MW), data source: MOD14A1). b. Forest fire severity (RdNBR, data source: calculated from the multi-spectral product MOD09A1). c. Forest burn area (data source: MCD64A1). d. The spatial composition of needleleaf and broadleaf forests (data source: MCD12Q1), where greener shades indicate a higher proportion of broadleaf forests (BF), while browner shades represent a higher proportion of needleleaf forests (NF).

7.3.2 Spatial patterns of first-year post-fire recovery of GPP (β_{GPP}) in forests

There is considerable spatial variation in β_{GPP} across forests in the northern high latitudes (Figure 7.3a). β_{GPP} was relatively lower in Siberia and Northern North America, where values ranged between 50% and 80%. In contrast, Northern Europe and Northern Asia had relatively higher β_{GPP}, exceeding 80%. The average β_{GPP} across forests in the entire northern high latitudes were 85%, indicating that, on average, GPP recovered to 85% of its pre-fire level within one year. The regional variation in β_{GPP} is fundamentally driven by the differing responses of forest types to wildfires. The mean β_{GPP} for needleleaf forests (β_{GPP}^{NF}) and broadleaf forests (β_{GPP}^{BF}) across the northern high latitudes were 80% and 88%, respectively (Figure 7.3b, c). This suggests that, compared to broadleaf forests, needleleaf forests experience more significant fire impacts and have smaller first-year post-fire GPP recovery. We divided the northern high latitude region into four subregions: Siberia, Northern North America, Northern Asia, and Northern Europe, and calculated the mean values of β_{GPP} in these four regions. The results show

that β_{GPP} is highest in Northern Asia and Northern Europe, followed by Siberia, with Northern North America exhibiting the lowest β_{GPP} (Figure 7.3d-e).

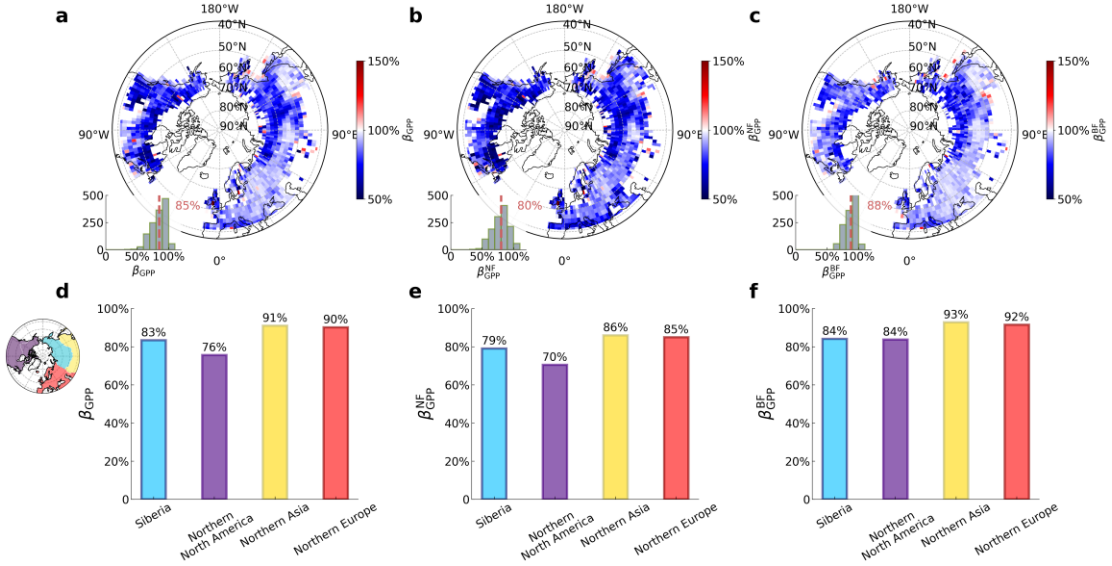

Figure 7.3: Post-fire recovery of forest GPP across the northern high latitudes. a, b, and c are the spatial distribution of β_{GPP}, β_{GPP}^{NF} (for needleleaf forests), and β_{GPP}^{BF} (for broadleaf forests), respectively. The maps show multi-year averages, with all datasets resampled to a 2° resolution. The red solid lines are regression fits based on segmented functions, while the green dashed lines are the breaking points (BP). d, e, and f are the mean values divided into four regions (Siberia, Northern North America, Northern Asia, and Northern Europe) corresponding to a, b, and c, respectively.

7.3.3 Temporal change of first-year post-fire recovery of GPP (β_{GPP}) in forests

We examined inter-annual changes in forest β_{GPP} across the northern high latitudes in 2002 and 2022 (Figure 7.4a). On the average, the forest β_{GPP} time series data can be divided into two phases: 2002-2007 and 2008-2022. β_{GPP} showed no significant inter-annual changes from 2002 to 2007 ($R^2 = 0.01$, $p = 0.882$), but decreased significantly

from 2008 to 2022 ($R^2 = 0.85$, $p < 0.01$), at an average rate of 0.85% per year. We further examined concurrent trends in fire intensity, fire severity, burned area, temperature, VPD, soil water, and radiation for each period. From 2002 to 2007, fire intensity, fire severity, and radiation decreased, while burned area, temperature, and VPD remained stable, and soil water increased. From 2008 to 2022, fire intensity, fire severity, burned area, temperature, and VPD increased, radiation remained stable, and soil water decreased.

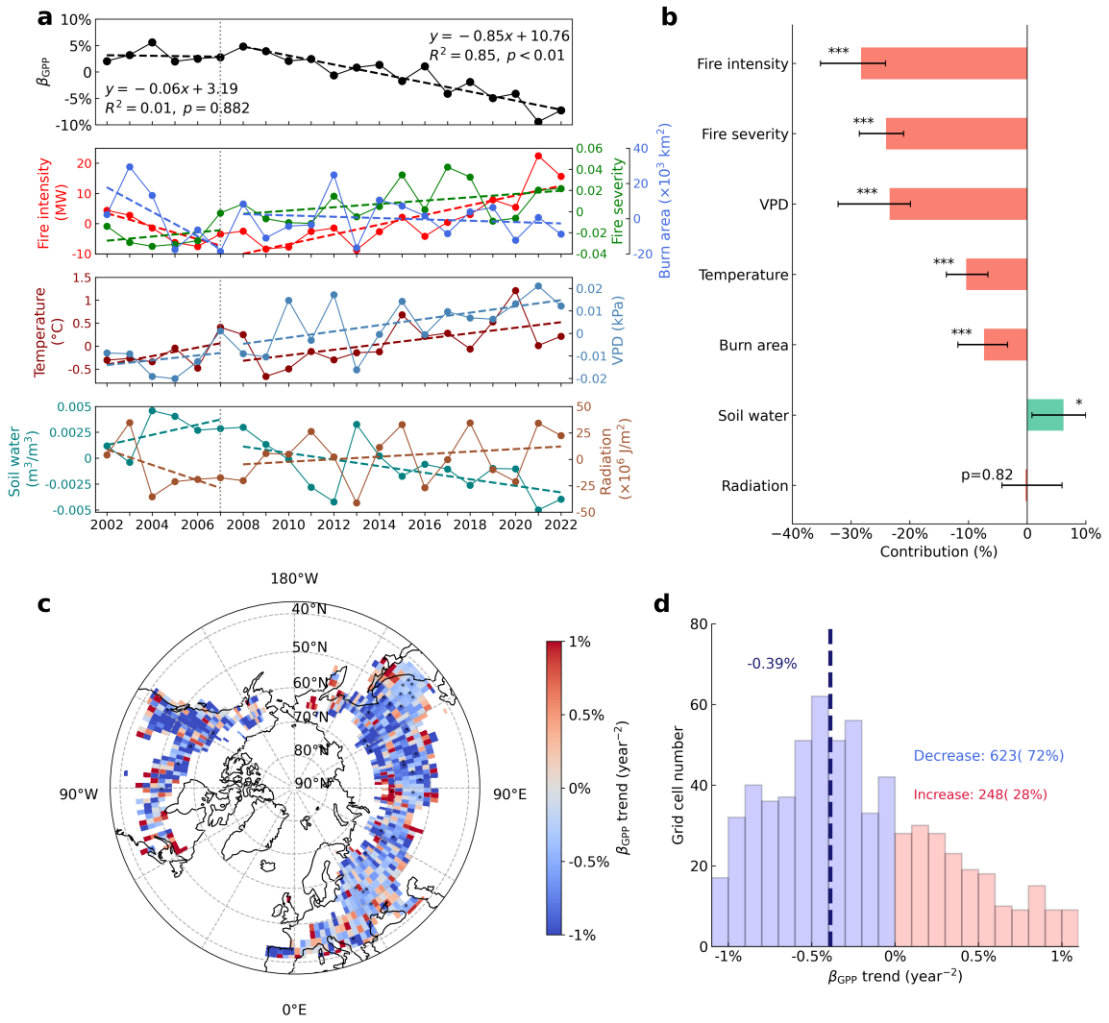

Figure 7.4: Interannual variability of βGPP from 2002 to 2022 in Northern high-latitude forests. a. Time series of the annual mean βGPP, fire-related indicators (fire

intensity, fire severity, and burn area), and climate-related indicators (temperature, VPD, soil water, and radiation) across the Northern high-latitude forests from 2002 to 2022. Each series is calculated as an interannual anomaly. The dashed lines represent the simple linear regression fit curve. Simple linear regression was performed over two periods: 2002-2007 and 2008-2022. b. The contribution of driving factors to the β_{GPP} trend from ridge regression analysis. The positive (+) and negative (-) signs represent the positive and negative impact of the driving factors on the β_{GPP} trend. * and * represent significance at the 0.01 and 0.05 levels, respectively. c. Trends of the annual mean β_{GPP} for each 2° grid cell from 2002 to 2022. The β_{GPP} trend is quantified using the slope of a simple linear regression model, with red and blue color gradients indicating increasing and decreasing trends, respectively. * denote statistically significant trends at the 0.01 level. d. Histogram of all 871 grid cells from c, where the red and blue bars represent the number of grid cells exhibiting increasing and decreasing β_{GPP} trends, respectively. The dark blue dashed line indicates the mean β_{GPP} trend across the Northern high-latitude forests.**

7.3.4 Attribution analysis of first-year post-fire recovery during 2002-2022

Attribution analysis using ridge regression reveals that increases in fire intensity, fire severity, burned area, temperature, and VPD each exert significant negative effects on β_{GPP} (Figure 7.4b). Fire intensity, fire severity, and burned area contributed −28%, −24%, and -7% respectively. Together, these three fire-related factors explain 59% of the observed β_{GPP} decrease. Increasing VPD and temperature contributed −23% and

−10%, respectively. Radiation had a negligible negative effect (−0.3%). In comparison, soil water exerted a positive influence (+6%). Overall, the significant decrease in β_{GPP} after 2008 is primarily attributed to larger, more intense, and more severe fires, coupled with higher VPD and temperature, as well as reduced soil water. Fire intensity and severity emerge as the major drivers.

To further examine spatial variations, we explored β_{GPP} trends at each 2° grid cell. For those grid cells with at least five observations during the study period, linear regression was performed, and the regression slope was used to quantify β_{GPP} trends (Figure 7.4c, d). Overall, β_{GPP} exhibited a decreasing trend across the northern high-latitude forests, with a mean β_{GPP} trend of -0.39% year^{-2}. Among the 871 grid cells with statistically meaningful trends, 623 cells (72%) showed a decreasing β_{GPP} trend, whereas 248 cells (28%) showed an increasing trend. Both decreasing and increasing trend grid cells were distributed across the Northern high-latitude forests without clear spatial clustering, although most grid cells experienced a decrease. These findings indicate that over the past two decades, the resilience of northern high-latitude forests to wildfire disturbances has progressively declined.

7.4 Discussions

7.4.1 First-year post-fire carbon uptake recovery in northern high latitudes

The intensification of wildfires in recent years has led to an increased attention on the impact of wildfires on forests in northern high latitudes (Yang Chen et al., 2021; Virkkala et al., 2025; Walker et al., 2019). Although many site- and regional-scale

studies have highlighted the significant effects of wildfires on forest carbon dynamics in northern high latitudes (Boby et al., 2010; Fan et al., 2023; Virkkala et al., 2025; Wilkinson et al., 2023), large-scale and long-term assessments of post-fire recovery of forests in the region remain insufficient. Our results reveal that over the past two decades, GPP of forests in the northern high latitudes can recovered to 85% of pre-fire levels within one year, while net carbon losses are around 10% to 30% per year (Harden et al., 2000). Our results also reveal that post-fire GPP recovery was relatively lower in higher latitude regions than in lower latitude regions, in particular in Siberia, Northern Asia, and Northern North America, which is consistent with previous site-scale studies in high-latitude North America (Boby et al., 2010; Bond-Lamberty et al., 2007), but not observed in Europe. Our analysis shows that, across the northern high latitudes, first-year post-fire forest CO_2 uptake recovery has declined steadily since 2008, indicating growing loss of resilience to wildfires. The decreasing recovery magnitude echoes the recent report of lengthening recovery times (Lv et al., 2025) and is primarily driven by larger, more intense, and more severe fires, compounded by higher VPD, elevated air temperatures and persistent soil-moisture deficits.

7.4.2 Trait-driven divergence in forest post-fire recovery responses to fires

Different forest types, such as needleleaf and broadleaf forests, exhibit significant variations in their responses to wildfires (de Groot et al., 2013; Rogers et al., 2015). Our results show that GPP responses to wildfires (first-year post-fire recovery) have notable differences in space and tree traits (needleleaf tree vs broadleaf tree), which can be explained from biological and ecological characteristics of these forest types. First,

needleleaf forests have high resin content, dense canopy structure, and significant accumulation of understory fuels (thick layer of litterfall) and are more susceptible to fire and have more intense crown fires, resulting larger damages of trees (de Groot et al., 2013; Harden et al., 2000). In contrast, broadleaf forests experience relatively lower fire-induced losses due to their higher leaf moisture content, more open canopy structure, and thick bark, which provide greater fire resistance (Richardson, 2000; Scott, 2001). Second, needleleaf forests have slower nutrient cycling, which limits their ability to recover and rapidly compensate for fire-induced carbon losses, whereas broadleaf forests have higher nutrient-use efficiency and can partially offset carbon losses through post-fire carbon uptake (Melvin et al., 2015). As needleleaf forests are more vulnerable to wildfires compared to broadleaf forests, many studies reported a shift in forest succession toward broadleaf-dominated ecosystems following severe wildfires (Jensen et al., 2021; Johnstone et al., 2010; Kim et al., 2024; Mack et al., 2021; J. A. Wang et al., 2020). A study in Canada found that increasing the proportion of broadleaf species after fire can markedly enhance post-fire recovery (Kim et al., 2024). In high-fire-risk areas, replacing needleleaf trees with broadleaf species to establish firebreaks could enhance forest resilience and recovery (Jie Zhao et al., 2024). These study and our findings highlight the greater fire resistance and resilience of broadleaf forests to wildfires than needleleaf forests, providing new scientific evidence for future wildfire recovery management, contributing to optimizing post-fire ecological restoration strategies. Therefore, while addressing climate change remains a priority, post-fire vegetation management should also be strengthened.

7.4.3 Drivers and attribution in declining post-fire recovery in Northern high-latitude forest

In our attribution analyses, increased fire intensity and severity have emerged as the two dominant factors, exerting a more substantial influence on post-fire recovery than the prevailing climatic conditions in the region. This finding contrasts with a recent global synthesis that identified climate as the primary driver of post-fire recovery (Xu et al., 2024), yet it concurs with several recent studies (Lv et al., 2025; Vieira et al., 2024). Fire intensity and severity affect carbon uptake capacity directly by fire-induced deforestation and forest degradation (Lapola et al., 2023) and indirectly by elevating land surface temperatures (LST), as seedlings are highly sensitive and vulnerable to rising LST (Vieira et al., 2024), and warmer surfaces can feed back positively on fire activity, creating fire cycles that are particularly pronounced at high latitudes (Liu et al., 2019; Jie Zhao et al., 2024). Our analysis also reveals that increasing VPD and air temperature decrease post-fire recovery, consistent with evidence from field observations, satellite products, and modelling studies (Fu et al., 2022; Hemes et al., 2023; Lv et al., 2025). VPD and air temperature are tightly coupled, and thus high VPD and air temperature raise atmospheric moisture demand, force stomatal closure, increase respiratory costs, and decrease post-fire soil moisture, ultimately slowing the post-fire carbon uptake recovery (S. Li et al., 2023; Massmann et al., 2019; Meyer et al., 2018). These factors help explain the continuous decrease in post-fire CO_2 uptake recovery that we have observed in high-latitude forests since the late 2000s under the prevailing climate regime. Nearly the entire land area north of 40° N exhibits this

decreasing trend, suggesting that it is challenging for forests to return to pre-fire levels, which could result in changes in forest types to adapt to fire (Mack et al., 2021). We are concerned that, if it persists, it could substantially heighten the risk of terrestrial carbon loss.

7.4.4 The rising threat of fires to the northern high-latitude forest carbon dynamics

Over the past decades, many publications reported the negative impacts of increased wildfires (spatial extent, fire intensity, frequency) and intensified climate extremes on terrestrial carbon fluxes and stocks in northern high latitudes (Balshi et al., 2009; Cattau et al., 2020; Yang Chen et al., 2021; Goetz et al., 2012; Li et al., 2025; Walker et al., 2019). Increased fire-driven losses of forest carbon fluxes and stocks indicate a loss of resistance to wildfires. Wildfire-induced CO_2 emissions in northern high latitudes continued to increase and have approached historical record levels (Van Der Werf et al., 2017; Zheng et al., 2023). These "increased CO_2 emissions from fire and reduced CO_2 uptake (GPP) after fire" in the norther high latitudes poses major concern on forests in the region as carbon sink, as it is difficult for post-fire carbon uptake to offset wildfire CO_2 emissions in the short term. In the future, wildfires are expected to become more frequent (Yang Chen et al., 2021; Jones et al., 2022), which may accelerate the weakening of forest carbon sinks and even lead to their transition into carbon sources. In fact, a recent research has shown that due to frequent or large-scale fire disturbances, approximately one-third of the Arctic–Boreal Zone has already shifted from a carbon sink to a carbon source (Virkkala et al., 2025). To date, most current terrestrial

ecosystem models tend to underestimate the impact of wildfires (Hantson et al., 2016; Quegan et al., 2011; Van Der Werf et al., 2017). Therefore, future Earth ecosystem models should integrate the declining post-fire GPP recovery trend caused by wildfires to more accurately predict the role of northern high-latitude forests in the global carbon cycle and develop more effective mitigation strategies.

7.5 Conclusion

In this chapter, we systematically assessed the spatial-temporal characteristics of forest wildfires and first-year post-fire GPP recovery from 2002 to 2022 in the northern high latitudes. Our findings reveal significant spatial heterogeneity and trait-driven (needleleaf forest vs broadleaf forest) divergence in forest post-fire recovery responses to wildfires in the region. Additionally, we analyzed inter-annual changes and trends in post-fire GPP recovery and their drivers. This study fills a critical knowledge gap regarding the large-scale and decadal responses of high-latitude forests' GPP to fire disturbance, and it highlights the heightened risk of carbon loss currently facing northern forests under the prevailing climate regime. We recommend incorporating these findings into Earth system models to improve the accuracy of wildfire risk assessments and carbon cycle simulations. Future research should integrate wildfire monitoring, risk assessment, and post-fire recovery management to further elucidate carbon dynamics in the region under the combined pressures of global warming and increasing wildfire severity, providing a scientific basis for wildfire prevention and ecological restoration strategies.

Chapter 8 : Conclusions and perspectives

Accurately estimating global gross primary production (GPP) is not only a central question in terrestrial carbon cycle research but also a fundamental prerequisite for quantifying the response of terrestrial ecosystems to climate change and disturbances. The reliability of assessments regarding carbon sink/source patterns, land–atmosphere feedback strength, and future scenario projections hinges directly on the precision of GPP estimates. Currently, substantial discrepancies remain among existing global GPP models and data products in terms of estimation magnitude, interannual variability, and long-term trends, underscoring the urgent need for continuous methodological and data-driven improvements.

This dissertation focuses on the classical light use efficiency (LUE) model, the Vegetation Photosynthesis Model (VPM), and introduces site-specific parameter inputs and a comprehensive set of environmental constraints into its structure and parameterization. Two improved versions, VPM v3.0 and VPM v4.0, were developed. Specifically, VPM v3.0 considers (1) light absorption influenced by chlorophyll content and leaf traits (broadleaf vs. needleleaf), and (2) CO_2 fixation determined by plant functional types (C_3 and C_4) and site-specific effects of air temperature and water availability. Building on this, VPM v4.0 further incorporates the direct effect of rising atmospheric CO_2 concentration on photosynthesis within its modeling framework. Accordingly, the two improved versions represent a model without CO_2 (VPM v3.0, w/o CO_2) and a model with CO_2 (VPM v4.0, w/ CO_2). Multi-source datasets including

eddy covariance flux tower observations and widely used benchmark GPP products were used to evaluate through systematic comparison. We evaluated the performance of VPM outputs at multiple spatial scales, including long-term observation sites and the global scale. Results show that the improved VPM models significantly improve the estimation of global GPP in terms of magnitude, interannual variation, and long-term trend.

Although VPM has demonstrated strong robustness in estimating GPP across site, regional, and global scales, there remains considerable room for improvement. Future advancements in LUE models are expected to focus on improving input datasets and enhancing spatiotemporal resolution.

At the data input level, there is an urgent need to shift from traditional vegetation indices to solar-induced chlorophyll fluorescence (SIF) as the primary driver. Vegetation indices are highly sensitive to geometric and atmospheric corrections of surface reflectance products. Any variation in viewing geometry or interference from clouds and aerosols can amplify errors, which then propagate through the LUE calculation chain. In contrast, SIF is a direct signal of photochemical energy release. It does not saturate under high leaf area index or intense radiation and is less sensitive to observational geometry and atmospheric disturbance. Using SIF to estimate effective light absorption can not only reduce uncertainty but also enhance the model's responsiveness to extreme climate events such as drought and wildfire. Additionally, with the rapid development of high-resolution satellite constellations, unmanned aerial systems, and automated ground-based observation networks, future LUE models

should integrate machine learning, data assimilation, and uncertainty quantification techniques to enhance their predictive capabilities. Leveraging multi-source datasets with higher spatial and temporal resolution will be key to reducing uncertainty and improving model accuracy.

There is a need to move beyond the daily-scale linear assumption in modeling GPP. VPM currently estimates GPP at a daily time step. However, future models should aim for a finer temporal resolution and adopt nonlinear radiation response functions at sub-daily scales. In tropical and high-radiation regions, midday canopy light saturation is a common phenomenon. Models that maintain the assumption of a linear relationship between incident and absorbed radiation risk overestimate light absorption and thus GPP during peak radiation periods. Incorporating SIF-based thresholds and nonlinear response functions can help address this limitation.

Building on the high-spatiotemporal resolution global GPP dataset derived by VPM v3.0, this dissertation further investigates the impacts of increasingly frequent wildfire disturbances on terrestrial ecosystem productivity and post-fire recovery trajectories. Focusing on fire-prone regions such as Australia and the high-latitude forests that serve as critical global carbon sinks, GPP is used as a proxy for vegetation function to reveal ecosystem resilience and sensitivities to fire behavior and climate conditions. These findings provide new insights into the coupled dynamics of fire and the carbon cycle under ongoing climate change.

Driven by global warming, the intensification of extreme events, and increased fire frequency, the scale and intensity of wildfires have shown an increasing trend over

recent decades. To better understand how terrestrial ecosystems respond to fire, future research must extend to broader spatial scales, including global assessments, and develop integrated analytical frameworks that span biogeographic regions. Ecosystems across different climate zones and functional types, such as forests, savannas, tundra, and Mediterranean shrublands, exhibit pronounced differences in fire behavior, fuel structure, vegetation adaptation strategies, background climate, and soil–microbe feedback. These differences result in highly variable responses to fire disturbances. Future work should integrate high-resolution global datasets on GPP, SIF, carbon emissions, and burned areas. Coupling these data with multi-source machine learning assimilation techniques will enable a more accurate assessment of fire risks and support the development of targeted, data-driven fire management strategies.

High-precision global GPP products not only enable tracking of ecosystem response to wildfire disturbances but also provide a foundation for assessing the terrestrial carbon cycle's response to global environmental change. When coupled with rising atmospheric CO_2 concentrations, climate reanalysis datasets, and inventories of extreme events such as heatwaves, droughts, and floods, the global GPP products can help reveal the responses of ecosystems to changing chemical, meteorological, and hydrological conditions.

For scenario-based projections, integrating global GPP with various temperature control pathways from CMIP project and the 1.5 °C targets of the Paris Agreement allow for quantifying the stability of terrestrial carbon sinks under different emissions trajectories, as well as their contribution to the global carbon budget. Moreover, linking

global GPP with socioeconomic data, such as land use change, crop yields, and urban expansion, can support comprehensive assessments of how ecosystem service dynamics influence food security and human well-being.

Bibliography

Abram, N. J., Henley, B. J., Sen Gupta, A., Lippmann, T. J. R., Clarke, H., Dowdy, A. J., . . . Wooster, M. J. (2021). Connections of climate change and variability to large and extreme forest fires in southeast Australia. *Communications Earth & Environment, 2*(1), 1-17 doi:https://doi.org/10.1038/s43247-020-00065-8

Ainsworth, E. A., & Rogers, A. (2007). The response of photosynthesis and stomatal conductance to rising [CO2]: mechanisms and environmental interactions. *Plant, cell & environment, 30*(3), 258-270. doi:https://doi.org/10.1111/j.1365-3040.2007.01641.x

Alemohammad, S. H., Fang, B., Konings, A. G., Aires, F., Green, J. K., Kolassa, J., . . . Gentine, P. (2017). Water, Energy, and Carbon with Artificial Neural Networks (WECANN): a statistically based estimate of global surface turbulent fluxes and gross primary productivity using solar-induced fluorescence. *Biogeosciences, 14*(18), 4101-4124. doi:https://doi.org/10.5194/bg-14-4101-2017

Alonso-González, E., & Fernández-García, V. (2021). MOSEV: a global burn severity database from MODIS (2000–2020). Earth Syst. Sci. Data 13, 1925–1938. In.

Anav, A., Friedlingstein, P., Beer, C., Ciais, P., Harper, A., Jones, C., . . . Peylin, P. (2015). Spatiotemporal patterns of terrestrial gross primary production: A review. *Reviews of Geophysics, 53*(3), 785-818. doi:https://doi.org/10.1002/2015RG000483

Anderson, L. O., Shimabukuro, Y. E., Defries, R. S., & Morton, D. (2005). Assessment

of deforestation in near real time over the Brazilian Amazon using multitemporal fraction images derived from Terra MODIS. *IEEE Geoscience and Remote Sensing Letters, 2*(3), 315-318. doi:https://doi.org/10.1109/LGRS.2005.850364.

Armstrong McKay, D. I., Staal, A., Abrams, J. F., Winkelmann, R., Sakschewski, B., Loriani, S., . . . Lenton, T. M. (2022). Exceeding 1.5 C global warming could trigger multiple climate tipping points. *Science, 377*(6611), eabn7950. doi:10.1126/science.abn7950

Arora, V. K., Boer, G. J., Friedlingstein, P., Eby, M., Jones, C. D., Christian, J. R., . . . Cadule, P. (2013). Carbon–concentration and carbon–climate feedbacks in CMIP5 Earth system models. *Journal of Climate, 26*(15), 5289-5314. doi:https://doi.org/10.1175/JCLI-D-12-00494.1

Badgley, G., Anderegg, L. D. L., Berry, J. A., & Field, C. B. (2019). Terrestrial gross primary production: Using NIRV to scale from site to globe. *Global Change Biology, 25*(11), 3731-3740. doi:https://doi.org/10.1111/gcb.14729

Badgley, G., Field, C. B., & Berry, J. A. (2017). Canopy near-infrared reflectance and terrestrial photosynthesis. *Science advances, 3*(3), e1602244.

Baig, S., Medlyn, B. E., Mercado, L. M., & Zaehle, S. n. (2015). Does the growth response of woody plants to elevated CO 2 increase with temperature? A modelâ€□oriented metaâ€□analysis. *Global Change Biology, 21*(12), 4303-4319. doi:https://doi.org/10.1111/gcb.12962

Baldocchi, D. (2014). Measuring fluxes of trace gases and energy between ecosystems

and the atmosphere–the state and future of the eddy covariance method. *Global Change Biology, 20*(12), 3600-3609. doi:https://doi.org/10.1111/gcb.12649

Baldocchi, D., Falge, E., Gu, L., Olson, R., Hollinger, D., Running, S., . . . Evans, R. (2001). FLUXNET: A new tool to study the temporal and spatial variability of ecosystem-scale carbon dioxide, water vapor, and energy flux densities. *Bulletin of the American Meteorological Society, 82*(11), 2415-2434. doi:https://doi.org/10.1175/1520-0477(2001)082<2415:FANTTS>2.3.CO;2

Baldocchi, D. D. (2003). Assessing the eddy covariance technique for evaluating carbon dioxide exchange rates of ecosystems: past, present and future. *Global Change Biology, 9*(4), 479-492. doi:https://doi.org/10.1046/j.1365-2486.2003.00629.x

Baldocchi, D. D. (2020). How eddy covariance flux measurements have contributed to our understanding of Global Change Biology. *Global Change Biology, 26*(1), 242-260. doi:https://doi.org/10.1111/gcb.14807

Balshi, M. S., McGuire, A. D., Duffy, P., Flannigan, M., Walsh, J., & Melillo, J. (2009). Assessing the response of area burned to changing climate in western boreal North America using a Multivariate Adaptive Regression Splines (MARS) approach. *Global Change Biology, 15*(3), 578-600. doi:https://doi.org/10.1111/j.1365-2486.2008.01679.x

Bao, S. G., Wang, W. J., Liu, Z., Zhang, H. K., Wang, L., Ma, J., . . . He, H. S. (2024). Revealing post-megafire spectral and compositional recovery in the Siberian boreal forest using Landsat time series and regression-based unmixing approach.

Remote Sensing of Environment, 311, 114307. doi:https://doi.org/10.1016/j.rse.2024.114307

Barlow, J., & Peres, C. A. (2008). Fire-mediated dieback and compositional cascade in an Amazonian forest. *Philosophical Transactions of the Royal Society B: Biological Sciences, 363*(1498), 1787-1794. doi:https://doi.org/10.1098/rstb.2007.0013

Bartels, S. F., Chen, H. Y. H., Wulder, M. A., & White, J. C. (2016). Trends in post-disturbance recovery rates of Canada's forests following wildfire and harvest. *Forest ecology and management, 361*, 194-207. doi:https://doi.org/10.1016/j.foreco.2015.11.015

Basistha, A., Arya, D. S., & Goel, N. K. (2009). Analysis of historical changes in rainfall in the Indian Himalayas. *International Journal of Climatology: A Journal of the Royal Meteorological Society, 29*(4), 555-572. doi:https://doi.org/10.1002/joc.1706

Baur, M. J., Friend, A. D., & Pellegrini, A. F. A. (2024). Widespread and systematic effects of fire on plant–soil water relations. *Nature Geoscience, 17*(11), 1115-1120. doi:https://doi.org/10.1038/s41561-024-01563-6

Beer, C., Reichstein, M., Tomelleri, E., Ciais, P., Jung, M., Carvalhais, N., . . . Bonan, G. B. (2010). Terrestrial gross carbon dioxide uptake: global distribution and covariation with climate. *Science, 329*(5993), 834-838. doi:https://doi.org/10.1126/science.1184984

Bekryaev, R. V., Polyakov, I. V., & Alexeev, V. A. (2010). Role of polar amplification

in long-term surface air temperature variations and modern Arctic warming. *Journal of Climate, 23*(14), 3888-3906. doi:https://doi.org/10.1175/2010JCLI3297.1

Bennett, A. C., Arndt, S. K., Bennett, L. T., Knauer, J., Beringer, J., Griebel, A., . . . Pendall, E. (2021). Thermal optima of gross primary productivity are closely aligned with mean air temperatures across Australian wooded ecosystems. *Global Change Biology, 27*(19), 4727-4744. doi:https://doi.org/10.1111/gcb.15760

Beringer, J., Hutley, L. B., Abramson, D., Arndt, S. K., Briggs, P., Bristow, M., . . . Edwards, A. C. (2015). Fire in Australian savannas: from leaf to landscape. *Global Change Biology, 21*(1), 62-81. doi:https://doi.org/10.1111/gcb.12686

Beringer, J., Hutley, L. B., Tapper, N. J., & Cernusak, L. A. (2007). Savanna fires and their impact on net ecosystem productivity in North Australia. *Global Change Biology, 13*(5), 990-1004. doi:https://doi.org/10.1111/j.1365-2486.2007.01334.x

Blanco-Rodríguez, M. Á., Ameztegui, A., Gelabert, P., Rodrigues, M., & Coll, L. (2023). Short-term recovery of post-fire vegetation is primarily limited by drought in Mediterranean forest ecosystems. *Fire Ecology, 19*(1), 68. doi:https://doi.org/10.1186/s42408-023-00228-w

Boby, L. A., Schuur, E. A. G., Mack, M. C., Verbyla, D., & Johnstone, J. F. (2010). Quantifying fire severity, carbon, and nitrogen emissions in Alaska's boreal forest. *Ecological Applications, 20*(6), 1633-1647.

doi:https://doi.org/10.1890/08-2295.1

Bond-Lamberty, B., Peckham, S. D., Ahl, D. E., & Gower, S. T. (2007). Fire as the dominant driver of central Canadian boreal forest carbon balance. *Nature, 450*(7166), 89-92. doi:https://doi.org/10.1038/nature06272

Bond, W. J., & Keeley, J. E. (2005). Fire as a global â€˜herbivoreâ€™: the ecology and evolution of flammable ecosystems. *Trends in ecology & evolution, 20*(7), 387-394. doi:https://doi.org/10.1016/j.tree.2005.04.025

Bond, W. J., & Midgley, J. J. (2001). Ecology of sprouting in woody plants: the persistence niche. *Trends in ecology & evolution, 16*(1), 45-51. doi:10.1016/S0169-5347(00)02033-4

Boschetti, L., Roy, D. P., Giglio, L., Huang, H., Zubkova, M., & Humber, M. L. (2019). Global validation of the collection 6 MODIS burned area product. *Remote Sensing of Environment, 235*, 111490. doi:https://doi.org/10.1016/j.rse.2019.111490

Botella-Martínez, M. A., & Fernández-Manso, A. (2017). Estudio de la severidad post-incendio en la Comunidad Valenciana comparando los índices dNBR, RdNBR y RBR a partir de imágenes Landsat 8. *Revista de Teledetección*(49), 33-47. doi:https://doi.org/10.4995/raet.2017.7095

Bounoua, L., Hall, F., Sellers, P., Kumar, A., Collatz, G., Tucker, C., & Imhoff, M. (2010). Quantifying the negative feedback of vegetation to greenhouse warming: A modeling approach. *Geophysical Research Letters, 37*(23). doi:https://doi.org/10.1029/2010GL045338

Brovkin, V., Brücher, T., Kleinen, T., Zaehle, S., Joos, F., Roth, R., . . . Leuenberger, M. (2016). Comparative carbon cycle dynamics of the present and last interglacial. *Quaternary Science Reviews, 137*, 15-32. doi:https://doi.org/10.1016/j.quascirev.2016.01.028

Buermann, W., Bikash, P. R., Jung, M., Burn, D. H., & Reichstein, M. (2013). Earlier springs decrease peak summer productivity in North American boreal forests. *Environmental Research Letters, 8*(2), 024027. doi:https://doi.org/10.1088/1748-9326/8/2/024027

Buermann, W., Forkel, M., O'sullivan, M., Sitch, S., Friedlingstein, P., Haverd, V., . . . Lienert, S. (2018). Widespread seasonal compensation effects of spring warming on northern plant productivity. *Nature, 562*(7725), 110-114. doi:https://doi.org/10.1038/s41586-018-0555-7

Burton, C. A., Kelley, D. I., Burke, E., Mathison, C., Jones, C. D., Betts, R. A., . . . Anderson, L. O. (2024). Fire weakens land carbon sinks before 1.5° C. *Nature Geoscience*, 1-7. doi:https://doi.org/10.1038/s41561-024-01554-7

Byrne, B., Liu, J., Lee, M., Yin, Y., Bowman, K. W., Miyazaki, K., . . . Griffith, D. W. T. (2021). The carbon cycle of southeast Australia during 2019–2020: Drought, fires, and subsequent recovery. *AGU Advances, 2*(4), e2021AV000469. doi:https://doi.org/10.1029/2021AV000469

Cai, J., Liu, Y., Lei, T., & Pereira, L. S. (2007). Estimating reference evapotranspiration with the FAO Penman–Monteith equation using daily weather forecast messages. *Agricultural and Forest Meteorology, 145*(1-2), 0168-1923.

doi:https://doi.org/10.1016/j.agrformet.2007.04.012

Campbell, J. E., Berry, J. A., Seibt, U., Smith, S. J., Montzka, S. A., Launois, T., . . . Laine, M. (2017). Large historical growth in global terrestrial gross primary production. *Nature, 544*(7648), 84-87. doi:https://doi.org/10.1038/nature22030

Canadell, J. G., & Jackson, R. B. (2021). Ecosystem collapse and climate change: an introduction. In *Ecosystem collapse and climate change* (pp. 1-9): Springer.

Canadell, J. G., Meyer, C. P., Cook, G. D., Dowdy, A., Briggs, P. R., Knauer, J. r., . . . Haverd, V. (2021). Multi-decadal increase of forest burned area in Australia is linked to climate change. *Nature communications, 12*(1), 6921. doi:https://doi.org/10.1038/s41467-021-27225-4

Cane, M. A. (2010). Decadal predictions in demand. *Nature Geoscience, 3*(4), 231-232. doi:https://doi.org/10.1038/ngeo823

Caon, L., Vallejo, V. R., Ritsema, C. J., & Geissen, V. (2014). Effects of wildfire on soil nutrients in Mediterranean ecosystems. *Earth-Science Reviews, 139*, 47-58. doi:https://doi.org/10.1016/j.earscirev.2014.09.001

Cattau, M. E., Wessman, C., Mahood, A., & Balch, J. K. (2020). Anthropogenic and lightning-started fires are becoming larger and more frequent over a longer season length in the USA. *Global Ecology and Biogeography, 29*(4), 668-681. doi:https://doi.org/10.1111/geb.13058

Celis, J., Xiao, X., Wagle, P., Basara, J., McCarthy, H., & Souza, L. (2024). A comparison of moderate and high spatial resolution satellite data for modeling gross primary production and transpiration of native prairie, alfalfa, and winter

wheat. *Agricultural and Forest Meteorology, 344*, 109797. doi:https://doi.org/10.1016/j.agrformet.2023.109797

Celis, J., Xiao, X., White Jr, P. M., Cabral, O. M. R., & Freitas, H. C. (2023). Improved Modeling of Gross Primary Production and Transpiration of Sugarcane Plantations with Time-Series Landsat and Sentinel-2 Images. *Remote Sensing, 16*(1), 46. doi:https://doi.org/10.3390/rs16010046

Cernusak, L. A., Hutley, L. B., Beringer, J., & Tapper, N. J. (2006). Stem and leaf gas exchange and their responses to fire in a north Australian tropical savanna. *Plant, cell & environment, 29*(4), 632-646. doi:https://doi.org/10.1111/j.1365-3040.2005.01442.x

Certini, G. (2005). Effects of fire on properties of forest soils: a review. *Oecologia, 143*, 1-10. doi:https://doi.org/10.1007/s00442-004-1788-8

Chang, Q., Xiao, X., Doughty, R., Wu, X., Jiao, W., & Qin, Y. (2021a). Assessing variability of optimum air temperature for photosynthesis across site-years, sites and biomes and their effects on photosynthesis estimation. *Agricultural and Forest Meteorology, 298*, 108277. doi:https://doi.org/10.1016/j.agrformet.2020.108277

Chang, Q., Xiao, X., Doughty, R., Wu, X., Jiao, W., & Qin, Y. (2021b). Assessing variability of optimum air temperature for photosynthesis across site-years, sites and biomes and their effects on photosynthesis estimation. *Agricultural and Forest Meteorology, 298*, 108277 %@ 100168-101923.

Chang, Q., Xiao, X., Wu, X., Doughty, R., Jiao, W., Bajgain, R., . . . Wang, J. (2020).

Estimating site-specific optimum air temperature and assessing its effect on the photosynthesis of grasslands in mid-to high-latitudes. *Environmental Research Letters, 15*(3), 034064. doi:https://doi.org/10.1088/1748-9326/ab70bb

Chang, Z., Fan, L., Wigneron, J.-P., Wang, Y.-P., Ciais, P., Chave, J., . . . Ju, W. (2023). Estimating Aboveground Carbon Dynamic of China Using Optical and Microwave Remote-Sensing Datasets from 2013 to 2019. *Journal of Remote Sensing, 3*, 0005. doi:https://doi.org/10.34133/remotesensing.0005

Change, I. P. O. C. (2007). Climate change 2007: the physical science basis. *Agenda, 6*(07), 333.

Chaves, M. M., Flexas, J., & Pinheiro, C. (2009). Photosynthesis under drought and salt stress: regulation mechanisms from whole plant to cell. *Annals of botany, 103*(4), 551-560. doi:https://doi.org/10.1093/aob/mcn125

Chen, A., Huang, L., Liu, Q., & Piao, S. (2021). Optimal temperature of vegetation productivity and its linkage with climate and elevation on the Tibetan Plateau. *Global Change Biology, 27*(9), 1942-1951.

Chen, C., Park, T., Wang, X., Piao, S., Xu, B., Chaturvedi, R. K., . . . Fensholt, R. (2019). China and India lead in greening of the world through land-use management. *Nature Sustainability, 2*(2), 122-129. doi:https://doi.org/10.1038/s41893-019-0220-7

Chen, C., Riley, W. J., Prentice, I. C., & Keenan, T. F. (2022). CO2 fertilization of terrestrial photosynthesis inferred from site to global scales. *Proceedings of the National Academy of Sciences, 119*(10), e2115627119.

doi:https://doi.org/10.1073/pnas.2115627119

Chen, X., Chen, T., Liu, S., Chai, Y., Guo, R., Dai, J., . . . Wei, X. (2024). Vegetation Index-Based Models Without Meteorological Constraints Underestimate the Impact of Drought on Gross Primary Productivity. *Journal of Geophysical Research: Biogeosciences, 129*(1), e2023JG007499 doi:https://doi.org/10.1029/2023JG007499

Chen, Y., Feng, X., Fu, B., Wu, X., & Gao, Z. (2021). Improved global maps of the optimum growth temperature, maximum light use efficiency, and gross primary production for vegetation. *Journal of Geophysical Research: Biogeosciences, 126*(4), e2020JG005651.

Chen, Y., Romps, D. M., Seeley, J. T., Veraverbeke, S., Riley, W. J., Mekonnen, Z. A., & Randerson, J. T. (2021). Future increases in Arctic lightning and fire risk for permafrost carbon. *Nature Climate Change, 11*(5), 404-410. doi:https://doi.org/10.1038/s41558-021-01011-y

Cheng, L., Zhang, L., Wang, Y.-P., Canadell, J. G., Chiew, F. H. S., Beringer, J., . . . Zhang, Y. (2017). Recent increases in terrestrial carbon uptake at little cost to the water cycle. *Nature communications, 8*(1), 110. doi:https://doi.org/10.1038/s41467-017-00114-5

Chu, H., Luo, X., Ouyang, Z., Chan, W. S., Dengel, S., Biraud, S. C., . . . Arain, M. A. (2021). Representativeness of Eddy-Covariance flux footprints for areas surrounding AmeriFlux sites. *Agricultural and Forest Meteorology, 301*, 108350. doi:https://doi.org/10.1016/j.agrformet.2021.108350

Ciais, P., Sabine, C., Bala, G., Bopp, L., Brovkin, V., & House, J. I. (2014). Carbon and other biogeochemical cycles. In *Climate Change 2013: The Physical Science Basis. Contribution of Working Group I to the Fifth Assessment Report of the Intergovernmental Panel on Climate Change Change* (pp. 465-570): Cambridge University Press.

Ciais, P., Tagliabue, A., Cuntz, M., Bopp, L., Scholze, M., Hoffmann, G., . . . Kelley, D. I. (2012). Large inert carbon pool in the terrestrial biosphere during the Last Glacial Maximum. *Nature Geoscience, 5*(1), 74-79. doi:https://doi.org/10.1038/ngeo1324

Clarke, P. J., & Knox, K. J. E. (2002). Post-fire response of shrubs in the tablelands of eastern Australia: do existing models explain habitat differences? *Australian Journal of Botany, 50*(1), 53-62. doi:https://doi.org/10.1071/BT01055

Clemente, A. S., Rego, F. C., & Correia, O. A. (2005). Growth, water relations and photosynthesis of seedlings and resprouts after fire. *Acta Oecologica, 27*(3), 233-243. doi:https://doi.org/10.1016/j.actao.2005.01.005

Cohen, I., Huang, Y., Chen, J., Benesty, J., Benesty, J., Chen, J., . . . Cohen, I. (2009). Pearson correlation coefficient. *Noise reduction in speech processing*, 1-4. doi:https://doi.org/10.1007/978-3-642-00296-0_5

Collatz, G. J., Ball, J. T., Grivet, C., & Berry, J. A. (1991). Physiological and environmental regulation of stomatal conductance, photosynthesis and transpiration: a model that includes a laminar boundary layer. *Agricultural and Forest Meteorology, 54*(2-4), 107-136. doi:https://doi.org/10.1016/0168-

1923(91)90002-8

Collatz, G. J., Ribas-Carbo, M., & Berry, J. A. (1992). Coupled photosynthesis-stomatal conductance model for leaves of C4 plants. *Functional Plant Biology, 19*(5), 519-538. doi:https://doi.org/10.1071/PP9920519

Cook, B. D., Davis, K. J., Wang, W., Desai, A., Berger, B. W., Teclaw, R. M., . . . Yi, C. (2004). Carbon exchange and venting anomalies in an upland deciduous forest in northern Wisconsin, USA. *Agricultural and Forest Meteorology, 126*(3-4), 271-295. doi:https://doi.org/10.1016/j.agrformet.2004.06.008

Costanza, R., Fisher, B., Mulder, K., Liu, S., & Christopher, T. (2007). Biodiversity and ecosystem services: A multi-scale empirical study of the relationship between species richness and net primary production. *Ecological economics, 61*(2-3), 478-491. doi:https://doi.org/10.1016/j.ecolecon.2006.03.021

Crisp, M. D., Burrows, G. E., Cook, L. G., Thornhill, A. H., & Bowman, D. M. J. S. (2011). Flammable biomes dominated by eucalypts originated at the Cretaceous–Palaeogene boundary. *Nature communications, 2*(1), 193. doi:https://doi.org/10.1038/ncomms1191

Cui, Y. (2013). Preliminary estimation of the realistic optimum temperature for vegetation growth in China. *Environmental management, 52*, 151-162.

Cui, Y., Xiao, X., Dong, J., Zhang, Y., Qin, Y., Doughty, R. B., . . . MooreIii, B. (2022). Continued increases of gross primary production in urban areas during 2000–2016. *Journal of Remote Sensing*. doi:https://doi.org/10.34133/2022/9868564

Danielson, J. J., & Gesch, D. B. (2011). Global multi-resolution terrain elevation data

2010 (GMTED2010). In: US Geological Survey.

Davidson, E. A., Janssens, I. A., & Luo, Y. (2006). On the variability of respiration in terrestrial ecosystems: moving beyond Q10. *Global Change Biology, 12*(2), 154-164. doi:https://doi.org/10.1111/j.1365-2486.2005.01065.x

Davis, K. T., Robles, M. D., Kemp, K. B., Higuera, P. E., Chapman, T., Metlen, K. L., . . . Addington, R. N. (2023). Reduced fire severity offers near-term buffer to climate-driven declines in conifer resilience across the western United States. *Proceedings of the National Academy of Sciences, 120*(11), e2208120120. doi:https://doi.org/10.1073/pnas.2208120120

de Groot, W. J., Cantin, A. S., Flannigan, M. D., Soja, A. J., Gowman, L. M., & Newbery, A. (2013). A comparison of Canadian and Russian boreal forest fire regimes. *Forest ecology and management, 294*, 23-34. doi:https://doi.org/10.1016/j.foreco.2012.07.033

De Kauwe, M. G., Keenan, T. F., Medlyn, B. E., Prentice, I. C., & Terrer, C. (2016). Satellite based estimates underestimate the effect of CO2 fertilization on net primary productivity. *Nature Climate Change, 6*(10), 892-893. doi:https://doi.org/10.1038/nclimate3105

DeBano, L. F. (2000). The role of fire and soil heating on water repellency in wildland environments: a review. *Journal of hydrology, 231*, 195-206. doi:https://doi.org/10.1016/S0022-1694(00)00194-3

DeBano, L. F., & Conrad, C. E. (1978). The effect of fire on nutrients in a chaparral ecosystem. *Ecology, 59*(3), 489-497. doi:https://doi.org/10.2307/1936579

Desai, A. R., Murphy, B. A., Wiesner, S., Thom, J., Butterworth, B. J., Koupaei-Abyazani, N., . . . Turner, J. (2022). Drivers of decadal carbon fluxes across temperate ecosystems. *Journal of Geophysical Research: Biogeosciences, 127*(12), e2022JG007014. doi:https://doi.org/10.1029/2022JG007014

Devineau, J.-L., Fournier, A., & Nignan, S. (2010). Savanna fire regimes assessment with MODIS fire data: Their relationship to land cover and plant species distribution in western Burkina Faso (West Africa). *Journal of Arid Environments, 74*(9), 1092-1101. doi:https://doi.org/10.1016/j.jaridev.2010.03.009

Didan, K., Munoz, A. B., Solano, R., & Huete, A. (2015). MODIS vegetation index user's guide (MOD13 series). *University of Arizona: Vegetation Index and Phenology Lab*.

Dong, J., Xiao, X., Kou, W., Qin, Y., Zhang, G., Li, L., . . . Biradar, C. (2015). Tracking the dynamics of paddy rice planting area in 1986–2010 through time series Landsat images and phenology-based algorithms. *Remote Sensing of Environment, 160*, 99-113.

Dong, J., Xiao, X., Wagle, P., Zhang, G., Zhou, Y., Jin, C., . . . Wang, J. (2015). Comparison of four EVI-based models for estimating gross primary production of maize and soybean croplands and tallgrass prairie under severe drought. *Remote Sensing of Environment, 162*, 154-168. doi:https://doi.org/10.1016/j.rse.2015.02.022

Donohue, R. J., Roderick, M. L., McVicar, T. R., & Farquhar, G. D. (2013). Impact of

CO2 fertilization on maximum foliage cover across the globe's warm, arid environments. *Geophysical Research Letters, 40*(12), 3031-3035. doi:https://doi.org/10.1002/grl.50563

Doughty, R., Köhler, P., Frankenberg, C., Magney, T. S., Xiao, X., Qin, Y., . . . Moore Iii, B. (2019). TROPOMI reveals dry-season increase of solar-induced chlorophyll fluorescence in the Amazon forest. *Proceedings of the National Academy of Sciences, 116*(44), 22393-22398. doi:https://doi.org/10.1073/pnas.1908157116

Doughty, R., Xiao, X., Köhler, P., Frankenberg, C., Qin, Y., Wu, X., . . . Moore Iii, B. (2021). Global-scale consistency of spaceborne vegetation indices, chlorophyll fluorescence, and photosynthesis. *Journal of Geophysical Research: Biogeosciences, 126*(6), e2020JG006136. doi:https://doi.org/10.1029/2020JG006136

Doughty, R., Xiao, X., Wu, X., Zhang, Y., Bajgain, R., Zhou, Y., . . . Friedman, J. (2018). Responses of gross primary production of grasslands and croplands under drought, pluvial, and irrigation conditions during 2010–2016, Oklahoma, USA. *Agricultural Water Management, 204*, 47-59. doi:https://doi.org/10.1016/j.agwat.2018.04.001

Dow, C., Kim, A. Y., D'Orangeville, L., Gonzalez-Akre, E. B., Helcoski, R., Herrmann, V., . . . McShea, W. J. (2022). Warm springs alter timing but not total growth of temperate deciduous trees. *Nature, 608*(7923), 552-557. doi:https://doi.org/10.1038/s41586-022-05092-3

Dozier, J., Painter, T. H., Rittger, K., & Frew, J. E. (2008). Time–space continuity of daily maps of fractional snow cover and albedo from MODIS. *Advances in Water Resources, 31*(11), 1515-1526. doi:https://doi.org/10.1016/j.advwatres.2008.08.011

Dragoni, D., Schmid, H. P., Wayson, C. A., Potter, H., Grimmond, C. S. B., & Randolph, J. C. (2011). Evidence of increased net ecosystem productivity associated with a longer vegetated season in a deciduous forest in south-central Indiana, USA. *Global Change Biology, 17*(2), 886-897. doi:https://doi.org/10.1111/j.1365-2486.2010.02281.x

Driscoll, D. A., Macdonald, K. J., Gibson, R. K., Doherty, T. S., Nimmo, D. G., Nolan, R. H., . . . Tasker, E. M. (2024). Biodiversity impacts of the 2019–2020 Australian megafires. *Nature*, 1-8. doi:https://doi.org/10.1038/s41586-024-08174-6

Du, S., Liu, X., Chen, J., & Liu, L. (2022). Prospects for solar-induced chlorophyll fluorescence remote sensing from the SIFIS payload onboard the TECIS-1 satellite. *Journal of Remote Sensing*. doi:https://doi.org/10.34133/2022/9845432

Dye, D. G. (2004). Spectral composition and quanta-to-energy ratio of diffuse photosynthetically active radiation under diverse cloud conditions. *Journal of Geophysical Research: Atmospheres, 109*(D10). doi:https://doi.org/10.1029/2003JD004251

Esseen, P.-A., Ehnström, B., Ericson, L., & Sjöberg, K. (1997). Boreal forests.

Ecological bulletins, 16-47. doi:https://www.jstor.org/stable/20113207

Falkowski, P., Scholes, R. J., Boyle, E., Canadell, J., Canfield, D., Elser, J., . . . Linder, S. (2000). The global carbon cycle: a test of our knowledge of earth as a system. *Science, 290*(5490), 291-296. doi:https://doi.org/10.1126/science.290.5490.291

Fan, L., Wigneron, J.-P., Ciais, P., Chave, J., Brandt, M., Sitch, S., . . . Qin, Y. (2023). Siberian carbon sink reduced by forest disturbances. *Nature Geoscience, 16*(1), 56-62. doi:https://doi.org/10.1038/s41561-022-01087-x

Fang, B., Lei, H., Zhang, Y., Quan, Q., & Yang, D. (2020). Spatio-temporal patterns of evapotranspiration based on upscaling eddy covariance measurements in the dryland of the North China Plain. *Agricultural and Forest Meteorology, 281*, 107844. doi:https://doi.org/10.1016/j.agrformet.2019.107844

Farquhar, G. D., & Sharkey, T. D. (1982). Stomatal conductance and photosynthesis. *Annual review of plant physiology, 33*(1), 317-345. doi:https://doi.org/10.1146/annurev.pp.33.060182.001533

Farquhar, G. D., von Caemmerer, S. v., & Berry, J. A. (1980). A biochemical model of photosynthetic CO2 assimilation in leaves of C3 species. *planta, 149*(1), 78-90. doi:https://doi.org/10.1007/BF00386231

Feng, X., Merow, C., Liu, Z., Park, D. S., Roehrdanz, P. R., Maitner, B., . . . Burger, J. R. (2021). How deregulation, drought and increasing fire impact Amazonian biodiversity. *Nature, 597*(7877), 516-521. doi:https://doi.org/10.1038/s41586-021-03876-7

Fernandez-Going, B. M., Anacker, B. L., & Harrison, S. P. (2012). Temporal variability

in California grasslands: soil type and species functional traits mediate response to precipitation. *Ecology, 93*(9), 2104-2114. doi:https://doi.org/10.1890/11-2003.1

Finzi, A. C., Giasson, M. A., Barker Plotkin, A. A., Aber, J. D., Boose, E. R., Davidson, E. A., . . . Goldman, E. (2020). Carbon budget of the Harvard Forest Long-Term Ecological Research site: Pattern, process, and response to global change. *Ecological Monographs, 90*(4), e01423. doi:https://doi.org/10.1002/ecm.1423

Flannigan, M. D., Krawchuk, M. A., de Groot, W. J., Wotton, B. M., & Gowman, L. M. (2009). Implications of changing climate for global wildland fire. *International journal of wildland fire, 18*(5), 483-507. doi:https://doi.org/10.1071/WF08187

Frankenberg, C., Fisher, J. B., Worden, J., Badgley, G., Saatchi, S. S., Lee, J. E., . . . Kuze, A. (2011). New global observations of the terrestrial carbon cycle from GOSAT: Patterns of plant fluorescence with gross primary productivity. *Geophysical Research Letters, 38*(17). doi:https://doi.org/10.1029/2011GL048738

Frey, R. A., Ackerman, S. A., Liu, Y., Strabala, K. I., Zhang, H., Key, J. R., & Wang, X. (2008). Cloud detection with MODIS. Part I: Improvements in the MODIS cloud mask for collection 5. *Journal of atmospheric and oceanic technology, 25*(7), 1057-1072. doi:https://doi.org/10.1175/2008JTECHA1052.1

Friedl, M. A., & Sulla-Menashe, D. (2022). *MODIS/Terra+Aqua Land Cover Type Yearly L3 Global 500m SIN Grid V061*.

Friedlingstein, P., Cox, P., Betts, R., Bopp, L., von Bloh, W., Brovkin, V., . . . Fung, I.

(2006). Climate–carbon cycle feedback analysis: results from the C4MIP model intercomparison. *Journal of Climate, 19*(14), 3337-3353.

Friedlingstein, P., O'Sullivan, M., Jones, M. W., Andrew, R. M., Hauck, J., Landschützer, P., . . . Olsen, A. (2024). Global Carbon Budget 2024. *Earth System Science Data Discussions, 2024*, 1-133. doi:https://doi.org/10.5194/essd-2024-519

Fu, Y. S., Campioli, M., Vitasse, Y., De Boeck, H. J., Van den Berge, J., AbdElgawad, H., . . . Janssens, I. A. (2014). Variation in leaf flushing date influences autumnal senescence and next year's flushing date in two temperate tree species. *Proceedings of the National Academy of Sciences, 111*(20), 7355-7360. doi:https://doi.org/10.1073/pnas.1321727111

Fu, Z., Ciais, P., Prentice, I. C., Gentine, P., Makowski, D., Bastos, A., . . . Yang, H. (2022). Atmospheric dryness reduces photosynthesis along a large range of soil water deficits. *Nature communications, 13*(1), 989. doi:https://doi.org/10.1038/s41467-022-28652-7

Fu, Z., Gerken, T., Bromley, G., Araújo, A., Bonal, D., Burban, B., . . . Hirano, T. (2018). The surface-atmosphere exchange of carbon dioxide in tropical rainforests: Sensitivity to environmental drivers and flux measurement methodology. *Agricultural and Forest Meteorology, 263*, 292-307. doi:https://doi.org/10.1016/j.agrformet.2018.09.001

Gampe, D., Zscheischler, J., Reichstein, M., O'Sullivan, M., Smith, W. K., Sitch, S., & Buermann, W. (2021). Increasing impact of warm droughts on northern ecosystem productivity over recent decades. *Nature Climate Change, 11*(9),

772-779. doi:https://doi.org/10.1038/s41558-021-01112-8

Gao, Y., Yu, G., Yan, H., Zhu, X., Li, S., Wang, Q., . . . Zhao, L. (2014). A MODIS-based Photosynthetic Capacity Model to estimate gross primary production in Northern China and the Tibetan Plateau. *Remote Sensing of Environment, 148*, 108-118. doi:https://doi.org/10.1016/j.rse.2014.03.006

García, M. J. L., & Caselles, V. (1991). Mapping burns and natural reforestation using Thematic Mapper data. *Geocarto International, 6*(1), 31-37. doi:https://doi.org/10.1080/10106049109354290

Gauthier, S., Bernier, P., Kuuluvainen, T., Shvidenko, A. Z., & Schepaschenko, D. G. (2015). Boreal forest health and global change. *Science, 349*(6250), 819-822. doi:https://doi.org/10.1126/science.aaa9092

Giglio, L., Boschetti, L., Roy, D. P., Humber, M. L., & Justice, C. O. (2018). The Collection 6 MODIS burned area mapping algorithm and product. *Remote Sensing of Environment, 217*, 72-85. doi:https://doi.org/10.1016/j.rse.2018.08.005

Giglio, L., Descloitres, J., Justice, C. O., & Kaufman, Y. J. (2003). An enhanced contextual fire detection algorithm for MODIS. *Remote Sensing of Environment, 87*(2-3), 273-282. doi:https://doi.org/10.1016/S0034-4257(03)00184-6

Giglio, L., & Justice, C. O. (2021). MODIS/Terra Thermal Anomalies/Fire Daily L3 Global 1km SIN Grid V061 [Data set]. NASA EOSDIS Land Processes Distributed Active Archive Center. Accessed 2024-09-16 from. doi:https://doi.org/10.5067/MODIS/MOD14A1.061

Giglio, L., Justice, C. (2015). MOD14A1 MODIS/Terra Thermal Anomalies/Fire Daily L3 Global 1km SIN Grid V006 [Data set]. NASA EOSDIS Land Processes Distributed Active Archive Center. Accessed 2025-06-13 from. doi:https://doi.org/10.5067/MODIS/MOD14A1.006

Giglio, L., Justice, C., Boschetti, L., Roy, D. (2021). MODIS/Terra+Aqua Burned Area Monthly L3 Global 500m SIN Grid V061 [Data set]. NASA EOSDIS Land Processes Distributed Active Archive Center. Accessed 2025-06-13 from. doi:https://doi.org/10.5067/MODIS/MCD64A1.061

Gitas, I., Mitri, G., Veraverbeke, S., & Polychronaki, A. (2012). Advances in remote sensing of post-fire vegetation recovery monitoring—A review. *Remote sensing of biomass-Principles and applications, 1*, 334.

Glenn, E. P., Huete, A. R., Nagler, P. L., & Nelson, S. G. (2008). Relationship between remotely-sensed vegetation indices, canopy attributes and plant physiological processes: What vegetation indices can and cannot tell us about the landscape. *Sensors, 8*(4), 2136-2160. doi:https://doi.org/10.3390/s8042136

Goetz, S. J., Bond-Lamberty, B., Law, B. E., Hicke, J. A., Huang, C., Houghton, R. A., . . . Meddens, A. J. H. (2012). Observations and assessment of forest carbon dynamics following disturbance in North America. *Journal of Geophysical Research: Biogeosciences, 117*(G2 %@ 0148-0227). doi:https://doi.org/10.1029/2011JG001733

Gonsamo, A., Croft, H., Chen, J. M., Wu, C., Froelich, N., & Staebler, R. M. (2015). Radiation contributed more than temperature to increased decadal autumn and

annual carbon uptake of two eastern North America mature forests. *Agricultural and Forest Meteorology, 201*, 8-16. doi:https://doi.org/10.1016/j.agrformet.2014.11.007

Guanter, L., Bacour, C., Schneider, A., Aben, I., van Kempen, T. A., Maignan, F., . . . Joiner, J. (2021). The TROPOSIF global sun-induced fluorescence dataset from the Sentinel-5P TROPOMI mission. *Earth System Science Data, 13*(11), 5423-5440. doi:https://doi.org/10.5194/essd-13-5423-2021

Guanter, L., Zhang, Y., Jung, M., Joiner, J., Voigt, M., Berry, J. A., . . . Lee, J.-E. (2014). Global and time-resolved monitoring of crop photosynthesis with chlorophyll fluorescence. *Proceedings of the National Academy of Sciences, 111*(14), E1327-E1333. doi:https://doi.org/10.1073/pnas.1320008111

Gui, Y., Wang, K., Huntingford, C., Wei, S., Li, X., Myneni, R. B., & Piao, S. (2025). Vegetation greenness in 2024. *Nature Reviews Earth & Environment, 6*(4), 255-257. doi:https://doi.org/10.1038/s43017-025-00656-z

Hantson, S., Arneth, A., Harrison, S. P., Kelley, D. I., Prentice, I. C., Rabin, S. S., . . . Artaxo, P. (2016). The status and challenge of global fire modelling. *Biogeosciences, 13*(11), 3359-3375. doi:https://doi.org/10.5194/bg-13-3359-2016

Harden, J. W., Trumbore, S. E., Stocks, B. J., Hirsch, A., Gower, S. T., O'Neill, K. P., & Kasischke, E. S. (2000). The role of fire in the boreal carbon budget. *Global Change Biology, 6*(S1), 174-184. doi:https://doi.org/10.1046/j.1365-2486.2000.06019.x

He, H., Liu, M., Xiao, X., Ren, X., Zhang, L., Sun, X., . . . Shi, P. (2014). Large-scale estimation and uncertainty analysis of gross primary production in Tibetan alpine grasslands. *Journal of Geophysical Research: Biogeosciences, 119*(3), 466-486. doi:https://doi.org/10.1002/2013JG002449

Heinsch, F. A., Zhao, M., Running, S. W., Kimball, J. S., Nemani, R. R., Davis, K. J., . . . Ricciuto, D. M. (2006). Evaluation of remote sensing based terrestrial productivity from MODIS using regional tower eddy flux network observations. *IEEE Transactions on Geoscience and Remote Sensing, 44*(7), 1908-1925.

Hemes, K. S., Norlen, C. A., Wang, J. A., Goulden, M. L., & Field, C. B. (2023). The magnitude and pace of photosynthetic recovery after wildfire in California ecosystems. *Proceedings of the National Academy of Sciences, 120*(15), e2201954120. doi:https://doi.org/10.1073/pnas.2201954120

Hermosilla, T., Wulder, M. A., White, J. C., Coops, N. C., & Hobart, G. W. (2018). Disturbance-informed annual land cover classification maps of Canada's forested ecosystems for a 29-year Landsat time series. *Canadian Journal of Remote Sensing, 44*(1), 67-87. doi:https://doi.org/10.1080/07038992.2018.1437719

Hersbach, H., Bell, B., Berrisford, P., Hirahara, S., Horányi, A., Muñoz-Sabater, J., . . . Schepers, D. (2020). The ERA5 global reanalysis. *Quarterly Journal of the Royal Meteorological Society, 146*(730), 1999-2049.

Holden, S. R., Rogers, B. M., Treseder, K. K., & Randerson, J. T. (2016). Fire severity influences the response of soil microbes to a boreal forest fire. *Environmental*

Research Letters, 11(3), 035004. doi:https://doi.org/10.1088/1748-9326/11/3/035004

Hu, X. M., Crowell, S., Wang, Q., Zhang, Y., Davis, K. J., Xue, M., . . . Choi, Y. (2020). Dynamical downscaling of CO2 in 2016 over the contiguous United States using WRF-VPRM, a weather-biosphere-online-coupled model. *Journal of Advances in Modeling Earth Systems, 12*(4), e2019MS001875. doi:https://doi.org/10.1029/2019MS001875

Huang, D., Chi, H., Xin, F., Miyata, A., Kang, M., Liu, K., . . . Xiao, X. (2021). Improved estimation of gross primary production of paddy rice cropland with changing model parameters over phenological transitions. *Ecological Modelling, 445*, 109492. doi:https://doi.org/10.1016/j.ecolmodel.2021.109492

Huang, M., Piao, S., Ciais, P., Peñuelas, J., Wang, X., Keenan, T. F., . . . Mao, J. (2019). Air temperature optima of vegetation productivity across global biomes. *Nature ecology & evolution, 3*(5), 772-779. doi:https://doi.org/10.1038/s41559-019-0838-x

Huete, A., Didan, K., Miura, T., Rodriguez, E. P., Gao, X., & Ferreira, L. G. (2002). Overview of the radiometric and biophysical performance of the MODIS vegetation indices. *Remote Sensing of Environment, 83*(1-2), 195-213. doi:https://doi.org/10.1016/S0034-4257(02)00096-2

Hunt Jr, E. R., Doraiswamy, P. C., McMurtrey, J. E., Daughtry, C. S. T., Perry, E. M., & Akhmedov, B. (2013). A visible band index for remote sensing leaf chlorophyll content at the canopy scale. *International Journal of Applied Earth*

Observation and Geoinformation, 21, 103-112. doi:https://doi.org/10.1016/j.jag.2012.07.020

Huntingford, C., Zelazowski, P., Galbraith, D., Mercado, L. M., Sitch, S., Fisher, R., . . . Booth, B. B. B. (2013). Simulated resilience of tropical rainforests to CO2-induced climate change. *Nature Geoscience, 6*(4), 268-273. doi:https://doi.org/10.1038/ngeo1741

Janssen, P. H. M., & Heuberger, P. S. C. (1995). Calibration of process-oriented models. *Ecological Modelling, 83*(1-2), 55-66 %@ 0304-3800. doi:https://doi.org/10.1016/0304-3800(95)00084-9

Jensen, A. M., Fastovich, D., Watson, B. I., Gill, J. L., Jackson, S. T., Russell, J. M., . . . Rubbelke, C. (2021). More than one way to kill a spruce forest: The role of fire and climate in the late-glacial termination of spruce woodlands across the southern Great Lakes. *Journal of Ecology, 109*(1), 459-477. doi:https://doi.org/10.1111/1365-2745.13517

Jensen, J. R. (2009). *Remote sensing of the environment: An earth resource perspective 2/e*: Pearson Education India.

Jeong, S. J., HO, C. H., GIM, H. J., & Brown, M. E. (2011). Phenology shifts at start vs. end of growing season in temperate vegetation over the Northern Hemisphere for the period 1982–2008. *Global Change Biology, 17*(7), 2385-2399. doi:https://doi.org/10.1111/j.1365-2486.2011.02397.x

Jian, J., Bailey, V., Dorheim, K., Konings, A. G., Hao, D., Shiklomanov, A. N., . . . Vargas, R. (2022). Historically inconsistent productivity and respiration fluxes

in the global terrestrial carbon cycle. *Nature communications, 13*(1), 1733. doi:https://doi.org/10.1038/s41467-022-29391-5

Jin, C., Xiao, X., Merbold, L., Arneth, A., Veenendaal, E., & Kutsch, W. L. (2013). Phenology and gross primary production of two dominant savanna woodland ecosystems in Southern Africa. *Remote Sensing of Environment, 135*, 189-201. doi:https://doi.org/10.1016/j.rse.2013.03.033

Jin, C., Xiao, X., Wagle, P., Griffis, T., Dong, J., Wu, C., . . . Cook, D. R. (2015). Effects of in-situ and reanalysis climate data on estimation of cropland gross primary production using the Vegetation Photosynthesis Model. *Agricultural and Forest Meteorology, 213*, 240-250.

John, R., Chen, J., Noormets, A., Xiao, X., Xu, J., Lu, N., & Chen, S. (2013). Modelling gross primary production in semi-arid Inner Mongolia using MODIS imagery and eddy covariance data. *International Journal of remote sensing, 34*(8), 2829-2857. doi:https://doi.org/10.1080/01431161.2012.746483

Johnstone, J. F., Chapin Iii, F. S., Foote, J., Kemmett, S., Price, K., & Viereck, L. (2004). Decadal observations of tree regeneration following fire in boreal forests. *Canadian Journal of Forest Research, 34*(2), 267-273. doi:https://doi.org/10.1139/x03-183

Johnstone, J. F., Hollingsworth, T. N., Chapin Iii, F. S., & Mack, M. C. (2010). Changes in fire regime break the legacy lock on successional trajectories in Alaskan boreal forest. *Global Change Biology, 16*(4), 1281-1295. doi:https://doi.org/10.1111/j.1365-2486.2009.02051.x

Jones, M. W., Abatzoglou, J. T., Veraverbeke, S., Andela, N., Lasslop, G., Forkel, M., . . . van der Werf, G. R. (2022). Global and regional trends and drivers of fire under climate change. *Reviews of Geophysics, 60*(3), e2020RG000726. doi:https://doi.org/10.1029/2020RG000726

Jung, M., Koirala, S., Weber, U., Ichii, K., Gans, F., Camps-Valls, G., . . . Reichstein, M. (2019). The FLUXCOM ensemble of global land-atmosphere energy fluxes. *Scientific data, 6*(1), 74. doi:https://doi.org/10.1038/s41597-019-0076-8

Jung, M., Reichstein, M., Margolis, H. A., Cescatti, A., Richardson, A. D., Arain, M. A., . . . Chen, J. (2011a). Global patterns of land-atmosphere fluxes of carbon dioxide, latent heat, and sensible heat derived from eddy covariance, satellite, and meteorological observations. *Journal of Geophysical Research: Biogeosciences, 116*(0148-0227). doi:https://doi.org/10.1029/2010JG001566

Jung, M., Reichstein, M., Margolis, H. A., Cescatti, A., Richardson, A. D., Arain, M. A., . . . Chen, J. (2011b). Global patterns of land-atmosphere fluxes of carbon dioxide, latent heat, and sensible heat derived from eddy covariance, satellite, and meteorological observations. *Journal of Geophysical Research: Biogeosciences, 116*(G3 %@ 0148-0227).

Jung, M., Schwalm, C., Migliavacca, M., Walther, S., Camps-Valls, G., Koirala, S., . . . Carvalhais, N. (2020). Scaling carbon fluxes from eddy covariance sites to globe: synthesis and evaluation of the FLUXCOM approach. *Biogeosciences, 17*, 1343–1365. doi:https://doi.org/10.5194/bg-17-1343-2020

Justice, C. O., Giglio, L., Korontzi, S., Owens, J., Morisette, J. T., Roy, D., . . . Kaufman,

Y. (2002). The MODIS fire products. *Remote Sensing of Environment, 83*(1-2), 244-262. doi:https://doi.org/10.1016/S0034-4257(02)00076-7

Justice, C. O., Townshend, J. R. G., Vermote, E. F., Masuoka, E., Wolfe, R. E., Saleous, N., . . . Morisette, J. T. (2002). An overview of MODIS Land data processing and product status. *Remote Sensing of Environment, 83*(1-2), 0034-4257. doi:https://doi.org/10.1016/S0034-4257(02)00084-6

Justice, C. O., Vermote, E., Townshend, J. R., Defries, R., Roy, D. P., Hall, D. K., . . . Strahler, A. (1998). The Moderate Resolution Imaging Spectroradiometer (MODIS): Land remote sensing for global change research. *IEEE Transactions on Geoscience and Remote Sensing, 36*(4), 1228-1249.

Kalfas, J. L., Xiao, X., Vanegas, D. X., Verma, S. B., & Suyker, A. E. (2011). Modeling gross primary production of irrigated and rain-fed maize using MODIS imagery and CO2 flux tower data. *Agricultural and Forest Meteorology, 151*(12), 1514-1528. doi:https://doi.org/10.1016/j.agrformet.2011.06.007

Kang, X., Hao, Y., Cui, X., Chen, H., Huang, S., Du, Y., . . . Cui, L. (2016). Variability and changes in climate, phenology, and gross primary production of an alpine wetland ecosystem. *Remote Sensing, 8*(5), 2072-4292. doi:https://doi.org/10.3390/rs8050391

Kang, X., Wang, Y., Chen, H., Tian, J., Cui, X., Rui, Y., . . . Xiao, X. (2014). Modeling carbon fluxes using multi-temporal MODIS imagery and CO 2 eddy flux tower data in Zoige alpine wetland, south-west China. *Wetlands, 34*, 603-618. doi:https://doi.org/10.1007/s13157-014-0529-y

Karavani, A., Boer, M. M., Baudena, M., Colinas, C., Díaz-Sierra, R., Pemán, J., . . . Resco de Dios, V. (2018). Fire-induced deforestation in drought-prone Mediterranean forests: drivers and unknowns from leaves to communities. *Ecological Monographs, 88*(2), 141-169. doi:https://doi.org/10.1002/ecm.1285

Kaufman, Y. J., Tanré, D., Gordon, H. R., Nakajima, T., Lenoble, J., Frouin, R., . . . Teillet, P. M. (1997). Passive remote sensing of tropospheric aerosol and atmospheric correction for the aerosol effect. *Journal of Geophysical Research: Atmospheres, 102*(D14), 16815-16830. doi:https://doi.org/10.1029/97JD01496

Keenan, T. F., Gray, J., Friedl, M. A., Toomey, M., Bohrer, G., Hollinger, D. Y., . . . Wing, I. S. (2014). Net carbon uptake has increased through warming-induced changes in temperate forest phenology. *Nature Climate Change, 4*(7), 598-604. doi:https://doi.org/10.1038/nclimate2253

Keenan, T. F., Hollinger, D. Y., Bohrer, G., Dragoni, D., Munger, J. W., Schmid, H. P., & Richardson, A. D. (2013). Increase in forest water-use efficiency as atmospheric carbon dioxide concentrations rise. *Nature, 499*(7458), 324-327. doi:https://doi.org/10.1038/nature12291

Keenan, T. F., Luo, X., Stocker, B. D., De Kauwe, M. G., Medlyn, B. E., Prentice, I. C., . . . Zhang, Y. (2023). A constraint on historic growth in global photosynthesis due to rising CO2. *Nature Climate Change, 13*(12), 1376-1381. doi:https://doi.org/10.1038/s41558-023-01867-2

Keenan, T. F., Prentice, I. C., Canadell, J. G., Williams, C. A., Wang, H., Raupach, M., & Collatz, G. J. (2016). Recent pause in the growth rate of atmospheric CO2

due to enhanced terrestrial carbon uptake. *Nature communications, 7*(1), 13428. doi:https://doi.org/10.1038/ncomms13428

Kim, J. E., Wang, J. A., Li, Y., Czimczik, C. I., & Randerson, J. T. (2024). Wildfire-induced increases in photosynthesis in boreal forest ecosystems of North America. *Global Change Biology, 30*(1), e17151. doi:https://doi.org/10.1111/gcb.17151

Knox, K. J. E., & Clarke, P. J. (2006). Fire season and intensity affect shrub recruitment in temperate sclerophyllous woodlands. *Oecologia, 149*(4), 730-739. doi:https://doi.org/10.1007/s00442-006-0480-6

Köhler, P., Frankenberg, C., Magney, T. S., Guanter, L., Joiner, J., & Landgraf, J. (2018). Global retrievals of solar-induced chlorophyll fluorescence with TROPOMI: First results and intersensor comparison to OCO-2. *Geophysical Research Letters, 45*(19), 10,456-410,463. doi:https://doi.org/10.1029/2018GL079031

Köhler, P., Guanter, L., Kobayashi, H., Walther, S., & Yang, W. (2018). Assessing the potential of sun-induced fluorescence and the canopy scattering coefficient to track large-scale vegetation dynamics in Amazon forests. *Remote Sensing of Environment, 204*, 769-785. doi:https://doi.org/10.1016/j.rse.2017.09.025

Kolby Smith, W., Reed, S. C., Cleveland, C. C., Ballantyne, A. P., Anderegg, W. R. L., Wieder, W. R., . . . Running, S. W. (2016). Large divergence of satellite and Earth system model estimates of global terrestrial CO2 fertilization. *Nature Climate Change, 6*(3), 306-310. doi:https://doi.org/10.1038/nclimate2879

Kurz, W. A., Dymond, C. C., Stinson, G., Rampley, G. J., Neilson, E. T., Carroll, A.

L., . . . Safranyik, L. (2008). Mountain pine beetle and forest carbon feedback to climate change. *Nature, 452*(7190), 987-990. doi:https://doi.org/10.1038/nature06777

Lai, J., Kooijmans, L. M. J., Sun, W., Lombardozzi, D., Campbell, J. E., Gu, L., . . . Sun, Y. (2024). Terrestrial photosynthesis inferred from plant carbonyl sulfide uptake. *Nature*, 1-7. doi:https://doi.org/10.1038/s41586-024-08050-3

Lan, X., Tans, P. and K.W. (2025). Trends in globally-averaged CO2 determined from NOAA Global Monitoring Laboratory measurements. doi:https://doi.org/10.15138/9N0H-ZH07

Lapola, D. M., Pinho, P., Barlow, J., AragÃ£o, L. E. O. C., Berenguer, E., Carmenta, R., . . . Silva-Junior, C. H. L. (2023). The drivers and impacts of Amazon forest degradation. *Science, 379*(6630), eabp8622. doi:https://doi.org/10.1126/science.abp8622

Lasslop, G., Reichstein, M., Papale, D., Richardson, A. D., Arneth, A., Barr, A., . . . Wohlfahrt, G. (2010). Separation of net ecosystem exchange into assimilation and respiration using a light response curve approach: critical issues and global evaluation. *Global Change Biology, 16*(1), 187-208. doi:https://doi.org/10.1111/j.1365-2486.2009.02041.x

Launiainen, S., Katul, G. G., Leppä, K., Kolari, P., Aslan, T., Grönholm, T., . . . Vesala, T. (2022). Does growing atmospheric CO2 explain increasing carbon sink in a boreal coniferous forest? *Global Change Biology, 28*(9), 2910-2929. doi:https://doi.org/10.1111/gcb.16117

Law, B. E., Van Tuyl, S., Cescatti, A., & Baldocchi, D. D. (2001). Estimation of leaf area index in open-canopy ponderosa pine forests at different successional stages and management regimes in Oregon. *Agricultural and Forest Meteorology, 108*(1), 1-14. doi:https://doi.org/10.1016/S0168-1923(01)00226-X

Lawrence, D. M., Fisher, R. A., Koven, C. D., Oleson, K. W., Swenson, S. C., Bonan, G., . . . Kennedy, D. (2019). The Community Land Model version 5: Description of new features, benchmarking, and impact of forcing uncertainty. *Journal of Advances in Modeling Earth Systems, 11*(12), 4245-4287. doi:https://doi.org/10.1029/2018MS001583

Lee, X., Fuentes, J. D., Staebler, R. M., & Neumann, H. H. (1999). Long-term observation of the atmospheric exchange of CO2 with a temperate deciduous forest in southern Ontario, Canada. *Journal of Geophysical Research: Atmospheres, 104*(D13), 15975-15984. doi:https://doi.org/10.1029/1999JD900227

Leng, J., Chen, J. M., Li, W., Luo, X., Xu, M., Liu, J., . . . Yan, Y. (2023). Global datasets of hourly carbon and water fluxes simulated using a satellite-based process model with dynamic parameterizations. *Earth System Science Data Discussions, 2023*, 1-23. doi:https://doi.org/10.5194/essd-2023-328

Li, B., Ryu, Y., Jiang, C., Dechant, B., Liu, J., Yan, Y., & Li, X. (2023). BESSv2. 0: A satellite-based and coupled-process model for quantifying long-term global land–atmosphere fluxes. *Remote Sensing of Environment, 295*, 113696.

doi:https://doi.org/10.1016/j.rse.2023.113696

Li, S.-X., Wang, Z.-H., Malhi, S. S., Li, S.-Q., Gao, Y.-J., & Tian, X.-H. (2009). Nutrient and water management effects on crop production, and nutrient and water use efficiency in dryland areas of China. *Advances in agronomy, 102*, 223-265. doi:https://doi.org/10.1016/S0065-2113(09)01007-4

Li, S., Wang, G., Chai, Y., Miao, L., Hagan, D. F. T., Sun, S., . . . Chen, T. (2023). Increasing vapor pressure deficit accelerates land drying. *Journal of hydrology, 625*, 130062. doi:https://doi.org/10.1016/j.jhydrol.2023.130062

Li, X., Ciais, P., Fensholt, R., Chave, J. r., Sitch, S., Canadell, J. G., . . . Wigneron, J.-P. (2025). Large live biomass carbon losses from droughts in the northern temperate ecosystems during 2016-2022. *Nature communications, 16*(1), 4980. doi:10.1038/s41467-025-59999-2

Li, X., Wang, K., Huntingford, C., Zhu, Z., PeÃ±uelas, J., Myneni, R. B., & Piao, S. (2024). Vegetation greenness in 2023. *Nature Reviews Earth & Environment, 5*(4), 241-243. doi:https://doi.org/10.1038/s43017-024-00543-z

Li, X., & Xiao, J. (2019). Mapping photosynthesis solely from solar-induced chlorophyll fluorescence: A global, fine-resolution dataset of gross primary production derived from OCO-2. *Remote Sensing, 11*(21), 2563. doi:https://doi.org/10.3390/rs11212563

Li, Y., Li, L., Dong, J., & Bai, J. (2021). Assessing MODIS carbon and water fluxes in grasslands and shrublands in semiarid regions using eddy covariance tower data. *International Journal of remote sensing, 42*(2), 595-616.

doi:https://doi.org/10.1080/01431161.2020.1811915

Li, Z., Yu, G., Xiao, X., Li, Y., Zhao, X., Ren, C., . . . Fu, Y. (2007). Modeling gross primary production of alpine ecosystems in the Tibetan Plateau using MODIS images and climate data. *Remote Sensing of Environment, 107*(3), 510-519.

Lian, X., Piao, S., Li, L. Z., Li, Y., Huntingford, C., Ciais, P., . . . Buermann, W. (2020). Summer soil drying exacerbated by earlier spring greening of northern vegetation. *Science advances, 6*(1), eaax0255. doi:https://doi.org/10.1126/sciadv.aax0255

Liang, S., Cheng, J., Jia, K., Jiang, B., Liu, Q., Xiao, Z., . . . Zhao, X. (2021). The global land surface satellite (GLASS) product suite. *Bulletin of the American Meteorological Society, 102*(2), E323-E337. doi:https://doi.org/10.1175/BAMS-D-18-0341.1

Lieth, H. (1973). Primary production: terrestrial ecosystems. *Human ecology, 1*, 303-332. doi:https://doi.org/10.1007/BF01536729

Linderholm, H. W., Walther, A., & Chen, D. (2008). Twentieth-century trends in the thermal growing season in the Greater Baltic Area. *Climatic Change, 87*(3-4), 405-419.

Liu, L., Xiao, X., Qin, Y., Wang, J., Xu, X., Hu, Y., & Qiao, Z. (2020). Mapping cropping intensity in China using time series Landsat and Sentinel-2 images and Google Earth Engine. *Remote Sensing of Environment, 239*, 111624. doi:https://doi.org/10.1016/j.rse.2019.111624

Liu, Z., Ballantyne, A. P., & Cooper, L. A. (2019). Biophysical feedback of global forest

fires on surface temperature. *Nature communications, 10*(1), 214. doi:https://doi.org/10.1038/s41467-018-08237-z

Lizundia-Loiola, J., OtÃ³n, G., Ramo, R. n., & Chuvieco, E. (2020). A spatio-temporal active-fire clustering approach for global burned area mapping at 250 m from MODIS data. *Remote Sensing of Environment, 236*, 111493. doi:https://doi.org/10.1016/j.rse.2019.111493

Lloyd, J., & Farquhar, G. D. (2008). Effects of rising temperatures and [CO2] on the physiology of tropical forest trees. *Philosophical Transactions of the Royal Society B: Biological Sciences, 363*(1498), 1811-1817.

Lorenz, K. (2010). *Carbon sequestration in forest ecosystems*: Springer.

Lv, Q., Chen, Z., Wu, C., PeÃ±uelas, J., Fan, L., Su, Y., . . . Hu, J. (2025). Increasing severity of large-scale fires prolongs recovery time of forests globally since 2001. *Nature ecology & evolution*, 1-13. doi:https://doi.org/10.1038/s41559-025-02683-x

Ma, J., Xiao, X., Zhang, Y., Doughty, R., Chen, B., & Zhao, B. (2018). Spatial-temporal consistency between gross primary productivity and solar-induced chlorophyll fluorescence of vegetation in China during 2007–2014. *Science of The Total Environment, 639*, 1241-1253. doi:https://doi.org/10.1016/j.scitotenv.2018.05.245

Ma, X., Huete, A., Yu, Q., Restrepo-Coupe, N., Beringer, J., Hutley, L. B., . . . Eamus, D. (2014). Parameterization of an ecosystem light-use-efficiency model for predicting savanna GPP using MODIS EVI. *Remote Sensing of Environment,*

154, 253-271. doi:https://doi.org/10.1016/j.rse.2014.08.025

Mack, M. C., Walker, X. J., Johnstone, J. F., Alexander, H. D., Melvin, A. M., Jean, M., & Miller, S. N. (2021). Carbon loss from boreal forest wildfires offset by increased dominance of deciduous trees. *Science, 372*(6539), 280-283. doi:https://doi.org/10.1126/science.abf3903

Magnani, F., Mencuccini, M., Borghetti, M., Berbigier, P., Berninger, F., Delzon, S., . . . Kolari, P. (2007). The human footprint in the carbon cycle of temperate and boreal forests. *Nature, 447*(7146), 849-851. doi:https://doi.org/10.1038/nature05847

Mahadevan, P., Wofsy, S. C., Matross, D. M., Xiao, X., Dunn, A. L., Lin, J. C., . . . Gottlieb, E. W. (2008). A satellite-based biosphere parameterization for net ecosystem CO2 exchange: Vegetation Photosynthesis and Respiration Model (VPRM). *Global biogeochemical cycles, 22*(2). doi:https://doi.org/10.1029/2006GB002735

Marshall, M., Tu, K., & Brown, J. (2018). Optimizing a remote sensing production efficiency model for macro-scale GPP and yield estimation in agroecosystems. *Remote Sensing of Environment, 217*, 258-271. doi:https://doi.org/10.1016/j.rse.2018.08.001

Martin, S. T., Andreae, M. O., Artaxo, P., Baumgardner, D., Chen, Q., Goldstein, A. H., . . . McMurry, P. H. (2010). Sources and properties of Amazonian aerosol particles. *Reviews of Geophysics, 48*(2). doi:https://doi.org/10.1029/2008RG000280

Masocha, M., Dube, T., Mpofu, N. T., & Chimunhu, S. (2018). Accuracy assessment of MODIS active fire products in southern African savannah woodlands. *African Journal of Ecology, 56*(3), 563-571. doi:https://doi.org/10.1111/aje.12494

Massmann, A., Gentine, P., & Lin, C. (2019). When does vapor pressure deficit drive or reduce evapotranspiration? *Journal of Advances in Modeling Earth Systems, 11*(10), 3305-3320. doi:https://doi.org/10.1029/2019MS001790

Masson-Delmotte, V. r., Zhai, P., Pirani, A., Connors, S. L., PÃ©an, C., Berger, S., . . . Gomis, M. I. (2021). Summary for policymakers.

McCallum, I., Franklin, O., Moltchanova, E., Merbold, L., Schmullius, C., Shvidenko, A., . . . Fritz, S. (2013). Improved light and temperature responses for light-use-efficiency-based GPP models. *Biogeosciences, 10*(10), 6577-6590. doi:https://doi.org/10.5194/bg-10-6577-2013

Medlyn, B., Dreyer, E., Ellsworth, D., Forstreuter, M., Harley, P., Kirschbaum, M., . . . Walcroft, A. (2002). Temperature response of parameters of a biochemically based model of photosynthesis. II. A review of experimental data. *Plant, cell & environment, 25*(9), 1167-1179.

Medlyn, B. E., Duursma, R. A., Eamus, D., Ellsworth, D. S., Prentice, I. C., Barton, C. V. M., . . . Wingate, L. (2011). Reconciling the optimal and empirical approaches to modelling stomatal conductance. *Global Change Biology, 17*(6), 2134-2144. doi:https://doi.org/10.1111/j.1365-2486.2010.02375.x

Meek, D., Hatfield, J., Howell, T., Idso, S., & Reginato, R. (1984). A generalized relationship between photosynthetically active radiation and solar radiation 1.

Agronomy journal, 76(6), 939-945. doi:https://doi.org/10.2134/agronj1984.00021962007600060018x

Melillo, J. M., McGuire, A. D., Kicklighter, D. W., Moore, B., Vorosmarty, C. J., & Schloss, A. L. (1993). Global climate change and terrestrial net primary production. *Nature, 363*(6426), 234-240. doi:https://doi.org/10.1038/363234a0

Melvin, A. M., Mack, M. C., Johnstone, J. F., David McGuire, A., Genet, H., & Schuur, E. A. G. (2015). Differences in ecosystem carbon distribution and nutrient cycling linked to forest tree species composition in a mid-successional boreal forest. *Ecosystems, 18*, 1472-1488. doi:https://doi.org/10.1007/s10021-015-9912-7

Meng, C., Xiao, X., Pan, L., Pan, B., Scott, R. L., Wagle, P., . . . Qin, Y. (2025). Interannual variability and trends of gross primary production and transpiration in savannas and grasslands from 2000 to 2021. *Frontiers of Earth Science*, 1-15. doi:https://doi.org/10.1007/s11707-024-1136-8

Meng, R., Dennison, P. E., Huang, C., Moritz, M. A., & D'Antonio, C. (2015). Effects of fire severity and post-fire climate on short-term vegetation recovery of mixed-conifer and red fir forests in the Sierra Nevada Mountains of California. *Remote Sensing of Environment, 171*, 311-325. doi:https://doi.org/10.1016/j.rse.2015.10.024

Meyer, N., Welp, G., & Amelung, W. (2018). The temperature sensitivity (Q10) of soil respiration: controlling factors and spatial prediction at regional scale based on environmental soil classes. *Global biogeochemical cycles, 32*(2), 306-323.

doi:https://doi.org/10.1002/2017GB005644

Miao, G., Guan, K., Yang, X., Bernacchi, C. J., Berry, J. A., DeLucia, E. H., . . . Cai, Y. (2018). Sun-induced chlorophyll fluorescence, photosynthesis, and light use efficiency of a soybean field from seasonally continuous measurements. *Journal of Geophysical Research: Biogeosciences, 123*(2), 610-623. doi:https://doi.org/10.1002/2017JG004180

Migliavacca, M., Musavi, T., Mahecha, M. D., Nelson, J. A., Knauer, J., Baldocchi, D. D., . . . Anderson, K. (2021). The three major axes of terrestrial ecosystem function. *Nature, 598*(7881), 468-472. doi:https://doi.org/10.1038/s41586-021-03939-9

Miller, J. D., & Thode, A. E. (2007). Quantifying burn severity in a heterogeneous landscape with a relative version of the delta Normalized Burn Ratio (dNBR). *Remote Sensing of Environment, 109*(1), 66-80. doi:https://doi.org/10.1016/j.rse.2006.12.006

Monteith, J. L. (1972). Solar radiation and productivity in tropical ecosystems. *Journal of applied ecology, 9*(3), 747-766. doi:https://doi.org/10.2307/2401901

Monteith, J. L. (1977). Climate and the efficiency of crop production in Britain. *Philosophical transactions of the royal society of London. B, Biological Sciences, 281*(980), 277-294. doi:https://doi.org/10.1098/rstb.1977.0140

Mooney, H. A., Björkman, O., & Collatz, G. J. (1978). Photosynthetic acclimation to temperature in the desert shrub, Larrea divaricata: I. Carbon dioxide exchange characteristics of intact leaves. *Plant Physiology, 61*(3), 406-410.

Motzkin, G., Wilson, P., Foster, D. R., & Allen, A. (1999). Vegetation patterns in heterogeneous landscapes: the importance of history and environment. *Journal of Vegetation Science, 10*(6), 903-920. doi:https://doi.org/10.2307/3237315

Muñoz-Sabater, J., Dutra, E., Agustí-Panareda, A., Albergel, C., Arduini, G., Balsamo, G., . . . Hersbach, H. (2021). ERA5-Land: A state-of-the-art global reanalysis dataset for land applications. *Earth System Science Data, 13*(9), 4349-4383. doi:https://doi.org/10.5194/essd-13-4349-2021

Muñoz Sabater, J. (2019). ERA5-Land hourly data from 1950 to present. Copernicus Climate Change Service (C3S) Climate Data Store (CDS). doi:10.24381/cds.e2161bac

Myneni, R., Knyazikhin, Y., & Park, T. (2015). MCD15A3H MODIS/Terra+Aqua Leaf Area Index/FPAR 4-day L4 Global 500m SIN Grid V006 [Data set]. NASA EOSDIS Land Processes Distributed Active Archive Center. Accessed 2024-09-16 from. doi:https://doi.org/10.5067/MODIS/MCD15A3H.006

Niu, S., Luo, Y., Fei, S., Yuan, W., Schimel, D., Law, B. E., . . . Aubinet, M. (2012). Thermal optimality of net ecosystem exchange of carbon dioxide and underlying mechanisms. *New Phytologist, 194*(3), 775-783. doi:https://doi.org/10.1111/j.1469-8137.2012.04095.x

Nolan, R. H., Collins, L., Leigh, A., Ooi, M. K. J., Curran, T. J., Fairman, T. A., . . . Bradstock, R. (2021). Limits to post-fire vegetation recovery under climate change. *Plant, cell & environment, 44*(11), 3471-3489. doi:https://doi.org/10.1111/pce.14176

Norby, R. J., De Kauwe, M. G., Domingues, T. F., Duursma, R. A., Ellsworth, D. S., Goll, D. S., . . . Medlyn, B. E. (2016). Modelâ€“data synthesis for the next generation of forest freeâ€□air CO 2 enrichment (FACE) experiments. *New Phytologist, 209*(1), 17-28. doi:https://doi.org/10.1111/nph.13593

Pan, B., Xiao, X., Pan, L., Meng, C., Blanken, P. D., Burns, S. P., . . . Qin, Y. (2025). Incorporation of needleleaf traits improves estimation of light absorption and gross primary production of evergreen needleleaf forests. *Agricultural and Forest Meteorology, 368*, 110526. doi:https://doi.org/10.1016/j.agrformet.2025.110526

Pan, L., Xiao, X., Pan, B., Meng, C., Doughty, R., Qin, Y., . . . Yin, S. (2025). VPM v3. 0 model: improved estimates of terrestrial gross primary production from individual eddy flux tower sites to the globe. *Journal of Remote Sensing, 5*, :Article 0471. doi:https://doi.org/10.34133/remotesensing.0471

Pan, L., Xiao, X., Pan, B., Meng, C., Staebler, R. M., Zhang, C., & Qin, Y. (2024). Interannual variations and trends of gross primary production and transpiration of four mature deciduous broadleaf forest sites during 2000–2020. *Remote Sensing of Environment, 304*, 114042. doi:https://doi.org/10.1016/j.rse.2024.114042

Pan, L., Xiao, X., Yao, Y., Pan, B., Yin, C., Meng, C., . . . Zhang, C. (2024). Site-specific apparent optimum air temperature for vegetation photosynthesis across the globe. *Scientific data, 11*(1), 758. doi:https://doi.org/10.1038/s41597-024-03603-7

Pan, Y., Birdsey, R. A., Fang, J., Houghton, R., Kauppi, P. E., Kurz, W. A., . . . Canadell, J. G. (2011). A large and persistent carbon sink in the world's forests. *Science, 333*(6045), 988-993. doi:https://doi.org/10.1126/science.1201609

Papale, D., Reichstein, M., Aubinet, M., Canfora, E., Bernhofer, C., Kutsch, W., . . . Vesala, T. (2006). Towards a standardized processing of Net Ecosystem Exchange measured with eddy covariance technique: algorithms and uncertainty estimation. *Biogeosciences, 3*(4), 571-583. doi:https://doi.org/10.5194/bg-3-571-2006

Pastorello, G., Agarwal, D., Papale, D., Samak, T., Trotta, C., Ribeca, A., . . . Hollowgrass, R. (2014). *Observational data patterns for time series data quality assessment.* Paper presented at the 2014 IEEE 10th International Conference on e-Science.

Pei, Y., Dong, J., Zhang, Y., Yuan, W., Doughty, R., Yang, J., . . . Xiao, X. (2022). Evolution of light use efficiency models: Improvement, uncertainties, and implications. *Agricultural and Forest Meteorology, 317*, 108905. doi:https://doi.org/10.1016/j.agrformet.2022.108905

Peng, Y., Gitelson, A. A., & Sakamoto, T. (2013). Remote estimation of gross primary productivity in crops using MODIS 250 m data. *Remote Sensing of Environment, 128*, 186-196. doi:https://doi.org/10.1016/j.rse.2012.10.005

Piao, S., Friedlingstein, P., Ciais, P., Viovy, N., & Demarty, J. (2007). Growing season extension and its impact on terrestrial carbon cycle in the Northern Hemisphere over the past 2 decades. *Global biogeochemical cycles, 21*(3).

doi:https://doi.org/10.1029/2006GB002888

Piao, S., Sitch, S., Ciais, P., Friedlingstein, P., Peylin, P., Wang, X., . . . Cong, N. (2013). Evaluation of terrestrial carbon cycle models for their response to climate variability and to CO2 trends. *Global Change Biology, 19*(7), 2117-2132. doi:https://doi.org/10.1111/gcb.12187

Piao, S., Wang, X., Park, T., Chen, C., Lian, X. U., He, Y., . . . TÃ¸mmervik, H. (2020). Characteristics, drivers and feedbacks of global greening. *Nature Reviews Earth & Environment, 1*(1), 14-27. doi:https://doi.org/10.1038/s43017-019-0001-x

Potapov, P., Li, X., Hernandez-Serna, A., Tyukavina, A., Hansen, M. C., Kommareddy, A., . . . Silva, C. E. (2021). Mapping global forest canopy height through integration of GEDI and Landsat data. *Remote Sensing of Environment, 253*, 112165. doi:https://doi.org/10.1016/j.rse.2020.112165

Potter, C. S., Randerson, J. T., Field, C. B., Matson, P. A., Vitousek, P. M., Mooney, H. A., & Klooster, S. A. (1993). Terrestrial ecosystem production: a process model based on global satellite and surface data. *Global biogeochemical cycles, 7*(4), 811-841. doi:https://doi.org/10.1029/93GB02725

Prentice, I. C., Balzarolo, M., Bloomfield, K. J., Chen, J. M., Dechant, B., Ghent, D., . . . Ryu, Y. (2024). Principles for satellite monitoring of vegetation carbon uptake. *Nature Reviews Earth & Environment*, 1-15. doi:https://doi.org/10.1038/s43017-024-00601-6

Prentice, I. C., Dong, N., Gleason, S. M., Maire, V., & Wright, I. J. (2014). Balancing the costs of carbon gain and water transport: testing a new theoretical

framework for plant functional ecology. *Ecology letters, 17*(1), 82-91. doi:https://doi.org/10.1111/ele.12211

Press, W. H., & Teukolsky, S. A. (1990). Savitzky-Golay smoothing filters. *Computers in Physics, 4*(6), 669-672. doi:https://doi.org/10.1063/1.4822961

Qin, Y., Xiao, X., Wigneron, J.-P., Ciais, P., Canadell, J. G., Brandt, M., . . . Tang, H. (2021). Annual maps of forests in Australia from analyses of microwave and optical images with FAO forest definition. *Journal of Remote Sensing*. doi:10.34133/2021/9784657

Qin, Y., Xiao, X., Wigneron, J.-P., Ciais, P., Canadell, J. G., Brandt, M., . . . Tang, H. (2022). Large loss and rapid recovery of vegetation cover and aboveground biomass over forest areas in Australia during 2019–2020. *Remote Sensing of Environment, 278*, 113087. doi:https://doi.org/10.1016/j.rse.2022.113087

Quegan, S., Beer, C., Shvidenko, A., McCallum, I. A. N., Handoh, I. C., Peylin, P., . . . Schmullius, C. (2011). Estimating the carbon balance of central Siberia using a landscape-ecosystem approach, atmospheric inversion and Dynamic Global Vegetation Models. *Global Change Biology, 17*(1), 351-365. doi:https://doi.org/10.1111/j.1365-2486.2010.02275.x

Raich, J., Rastetter, E., Melillo, J. M., Kicklighter, D. W., Steudler, P., Peterson, B., . . . Vorosmarty, C. J. (1991). Potential net primary productivity in South America: application of a global model. *Ecological Applications, 1*(4), 399-429.

Ramankutty, N., A.T. Evan, C. Monfreda, and J.A. Foley. (2008). *Farming the planet: 1. Geographic distribution of global agricultural lands in the year 2000*.

Reichstein, M., Falge, E., Baldocchi, D., Papale, D., Aubinet, M., Berbigier, P., . . . Granier, A. (2005). On the separation of net ecosystem exchange into assimilation and ecosystem respiration: review and improved algorithm. *Global Change Biology, 11*(9), 1424-1439. doi:https://doi.org/10.1111/j.1365-2486.2005.001002.x

Richardson, A. D., Andy Black, T., Ciais, P., Delbart, N., Friedl, M. A., Gobron, N., . . . Luyssaert, S. (2010). Influence of spring and autumn phenological transitions on forest ecosystem productivity. *Philosophical Transactions of the Royal Society B: Biological Sciences, 365*(1555), 3227-3246. doi:https://doi.org/10.1098/rstb.2010.0102

Richardson, D., Black, A. S., Irving, D., Matear, R. J., Monselesan, D. P., Risbey, J. S., . . . Tozer, C. R. (2022). Global increase in wildfire potential from compound fire weather and drought. *NPJ climate and atmospheric science, 5*(1), 23. doi:https://doi.org/10.1038/s41612-022-00248-4

Richardson, D. M. (2000). *Ecology and biogeography of Pinus*: Cambridge University Press.

Rogers, A. (2014). The use and misuse of V c, max in Earth System Models. *Photosynthesis research, 119*, 15-29. doi:https://doi.org/10.1007/s11120-013-9818-1

Rogers, A., Medlyn, B. E., Dukes, J. S., Bonan, G., Von Caemmerer, S., Dietze, M. C., . . . Niinemets, Ü. (2017). A roadmap for improving the representation of photosynthesis in Earth system models. *New Phytologist, 213*(1), 22-42.

doi:https://doi.org/10.1111/nph.14283

Rogers, B. M., Soja, A. J., Goulden, M. L., & Randerson, J. T. (2015). Influence of tree species on continental differences in boreal fires and climate feedbacks. *Nature Geoscience, 8*(3), 228-234. doi:https://doi.org/10.1038/ngeo2352

Rouse, J. W., Haas, R. H., Schell, J. A., & Deering, D. W. (1974). Monitoring vegetation systems in the Great Plains with ERTS. *NASA Spec. Publ, 351*(1), 309. doi:https://doi.org/10.4236/ajps.2018.97101

Running, S. W., Nemani, R., Glassy, J. M., & Thornton, P. E. (1999). MODIS daily photosynthesis (PSN) and annual net primary production (NPP) product (MOD17) Algorithm Theoretical Basis Document. In.

Running, S. W., Nemani, R. R., Heinsch, F. A., Zhao, M., Reeves, M., & Hashimoto, H. (2004). A continuous satellite-derived measure of global terrestrial primary production. *Bioscience, 54*(6), 547-560. doi:https://doi.org/10.1641/0006-3568(2004)054[0547:ACSMOG]2.0.CO;2

Running, S. W., Thornton, P. E., Nemani, R., & Glassy, J. M. (2000). Global terrestrial gross and net primary productivity from the earth observing system. *Methods in ecosystem science*, 44-57. doi:https://doi.org/10.1007/978-1-4612-1224-9_4

Running, S. W., & Zhao, M. (2015). Daily GPP and annual NPP (MOD17A2/A3) products NASA Earth Observing System MODIS land algorithm. *MOD17 User's Guide, 2015*, 1-28.

Ryu, Y., Berry, J. A., & Baldocchi, D. D. (2019). What is global photosynthesis? History, uncertainties and opportunities. *Remote Sensing of Environment, 223*, 95-114.

doi:https://doi.org/10.1016/j.rse.2019.01.016

Ryu, Y., Jiang, C., Kobayashi, H., & Detto, M. (2018). MODIS-derived global land products of shortwave radiation and diffuse and total photosynthetically active radiation at 5 km resolution from 2000. *Remote Sensing of Environment, 204*, 812-825. doi:https://doi.org/10.1016/j.rse.2017.09.021

Sage, R. F., & Kubien, D. S. (2007). The temperature response of C3 and C4 photosynthesis. *Plant, cell & environment, 30*(9), 1086-1106. doi:https://doi.org/10.1111/j.1365-3040.2007.01682.x

Salazar-Martínez, D., Holwerda, F., Holmes, T. R., Yépez, E. A., Hain, C. R., Alvarado-Barrientos, S., . . . Figueroa-Espinoza, B. (2022). Evaluation of remote sensing-based evapotranspiration products at low-latitude eddy covariance sites. *Journal of hydrology, 610*, 127786. doi:https://doi.org/10.1016/j.jhydrol.2022.127786

Santos, A. J. B., Silva, G., Miranda, H. S., Miranda, A. C., & Lloyd, J. (2003). Effects of fire on surface carbon, energy and water vapour fluxes over campo sujo savanna in central Brazil. *Functional Ecology, 17*(6), 711-719. doi:https://doi.org/10.1111/j.1365-2435.2003.00790.x

Savitzky, A., & Golay, M. J. (1964). Smoothing and differentiation of data by simplified least squares procedures. *Analytical chemistry, 36*(8), 1627-1639.

Schaefer, K., Schwalm, C. R., Williams, C., Arain, M. A., Barr, A., Chen, J. M., . . . Hollinger, D. Y. (2012). A model-data comparison of gross primary productivity: Results from the North American Carbon Program site synthesis. *Journal of*

Geophysical Research: Biogeosciences, 117(G3). doi:https://doi.org/10.1029/2012JG001960

Schlemmer, M., Gitelson, A., Schepers, J., Ferguson, R., Peng, Y., Shanahan, J., & Rundquist, D. (2013). Remote estimation of nitrogen and chlorophyll contents in maize at leaf and canopy levels. *International Journal of Applied Earth Observation and Geoinformation, 25*, 47-54. doi:https://doi.org/10.1016/j.jag.2013.04.003

Scott, J. H. (2001). *Assessing crown fire potential by linking models of surface and crown fire behavior*: US Department of Agriculture, Forest Service, Rocky Mountain Research Station.

Sellers, P. J. (1985). Canopy reflectance, photosynthesis and transpiration. *International Journal of remote sensing, 6*(8), 1335-1372. doi:https://doi.org/10.1080/01431168508948283

Serbin, S. P., Ahl, D. E., & Gower, S. T. (2013). Spatial and temporal validation of the MODIS LAI and FPAR products across a boreal forest wildfire chronosequence. *Remote Sensing of Environment, 133*, 71-84. doi:https://doi.org/10.1016/j.rse.2013.01.022

Sitch, S., Friedlingstein, P., Gruber, N., Jones, S. D., Murray-Tortarolo, G., Ahlström, A., . . . Huntingford, C. (2015). Recent trends and drivers of regional sources and sinks of carbon dioxide. *Biogeosciences, 12*(3), 653-679. doi:https://doi.org/10.5194/bg-12-653-2015

Sitch, S., Smith, B., Prentice, I. C., Arneth, A., Bondeau, A., Cramer, W., . . . Sykes, M.

T. (2003). Evaluation of ecosystem dynamics, plant geography and terrestrial carbon cycling in the LPJ dynamic global vegetation model. *Global Change Biology, 9*(2), 161-185. doi:https://doi.org/10.1046/j.1365-2486.2003.00569.x

Sperry, J. S., Venturas, M. D., Todd, H. N., Trugman, A. T., Anderegg, W. R., Wang, Y., & Tai, X. (2019). The impact of rising CO2 and acclimation on the response of US forests to global warming. *Proceedings of the National Academy of Sciences, 116*(51), 25734-25744. doi:https://doi.org/10.1073/pnas.1913072116

Stevens-Rumann, C. S., Kemp, K. B., Higuera, P. E., Harvey, B. J., Rother, M. T., Donato, D. C., . . . Veblen, T. T. (2018). Evidence for declining forest resilience to wildfires under climate change. *Ecology letters, 21*(2), 243-252. doi:https://doi.org/10.1111/ele.12889

Still, C. J., J.A. Berry, G.J. Collatz, and R.S. DeFries. (2009). *ISLSCP II C4 Vegetation Percentage*.

Sulla-Menashe, D., & Friedl, M. A. (2018). User guide to collection 6 MODIS land cover (MCD12Q1 and MCD12C1) product. *Usgs: Reston, Va, Usa, 1*, 18. doi:https://doi.org/10.5067/MODIS/MCD12Q1.006

Sun, Q., Meyer, W. S., Koerber, G. R., & Marschner, P. (2016). A wildfire event influences ecosystem carbon fluxes but not soil respiration in a semi-arid woodland. *Agricultural and Forest Meteorology, 226*, 57-66. doi:https://doi.org/10.1016/j.agrformet.2016.05.019

Sun, Z., Wang, X., Zhang, X., Tani, H., Guo, E., Yin, S., & Zhang, T. (2019). Evaluating and comparing remote sensing terrestrial GPP models for their response to

climate variability and CO2 trends. *Science of The Total Environment, 668*, 696-713. doi:https://doi.org/10.1016/j.scitotenv.2019.03.025

Tagesson, T., Schurgers, G., Horion, S., Ciais, P., Tian, F., Brandt, M., . . . Olin, S. (2020). Recent divergence in the contributions of tropical and boreal forests to the terrestrial carbon sink. *Nature ecology & evolution, 4*(2), 202-209. doi:https://doi.org/10.1038/s41559-019-1090-0

Tagesson, T., Tian, F., Schurgers, G., Horion, S., Scholes, R., AhlstrÃ¶m, A., . . . Olin, S. (2021). A physiologyâ€□based Earth observation model indicates stagnation in the global gross primary production during recent decades. *Global Change Biology, 27*(4), 836-854. doi:https://doi.org/10.1111/gcb.15424

Tepley, A. J., Thomann, E., Veblen, T. T., Perry, G. L. W., Holz, A., Paritsis, J., . . . Anderson-Teixeira, K. J. (2018). Influences of fire–vegetation feedbacks and post-fire recovery rates on forest landscape vulnerability to altered fire regimes. *Journal of Ecology, 106*(5), 1925-1940. doi:https://doi.org/10.1111/1365-2745.12950

Tramontana, G., Jung, M., Schwalm, C. R., Ichii, K., Camps-Valls, G., Ráduly, B., . . . Kiely, G. (2016). Predicting carbon dioxide and energy fluxes across global FLUXNET sites with regression algorithms. *Biogeosciences, 13*(14), 4291-4313. doi:https://doi.org/10.5194/bg-13-4291-2016

Trueba, S., Théroux-Rancourt, G., Earles, J. M., Buckley, T. N., Love, D., Johnson, D. M., & Brodersen, C. (2022). The three-dimensional construction of leaves is coordinated with water use efficiency in conifers. *New Phytologist, 233*(2), 851-

861. doi:https://doi.org/10.1111/nph.17772

Turner, D. P., Ritts, W. D., Cohen, W. B., Gower, S. T., Running, S. W., Zhao, M., . . . Saleska, S. R. (2006). Evaluation of MODIS NPP and GPP products across multiple biomes. *Remote Sensing of Environment, 102*(3-4), 282-292. doi:https://doi.org/10.1016/j.rse.2006.02.017

Turner, D. P., Ritts, W. D., Cohen, W. B., Gower, S. T., Zhao, M., Running, S. W., . . . Munger, J. W. (2003). Scaling gross primary production (GPP) over boreal and deciduous forest landscapes in support of MODIS GPP product validation. *Remote Sensing of Environment, 88*(3), 256-270. doi:https://doi.org/10.1016/j.rse.2003.06.005

Turner, M. G. (2010). Disturbance and landscape dynamics in a changing world. *Ecology, 91*(10), 2833-2849. doi:https://doi.org/10.1890/10-0097.1

van der Velde, I. R., van der Werf, G. R., Houweling, S., Maasakkers, J. D., Borsdorff, T., Landgraf, J., . . . Hoogeveen, R. (2021). Vast CO2 release from Australian fires in 2019–2020 constrained by satellite. *Nature, 597*(7876), 366-369. doi:https://doi.org/10.1038/s41586-021-03712-y

Van Der Werf, G. R., Randerson, J. T., Giglio, L., Van Leeuwen, T. T., Chen, Y., Rogers, B. M., . . . Collatz, G. J. (2017). Global fire emissions estimates during 1997–2016. *Earth System Science Data, 9*(2), 697-720. doi:https://doi.org/10.5194/essd-9-697-2017

Vermote, E. (2021). MODIS/Terra Surface Reflectance 8-Day L3 Global 500 m SIN Grid V061. *NASA EOSDIS Land Processes DAAC: Missoula, MT, USA*.

doi:https://doi.org/10.5067/MODIS/MOD09A1.061

Vermote, E. F. (2015). MOD09A1 MODIS/Terra Surface Reflectance 8-Day L3 Global 500m SIN Grid V006 [Data set]. NASA EOSDIS Land Processes Distributed Active Archive Center. Accessed 2024-09-16 from. doi:https://doi.org/10.5067/MODIS/MOD09A1.006

Vieira, S. T., Davis, K. T., Holden, Z. A., Larson, A. J., & Higuera, P. E. (2024). Western larch regeneration more sensitive to wildfire-related factors than seasonal climate variability. *Forest ecology and management, 565*, 122011. doi:https://doi.org/10.1016/j.foreco.2024.122011

Villalobos, Y., Canadell, J. G., Keller, E. D., Briggs, P. R., Bukosa, B., Giltrap, D. L., . . . Lauerwald, R. (2023). A comprehensive assessment of anthropogenic and natural sources and sinks of Australasia's carbon budget. *Global biogeochemical cycles, 37*(12), e2023GB007845. doi:https://doi.org/10.1029/2023GB007845

Viovy, N., Arino, O., & Belward, A. (1992). The Best Index Slope Extraction (BISE): A method for reducing noise in NDVI time-series. *International Journal of remote sensing, 13*(8), 1585-1590. doi:https://doi.org/10.1080/01431169208904212

Virkkala, A.-M., Rogers, B. M., Watts, J. D., Arndt, K. A., Potter, S., Wargowsky, I., . . . Boike, J. (2025). Wildfires offset the increasing but spatially heterogeneous Arctic–boreal CO2 uptake. *Nature Climate Change*, 1-8. doi:https://doi.org/10.1038/s41558-024-02234-5

Wagle, P., Xiao, X., & Suyker, A. E. (2015). Estimation and analysis of gross primary production of soybean under various management practices and drought conditions. *ISPRS Journal of Photogrammetry and Remote Sensing, 99*, 70-83. doi:https://doi.org/10.1016/j.isprsjprs.2014.10.009

Wagle, P., Xiao, X., Torn, M. S., Cook, D. R., Matamala, R., Fischer, M. L., . . . Biradar, C. (2014). Sensitivity of vegetation indices and gross primary production of tallgrass prairie to severe drought. *Remote Sensing of Environment, 152*, 1-14. doi:https://doi.org/10.1016/j.rse.2014.05.010

Wagle, P., Zhang, Y., Jin, C., & Xiao, X. (2016). Comparison of solar-induced chlorophyll fluorescence, light-use efficiency, and process-based GPP models in maize. *Ecological Applications, 26*(4), 1211-1222. doi:https://doi.org/10.1890/15-1434

Walker, A. P., De Kauwe, M. G., Bastos, A., Belmecheri, S., Georgiou, K., Keeling, R. F., . . . Norby, R. J. (2021). Integrating the evidence for a terrestrial carbon sink caused by increasing atmospheric CO2. *New Phytologist, 229*(5), 2413-2445. doi:https://doi.org/10.1111/nph.16866

Walker, X. J., Baltzer, J. L., Cumming, S. G., Day, N. J., Ebert, C., Goetz, S., . . . Schuur, E. A. G. (2019). Increasing wildfires threaten historic carbon sink of boreal forest soils. *Nature, 572*(7770), 520-523. doi:https://doi.org/10.1038/s41586-019-1474-y

Wan, Z., Hook, S., Hulley, G. (2021). *MODIS/Aqua Land Surface Temperature/Emissivity 8-Day L3 Global 1km SIN Grid V061*.

Wang, B., Chen, W., Tian, D., Li, Z., Wang, J., Fu, Z., . . . Niu, S. (2023). Dryness limits vegetation pace to cope with temperature change in warm regions. *Global Change Biology, 29*(17), 4750-4757.

Wang, H., Prentice, I. C., Keenan, T. F., Davis, T. W., Wright, I. J., Cornwell, W. K., . . . Peng, C. (2017). Towards a universal model for carbon dioxide uptake by plants. *Nature Plants, 3*(9), 734-741. doi:https://doi.org/10.1038/s41477-017-0006-8

Wang, J., Xiao, X., Liu, L., Wu, X., Qin, Y., Steiner, J. L., & Dong, J. (2020). Mapping sugarcane plantation dynamics in Guangxi, China, by time series Sentinel-1, Sentinel-2 and Landsat images. *Remote Sensing of Environment, 247*, 111951.

Wang, J., Xiao, X., Zhang, Y., Qin, Y., Doughty, R. B., Wu, X., . . . Du, L. (2018). Enhanced gross primary production and evapotranspiration in juniper-encroached grasslands. *Global Change Biology, 24*(12), 5655-5667. doi:https://doi.org/10.1111/gcb.14441

Wang, J. A., Sulla-Menashe, D., Woodcock, C. E., Sonnentag, O., Keeling, R. F., & Friedl, M. A. (2020). Extensive land cover change across Arctic–Boreal Northwestern North America from disturbance and climate forcing. *Global Change Biology, 26*(2), 807-822. doi:https://doi.org/10.1111/gcb.14804

Wang, Z., Xiao, X., & Yan, X. (2010). Modeling gross primary production of maize cropland and degraded grassland in northeastern China. *Agricultural and Forest Meteorology, 150*(9), 1160-1167. doi:https://doi.org/10.1016/j.agrformet.2010.04.015

Welp, L. R., Keeling, R. F., Meijer, H. A., Bollenbacher, A. F., Piper, S. C., Yoshimura,

K., . . . Wahlen, M. (2011). Interannual variability in the oxygen isotopes of atmospheric CO2 driven by El Niño. *Nature, 477*(7366), 579-582. doi:https://doi.org/10.1038/nature10421

Welp, L. R., Keeling, R. F., Meijer, H. A. J., Bollenbacher, A. F., Piper, S. C., Yoshimura, K., . . . Wahlen, M. (2011a). Interannual variability in the oxygen isotopes of atmospheric CO2 driven by El NiÃ±o. *Nature, 477*(7366), 579-582. doi:https://doi.org/10.1038/nature10421

Welp, L. R., Keeling, R. F., Meijer, H. A. J., Bollenbacher, A. F., Piper, S. C., Yoshimura, K., . . . Wahlen, M. (2011b). Interannual variability in the oxygen isotopes of atmospheric CO2 driven by El Niño. *Nature, 477*(7366), 579-582. doi:https://doi.org/10.1038/nature10421

Wilkinson, S. L., Andersen, R., Moore, P. A., Davidson, S. J., Granath, G., & Waddington, J. M. (2023). Wildfire and degradation accelerate northern peatland carbon release. *Nature Climate Change, 13*(5), 456-461. doi:https://doi.org/10.1038/s41558-023-01657-w

Williams, R. J., Hutley, L. B., Cook, G. D., Russell-Smith, J., Edwards, A., & Chen, X. (2004). Assessing the carbon sequestration potential of mesic savannas in the Northern Territory, Australia: approaches, uncertainties and potential impacts of fire. *Functional Plant Biology, 31*(5), 415-422. doi:https://doi.org/10.1071/FP03215

Woodgate, W., Phinn, S., Devereux, T., & Aryal, R. R. (2025). Bushfire recovery at a long-term tall eucalypt flux site through the lens of a satellite: Combining multi-

scale data for structural-functional insight. *Remote Sensing of Environment, 317*, 114530. doi:https://doi.org/10.1016/j.rse.2024.114530

Wu, G., Guan, K., Jiang, C., Peng, B., Kimm, H., Chen, M., . . . Bernacchi, C. J. (2020). Radiance-based NIRv as a proxy for GPP of corn and soybean. *Environmental Research Letters, 15*(3), 034009.

Wu, J. B., Xiao, X. M., Guan, D. X., Shi, T. T., Jin, C. J., & Han, S. J. (2009). Estimation of the gross primary production of an old-growth temperate mixed forest using eddy covariance and remote sensing. *International Journal of remote sensing, 30*(2), 463-479. doi:https://doi.org/10.1080/01431160802372143

Wu, X., Xiao, X., Yang, Z., Wang, J., Steiner, J., & Bajgain, R. (2021). Spatial-temporal dynamics of maize and soybean planted area, harvested area, gross primary production, and grain production in the Contiguous United States during 2008-2018. *Agricultural and Forest Meteorology, 297*, 108240. doi:https://doi.org/10.1016/j.agrformet.2020.108240

Wu, X., Xiao, X., Zhang, Y., He, W., Wolf, S., Chen, J., . . . Zhou, Y. (2018). Spatiotemporal consistency of four gross primary production products and solar-induced chlorophyll fluorescence in response to climate extremes across CONUS in 2012. *Journal of Geophysical Research: Biogeosciences, 123*(10), 3140-3161. doi:https://doi.org/10.1029/2018JG004484

Xia, J., Niu, S., Ciais, P., Janssens, I. A., Chen, J., Ammann, C., . . . Bonal, D. (2015). Joint control of terrestrial gross primary productivity by plant phenology and physiology. *Proceedings of the National Academy of Sciences, 112*(9), 2788-

2793. doi:https://doi.org/10.1073/pnas.14130901

Xiao, X. (2006). Light absorption by leaf chlorophyll and maximum light use efficiency. *IEEE Transactions on Geoscience and Remote Sensing, 44*(7), 1933-1935. doi:https://doi.org/10.1109/TGRS.2006.874796.

Xiao, X., Hollinger, D., Aber, J., Goltz, M., Davidson, E. A., Zhang, Q., & Moore III, B. (2004). Satellite-based modeling of gross primary production in an evergreen needleleaf forest. *Remote Sensing of Environment, 89*(4), 519-534. doi:https://doi.org/10.1016/j.rse.2003.11.008

Xiao, X., Zhang, Q., Braswell, B., Urbanski, S., Boles, S., Wofsy, S., . . . Ojima, D. (2004). Modeling gross primary production of temperate deciduous broadleaf forest using satellite images and climate data. *Remote Sensing of Environment, 91*(2), 256-270. doi:https://doi.org/10.1016/j.rse.2004.03.010

Xiao, X., Zhang, Q., Hollinger, D., Aber, J., & Moore Iii, B. (2005). Modeling gross primary production of an evergreen needleleaf forest using MODIS and climate data. *Ecological Applications, 15*(3), 954-969. doi:https://doi.org/10.1890/04-0470

Xie, S., Mo, X., Hu, S., & Liu, S. (2020). Contributions of climate change, elevated atmospheric CO2 and human activities to ET and GPP trends in the Three-North Region of China. *Agricultural and Forest Meteorology, 295*, 108183. doi:https://doi.org/10.1016/j.agrformet.2020.108183

Xin, F., Xiao, X., Cabral, O. M. R., White Jr, P. M., Guo, H., Ma, J., . . . Zhao, B. (2020). Understanding the land surface phenology and gross primary production of

sugarcane plantations by eddy flux measurements, MODIS images, and data-driven models. *Remote Sensing, 12*(14), 2186. doi:https://doi.org/10.3390/rs12142186

Xin, F., Xiao, X., Dong, J., Zhang, G., Zhang, Y., Wu, X., . . . Du, G. (2020). Large increases of paddy rice area, gross primary production, and grain production in Northeast China during 2000–2017. *Science of The Total Environment, 711*, 135183. doi:https://doi.org/10.1016/j.scitotenv.2019.135183

Xin, F., Xiao, X., Zhao, B., Miyata, A., Baldocchi, D., Knox, S., . . . Chen, B. (2017). Modeling gross primary production of paddy rice cropland through analyses of data from CO2 eddy flux tower sites and MODIS images. *Remote Sensing of Environment, 190*, 42-55. doi:https://doi.org/10.1016/j.rse.2016.11.025

Xu, H., Chen, H. W., Chen, D., Wang, Y., Yue, X., He, B., . . . Huang, L. (2024). Global patterns and drivers of post-fire vegetation productivity recovery. *Nature Geoscience*, 1-8. doi:https://doi.org/10.1038/s41561-024-01520-3

Yamori, W., Hikosaka, K., & Way, D. A. (2014). Temperature response of photosynthesis in C 3, C 4, and CAM plants: temperature acclimation and temperature adaptation. *Photosynthesis research, 119*, 101-117. doi:https://doi.org/10.1007/s11120-013-9874-6

Yamori, W., Noguchi, K., Hikosaka, K., & Terashima, I. (2010). Phenotypic plasticity in photosynthetic temperature acclimation among crop species with different cold tolerances. *Plant Physiology, 152*(1), 388-399. doi:https://doi.org/10.1104/pp.109.145862

Yan, H., Fu, Y., Xiao, X., Huang, H. Q., He, H., & Ediger, L. (2009). Modeling gross primary productivity for winter wheat–maize double cropping system using MODIS time series and CO2 eddy flux tower data. *Agriculture, ecosystems & environment, 129*(4), 391-400. doi:https://doi.org/10.1016/j.agee.2008.10.017

Yan, H., Wang, S.-q., Billesbach, D., Oechel, W., Bohrer, G., Meyers, T., . . . Rahman, F. (2015). Improved global simulations of gross primary product based on a new definition of water stress factor and a separate treatment of C3 and C4 plants. *Ecological Modelling, 297*, 42-59. doi:https://doi.org/10.1016/j.ecolmodel.2014.11.002

Yang, K., Ryu, Y., Dechant, B., Berry, J. A., Hwang, Y., Jiang, C., . . . Kornfeld, A. (2018). Sun-induced chlorophyll fluorescence is more strongly related to absorbed light than to photosynthesis at half-hourly resolution in a rice paddy. *Remote Sensing of Environment, 216*, 658-673. doi:https://doi.org/10.1016/j.rse.2018.07.008

Yang, X., Tang, J., Mustard, J. F., Lee, J. E., Rossini, M., Joiner, J., . . . Richardson, A. D. (2015). Solar-induced chlorophyll fluorescence that correlates with canopy photosynthesis on diurnal and seasonal scales in a temperate deciduous forest. *Geophysical Research Letters, 42*(8), 2977-2987. doi:https://doi.org/10.1002/2015GL063201

Yin, S. (2020). Biomass burning spatiotemporal variations over South and Southeast Asia. *Environment International, 145*, 106153. doi:https://doi.org/10.1016/j.envint.2020.106153

Yuan, W., Liu, S., Zhou, G., Zhou, G., Tieszen, L. L., Baldocchi, D., . . . Goulden, M. L. (2007). Deriving a light use efficiency model from eddy covariance flux data for predicting daily gross primary production across biomes. *Agricultural and Forest Meteorology, 143*(3-4), 189-207. doi:https://doi.org/10.1016/j.agrformet.2006.12.001

Yuan, W., Luo, Y., Liang, S., Yu, G., Niu, S., Stoy, P., . . . Gough, C. M. (2011). Thermal adaptation of net ecosystem exchange. *Biogeosciences, 8*(6), 1453-1463.

Yue, C., Ciais, P., Cadule, P., Thonicke, K., Archibald, S., Poulter, B., . . . Friedlingstein, P. (2014). Modelling the role of fires in the terrestrial carbon balance by incorporating SPITFIRE into the global vegetation model ORCHIDEEâ€“Part 1: simulating historical global burned area and fire regimes. *Geoscientific Model Development, 7*(6), 2747-2767. doi:https://doi.org/10.5194/gmd-7-2747-2014

Yue, S., Pilon, P., & Cavadias, G. (2002). Power of the Mann–Kendall and Spearman's rho tests for detecting monotonic trends in hydrological series. *Journal of hydrology, 259*(1-4), 254-271. doi:https://doi.org/10.1016/S0022-1694(01)00594-7

Zhang-Zheng, H., Adu-Bredu, S., Duah-Gyamfi, A., Moore, S., Addo-Danso, S. D., Amissah, L., . . . Quansah, J. (2024). Contrasting carbon cycle along tropical forest aridity gradients in West Africa and Amazonia. *Nature communications, 15*(1), 3158. doi:https://doi.org/10.1038/s41467-024-47202-x

Zhang, Y., & Biswas, A. (2017). The effects of forest fire on soil organic matter and

nutrients in boreal forests of North America: a review. *Adaptive soil management: from theory to practices*, 465-476. doi:https://doi.org/10.1007/978-981-10-3638-5_21

Zhang, Y., Guanter, L., Berry, J. A., van der Tol, C., Yang, X., Tang, J., & Zhang, F. (2016). Model-based analysis of the relationship between sun-induced chlorophyll fluorescence and gross primary production for remote sensing applications. *Remote Sensing of Environment, 187*, 145-155. doi:https://doi.org/10.1016/j.rse.2016.10.016

Zhang, Y., & Peñuelas, J. (2023). Combining solar-induced chlorophyll fluorescence and optical vegetation indices to better understand plant phenological responses to global change. *Journal of Remote Sensing, 3*, 0085. doi:https://doi.org/10.34133/remotesensing.0085

Zhang, Y., Xiao, X., Jin, C., Dong, J., Zhou, S., Wagle, P., . . . Zhang, G. (2016). Consistency between sun-induced chlorophyll fluorescence and gross primary production of vegetation in North America. *Remote Sensing of Environment, 183*, 154-169. doi:https://doi.org/10.1016/j.rse.2016.05.015

Zhang, Y., Xiao, X., Wu, X., Zhou, S., Zhang, G., Qin, Y., & Dong, J. (2017). A global moderate resolution dataset of gross primary production of vegetation for 2000–2016. *Scientific data, 4*(1), 1-13. doi:https://doi.org/10.1038/sdata.2017.165

Zhao, J., Yue, C., Wang, J., & Hantson, S. (2024). Forest fire size amplifies postfire land surface warming. *Nature*(633), 828-834. doi:https://doi.org/10.1038/s41586-024-07918-8

Zhao, J., Yue, C., Wang, J., Hantson, S., Wang, X., He, B., . . . Luyssaert, S. (2024). Forest fire size amplifies postfire land surface warming. *Nature, 633*(8031), 828-834. doi:https://doi.org/10.1038/s41586-024-07918-8

Zhao, M., Heinsch, F. A., Nemani, R. R., & Running, S. W. (2005). Improvements of the MODIS terrestrial gross and net primary production global data set. *Remote Sensing of Environment, 95*(2), 164-176. doi:https://doi.org/10.1016/j.rse.2004.12.011

Zhao, W., Yu, X., Jiao, C., Xu, C., Liu, Y., & Wu, G. (2021). Increased association between climate change and vegetation index variation promotes the coupling of dominant factors and vegetation growth. *Science of The Total Environment, 767*, 144669. doi:https://doi.org/10.1016/j.scitotenv.2020.144669

Zheng, B., Ciais, P., Chevallier, F., Yang, H., Canadell, J. G., Chen, Y., . . . Davis, S. J. (2023). Record-high CO2 emissions from boreal fires in 2021. *Science, 379*(6635), 912-917. doi:10.1126/science.ade0805

Zheng, Y., Shen, R., Wang, Y., Li, X., Liu, S., Liang, S., . . . Yuan, W. (2020a). Improved estimate of global gross primary production for reproducing its long-term variation, 1982–2017. *Earth System Science Data, 12*(4), 2725-2746. doi:https://doi.org/10.5194/essd-12-2725-2020

Zheng, Y., Shen, R., Wang, Y., Li, X., Liu, S., Liang, S., . . . Yuan, W. (2020b). Improved estimate of global gross primary production for reproducing its long-term variation, 1982â€“2017. *Earth System Science Data, 12*(4), 2725-2746. doi:https://doi.org/10.5194/essd-12-2725-2020

Zheng, Y., Zhang, L., Xiao, J., Yuan, W., Yan, M., Li, T., & Zhang, Z. (2018). Sources of uncertainty in gross primary productivity simulated by light use efficiency models: Model structure, parameters, input data, and spatial resolution. *Agricultural and Forest Meteorology, 263*, 242-257. doi:https://doi.org/10.1016/j.agrformet.2018.08.003

Zhu, J., Xie, A., Qin, X., Wang, Y., Xu, B., & Wang, Y. (2021). An assessment of ERA5 reanalysis for Antarctic near-surface air temperature. *Atmosphere, 12*(2), 217. doi:https://doi.org/10.3390/atmos12020217

Zhu, Z., Piao, S., Myneni, R. B., Huang, M., Zeng, Z., Canadell, J. G., . . . Arneth, A. (2016). Greening of the Earth and its drivers. *Nature Climate Change, 6*(8), 791-795. doi:https://doi.org/10.1038/nclimate3004

Zong, X., Tian, X., Liu, X., & Shu, L. (2024). Drought threat to terrestrial gross primary production exacerbated by wildfires. *Communications Earth & Environment, 5*(1), 225. doi:https://doi.org/10.1038/s43247-024-01406-7

Zou, K. H., Tuncali, K., & Silverman, S. G. (2003). Correlation and simple linear regression. *Radiology, 227*(3), 617-628. doi:https://doi.org/10.1148/radiol.2273011499